

SUBSURFACE IMPACT OF CO₂

**Response of carbonate rocks and
wellbore cement to supercritical
CO₂ injection and long-term storage**

**Geologica Ultraiectina
Mededelingen van de
Faculteit Aardwetenschappen
der Rijksuniversiteit te Utrecht
Nr. 310**

The research described in this thesis was carried out under the program – Geo-Energie Project 5B of Utrecht Center of Geosciences (UCG) and was a part of the Dutch national research program on CO₂ Capture, Transport and Storage (CATO).

This research was carried out at:
Experimental Rock Deformation Laboratory (HPT) Lab
Faculty of Geosciences, Department of Earth Sciences
Utrecht University,
Budapestlaan 4,
PO Box 80.021,
3508 TA UTRECHT,
THE NETHERLANDS.

@ 2009 Emilia Liteanu
ISBN/EAN: 978-90-5744-171-4

SUBSURFACE IMPACT OF CO₂

response of carbonate rocks and wellbore cement to supercritical CO₂ injection and long-term storage

Proefschrift

ter verkrijging van de graad van doctor aan de Universiteit
Utrecht op gezag van de rector magnificus, prof.dr. J.C. Stoof,
ingevolge het besluit van het college voor promoties in het
openbaar te verdedigen op dinsdag 15 december 2009 des
middags te 2.30 uur

door

Emilia Liteanu

geboren op 1 Januari 1977
te Boekarest, Roemenie

Promotor: Prof.dr. C. J. Spiers
Co-promotoren: Dr. C. J. Peach
Dr. J.H.P de Bresser

Members of the dissertation committee:

PROF. DR. T. AUSTAD (University of Stavanger, Norway)
DR. B. G. KUTCHKO (U.S. Department of Energy, United States of America)
PROF. DR. F. RENARD (Université Joseph Fourier, Grenoble, France)
PROF. T.-F. WONG (State University of New York at Stony Brook, United States of America)
PROF. DR. R. ZIMMERMAN (Imperial College London, UK)

Familiei mele

**"To achieve the impossible, it
is precisely the unthinkable
that must be thought."**

Tom Robbins



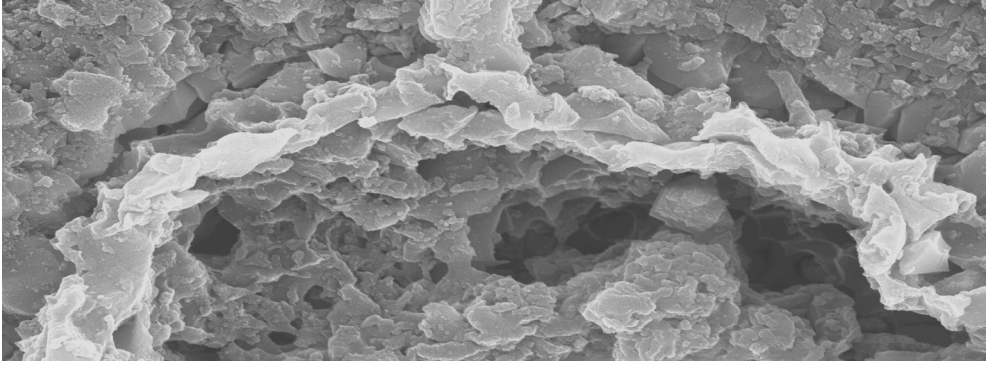
"Humanity has advanced, when it has advanced, not because it has been sober, responsible, and cautious, but because it has been playful, rebellious, and immature."

Tom Robbins

CONTENTS

SUMMARY

1. INTRODUCTION: PROBLEM STATEMENT AND AIMS.....	1
2. THE EFFECT OF SUPERCRITICAL CO ₂ ON CREEP OF WET CALCITE AGGREGATES.....	15
3. INFLUENCE OF PORE FLUID SALT CONTENT ON COMPACTION CREEP OF CALCITE AGGREGATES IN THE PRESENCE OF CO ₂	53
4. THE INFLUENCE OF WATER AND SUPERCRITICAL CO ₂ ON THE FAILURE BEHAVIOR OF CHALK.....	81
5. MECHANICAL FAILURE OF WELLBORE CEMENT AND THE INFLUENCE OF SUPERCRITICAL CO ₂	109
6. HEALING/SEALING AND TRANSPORT PROPERTIES OF WELLBORE CEMENT IN THE PRESENCE OF CO ₂	149
7. GENERAL CONCLUSIONS AND SUGGESTIONS FOR FURTHER WORK.....	177
ACKNOWLEDGMENTS	185



S U M M A R Y

Capture of CO₂ at fossil fuel power stations, coupled with geological storage in empty oil and gas reservoirs is widely viewed as the most promising option for reducing CO₂ emissions to the atmosphere, i.e. for climate change mitigation. Injection of CO₂ into such reservoirs will change their chemical and mechanical state, for example through acidification of the pore fluid or changes in the state of stress. Similar effects may influence the integrity of overlying caprocks and of plugged wells. To fully assess storage system integrity, these effects must be understood. Gaining insight into the mechanisms triggered or enhanced by CO₂ injection and storage, and acquiring knowledge on the porosity/permeability evolution or the coupled chemical and mechanical behaviour of such complex systems, are therefore vital for site characterization and performance evaluation.

This research aims at investigating the mechanisms occurring in carbonate rich reservoirs (i.e. limestones, carbonate-cemented sandstones or chalks) and in wellbore cements, in the context of supercritical CO₂ injection and storage. The following types of experimental investigations were employed: compaction experiments on simulated porous carbonates in order to investigate time-dependent compaction phenomena, triaxial compression tests to determine the mechanical failure behaviour of chalks and wellbore cements, and reaction experiments to explore the long-term chemical effects of CO₂ on cement.

The main aims are presented in **Chapter 1**, together with a general background on the geological storage of CO₂ in depleted oil and gas reservoirs. The following chapter, **Chapter 2** focuses on the coupled chemical and mechanical effects of supercritical CO₂ granular calcite, i.e. simulated carbonate reservoir materials. Uniaxial compaction tests were performed on these materials, employing grain sizes ranging from 1 to 250 μm, under dry, and wet conditions, and with supercritical CO₂ injected into wet samples (wet/CO₂ tests) at temperatures in the range 28-100°C, effective stresses between 4 and 40 MPa and CO₂ (partial) pressures in the range $4 \cdot 10^{-5}$ - 10 MPa. The experiments were designed to investigate whether compaction creep is accelerated by increasing CO₂ partial pressure in wet carbonate rocks, what the mechanisms responsible for such acceleration might be, and what the effect of pore fluid content is on compaction creep in the presence of supercritical CO₂. Dry samples showed nearly instantaneous, time independent compaction, with little or no measurable creep thereafter. In contrast, wet samples showed significant creep at volumetric strain rates ranging from 10⁻⁵ to 10⁻⁹ s⁻¹, depending on conditions. The mechanical data obtained for wet samples, along with microstructural evidence and modeling considerations, suggest that compaction creep involved subcritical microcracking and probably a component of intergranular pressure solution. Compaction creep of wet samples was accelerated by injection of supercritical CO₂. However, loading of wet samples in the presence of supercritical CO₂ from the start of the experiments led to time-dependent compaction, with strain rates being dependent on grain size, stress, CO₂ partial pressure and temperature. The strain rates varied inversely with grain size, for grain size below 106

μm , while for grain sizes above $106\ \mu\text{m}$, the strain rates increase with increasing grain size. This behavior together with microstructural evidence, such as sutured contacts, truncated or indented grains as well as microcracks, suggests that microcracking and intergranular pressure solution creep operate in parallel and that the fastest mechanism controls the overall deformation rate. In the fine-grained material, pressure solution creep rates are faster than microcracking, while microcracking is favored at coarser grain size (above $106\ \mu\text{m}$). In the pressure solution regime, the rate of creep was clearly accelerated by increasing the partial pressure of CO_2 , qualitatively confirming expectations for diffusion controlled pressure solution based on modeling studies. The results imply that under *in-situ* conditions, if measurable compaction creep occurs in a carbonate reservoir, such creep can be enhanced by up to 50 times when CO_2 pressure is increased up to 10 MPa, notably when deformation occur by pressure solution creep.

In **Chapter 3**, the uniaxial compaction creep behaviour of wet calcite aggregates is investigated further in the presence of both CO_2 and added salts. Addition NaCl or MgCl_2 only caused a reduction in the compaction creep rate, relative to wet samples compacted with CO_2 only, at low salt concentrations (0.6-1 M). However, salt concentrations in the range 2 to 3 M, led to an increase in creep rates to values approaching or even exceeding those obtained in salt-free experiments. The deceleration of creep, at low salt concentrations, likely, reflects a slowing of pressure solution. On the basis of microstructural evidence, the increase in strain rate at high salt concentrations was attributed to a relative enhancement of the role of subcritical crack growth. The results findings suggest that, for typical formation fluid salt concentrations (0.5 – 1 M), storage of CO_2 in highly porous carbonate formations has the potential to increase creep rates by up to ten times.

Chapter 4 focuses on investigating the effect of supercritical CO_2 on the mechanical stability and failure mode of chalks by means of triaxial compression experiments. The tests were carried out on Maastricht chalk cores under dry conditions, in the presence of saturated chalk solution (i.e. wet), and with fluid pressurized with CO_2 , at temperatures simulating reservoir conditions (20-80°C) and effective confining pressures varying between 0.5 and 7 MPa. At low mean effective stresses (<3 MPa), most of the samples failed in shear failure mode, on a single macroscopic shear fracture, giving way at higher mean effective stresses (> 4 MPa) to compaction and pore collapse. Increasing temperature from 20 to 80°C did not show any significant effects on the strength of the dry samples. Addition of aqueous solution to the samples led to drastic weakening of the chalk, the effect being more pronounced at high effective confining pressures ($P_{eff} > 3\ \text{MPa}$). Addition of 10 MPa supercritical CO_2 to the wet samples did not produce any significant additional effect in comparison with the wet samples. The weakening effect of aqueous solution was explained in terms of reduction in frictional resistance of the material, due to water-enhanced grain-contact cracking, and perhaps pressure solution, with a possible contribution by disjoining pressure effects caused by water adsorption. While CO_2 does not seem to reduce short term failure strength of chalk, processes such as intergranular

pressure solution have to be considered for assessing mechanical stability of chalk, in the context of long term CO₂ storage or EOR/EGR operations.

While the previous chapters deal mainly with the response of carbonate reservoir rocks to CO₂ injection, **Chapters 5 and 6** addresses the influence of CO₂ on the mechanical stability and on the sealing/healing capacity of wellbore cements. **Chapter 5** addresses the influence of water and of combined water and CO₂ (wet/ CO₂ tests) on the compressive strength of wellbore cement by means of conventional triaxial deformation tests performed on standard, Portland Class A wellbore cement. The tests were carried out on dry samples, wet samples, combining fluid (water) in equilibrium with the cement, and on wet samples with added supercritical CO₂. *In-situ* conditions were simulated using temperatures of 20 and 80°C, effective confining pressures of 1.5-30 MPa, and pore fluid pressures up to 10 MPa. The results demonstrated that under dry, wet and wet/CO₂ conditions, Class A cement samples fail in a brittle manner marked by localized shear fracture at low (effective) confining pressures (1.5 to 10 MPa). At higher confining pressures, the samples failed in a ductile manner, characterized by pervasive compactional deformation and strain hardening. The compressive strength of the dried samples was insensitive to temperature, but about twice the value obtained for wet samples, deformed at otherwise similar conditions. Addition of supercritical CO₂ to wet samples led to a strengthening of the material in the compaction field, however it remained well below that of dry samples. The weakening effect of the wet material compared with the dried samples was explained as due to a lowering of the surface energy of the cement by wetting, which promotes equilibrium (Griffith-type) crack extension. The presence of water may also promote subcritical or stress corrosion crack growth. The increase in strength of the wet samples deformed in the presence of supercritical CO₂ was inferred to be due to an increase in the net energy of the cement-fluid interface, caused by CO₂ dissolution in the pore fluid, and to a decrease in subcritical crack growth rates caused by a shift in the pH of the pore fluid towards the point of zero charge of the calcium silicate hydrate gel phase present in the cement. We compared our results, compiled in terms of strength envelopes, with previous calculations on stress development in wellbore cement plugs located in a typical caprock. This comparison showed that injection of fluids into depleted reservoirs will result in increased compressive stresses developing in the plugs. However, when compared to strength envelopes constructed from the present data for Class A cement, it is clear that such stress changes will not lead to compressive failure of the cement. Tensile failure (hydrofracture) of cement plugs cannot be eliminated, but is unlikely to proceed far into the wellbore, as carbonation reactions are expected to seal the cement plug, thus preventing any significant penetration of the cement by CO₂. For CO₂ injection into a depleted gas or oil reservoir overlain by a typical caprock, the stress changes that are expected to occur in the plugs, therefore, pose little risk for CO₂ storage integrity.

Building on these results, **Chapter 6** reports the experiments on carbonation

reactions in wellbore cements and their effects on the transport properties of intact and fractured cement plugs. Batch reaction experiments were performed for up to three months, on intact and axially fractured Class A Portland cement cylinders, at a constant confining pressure of 30 MPa, a temperature of 80°C and a CO₂ pressure of 10 MPa. The experiments were carried out on water-saturated samples, exposing them to the supercritical CO₂ at one end. The results show that a dense carbonation front developed at the surfaces directly exposed to supercritical CO₂. Such carbonation fronts advanced faster at the top end of the fractured samples than at axial fracture planes, indicating that front development depends on the availability of supercritical CO₂ for reaction, i.e. on CO₂ diffusion. Scanning electron microscopy showed that carbonation led to healing of the axial fractures present in the cement. This was confirmed by thermogravimetric analyses, which showed that carbonation involves dissolution of portlandite and other phases coupled with diffusion towards the fracture plane and precipitation of calcium carbonate within or adjacent to it. Permeability measurements of unfractured cement showed a continuous and strong decrease during exposure to static CO₂ rich-fluids, implying that carbonation reactions have the potential to reduce the permeability of intact cement, at the CO₂ cement interface, to values for which cement can be considered effectively impermeable ($\kappa < 10^{-21} \text{ m}^2$) in around one year. For fractured samples, permeability reduction was not as rapid or as efficient as in the intact samples, but by comparison with samples retrieved from the SACROC Unit is believed to have the potential to reduce the overall permeability of fractured wellbore cement to an impermeable state, on the time scales of the order of 30 years. Crucially, proper cementation of the wellbores and good bonding with the casing and with the surrounding rocks is necessary to ensure the long-term confinement and safety of the storage.

Finally, the conclusions of this work are wrapped up in **Chapter 7**, where recommendations for applications are made, the implications of the various findings for geological storage of CO₂ are discussed, and possible directions for future research are identified.

Chapter 1

1.1 Background and scope of work

It is now widely accepted that the Earth's climate system is warming rapidly in comparison with pre-industrial times and that the main cause for this is anthropogenic emissions of greenhouse gases. The most significant of these gases is carbon dioxide (CO₂) released by the combustion of fossil fuel to produce energy, and by industrial processes such as steel and cement making [Gale, 2004]. Annual global emissions are presently at ~29 Gt [EIA, 2007]. To limit climate change, it is agreed that stabilization of the concentration of greenhouse gases in the atmosphere requires global CO₂ emissions reduction of at least 50 % below 1990 levels by 2050 [International Panel on Climate Control, 2007]. To achieve this goal, measures such as improved energy efficiency and use of alternatives to fossil fuel, such as nuclear energy and renewable energy (biomass, wind, hydroelectric, solar-heating, solar-thermal and solar-photovoltaic), have been suggested, along with carbon capture and storage or CCS [International Panel on Climate Control, 2007].

Carbon dioxide capture at source coupled with long-term geological storage is viewed as one of the most promising strategies for reducing greenhouse gases emissions [Bachu, 2003; Lackner, 2003; Gale, 2004; Pacala and Socolow, 2004; Rochelle et al., 2004; Gozalpour, 2005; Preston et al., 2005; Ambrose, 2008; Bachu, 2008; Goldberg et al., 2008; Gilfillan et al., 2009]. This process implies capture of CO₂ at power stations and other large industrial sources, transport through pipelines or by tankers and injection into a suitable porous geological formation. Potential geological sites for long-term storage include:

- Depleted oil and gas reservoirs. These have an estimated global storage capacity of about 810 Gt CO₂. They can trap CO₂ in the pore space as a supercritical fluid beneath the caprock, as a dissolved species, saturating water present in the formation [Xu et al., 2007; Gilfillan et al., 2009], and to some extent as carbonated minerals [Newall et al., 2000; Haywood et al., 2001],
- Deep saline aquifers. Aquifers can potentially sequester 10 000 Gt CO₂ globally, in the form of dissolved species saturating the formation water with minor mineralization in the long-term [Xu et al., 2007; Gilfillan et al., 2009]
- Unmineable coal beds. These may offer up to 40 Gt sequestration capacity for CO₂ as an adsorbed phase [Damen et al., 2005; White et al., 2005; van Bergen et al., 2006].

Such estimates are made assuming that geological formations used are located at depths of at least 800 m depth so that the CO₂ will be injected in the supercritical state (the critical temperature of pure CO₂ is 31.1°C and its critical pressure is 7.38 MPa). However, before such storage options are implemented it is clearly of vital importance to assess their subsurface impact and safety.

The research reported in this thesis addresses the mechanical and chemical response of carbonate-rich reservoir rocks, and of wellbore cements to CO₂ injection and storage. State of the art experimental techniques were employed. These included compaction

experiments on simulated porous carbonates, in order to investigate time-dependent compaction phenomena, compression tests to determine the mechanical failure behaviour of chalks and wellbore cements, and reaction experiments to explore the long-term chemical effects of CO₂ on cement.

1.2 Geological storage of CO₂ in depleted reservoirs – the integrity issue

To assess the feasibility and safety of geological storage of CO₂ in depleted oil and gas reservoirs, the impact of both injection and long-term storage implementation depends on the feasibility and long-term fate of storage, therefore preliminary risk assessment is necessary. Critical for storage integrity is the potential of CO₂ migration and leakage through **a**) natural faults and fractures present in the reservoir or caprock [*International Panel on Climate Control*, 2005; *Pruess*, 2005], **b**) man-made paths such as wells drilled through the caprock [*Gasda et al.*, 2004; *International Panel on Climate Control*, 2005; *Pruess*, 2005; *Carey et al.*, 2007; *Hofstee et al.*, 2008; *Bachu and Bennion*, 2009] and **c**) faults and (micro) fractures induced or re-activated by excessive deformation of the reservoir formation [*Gale*, 2004; *Emberlery et al.*, 2005; *Gozalpour*, 2005; *Madland et al.*, 2006; *Bachu and Bennion*, 2007; *Le Guen et al.*, 2007; *Ambrose*, 2008]- see Figure 1.1. Assessing the risk of leakage therefore requires data on the coupled chemical and mechanical effects of CO₂ on reservoir rocks, on caprocks and on the cements used to seal abandoned wells (so-called wellbore cement).

Combining experimental studies with field observations acquired from enhanced oil recovery operations using CO₂, from pilot CO₂ injection projects and from natural gas reservoirs containing large amounts of CO₂ provide valuable information for assessing the safety of long-term CO₂ storage. Some of the best-known CO₂ injection test fields internationally are the Weyburn field (Alberta Basin, Canada), the Sleipner field (Norwegian North Sea), the Frio Brine Pilot (Gulf Coast of Texas, USA) and the In Salah field (Algeria Central Sahara) [*Emberlery et al.*, 2005; *Gozalpour*, 2005; *Preston et al.*, 2005; *Ambrose*, 2008; *Kharaka et al.*, 2009], while in the Netherlands, the K-12B field is the best known off-shore gas field used for CO₂ injection [*van der Meer et al.*, 2004]. Weyburn field project has proven that oil reservoirs are good candidates for both enhanced oil recovery and CO₂ storage. Since injection started in 2000, more than 20 million tonnes of CO₂ have been injected. Operations prove that this is a safe and feasible option for CO₂ storage [*Emberlery et al.*, 2005; *Preston et al.*, 2005]. Injection of CO₂, separated from gas extracted from the Sleipner field, into the nearby Utsira sand aquifer has led to similar conclusions. No significant problems have been observed since injection started in 1996, though more than 10 million tonnes of CO₂ have been injected. Limited leakage has been observed at the Frio Brine Pilot test field between different units of the reservoir. However the overlying caprock remained a good seal after about 1600 tonnes CO₂ were injected over a period of 15 months [*Kharaka et al.*, 2006; *Kharaka et al.*, 2009]. Similarly, after injection of 60 ktonnes of CO₂ in the depleted K12-B gas field, no leakage has been observed [*van der Meer et al.*, 2004]. Natural CO₂ accumulations, which can be seen as analogues for geological storage of anthropogenic CO₂, provide the great advantage of offering information on the long-term effects (10³ to 10⁷ years) of chemical reaction in the

system water-rock-CO₂. Examples of CO₂-rich natural gas fields include the Otway Basin, Australia [Bradshaw *et al.*, 2002], the Four Corners and Colorado Plateau fields of the western U.S. [Allis *et al.*, 2001], in eastern China [Huang *et al.*, 2005; Li *et al.*, 2008].

In general, CO₂ injection into reservoir rocks leads to changes in the *in-situ* state of stress and in the chemical and temperature conditions (Figure 1.1). These changes can result in deformation of the reservoir and caprock. The mechanical and transport properties of the reservoir and caprock may also change through interaction with the injected supercritical CO₂ and the pore fluid, on both short and long time scales.

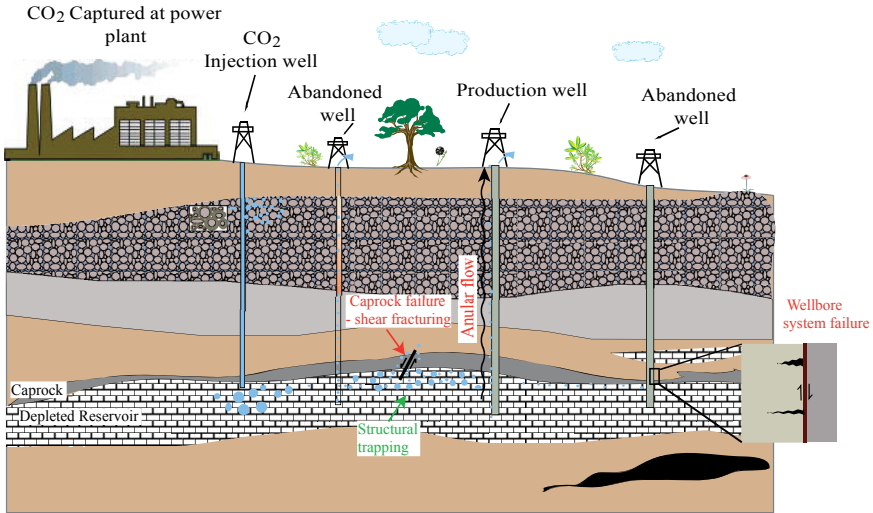


Figure 1.1 Schematic representation of depleted reservoir penetrated by wellbore plugs with cement, considered for CO₂ injection and storage. CO₂ injection into reservoir rocks leads to changes in the *in-situ* state of stress and in the chemical conditions, which can potentially lead to leakage and can impair its long-term sequestration.

Taken together these changes have the potential to cause surface compaction, to reactivate existing faults, to produce micro-seismic events and to damage the caprock. In addition, the mechanical and chemical integrity of cement-plugged wellbores may be degraded. Because of their relative reactivity with CO₂ and water, carbonate reservoir rocks such as limestones and chalks, and standard Portland-type wellbore cements are widely believed to be relatively vulnerable to effects of CO₂ injection and storage. In the following, the integrity of these materials will be considered further.

1.2.1 Carbonate reservoir rocks

Carbonate host rocks, and carbonate overburden formations into which stored CO₂ might migrate in the long term, constitute a particularly interesting case. Such rocks have a high solubility in the CO₂-water system, so that chemically induced porosity-permeability changes and increased compaction are widely expected [Portier and Rochelle, 2005;

Renard et al., 2005; *Madland et al.*, 2006; *Le Guen et al.*, 2007; *Xu et al.*, 2007; *Izgec et al.*, 2008]. Nonetheless, carbonate reservoirs are of major interest for CO₂ storage as they offer vast capacity for storage, with around 60% of known oil reserves and 40% of gas reserves being located in such formations [*Roehl*, 1985]. Furthermore, such formations often have quite low permeability, and are good candidates for CO₂-based Enhanced Oil or Gas Recovery (EOR/EGR) liberating valuable hydrocarbons while trapping much of the injected CO₂ in the reservoir, as demonstrated by pilot studies in locations such as the Weyburn Field in Canada [*Gozalpour et al.*, 2005]. Carbonate reservoir rocks are mostly composed of calcite (CaCO₃) and dolomite (CaMg(CO₃)₂), and are bioclastic or chemical in origin, or a combination of the two. Secondary dolomitization is common when Mg-rich fluids are available and may produce important secondary porosity. The primary source of the calcite in limestone is most commonly the exoskeletons of marine organisms. Such reservoirs are characterized by porosities ranging from 2-20%, while the permeability can range from almost zero to 100 millidarcy (mD) depending on the nature of the rock matrix and rock fracture system. Chalk is a particular case of a carbonate rock of biogenic origin; whereby the bioclastic matrix consists largely of microfossils such as coccolithophores, forams or ostracods. Chalk constitutes an important oil and gas reservoir rock in the North Sea. Such formations have a high porosity, reaching values up to 50%, but with low permeability of typically 1-5 mD. Chalks are therefore hard to produce oil from and they are key targets for EOR technology development [*Yu et al.*; *Jensen et al.*, 2000; *Austad et al.*, 2005; *Strand et al.*, 2008].

Injection of CO₂ into a carbonate or indeed any depleted reservoir rock changes the pore fluid pressure, temperature and effective stress state in the host rock. In general, this will lead to a vertical, poro-elastic expansion of the reservoir that depends only on the internal reservoir pressure and which tends to reverse any poro-elastic compaction that occurred during oil and gas production. This expansion may be reduced or even exceeded by permanent compaction of the host rock involving chemically coupled deformation processes [*Xu et al.*, 2004; *Portier and Rochelle*, 2005]. Such deformation occurs by relatively short-term, or time-independent processes and long-term, or time-dependent processes. Relatively short-term compaction of porous rocks such as granular limestones or chalks can occur irreversibly by initial rapid dissolution of grain contacts, by grain fracture, by contact de-bonding, through mechanical and capillary effects, and by accompanying grain rearrangements [*Wong et al.*, 1997; *Wong and Baud*, 1999; *David et al.*, 2001; *Renard et al.*, 2005; *Risnes et al.*, 2005; *Le Guen et al.*, 2007]. In calcite rocks, crystal plastic process such as deformation twinning can also play a role [*Zhu et al.*, 1999; *Xiao and Evans*, 2003; *Zubtsov et al.*, 2005].

Irreversible, time-dependent compaction processes may play a role in the long-term, as such processes are thermally activated kinetic processes. The most important candidate mechanisms include grain- to- grain contact failure through fluid-enhanced subcritical cracking and/or reaction [*Atkinson and Meredith*, 1987; *Lockner and Stanchits*, 2002], associated pore collapse and grain re-arrangement phenomena [*Delage et al.*, 1996; *Austad et al.*, 2005; *Madland et al.*, 2006], and pressure solution creep [*Renard et al.*, 2005; *Le Guen et al.*, 2007]. In the presence of chemically active CO₂-rich fluids, subcritical crack growth or stress

1

corrosion cracking are assumed to be accelerated in carbonates [Le Guen et al., 2007]. Such mechanisms involve progressive grain or grain-framework failure due to stress-induced chemical attack at crack tips [Atkinson, 1982; 1984; Atkinson and Meredith, 1989; Chester et al., 2004; Karner et al., 2005; Chester et al., 2007]. Intergranular pressure solution involves dissolution of material at grain contacts under high normal stress, diffusive transport through the intergranular fluid and precipitation on pore walls (or else removal in through-flowing pore fluid), thus effecting local mass transfer and hence creep [Rutter, 1976; Rutter, 1983; Lehner, 1990; de Meer and Spiers, 1999; Gundersen et al., 2002; Hellmann et al., 2002; Spiers et al., 2004]. In the case of supercritical CO₂ injection into carbonates, it is predicted to be substantially accelerated due to the enhanced solubility of carbonate rocks under such conditions [Renard et al., 2005].

However, while much research has been done on the purely chemical effects of CO₂ on calcite solubility and dissolution at CO₂ pressures up to 5 MPa [Ellis, 1959; Segnit et al., 1962; Plummer et al., 1978; Plummer and Busenberg, 1982; Buhmann and Dreybrodt, 1987; Alkattan et al., 2002; Pokrovsky et al., 2005; Gledhill and Morse, 2006; Kaufmann and Dreybrodt, 2007], very few concrete, experimental results are available on the influence of CO₂ on the chemically coupled mechanical effects of CO₂ on carbonate rocks [Renard et al., 2005; Madland et al., 2006; Le Guen et al., 2007; Izgec et al., 2008]. The few studies that have been conducted do point to an acceleration of creep by intergranular pressure solution [Renard et al., 2005; Madland et al., 2006; Le Guen et al., 2007] or by sub-critical cracking phenomena [Le Guen et al., 2007], independently of purely dissolution effects. Nevertheless, studies that verify the underlying mechanisms and allow reliable extrapolation to storage system conditions are still lacking.

Indeed, several important questions remain unanswered. These include issues such as: **a)** does increasing CO₂ partial pressure demonstrably accelerate pressure solution creep in carbonate rocks, **b)** can other mechanisms be proven to operate in the presence of CO₂, **c)** what are the effects of pore fluid salinity and impurity content on the operative deformation mechanisms when CO₂ is present, **d)** what type of failure behaviour characterizes the porous carbonate rocks in the presence of supercritical CO₂, and **e)** does carbon dioxide degrade the mechanical stability of such rocks?

1.2.2 Wellbore cement

Oil and gas reservoirs are explored and exploited by means of wells that enter the trap via the caprock or top seal. Therefore, upon abandonment of a depleted reservoir, significant number of wellbores generally penetrate the reservoir. For example some 300 000 wells are present throughout the province of Alberta, Canada with a density of 4 wells/km² [Gasda et al., 2004]. Similarly, around 140 000 wells exist only in the Tertiary section of Gulf Coast, (USA) reaching in places a density of hundreds of wells/ km², whereby about 30 % are abandoned wells [Nicot, 2009]. The small De Lier field in The Netherlands is penetrated by 51 abandoned wells [Hofstee et al., 2008]. After drilling, wellbores are typically lined with a steel casing and the caprock-casing contact is sealed

with cement slurry to prevent fluid migration along the caprock-casing interface or annulus. Upon completion, a cement plug is placed into the cased wellbore to block vertical migration of fluids, as shown in Figure 1.1. Portland cement is used in more than 80 % of the reservoirs around the world [Barlet-Gouédard *et al.*, 2009]. The effectiveness of sealing depends on the initial cementing job quality, on the permeability of the cement, and on whether any fractures developed in the cement-casing-caprock system with time (either during fluid depletion or injection).

Thus, despite the fact that oil and gas exploration and production wells are sealed and plugged with cement after abandonment, the risk exists that leakage might still occur during CO₂ storage, due to poor completion or abandonment procedures, due to geochemical degradation of the cement and casing, or due to geomechanical failure of the cement, the casing or the caprock-cement-casing interfaces [Gasda *et al.*, 2004; *International Panel on Climate Control*, 2005; Pruess, 2005; Barlet-Gouédard *et al.*, 2007; Carey *et al.*, 2007; Bachu, 2008; Hofstee *et al.*, 2008].

Most wells are completed using Portland cement (Type A, G or H) mixed with water in various proportions, depending on the in-situ pressure and temperature conditions. The dry cement consists of four main oxide components, namely: CaO, SiO₂, Al₂O₃ and Fe₂O₃. These make up the initially present cement compounds, i.e. tricalcium silicate (Ca₃SiO₅ or C₃S), dicalcium silicate (Ca₂SiO₄ or C₂S), tricalcium aluminate (Ca₃Al₂O₆ or C₃A) and tetracalcium aluminoferrite (Ca₄(Al,Fe)₂O₅ or C₄AF), with small quantities of CaSO₄, MgO and CaO. After mixing with water, hydration reactions lead to the formation of calcium hydroxide or portlandite, calcium silicate hydrate or C-S-H gel, calcium sulfoaluminate (AF_(m,t)) or ettringite, and a range of calcium aluminates (CA) and calcium aluminate ferrite (C₄AF) [Mindess and Young, 1981; Neville, 1996; Kutchko *et al.*, 2007]. After hydration and curing, C-S-H gel makes up around 50-60 % of the material. This has a poorly crystalline structure, similar to jennite or tobermorite, with platy crystals being separated by a water film when the material is wet [Lea, 1970; Mindess and Young, 1981]. C-S-H gel contributes mainly to the strength of the material, due to the covalent and van der Waals bonds within its complex structure. Calcium hydroxide or portlandite is present in proportions of ~20 to 25 % of the hydrated cement and occurs as weak blebs or hexagonal plates [Mehta and Monteiro, 2006]. The C₃A and AF_(m,t) phases contribute further to stiffening and strengthening the material through their needle-like (C₃A) and hexagonal-plate morphology (AF_(m,t)), making up to 15-20 % of the volume of hydrated cement [Lea, 1970; Mindess and Young, 1981; Neville, 1996]. From a mechanical point of view, the cement within a wellbore is expected to reach equilibrium with the state of stress in the reservoir [Mainguy *et al.*, 2007].

To date, numerous experimental studies have investigated geochemical degradation of wellbore cement and its effect on transport properties – i.e. on porosity and permeability [Duguid, 2005; Barlet-Gouédard *et al.*, 2007; Carey *et al.*, 2007; Kutchko *et al.*, 2007; Kutchko *et al.*, 2008; Rimmelé *et al.*, 2008; Bachu and Bennion, 2009; Barlet-Gouédard *et al.*, 2009]. Contradictory results have been obtained for both type G and H Portland cement. Porous degradation fronts penetrating a drastic 20 - 25 mm have been reported to develop after one

1

year of immersion in large volumes of (freely convecting) CO₂-water solutions at a pressure of 28 MPa and temperature of 90°C. Similar fronts, but less than 1 mm thick, have been reported to form on comparable time scales at 50°C and pressures ranging from 0.1-30 MPa. By contrast, flow-through experiments conducted on confined samples by [Bachu and Bennion, 2009] at an external confining pressure of 29 MPa and a mean internal fluid pressure of 15 MPa at 65°C, showed a decrease in permeability to CO₂-saturated water from 10⁻¹⁹ m² to 10⁻²⁰ m² after 90 days. In addition, Class A wellbore cement samples recovered from the well-known SACROC Unit in the Permian Basin of West Texas, after exposure to supercritical CO₂ over 30 years of enhanced oil recovery (EOR) operations, retained their sealing capacity despite clear evidence of carbonation [Carey et al., 2007].

However, little attention has been paid to addressing the effects of CO₂ injection on the mechanical behaviour of wellbore cement, despite the fact that mechanical failure of wellbore cement has been widely identified as providing a possible route for CO₂ leakage from host reservoirs [Bonett and Pafitis, 1996; Dusseault et al., 2000; Mainguy et al., 2007 2008; Bachu and Bennion, 2009]. During injection of fluids such as CO₂ into a reservoir, temperature and pressure changes generate a decrease in the effective stress in the reservoir that subsequently leads not only to vertical reservoir expansion but also to changes in the horizontal stresses within the reservoir and caprock [Mainguy et al., 2007]. Shear stresses will accordingly be generated at the interfaces between reservoir rock, caprock and wellbore, and tensile or compressive stresses will similarly develop in the wellbore plugs [Mainguy et al., 2007; Soltanzadeh et al., 2007; Rutqvist et al., 2008]. These stress changes can potentially result in plug integrity loss and CO₂ leakage, through plug failure (tensile cracking or shear failure) or cement-casing debonding [Bonett and Pafitis, 1996; Dusseault et al., 2000; Mainguy et al., 2007 2008; Bachu and Bennion, 2009].

Therefore, for a reliable assessment of wellbore integrity in the context of CO₂ storage, data are needed on the compressive and tensile strengths of wellbore cement, on the possible effects of CO₂ on these and on the stress path evolution in reservoirs, caprocks and wellbores due to CO₂ injection. Also, of major interest is the long-term evolution of fractures or cracks induced in the wellbore cement by CO₂ injection. A key issue here is whether such mechanical defects have the potential for self-healing/sealing or whether they become conduits for CO₂.

1.3 Research questions and aims of the study

The main objective of the present work is to gain insight into the effects of supercritical CO₂ injection and storage on simulated carbonate reservoirs rocks, on chalks rocks and on wellbore cement, and to study in detail the mechanisms responsible for the observed processes. The results are intended to provide input for numerical simulations and risk assessment exercises directed at long-term geological storage of CO₂.

In particular, the main questions addressed are as follows:

1. What is the effect of supercritical CO₂ on mechanisms of compaction creep in wet

calcite rocks under *in-situ* conditions? (Chapter 2).

1. What is the effect of pore fluid salinity on mechanisms of compaction in simulated calcite reservoir rocks with and without added supercritical CO₂ under geological storage conditions? (Chapter 3).

1. Is the stability of wet chalks further affected by the injection of CO₂ and what are the mechanisms responsible for the strong compaction often observed in wet chalk and for any additional effects of CO₂? (Chapter 4).

1. What is the effect of water and CO₂ on the failure mode and compressive strength of wellbore cement under down-hole conditions? And can such effects lead to wellbore cement failure as a result of stress-strain changes that occur during CO₂ injection? (Chapter 5)

1. Will long-term carbonation reactions improve or degrade the sealing capacity of intact wellbore cement and will such reactions heal or leach out old or developing fractures? (Chapter 6).

Reference list

- Alkattan, M., E. H. Oelkers, J.-L. Dandurand, and J. Schott (2002), An experimental study of calcite dissolution rates at acidic conditions and 25 °C in the presence of NaPO₃ and MgCl₂, *Chemical Geology*, 190(1-4), 291-302.
- Allis, R. G., T. Chidsey, W. Gwynn, C. Morgan, S. P. White, M. Adams, and J. Moore (2001), Natural CO₂ reservoirs on the Colorado Plateau and Southern Rocky Mountains: candidates for CO₂ sequestration. , paper presented at 1st National Conference on Carbon Sequestration, DOE-NETL, Washington DC, May 14-17, 2001.
- Ambrose, W. A., Lakshminarasimhan, S., Holtz, M.H., Nunez-Lopez, V., Hovorka, S.D., Duncan, I. (2008), Geologic factors controlling CO₂ storage capacity and permanence: case studies based on experience with heterogeneity in oil and gas reservoirs applied to CO₂ storage, *Environmental Geology* 54, 1619-1633.
- Atkinson, B. K. (1982), Subcritical crack propagation in rocks: theory, experimental results and applications. , *Journal of Structural Geology* 4, 41-56.
- Atkinson, B. K. (1984), Subcritical crack growth in geological materials., *Journal of Geophysical Research*, 89, 4077-4114.
- Atkinson, B. K., and P. G. Meredith (1987), The theory of subcritical crack growth with applications to minerals and rocks, in *Fracture Mechanics of Rock*, edited by A. B.K., pp. 111-166, Academic Press.
- Atkinson, B. K., and R. G. Meredith (1989), The theory of subcritical crack growth with applications to minerals and rocks, *Fracture mechanics of rock*, 111-166.
- Austad, T., S. Strand, E. J. Høgenesen, and P. Zhang (2005), Seawater as IOR fluid in fractured chalk. , in *Oilfield Chemistry Symposium*, edited, PE Paper 93000, Houston, TX.
- Bachu, S. (2003), Screening and ranking of sedimentary basins for sequestration of CO₂ in geological media in response to climate change, *Environmental Geology*, 44(3), 277-289.
- Bachu, S., and B. Bennion (2007), Effects of in-situ conditions on relative permeability characteristics of CO₂-brine systems, *Environmental Geology*.
- Bachu, S. (2008), CO₂ storage in geological media: Role, means, status and barriers to deployment, *Progress in Energy and Combustion Science*, 34(2), 254-273.
- Bachu, S., and D. B. Bennion (2009), Experimental assessment of brine and/or CO₂ leakage through well cements at reservoir conditions, *International Journal of Greenhouse Gas Control*, 3(4), 494-501.
- Barlet-Gouédard, V., G. Rimmelé, B. Goffé, and O. Porcherie (2007), Well technologies for CO₂ geological storage: CO₂-resistant cement, *Oil and Gas Science and Technology, Review IFP*, 62(3), 1-12.
- Barlet-Gouédard, V., G. Rimmelé, O. Porcherie, N. Quisel, and J. Desroches (2009), A solution against well cement degradation under CO₂ geological storage environment, *International Journal of Greenhouse Gas Control*, 3(2), 206-216.
- Bonett, A., and D. Pafitis (1996), Getting to the root of gas migration, *Oilfield review*, 8(1), 36-49.
- Bradshaw, J., B. E. Bradshaw, G. Allinson, A. J. Rigg, V. Nguyen, and L. Spencer (2002), The potential for geological sequestration of CO₂ in Australia: preliminary findings and implications for new gas field development, *APPEA Journal*, 42(1), 25-45.
- Buhmann, D., and W. Dreybrodt (1987), Calcite dissolution kinetics in the system H₂O---CO₂---CaCO₃ with participation of foreign ions, *Chemical Geology*, 64(1-2), 89-102.
- Carey, J. W., M. Wigand, S. J. Chipera, G. WoldeGabriel, R. Pawar, P. C. Lichtner, S. C. Wehner, M. A. Raines, and J. G. D. Guthrie (2007), Analysis and performance of oil well cement with 30 years of CO₂ exposure from the SACROC Unit, West Texas, USA, *International Journal of Greenhouse Gas Control*, 1(1), 75-85.
- Chester, F. M., J. S. Chester, A. K. Kronenberg, and A. Hajash (2007), Subcritical creep compaction of quartz sand at diagenetic conditions: Effects of water and grain size, *J. Geophys. Res.*, 112.
- Chester, J. S., S. C. Lenz, F. M. Chester, and R. A. Lang (2004), Mechanisms of compaction of quartz sand at diagenetic conditions, *Earth and Planetary Science Letters*, 220(3-4), 435-451.
- Damen, K., A. Faaij, F. van Bergen, J. Gale, and E. Lysen (2005), Identification of early opportunities for CO₂ sequestration—worldwide screening for CO₂-EOR and CO₂-ECBM projects, *Energy*, 30, 1931-1952.
- David, C., B. Menendez, W. Zhu, and T. f. Wong (2001), Mechanical compaction, microstructures and permeability evolution in sandstones, *Physics and Chemistry of the Earth, Part A: Solid Earth and Geodesy*, 26(1-2), 45-51.
- de Meer, S., and C. J. Spiers (1999), Influence of pore-fluid salinity on pressure solution creep in gypsum, *Tectonophysics*, 308(3), 311-330.
- Delage, P., C. Schroeder, and Y. J. Cui (1996), Subsidence and capillary effects in chalks, in *EUROCK '96, Prediction and performance on rock mechanics and rock engineering - ISRM International symposium*, edited, Torino, Italy.
- Duguid, A. R., M.; Scherer, G. (2005), *Degradation of Well Cement Exposed to Carbonated Brine*, paper

presented at 4th Annual Conference on Carbon Capture and Sequestration, Exchange and Monitor Publications and Forum, Alexandria, VA, 2006.

Dusseault, M. B., M. N. Gray, and P. A. Nawrocki (2000), Why oilwells leak: Cement behavior and long-term consequences. , paper presented at SPE International Oil and Gas Conference and Exhibition in China, SPE Beijing, China, 7-10 November 2000.

EIA, E. I. A. (2007), *Annual Energy Outlook 2004, With Projections to 2030*, Washington, DC. .

Ellis, A. (1959), The solubility of calcite in carbon dioxide solutions, *American Journal of Science*, 257, 354-365.

Emberlery, S., I. Hutcheon, M. Shevalier, K. Durocher, B. Mayer, W. D. Gunter, and E. H. Perkins (2005), Monitoring of fluid-rock interaction and CO₂ storage through produced fluid sampling at the Weyburn CO₂-injection enhanced oil recovery site, Saskatchewan, Canada., *Applied geochemistry* 20(6), 1131-1157.

Gale, J. (2004), Geological storage of CO₂: What do we know, where are the gaps and what more needs to be done?, *Energy*, 29(9-10), 1329-1338.

Gasda, S. E., S. Bachu, and M. A. Celia (2004), Spatial characterization of the location of potentially leaky wells penetrating a deep saline aquifer in a mature sedimentary basin, *Environmental Geology*, 46(6), 707-720.

Gillfillan, S. M. V., B. S. Lollar, G. Holland, D. Blagburn, S. Stevens, M. Schoell, M. Cassidy, Z. Ding, Z. Zhou, G. Lacrampe-Couloume, and C. J. Ballentine (2009), Solubility trapping in formation water as dominant CO₂ sink in natural gas fields, *Nature*, 458(7238), 614-618.

Gledhill, D. K., and J. W. Morse (2006), Calcite solubility in Na-Ca-Mg-Cl brines, *Chemical Geology*, 233(3-4), 249-256.

Goldberg, D. S., T. Takahashi, and A. L. Slagle (2008), Carbon dioxide sequestration in deep-sea basalt, *Proceedings of the National Academy of Sciences*, 105(29), 9920-9925.

Gozalpour, F., S. R. Ren, and B. Tohidi (2005), CO₂ EOR and storage in oil reservoirs. , *Oil and Gas Science and Technology - Rev IFP*, 60(3), 537-546.

Gozalpour, F., Ren, S.R., Tohidi, B (2005), CO₂ EOR and storage in oil reservoirs. , *Oil and Gas Science and Technology - Rev IFP*, 60(3), 537-546.

Gundersen, E., F. o. Renard, D. K. Dysthe, K. Bjorlykke, and B. R. Jamtveit (2002), Coupling between pressure solution creep and diffusive mass transport in porous rocks, *J. Geophys. Res.*, 107.

Haywood, H. M., J. M. Eyre, and H. Scholes (2001), Carbon dioxide sequestration as stable carbonate minerals - Environmental barriers, *Environmental Geology*, 41(1-2), 11-16.

Hellmann, R., P. J. N. Renders, G. J.-P., and R. Guiguet (2002), Experimental pressure solution of chalk in aqueous solutions: Part 1. Deformation behaviour and chemistry., in *Water-Rock Interactions, Ore Deposits, and Environmental Geochemistry: A Tribute to David A. Crerar*, edited by T. G. Society.

Hofstee, C., F. Seeberger, B. Orlic, F. Mulders, F. van Bergen, and R. Bisschop (2008), The feasibility of effective and safe carbon dioxide storage in the De Lier gas field, *First break*, 26(1), 53-57.

Huang, B., X. Xiao, Z. Hu, and P. Yi (2005), Geochemistry and episodic accumulation of natural gases from the Ledong gas field in the Yinggehai Basin, offshore South China Sea, *Organic Geochemistry*, 36(12), 1689-1702.

International Panel on Climate Control, I. (Ed.) (2005), *Carbon Dioxide Capture and Storage. Special Report*. , 442 pp., Cambridge University Press, Cambridge, United Kingdom and New York, NY, USA.

International Panel on Climate Control, I. (2007), *Climate Change 2007: The Physical Science Basis. Contribution of Working Group I to the Fourth Assessment Report of the Intergovernmental Panel on Climate Change*, 996 pp, Cambridge University Press, Cambridge, United Kingdom and New York, NY, USA.

Izgec, O., B. Demiral, H. Bertin, and S. Akin (2008), CO₂ injection into saline carbonate aquifer formations II: Comparison of numerical simulations to experiments. , *Transport in Porous Media*, 73, 57-74. .

Jensen, T. B., K. J. Harpole, and A. Osthus (2000), EOR Screening for Ekofisk, in *SPE European Petroleum Conference*, edited, Paris, France.

Karner, S. L., J. S. Chester, F. M. Chester, A. K. Kronenberg, and A. Hajash (2005), Laboratory deformation of granular quartz sand: Implications for the burial of clastic rocks, *American Association of Petroleum Geology Bulletin*, 89, 603-625.

Kaufmann, G., and W. Dreybrodt (2007), Calcite dissolution kinetics in the system CaCO₃-H₂O-CO₂ at high undersaturation, *Geochimica et Cosmochimica Acta*, 71(6), 1398-1410.

Kharaka, Y. K., D. R. Cole, S. D. Hovorka, W. D. Gunter, K. G. Knauss, and B. M. Freifeld (2006), Gas-water-rock interactions in Frio Formation following CO₂ injection: Implications for the storage of greenhouse gases in sedimentary basins, *Geology*, 34(7), 577-580.

Kharaka, Y. K., J. J. Thordsen, S. D. Hovorka, H. Seay Nance, D. R. Cole, T. J. Phelps, and K. G. Knauss (2009), Potential environmental issues of CO₂ storage in deep saline aquifers: Geochemical results from the Frio-I Brine Pilot test, Texas, USA, *Applied geochemistry*, 24(6), 1106-1112.

Kutchko, B. G., B. R. Strazisar, D. A. Dzombak, G. V. Lowry, and N. Thaulow (2007), Degradation of Well Cement by

CO₂ under Geologic Sequestration Conditions, *Environmental Science & Technology*, 41(13), 4787-4792.

Kutchko, B. G., B. R. Strazisar, G. V. Lowry, D. A. Dzombak, and N. Thaulow (2008), Rate of CO₂ Attack on Hydrated Class H Well Cement under Geologic Sequestration Conditions, *Environmental Science & Technology*, 42(16), 6237-6242.

Lackner, K. S. (2003), Climate change: A Guide to CO₂ Sequestration, *Science*, 300(5626), 1677-1678.

Le Guen, Y., F. Renard, R. Hellmann, E. Brosse, M. Collombet, D. Tisserand, and J.-P. Gratier (2007), Enhanced deformation of limestone and sandstone in the presence of high PCO₂ fluids, *Journal of Geophysical Research*, 112(B05421).

Lea, F. M. (1970), *The Chemistry of Cement and Concrete*, 3rd ed., Edward Arnold Ltd, London.

Lehner, F. K. (1990), Thermodynamics of rock deformation by pressure solution., in *Deformation processes in minerals, ceramics and rocks*, edited by D. J. Barber, Meredith, P.G., pp. 296-333, Unwin Hyman, London.

Li, M., T. Wang, J. Liu, H. Lu, W. Wu, and L. Gao (2008), Occurrence and origin of carbon dioxide in the Fushan Depression, Beibuwan Basin, South China Sea, *Marine and Petroleum Geology*, 25(6), 500-513.

Lockner, D. A., and S. A. Stanchits (2002), Undrained poroelastic response of sandstones to deviatoric stress change, *J. Geophys. Res.*, 107.

Madland, M. V., A. Finsnes, A. Alkafadgi, R. Risnes, and T. Austad (2006), The influence of CO₂ gas and carbonate water on the mechanical stability of chalk, *Journal of Petroleum Science and Engineering*, 51(3-4), 149-168.

Mainguy, M., P. Longuemare, A. Audibert, and E. Lecolier (2007), Analyzing the risk of well plug failure after abandonment, *Oil & Gas Sci. and Tech. - Rev. IFP*, 62(3), 311-324.

Mehta, P., and P. Monteiro (2006), *Concrete: Microstructure, Properties, and Materials* The McGraw-Hill Companies, Inc.

Mindess, S., and J. F. Young (1981), *Concrete*, Prentice-Hall, Inc., Englewood Cliffs, New Jersey.

Neville, A. M. (1996), *Properties of Concrete*, John Wiley and Sons, Inc., New York.

Newall, P. S., S. J. Clarke, H. M. Haywood, H. Scholes, N. R. Clarke, and P. A. King (2000), CO₂ storage as carbonate minerals, IEA Greenhouse Gas R&D Prog, Cornwall, UK.

Nicot, J.-P. (2009), A survey of oil and gas wells in the Texas Gulf Coast, USA, and implications for geological sequestration of CO₂, *Environmental Geology*, 57(7), 1625-1638.

Pacala, S., and R. Socolow (2004), Stabilization Wedges: Solving the Climate Problem for the Next 50 Years with Current Technologies, *Science*, 305(5686), 968-972.

Plummer, L. N., T. M. L. Wigley, and D. L. Parkhurst (1978), The kinetics of calcite dissolution in CO₂-water systems at 5 degrees to 60 degrees C and 0.0 to 1.0 atm CO₂, *Am J Sci*, 278(2), 179-216.

Plummer, L. N., and E. Busenberg (1982), The solubilities of calcite, aragonite and vaterite in CO₂-H₂O solutions between 0 and 90°C, and an evaluation of the aqueous model for the system CaCO₃-CO₂-H₂O, *Geochimica et Cosmochimica Acta*, 46(6), 1011-1040.

Pokrovsky, O. S., S. V. Golubev, and J. Schott (2005), Dissolution kinetics of calcite, dolomite and magnesite at 25 °C and 0 to 50 atm pCO₂, *Chemical Geology*, 217(3-4), 239-255.

Portier, S., and C. Rochelle (2005), Modelling CO₂ solubility in pure water and NaCl-type waters from 0 to 300 °C and from 1 to 300 bar: Application to the Utsira Formation at Sleipner, *Chemical Geology*, 217(3-4), 187-199.

Preston, C., M. Monea, W. Jazrawi, K. Brown, W. S., D. White, D. Law, R. Chalaturnyk, and B. Roston (2005), IEA GHG Weyburn CO₂ monitoring and storage project, *Fuel Processing Technology*, 86(15), 1547-1568.

Pruess, K. (2005), Numerical studies of fluid leakage from a geologic disposal reservoir for CO₂ show self-limiting feedback between fluid flow and heat transfer, *Geophys. Res. Lett.*, 32(L14404).

Renard, F., E. Gundersen, R. Hellmann, M. Collombet, and Y. Le Guen (2005), Numerical modeling of carbon dioxide sequestration on the rate of pressure solution creep in limestone: Preliminary results, *Oil & Gas Science and Technology*, 60, 381-399

Rimmelé, G., V. Barlet-Gouédard, O. Porcherie, B. Goffé, and F. Brunet (2008), Heterogeneous porosity distribution in Portland cement exposed to CO₂-rich fluids, *Cement and Concrete Research*, 38(8-9), 1038-1048.

Risnes, R., M. V. Madland, M. Hole, and N. K. Kwabiah (2005), Water weakening of chalk - Mechanical effects of water-glycol mixtures, *Journal of Petroleum Science and Engineering*, 48, 21-36.

Rochelle, C. A., I. Czernichowski-Lauriol, i. A. E. Milodowsk, S. J. Baines, and R. H. Worden (2004), The impact of chemical reactions on CO₂ storage in geological formations: A brief review., in *Geological Storage of Carbon Dioxide*, edited by W. R. Baines SJ, pp. 87-106, Geological Society of Londo, London.

Roehl, P. O., and P.W. Choquette (1985), Carbonate Petroleum Reservoirs, 622.

Rutqvist, J., J. T. Birkholzer, and C. F. Tsang (2008), Coupled reservoir-geomechanical analysis of the potential for tensile and shear failure associated with CO₂ injection in multilayered reservoir-caprock systems, *International Journal of Rock Mechanics and Mining Sciences*, 45, 132-143.

Rutter, E. H. (1976), The kinetics of rock deformation by pressure solution, *Philosophical Transactions of the Royal Society of London*, 283, 203- 219.

Rutter, E. H. (1983), Pressure solution in nature, theory and experiment, *Journal of the Geological Society*, 140(5), 725-740.

Segnit, E. R., H. D. Holland, and C. J. Biscardi (1962), The solubility of calcite in aqueous solutions--I The solubility of calcite in water between 75° and 200° at CO₂ pressures up to 60 atm, *Geochimica et Cosmochimica Acta*, 26(12), 1301-1331.

Soltanzadeh, H., C. D. Hawkes, and J. S. Sharma (2007), Poroelastic model for production and injection-induced stresses in reservoirs with elastic properties different from the surrounding rock., *International Journal of Geomechanics*, 7, 353-361.

Spiers, C. J., S. De Meer, A. R. Niemeijer, and X. Zhang (2004), Kinetics of rock deformation by pressure solution and the role of thin aqueous films, in *Physicochemistry of Water in Geological and Biological Systems-Structures and Properties of Thin Aqueous Films*, edited by S. Nakashima, pp. 129-158, Universal Acad. Press, Tokyo.

Strand, S., T. Puntervold, and T. Austad (2008), Effect of Temperature on Enhanced Oil Recovery from Mixed-Wet Chalk Cores by Spontaneous Imbibition and Forced Displacement Using Seawater, *Energy & Fuels*, 22(5), 3222-3225.

van Bergen, F., H. Pagnier, and P. Krzystalik (2006), Field experiments of enhanced coalbed methane-CO₂ in the upper Silesian basin of Poland, *Environmental geosciences*, 13(3), 201-224.

van der Meer, L. G. H., J. Hartman, C. Geel, and E. Kreft (2004), Re-Injecting CO₂ into an offshore gas reservoir at a depth of nearly 4000 metres sub sea, in *7th International Conference on Greenhouse Gas Control Technologies*, edited by D. W. K. a. C. F. G. E.S. Rubin, Vancouver.

White, C. M., D. H. Smith, K. L. Jones, A. L. Goodman, S. A. Jikich, R. B. LaCount, S. B. DuBose, E. Ozdemir, B. I. Morsi, and K. T. Schroeder (2005), Sequestration of carbon dioxide in coal with enhanced coalbed methane recovery - A review, *Energy & Fuels*, 19(3), 659-724.

Wong, T.-f., C. David, and W. Zhu (1997), The transition from brittle faulting to cataclastic flow in porous sandstones: Mechanical deformation, *J. Geophys. Res.*, 102.

Wong, T.-f., and P. Baud (1999), Mechanical Compaction of Porous Sandstone, *Oil & Gas Sci. and Tech. - Rev. IFP*, 54(6), 715-727.

Xiao, X., and B. Evans (2003), Shear-enhanced compaction during non-linear viscous creep of porous calcite-quartz aggregates, *Earth and Planetary Science Letters*, 216(4), 725-740.

Xu, T., J. A. Apps, and K. Pruess (2004), Numerical simulation of CO₂ disposal by mineral trapping in deep aquifers, *Applied geochemistry*, 19(6), 917-936.

Xu, T., J. A. Apps, K. Pruess, and H. Yamamoto (2007), Numerical modeling of injection and mineral trapping of CO₂ with H₂S and SO₂ in a sandstone formation, *Chemical Geology*, 242(3-4), 319-346.

Yu, L., S. Evje, H. Kleppe, T. Kårstad, I. Fjelde, and S. M. Skjæveland Spontaneous Imbibition of Seawater Into Preferentially Oil-Wet Chalk Cores-Experiments and Simulations, *Journal of Petroleum Science and Engineering*, In Press, Accepted Manuscript.

Zhu, W., B. Evans, and Y. Bernabe (1999), Densification and permeability reduction in hot-pressed calcite: A kinetic model, *J. Geophys. Res.*, 104.

Zubtsov, S., F. Renard, J.-P. Gratier, D. K. Dysthe, and V. Traskine (2005), Single-contact pressure solution creep on calcite monocrystals, *Geological Society, London, Special Publications*, 243(1), 81-95.

Chapter 2

ABSTRACT

We report systematic, uniaxial, compaction creep experiments performed on porous calcite aggregates in the presence of CO₂ at conditions similar to reservoir conditions. The experiments were conducted on dry and wet aggregates with grain sizes in the range 1 to 250 μm, at 28-100°C (80°C), applied effective stresses of 4-40 MPa, and CO₂ partial pressures of 4·10⁻⁵-10 MPa. Compaction creep is enhanced by saturated CaCO₃ solution, and the strain rate increases with increasing grain size and applied stress. Addition of supercritical (SC) CO₂ after 1 hour of creep increased strain rates by 1-3 orders. When SCCO₂ is added before loading, creep rates decrease with increasing grain size up to 106 μm, and increase with grain size above 106 μm. Below 106 μm, the strain rate increases with increasing temperature, applied stress and CO₂ partial pressure. The mechanical data together with microstructural evidence indicate that combined grain scale microcracking and diffusion controlled pressure solution best explain the behaviour observed. Notably in experiments where CO₂ was added before loading, pressure solution dominated creep at fine grain size, giving way to subcritical cracking control at grain sizes above 106 μm. Our results point to pressure solution accelerating by up to 50 times at CO₂ pressures increased from 6 to 10 MPa. Integrating our findings, we suggest that if a depleted carbonate reservoir exhibits measurable compaction creep, then injection of CO₂ has the potential to speed this up by amounts up to 50 times, notably if creep is due to diffusion-controlled pressure solution.

Based on:

Liteanu E., Spiers C.J., Peach C.J., Bresser J.H.P. - The effect of CO₂ on creep of wet calcite aggregates. *Journal of Geophysical Research* (submitted)

2.1 Introduction

Capture of carbon dioxide (CO₂) at fossil fuel power stations coupled with long-term (> 10³ years) geological storage is now being widely considered as a means of reducing CO₂ emissions to the atmosphere [IPCC, 2005]. Prospective host rocks for geological storage include depleted oil and gas reservoirs, saline aquifers and coal beds [Bachu, 2003; IPCC, 2005; Xu *et al.*, 2007; Gilfillan *et al.*, 2009]. Since more than 50 % of known oil and gas reserves worldwide are located in carbonates [Roehl and Choquette, 1985], depleted carbonate reservoirs offer a major CO₂ storage option. In addition, injection of CO₂ into depleted carbonate reservoirs may present significant potential for enhanced oil and gas recovery (EOR/EGR), while trapping much of the injected CO₂ in the reservoir [Gozalpour *et al.*, 2005]. There is therefore much interest in using depleted carbonate reservoirs for CO₂ storage, where possible in combination with EOR and/or EGR, and several pilot injection projects are currently in progress [Emberley *et al.*, 2005; Gozalpour *et al.*, 2005; Preston *et al.*, 2005; Ambrose *et al.*, 2008].

In general, injection of supercritical CO₂ into clastic or carbonate host rocks will change the chemical, mechanical, and microstructural state of the reservoir, its caprock and any associated faults. These changes may in turn affect reservoir porosity, permeability and seal integrity [Grasso, 1992; Gaus *et al.*, 2002; Zoback and Zinke, 2002]. Purely chemical changes will occur due to the fact that carbon dioxide lowers the pH of the formation fluid, leading to mineral dissolution and precipitation phenomena that directly modify porosity and permeability [Le Guen *et al.*, 2007; Izgec *et al.*, 2008]. Mechanical effects include poro-elastic expansion of the host rock, but also the possibility of permanent reservoir compaction by chemically coupled deformation processes [Xu *et al.*, 2004; Portier and Rochelle, 2005], such as grain (contact) failure due to stress corrosion cracking and/or dissolution [Atkinson and Meredith, 1987; Lockner, 1998], associated pore collapse phenomena [Madland *et al.*, 2006], and pressure solution creep [Renard *et al.*, 2005; Le Guen *et al.*, 2007].

Understanding and quantifying the mechanical and chemical effects of CO₂ injection is key to evaluating the long-term performance of geological CO₂ storage systems [Benson *et al.*, 2002; Ennis-King and Paterson, 2003; Cailly *et al.*, 2005; Li *et al.*, 2006; Ambrose *et al.*, 2008]. This is particularly so for the case of carbonate host rocks, and for carbonate formations into which CO₂ might migrate. Because of their high solubility in acid solutions, such lithologies are expected to be especially prone to coupled chemical-mechanical effects [Renard *et al.*, 2005; Madland *et al.*, 2006; Bachu and Bennion, 2007; Le Guen *et al.*, 2007; Izgec *et al.*, 2008].

However, only a limited number of studies have addressed the coupled chemical - mechanical response of carbonates to CO₂ injection or infiltration. In a recent numerical modeling study, Renard *et al.* [2005] concluded that CO₂ injection into water-saturated limestones will increase compaction creep rates due to intergranular pressure solution (IPS) by 50-75 times, leading to significant deformation. The predicted enhancement of

compaction rate is due to the increase in carbonate solubility caused by a drop in pore fluid pH. This accelerates grain boundary diffusion, which the model predicts is the rate-controlling step for pressure solution. However, it is unclear what the rate-controlling step and the absolute rate of IPS will actually be under in-situ conditions, since both are strongly influenced by pore fluid impurities [Zhang and Spiers, 2005 a, 2005b], and since there are major uncertainties in the values of the relevant thermodynamic and kinetic parameters. The applicability of the model presented by Renard *et al.* [2005] to carbonate rocks is therefore unknown.

Experimental work on the effect of CO₂ on creep of carbonates is also very limited. Recent triaxial compression tests conducted by Le Guen *et al.* [2007] showed that injection of high pressure CO₂ into water-saturated limestone samples led to an increase in creep rate by a factor of up to 5 to 7.5, a far smaller effect than predicted by Renard *et al.* [2005]. No systematic evaluation was conducted into the effect on strain rate of variables such as grain size, effective stress, temperature or CO₂ pressure. It is therefore unclear what the mechanism of deformation was, what the role of simple dissolution may have been, and what might be an appropriate constitutive equation for creep of the limestones studied. Much more work has been done on calcite solubility and dissolution, at CO₂ pressures varying from < 0.1 MPa up to 5 MPa [Ellis, 1959; Segnit *et al.*, 1962; Plummer *et al.*, 1978; Sjöberg, 1978; Plummer and Busenberg, 1982; Buhmann and Dreybrodt, 1985; Svensson and Dreybrodt, 1992; Liu and Dreybrodt, 1997; Alkattan *et al.*, 1998; Gledhill and Morse, 2006; Pokrovsky *et al.*, 2005; Kaufmann and Dreybrodt, 2007]. However, the influence of CO₂ on chemically coupled mechanical effects in carbonates remains poorly understood.

The main question that we address in this paper is “What is the effect of CO₂ partial pressure on mechanisms of compaction creep in wet calcite rocks?”. In particular, we aim to assess experimentally if intergranular pressure solution is an active mechanism of compaction in wet calcite aggregates, and whether it is accelerated by increasing CO₂ pressure, as predicted by Renard *et al.* [2005]. To this end, we report the results of uniaxial compaction creep experiments performed on wet granular calcite aggregates with grain sizes between 1 and 250 μm, at applied effective stresses in the range 4 to 40 MPa, at CO₂ partial pressures in the range ~4·10⁻⁵ to 10 MPa and at temperatures varying from 28 to 100°C (mostly at 80°C). These conditions were chosen to simulate in-situ conditions relevant for CO₂ storage. The results show that the mechanisms controlling the compaction creep of wet calcite aggregates are very sensitive to the variables investigated, and that both grain scale microcracking and pressure solution creep play a role in the presence of supercritical CO₂.

2.2 Intergranular Pressure Solution (IPS) – theoretical background

As one of our key aims is to test whether IPS is an active mechanism of compaction in wet calcite aggregates and whether it is accelerated by increasing CO₂ partial pressure, it is useful to begin by presenting some background on the theory of IPS. The symbols used here and throughout this paper are defined in Table 2.1.

Pressure solution creep or IPS is one of the principal mechanisms involved in diagenetic compaction of sediments, in rock deformation at low metamorphic grade, and in controlling the sealing/healing and creep behaviour of faults in the upper crust [Rutter, 1976; Gratier and Guiguet, 1986; Spiers et al., 1990; Hickman and Evans, 1991; Niemeijer et al., 2002, Nakatani and Scholz, 2004; Niemeijer et al., 2008; Van Noort et al., 2008].

On the basis of field and petrographic evidence, IPS is known to be especially important in carbonate rocks [Bathurts, 1975; Rutter, 1983; Tada and Siever, 1989; Renard et al., 2004]. Microstructurally, it is characterized by grain-to grain indentations and overgrowths, grain truncations and micro-stylolites [Rutter, 1976; Tada and Siever, 1989; Dewers and Ortoleva, 1990; Renard et al., 2004; Tondi et al., 2006], and it is often associated with grain scale microcracking [Den Brok, 1990; Gratier et al., 1999; Van Noort et al., 2008].

Symbol	Description	S.I. unit
A_α	Geometric constant – subscript $\alpha = s, d, p$ (s =dissolution, d = diffusion, p = precipitation)	-
$B(\phi_0, \phi)$	Stress concentration factor at grain contacts due to aggregate structure (function of porosity)	-
C	Solubility of solute in grain boundary fluid	$\text{m}^3 \cdot \text{m}^{-3}$
C_0	Solubility of solid under hydrostatic reference conditions	$\text{m}^3 \cdot \text{m}^{-3}$
C_{pores}	Solubility of solid at pore walls	$\text{m}^3 \cdot \text{m}^{-3}$
D	Diffusion coefficient in grain boundary fluid	$\text{m}^2 \cdot \text{s}^{-1}$
d	Initial grain size	m
e_v	Finite volumetric strain	$\text{m} \cdot \text{m}^{-1}$
$f_{\alpha}(\phi_0, \phi)$	Porosity function in IPS models. Expresses changes in grain contact area, transport path length and pore wall area during compaction, $\alpha = p, d, s$ (s =dissolution, d = diffusion, p = precipitation).	-
$g_{\alpha}(\phi_0, \phi)$	Function of porosity and stress concentration factor (B) in models for IPS, $\alpha = p, d, s$ (s =dissolution, d = diffusion, p = precipitation).	-
I_α	Reaction rate coefficient giving velocity of dissolution (I_s) or precipitation (I_p) at unit driving force	$\text{m} \cdot \text{s}^{-1}$
l_0	Initial length of sample	m
l	Instantaneous length of sample	m
R	Universal gas constant	$\text{J} \cdot \text{K}^{-1} \cdot \text{mol}^{-1}$
S	Mean grain boundary width, hence fluid thickness	m
T	Temperature	K
x	Sample length change ($x = l - l_0$)	m
$Z_\alpha(T)$	Temperature dependent coefficient describing the kinetics of dissolution ($\alpha=s$), diffusion ($\alpha=d$), precipitation ($\alpha=p$) controlled IPS	-
ΔC	Enhancement of solid solubility at stressed grain contacts relative to its solubility at pore walls	$\text{m}^3 \cdot \text{m}^{-3}$
t	Time	s
$\Delta\mu$	Chemical potential drop between source and sink sites	$\text{J} \cdot \text{mol}^{-1}$
$\dot{\epsilon}_\alpha$	Volumetric strain rate due to dissolution ($\alpha=s$), diffusion ($\alpha=d$), precipitation ($\alpha=p$) controlled pressure solution	s^{-1}
$\dot{\epsilon}$	Measured axial strain rate	s^{-1}
Φ_0	Initial porosity	%
Φ	Instantaneous porosity	%
μ_{gb}	Average chemical potential of solid in grain boundary segment	$\text{J} \cdot \text{mol}^{-1}$
μ_{pores}	Average chemical potential of solid at pore walls	$\text{J} \cdot \text{mol}^{-1}$
μ	Chemical potential of dissolved solid	$\text{J} \cdot \text{mol}^{-1}$
Ω	Molar volume of solid phase (for calcite $\Omega = 3.69 \cdot 10^{-5} \text{ m}^3 \cdot \text{mol}^{-1}$)	$\text{m}^3 \cdot \text{mol}^{-1}$
σ_e	Applied effective axial stress	Pa
σ_n	Effective normal stress at grain contact	Pa

Table 2.1. List of symbols used in this paper.

On the basis of field and petrographic evidence, IPS is known to be especially important in carbonate rocks [Bathurts, 1975; Rutter, 1983; Tada and Siever, 1989; Renard et al., 2004]. Microstructurally, it is characterized by grain-to-grain indentations and overgrowths, grain truncations and micro-stylolites [Rutter, 1976; Tada and Siever, 1989; Dewers and Ortoleva, 1990; Renard et al., 2004; Tondi et al., 2006], and it is often associated with grain scale microcracking [Den Brok, 1990; Gratier et al., 1999; Van Noort et al., 2008].

Pressure solution creep of rocks requires an intergranular fluid to be present either in an adsorbed grain boundary fluid film or grain boundary micro-channel network [Rutter, 1976; Spiers and Schutjens, 1990; Hickman and Evans, 1991]. In chemically closed systems, it involves three steps: 1) dissolution of material at grain contacts under high normal stress, 2) diffusive transport through the grain boundary fluid film or channel network, and 3) precipitation at grain contacts or pore walls under low normal stress [Rutter, 1976; Lehner, 1990; De Meer et al., 2000; Gundersen et al., 2002]. At steady state, the overall process is accordingly controlled by the slowest step. It is driven by the differences in the effective normal stress (σ_n) around grain boundaries. In the case of a porous rock subjected to isostatic compaction, for example, these lead to a difference in the surface chemical potential between grain boundaries (μ_{gb}) and pore walls (μ_{pores}) [Rutter, 1976; Lehner, 1990; De Meer and Spiers, 1999] given:

$$\Delta\mu \approx \mu_{gb} - \mu_{pores} \approx \Delta\sigma_n \times \Omega \quad (2.1)$$

This drop in chemical potential ($\Delta\mu$) generates a difference in solubility (ΔC) which leads to mass transfer from highly stressed grain contacts to the pore walls. Assuming that the pore fluid behaves as an ideal solution (for which $\mu = \mu_0 + RT \ln C_0$), the relationship between potential drop and solubility difference can be written as:

$$\Delta\mu = RT \ln \left(\frac{C_{pores} + \Delta C}{C_{pores}} \right) = RT \ln \left(1 + \frac{\Delta C}{C_{pores}} \right) \approx RT \frac{\Delta C}{C_0} \quad (2.2)$$

Here, the solubility at the pore walls (C_{pores}) is assumed to be equal to the solubility of the solid under purely hydrostatic conditions (C_0), neglecting minor deformation of the solid at the free grain surfaces (pore walls). The transport of material from grain contacts to pore walls, due to $\Delta\mu$ and ΔC , leads to time-dependent rock compaction and porosity/permeability reduction.

Taking the above expressions for driving force (equations 2.1 and 2.2), assuming that the approximation $\ln(1 + \Delta C/C_{pores}) \approx \Delta C/C_0$ is valid (i.e. assuming that $\Delta C/C_{pores} \ll 1$) and assuming that linear kinetic laws apply, theoretical constitutive flow laws can be derived describing the rate of compaction of a porous aggregate by IPS under isostatic or uniaxial compaction conditions [Rutter, 1976; Lehner, 1990; Spiers and Schutjens, 1990; Spiers et al., 2004]. The results obtained for the three possible rate-controlling processes under closed system conditions (no long range transport) take the form:

$$\dot{\epsilon}_s = A_s \cdot \frac{I_s}{d} \cdot \frac{\sigma_e \Omega}{RT} \cdot f_s(\phi_0, \phi) \quad \text{Dissolution control} \quad (2.3)$$

$$\dot{\epsilon}_d = A_d \cdot \frac{I_d}{d^3} \cdot \frac{\sigma_e \Omega}{RT} \cdot f_d(\phi_0, \phi) \quad \text{Grain boundary diffusion control} \quad (2.4)$$

$$\dot{\epsilon}_p = A_p \cdot \frac{I_p}{d} \cdot \frac{\sigma_e \Omega}{RT} \cdot f_p(\phi_0, \phi) \quad \text{Precipitation control} \quad (2.5)$$

As these equations show, the predicted compaction strain rates ($\dot{\epsilon}_{\alpha=s,d,p}$) depend inversely on grain size (d) in either a linear manner, for the dissolution and precipitation controlled mechanisms, or in a cubic manner, for diffusion-controlled creep. In addition, creep is characterized by a linear dependence of strain rate on applied effective stress (σ_e) [Rutter, 1976; Lehner, 1990; Spiers and Brzesowsky, 1993]. This directly reflects the linear approximation embodied in equation (2.2) and in the assumed linear kinetic laws characterized by the coefficients I_s , [DCS] and I_p . Here I_s and I_p incorporate the temperature - dependent dissolution and precipitation rate coefficients, while [DCS] is a temperature - dependent term incorporating the diffusivity (D) and solubility (C) of the solute in the grain boundary fluid, plus the mean grain boundary width (S). The A_α are geometric constants defined for dissolution, diffusion and precipitation controlled compaction, while the $f_\alpha(\phi_0, \phi)$ are functions of initial porosity (ϕ_0) and instantaneous porosity (ϕ) that express changes in the grain contact area, in the length of the transport path and in the pore wall area during compaction [Spiers et al., 2004].

Recent studies [Dewers and Hajash, 1995; Niemeijer et al., 2002] indicate that for IPS in minerals with a large molar volume (Ω), such as calcite ($\Omega = 3.69 \cdot 10^{-5} \text{ m}^3 \cdot \text{mol}^{-1}$) or quartz ($\Omega = 2.27 \cdot 10^{-5} \text{ m}^3 \cdot \text{mol}^{-1}$), the assumption of a small solubility enhancement ($\Delta C/C_{\text{pores}} \ll 1$) at grain contacts used to derive equations (2.3) – (2.5) is no longer valid, notably when grain contact stresses, hence $\Delta\mu$, are high. In such cases, the stress term $\sigma_e \Omega/RT$ in equations (2.3) – (2.5) must be replaced by the term $\exp\left(\frac{B(\phi_0, \phi) \cdot \sigma_e \Omega}{RT}\right) - 1$, where $B(\phi_0, \phi)$ is a grain contact stress concentration factor that accounts for the evolution of the grain contact area during compaction [Dewers and Hajash, 1995; Niemeijer et al., 2002]. The new constitutive equations obtained for the three rate controlling mechanisms ($\alpha = s, d, p$) can be written in the form:

$$\dot{\epsilon}_\alpha = A_\alpha \cdot Z_\alpha(T) \cdot \left(\exp\left(\frac{B(\phi_0, \phi) \cdot \sigma_e \Omega}{RT}\right) - 1 \right) \cdot \frac{g_\alpha(\phi_0, \phi)}{d^m} \quad (2.6)$$

where $m = 1$ for precipitation/dissolution controlled pressure solution creep, $m = 3$ for the diffusion controlled case, $Z_\alpha(T)$ is the temperature dependent coefficient describing the kinetics of each mechanism, and $g_\alpha(\phi_0, \phi) = f_\alpha(\phi_0, \phi) / B(\phi_0, \phi)$.

From the above theoretical equations for IPS (i.e. eq. 2.3-2.6), it can be seen that the rate-controlling mechanism under given conditions can be identified by comparing experimental data on the effects of grain size and temperature on strain rate with these equations, at fixed porosity ϕ (or at fixed volumetric strain ϵ_v) – assuming that ϕ_0 is ~ constant. To date, several experimental studies have been performed in an attempt to identify and quantify the intergranular pressure solution mechanism in carbonate rocks tested without added CO₂ [Hellmann et al., 2002; Zhang and Spiers, 2005a, 2005b; Heggheim et al., 2005; Zubtsov et al., 2005]. These studies point to pressure solution creep being the dominant mechanism, with diffusion (cf. eq. 2.4) being the most likely

rate-controlling step, at least at low strains. Our main aim is to systematically investigate the effects of grain size, stress and CO_2 partial pressure on the compaction creep of wet calcite aggregates at conditions relevant for CO_2 storage, and to gain insight into whether IPS operates and what the rate controlling mechanism might be.

2.3 Experimental method

2.3.1 Sample and pore fluid preparation

The present uniaxial creep experiments were carried out on pre-compacted, 1-gram samples of granular calcite of specific grain size and porosity. We used crushed Carrara Marble fractions with grain sizes of $28 \pm 3 \mu\text{m}$, $37 \pm 10 \mu\text{m}$, $50 \pm 7 \mu\text{m}$, $85 \pm 5 \mu\text{m}$, $106 \pm 10 \mu\text{m}$, $125 \pm 5 \mu\text{m}$, $210 \pm 10 \mu\text{m}$ and $250 \pm 10 \mu\text{m}$, as well as Merck reagent fractions with grain sizes of $1 \pm 0.5 \mu\text{m}$, $14 \pm 5 \mu\text{m}$, and $30 \pm 5 \mu\text{m}$. The Carrara Marble fractions were obtained by ball-milling and sieving the crushed material, followed by cleaning in an ultrasonic bath to eliminate very fine particles. Merck reagent fractions were obtained by direct separation through sedimentation from suspension in a column of distilled water, applying the principles of Stokes Law. Grain size distributions were measured using a particle sizer laser. In all cases more than 80 % of the grains fell into the size ranges mentioned above. According to the manufacturer's specifications, the main impurities in the Merck material (99.7 % pure) were Sr (< 0.1 %), Na (< 0.2 %) and Mg (<0.005 %), while in the Carrara Marble the main impurities were MgO (< 0.30 %), K_2O (< 0.13 %), SiO_2 (< 0.06 %) and Fe_2O_3 (< 0.05 %), as indicated by XRF analysis. No measurements of the specific surface area of the calcite fractions were made.

Prior to conducting our compaction experiments, pre-saturated pore fluid was prepared by adding excess calcite grains, of the same composition and granulometry as the material to be mechanically tested, to boiled, distilled water. The solution was stirred for 48 hours in an open flask at room temperature and atmospheric pressure. This procedure was based on the studies of *Rickard and Sjöberg* [1983] and of *Pokrovsky and Schott* [2002], who showed that 48 hours is sufficient to produce an equilibrated calcite solution under ambient laboratory conditions.

2.3.2 Experimental set-up

Uniaxial compaction creep tests were performed on the granular calcite samples described above using an Instron 8562 servo-controlled testing machine, equipped with a 10 kN load cell (accuracy 0.10 %) plus a 1-D compaction vessel made from hardened stainless steel (Remanit 4122). A semi-schematic representation of the set-up is shown in Figure 2.1. To reduce any contamination of the sample with metal ions, the compaction vessel was lined with a titanium inner vessel (inner diameter 10 mm), which contained the sample. The sample was loaded axially by means of two closely fitting titanium pistons, driven by upper and lower Remanit pistons sealed against the outer Remanit vessel with Viton O-rings. The outer vessel and its contents were heated using an external furnace regulated by means of a Eurotherm temperature controller connected to a Type

K (Chromel/Alumel) thermocouple, located in a well in the external skin of the Remanit vessel. A second Type K thermocouple was placed in a deeper well at a distance of 0.5 mm from the titanium insert containing the sample. On the basis of previous calibrations this was assumed to yield the sample temperature. The piston displacement obtained during uniaxial loading was measured using a Linear Variable Differential Transducer (LVDT) located in the Instron drive unit, plus an external Sangamo LVDT with a range of ± 1 mm for more precise measurements (0.05 % resolution). The Sangamo LVDT was positioned such that it measured the relative displacement between the upper Remanit piston and the top part of the outer vessel during the compaction tests (see Figure 2.1).

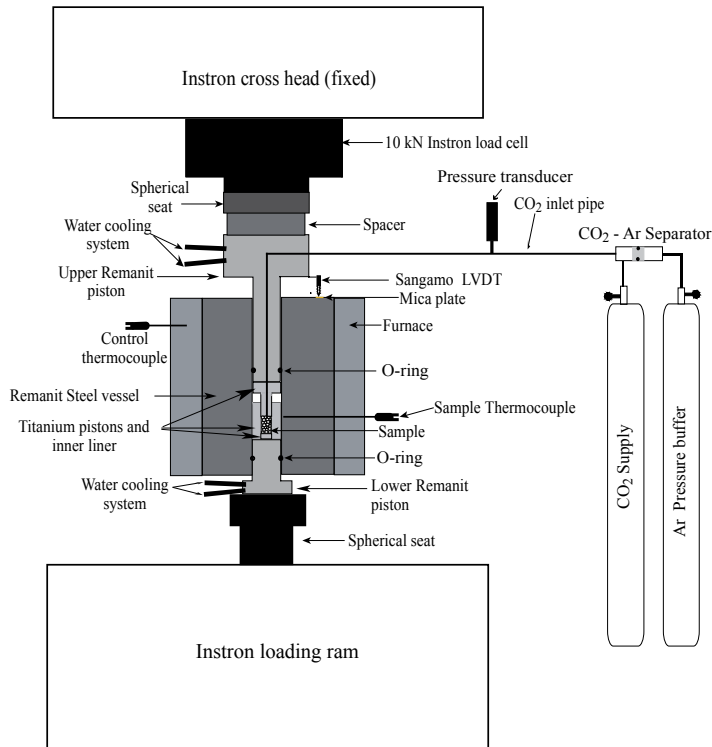


Figure 2.1. Semi-schematic representation of the central elements of the present experimental set-up, including the stainless steel compaction vessel, the titanium inner vessel/liner and the pore fluid system.

In all compaction experiments performed under wet conditions, pre-saturated solution was added to the sample during assembly of the vessel. High purity carbon dioxide was introduced, after vessel assembly, via the inlets in the upper Remanit piston and titanium vessel, using an Air Products CO₂ cylinder. The CO₂ was initially introduced at pressures up to 5 MPa, and then boosted to higher pressures (up to 10 MPa) using an argon-backed separator (Figure 2.1). The applied CO₂ pressure, which is approximately equal to the

CO₂ partial pressure at the temperatures of 28-100°C employed in our experiments, was measured to within 0.1 MPa using an MSI US 175 pressure transducer. The argon buffer system shown in Figure 2.1 maintained constant fluid pressure in the sample and pore fluid system during experiments performed with CO₂, despite advancement of the loading piston. In experiments at atmospheric pressure, the sample and pore fluid system were simply vented to air.

2.3.3 Data acquisition and processing

Our raw experimental data (load, displacement, temperature and carbon dioxide pressure signals) were logged using a PC plus 16-bit A/D converter along with standard Instron software employing a 10 second sampling cycle. The required loading history for each test was programmed and controlled using Instron routines. Displacement data were corrected for temperature fluctuations and for apparatus distortion, based on calibration tests performed using a Remanit 4122 stainless steel dummy sample of known elastic modulus (215 GPa) and thermal expansion coefficient ($17.3 \times 10^{-6} \text{ K}^{-1}$). The displacement data were subsequently smoothed using a moving average method, and processed to yield sample shortening, instantaneous porosity, volumetric strain and strain rate versus time. The finite volumetric strain (e_v) and the volumetric strain rate ($\dot{\epsilon}$) at any instant were calculated as a function of time (t) from the corrected and smoothed displacement data, i.e. sample shortening (data: $x=l_0-l$) using the relations:

$$e_v = \frac{x}{l} \text{ and } \dot{\epsilon} = \frac{1}{l} \cdot \frac{\Delta x}{\Delta t} \quad (2.7, 2.8)$$

where l_0 and l are the initial and instantaneous sample lengths, taking shortening as positive. The instantaneous strain rate was calculated using a moving window method over a constant displacement interval (Δx) in varying time intervals (Δt), such that the maximum error was 5 % for the experiments performed on crushed Carrara Marble and 10 % for the ones on Merck reagent. The porosity of the samples during compaction was calculated from the sample mass, cross-section and length, using the density of pure calcite ($2710 \text{ kg} \cdot \text{m}^{-3}$) for the solid phase.

2.3.4 Testing procedure

Three different types of uniaxial compaction experiments were carried out:

- Type A: Control experiments on dry and wet samples without CO₂
- Type B: Wet compaction experiments with CO₂ injection after one hour of creep
- Type C: Wet compaction experiments with CO₂ injection before loading.

A summary of all experiments performed is provided in Table 2.2, while a schematic representation of the steps followed in each type of test can be found in Figure 2.2.

Note that Type A and C tests were performed on crushed Carrara Marble, while Type B were performed on both crushed Carrara Marble and on Merck reagent (denoted in Figure 2.2 as B_(C) and B_(M) respectively).

The main procedure used in all of the tests was as follows. First, one gram of sample

material was placed into the assembly formed by the titanium vessel and the lower titanium piston. In the wet compaction tests, a volume of saturated solution corresponding to a pore volume equivalent to 25-35 % porosity was then mixed with the sample, to insure a fully wetted state of the material. The titanium vessel assembly, complete with the upper titanium piston, was subsequently positioned in the outer Remanit vessel, and the upper and lower Remanit pistons inserted. The entire assembly was finally bolted to the Instron loading ram. A small fixed load, of around 10 N, was then applied to the sample by advancing the Instron ram. The compaction vessel was subsequently heated using the external furnace until the sample reached the temperature assigned for the test. Temperatures employed ranged from 28-100°C, though most experiments were done at 80°C (temperature corresponding to 2-3 km depth). When the desired temperature was attained, all samples were subjected to a pre-compaction phase, whereby the sample was loaded for 30–60 minutes at effective axial stresses of 40 - 50 MPa, to obtain a reproducible “starting porosity” (ϕ_0) of 25-29 % (for the wet samples) or 35 % (for the dry samples).

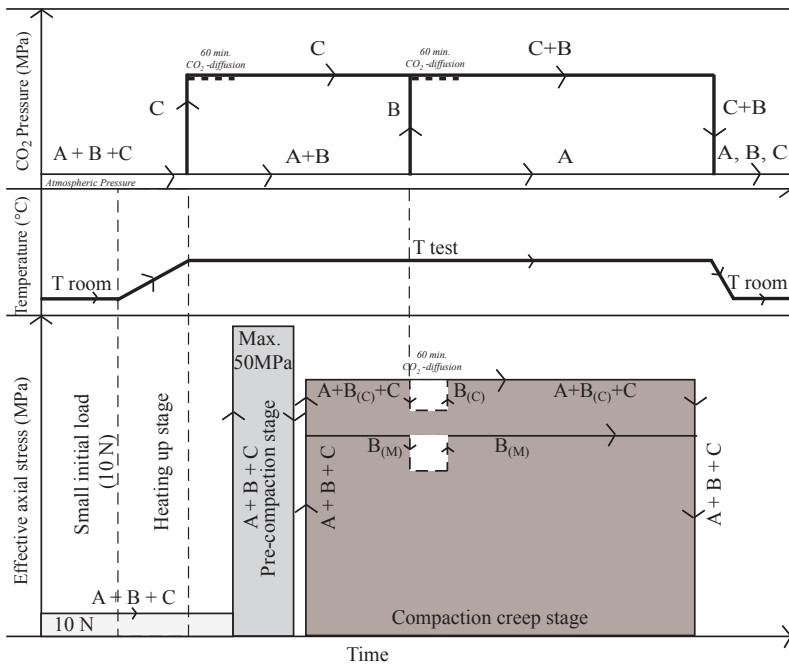


Figure 2.2. Schematic representation of the procedure followed for each type of test performed (Types A, B, C), including the stress paths, the CO₂ pressure and the temperature paths followed during the tests. Note: Type B and C tests were performed at effective axial stresses varying from 4 to 40 MPa. Here B_(C) represents Type B tests performed on Carrara Marble samples, while B_(M) represents Type B tests performed on Merck reagent material.

Note: All experiments were performed with calcite-saturated solution as pore fluid, with the exception of test A-1 and A-1* which were performed under dry (lab air) conditions. Experiments A-1* and A-2* were used for microstructural purposes only. Here PCO₂ represents the CO₂ pressure applied to the fluid filled samples via the pore fluid system. This was approximately equal to the CO₂ partial

pressure at the temperatures of 28-100°C employed in the present experiments. ϕ_0 represents the initial porosity of the samples.

Type	Sample ID	Material	Mean initial grain size [μm]	Applied effective stress [MPa]	PCO ₂ [MPa]	Temperature [°C]	ϕ [%]	Final strain ϵ_c [%]	vol.
A	A-1	Crushed Marble (dry)	28	40	$-4 \cdot 10^{-5}$	80	34.95	0.01	
	A-2	Crushed Marble	28	40	$-4 \cdot 10^{-5}$	80	29.17	0.50	
	A-1*	Merck reagent (dry)	14	30	$-4 \cdot 10^{-5}$	80	34.95	-	
	A-2*	Merck reagent	14	30	$-4 \cdot 10^{-5}$	80	29.76	-	
B	B-1	Merck reagent	1	30	10	80	28.99	0.83	
	B-2	Merck reagent	14	30	10	80	29.12	1.48	
	B-3	Merck reagent	30	30	10	80	28.82	1.82	
	B-4	Crushed Marble	28	40	10	80	26.66	3.89	
	B-5	Crushed Marble	37	40	10	80	26.69	3.51	
	B-6	Crushed Marble	50	40	10	80	26.72	5.90	
	B-7	Crushed Marble	106	40	10	80	26.51	5.45	
	B-8	Merck reagent	1	4	10	80	28.73	0.35	
	B-9	Merck reagent	1	20	10	80	28.91	0.68	
	B-10	Merck reagent	1	30	10	80	29.05	0.81	
	B-11	Crushed Marble	28	20	10	80	26.30	0.73	
	B-12	Crushed Marble	28	30	10	80	26.98	1.91	
	B-13	Crushed Marble	28	40	10	80	27.12	3.87	
C	C-1	Crushed Marble	28	30	10	80	25.93	2.09	
	C-2	Crushed Marble	50	30	10	80	24.84	0.94	
	C-3	Crushed Marble	85	30	10	80	24.56	0.47	
	C-4	Crushed Marble	106	30	10	80	24.93	0.33	
	C-5	Crushed Marble	28	20	10	80	25.13	0.11	
	C-6	Crushed Marble	28	25	10	80	25.29	0.20	
	C-7	Crushed Marble	28	30	10	80	25.20	0.34	
	C-8	Crushed Marble	28	35	10	80	25.55	0.52	
	C-9	Crushed Marble	28	40	10	80	24.98	0.72	
	C-10	Crushed Marble	28	30	6	80	24.79	0.89	
	C-11	Crushed Marble	28	30	8	80	25.31	0.34	
	C-12	Crushed Marble	28	30	10	28	25.01	2.24	
	C-13	Crushed Marble	28	30	10	60	24.99	0.45	
	C-14	Crushed Marble	28	30	10	100	24.86	0.17	
	C-15	Crushed Marble	125	30	10	80	24.93	0.60	
	C-16	Crushed Marble	210	30	10	80	24.75	0.76	
	C-17	Crushed Marble	250	30	10	80	24.60	0.96	

Table 2.2. List of the experiments reported in this paper and the conditions at which the tests were conducted.

This procedure was adopted to produce samples with a reproducible “locked” structure, and was employed to eliminate deformation by simple grain rearrangement during subsequent creep testing at lower stresses. When the desired starting porosity was reached (determined from the length change of the sample), the compaction creep phase of the tests was started by first fully unloading the sample and then applying the desired load. The progress of compaction was subsequently monitored for periods up to 2 days. Note that in the Type A control experiments, no CO₂ was injected at any stage – the experiments were simply performed dry or with added solution (wet) vented to air, following the procedure described above. In the Type B tests, CO₂ was injected into the wet samples at 10 MPa pressure about 1 hour into the creep stage (Figure 2.2). Immediately before injection of CO₂, the Instron was switched to position control, such that during the ~ 60-minute period allowed for CO₂ to diffuse through and dissolve in the pore fluid, the length of the sample remained constant and no creep occurred. One hour was allowed following CO₂-water equilibration times measured independently using a Fourier Transform Infrared (FTIR) microscope plus high-pressure optical cell of similar dimensions

to the inner titanium vessel. Finally, the effective applied stress was returned to the value assigned for the test and creep was restarted (see Type B tests, Figure 2.2). In the Type C tests, heating of the sample to the desired test temperature was followed by CO₂ injection at 6-10 MPa pressure while maintaining a constant effective axial force of ~10 N. After allowing ~60 minutes for the CO₂ to diffuse through and dissolve in the pore fluid, the pre-compaction and then the compaction creep stages were initiated by adjusting the applied axial force to the required values (see Type C tests, Figure 2.2). All tests were terminated by unloading the sample, releasing the CO₂ pressure and allowing the apparatus to cool down, followed by careful removal of the sample from the vessel.

2.4 Results

2.4.1 Mechanical data

2.4.1.1 Type A experiments

The pre-compaction stage of our dry and wet control experiments, A-1 and A-2, on crushed Carrara Marble (80°C, 40 MPa and 28 μm grain size) produced starting porosities (ϕ_0) of 35 % and 29 %, respectively (Table 2.2). When reloaded in creep mode at a constant axial stress of 40 MPa, dry sample A-1 showed a more or less instantaneous deformation of 0.02 % shortening, but little or no measurable creep (Figure 2.3). By contrast, wet control sample A-2 showed rapid creep in this stage, achieving a strain of almost 0.5 % in 1 hour despite its much lower starting porosity (Figure 2.3).

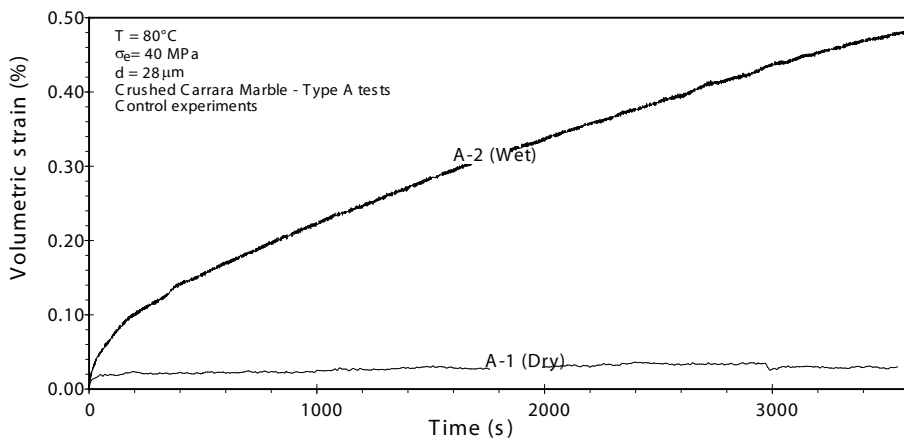


Figure 2.3. Volumetric strain versus time data for dry (A-1) and wet (A-2) samples of crushed Carrara Marble ($d = 28 \mu\text{m}$) compacted in creep mode at 80°C and 40 MPa applied effective stress without added CO₂ (Type A tests). Dry loading (A-1) resulted in initial time-independent compaction only, whereas the addition of CaCO₃ saturated solution promoted time-dependent compaction, resulting in around 15 times more volumetric strain after 1 hour.

2.4.1.2 Type B experiments

Pre-compaction in the Type B experiments led to a starting porosity (ϕ_0) of around 29

% for Merck reagent ($d = 1\text{--}30\ \mu\text{m}$) and 26 % for crushed Carrara Marble ($d = 28\text{--}106\ \mu\text{m}$) attained in one hour. Subsequent reloading in creep mode led to rapid creep similar to that seen in wet control test A-2. However, injection of CO_2 , after ~ 1 hour of creep, brought about a dramatic increase in volumetric strain and strain rate upon reloading.

Reloading was followed by rapidly decelerating creep as illustrated in Figures 2.4a and b. Typical strain rate data obtained in the Type B tests are depicted in the form of log volumetric strain rate ($\dot{\epsilon}_v$) vs. log volumetric strain (e_v) curves in Figures 2.5a-d for both Merck reagent and crushed Carrara Marble.

The data are represented in terms of strain rate versus volumetric strain; since each set of tests is characterized by a narrow range of porosities (Table 2.1), volumetric strain is a good measure of the evolving structure of the material.

These data show not only the effect of CO_2 injection, but also the effect of initial grain size and applied effective stress on strain rate for individual samples at 80°C .

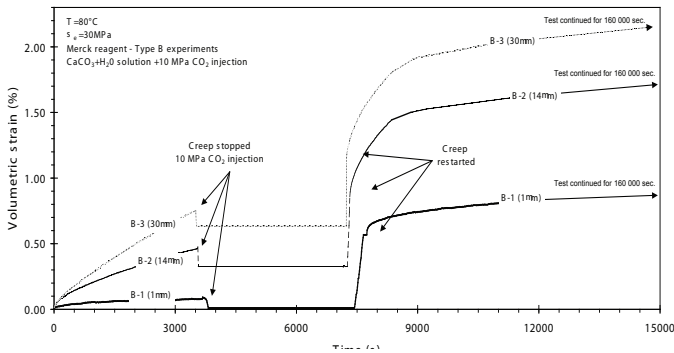


Figure 2.4a. Volumetric strain versus time data obtained in Type B experiments for wet samples of Merck reagent compacted in creep mode at 80°C and 30 MPa applied effective stress. Addition of supercritical CO_2 at a pressure of 10 MPa after ~ 60 minutes resulted in a sharp increase in strain and strain rate.

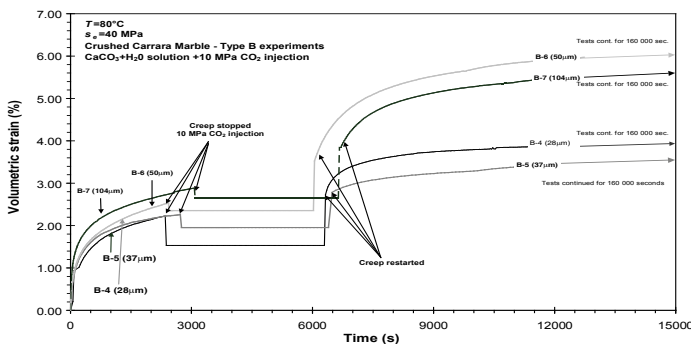


Figure 2.4b. Volumetric strain versus time data obtained in Type B experiments for wet samples crushed Carrara Marble compacted in creep mode at 80°C and 40 MPa applied effective stress. Addition of supercritical CO_2 at a pressure of 10 MPa after ~ 60 minutes resulted in a sharp increase in strain and strain rate.

Note that before the addition of CO₂, at similar volumetric strain (e_v) and conditions (e.g. for a grain size $d \sim 30 \mu\text{m}$, effective applied stress of 30 MPa and at a volumetric strain of 0.6 %, i.e. $\log e_v = -0.2$), Merck reagent crept at a strain rate about 25 times slower than the crushed Carrara - see Figures 2.5a and d (e.g. tests B-3 vs. B-12). In both the Merck and crushed Carrara Marble samples, injection of CO₂ at 10 MPa, under conditions of constant effective stress, led to an increase in strain rate of 1-3 orders of magnitude (Figure 2.5a and b). After injection, however, creep rates decreased much more rapidly with strain than before injection, and in some cases virtually halted (e.g. test B-9, Figure 2.5c).

Focusing now on the effect of grain size, the strain rates measured for the Type B samples compacted wet, before injection of supercritical CO₂, increase with increasing grain size (Figure 2.5a, b).

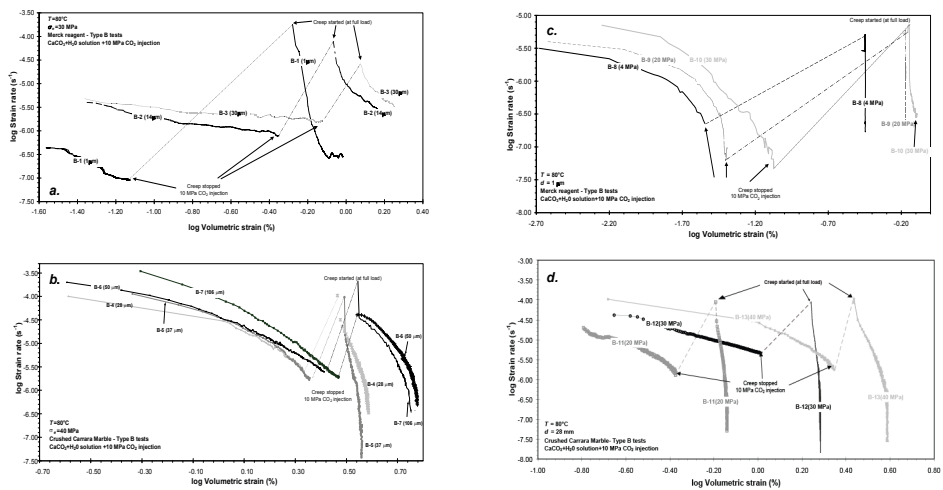


Figure 2.5. Log axial strain rate ($\dot{\epsilon}$) versus log volumetric strain (e_v) data obtained in the Type B experiments. Data obtained for a) wet Merck reagent at various grain sizes and 30 MPa, b) wet Carrara Marble of varying grain sizes and 40 MPa, c) wet samples of Merck reagent with a grain size of 1 μm and varying effective stress, and d) wet crushed Carrara Marble with a grain size of 28 μm at various effective applied stresses. In all the plots, the dotted line represents the CO₂ addition/equilibration phase employed in the Type B experiments. Subsequent creep data are plotted from the moment that full load was re-applied. Strain rates generally increase with increasing grain size and increasing stress. Addition of 10 MPa CO₂ after one hour of creep resulted in an increase in strain rate by up to 1-3 orders of magnitude.

Plots of log strain rate ($\dot{\epsilon}$) measured at fixed volumetric strain (e_v) (hence \sim constant porosity) versus log initial grain size confirm this (Figure 2.6) and suggest a direct, near linear relation between strain rate and grain size, described by a grain size power law exponent $m = -1.1 \pm 0.1$ (i.e. $\dot{\epsilon} \propto d^{1.1 \pm 0.1}$) for Merck reagent and $m = -0.9 \pm 0.1$ (i.e. $\dot{\epsilon} \propto d^{0.9 \pm 0.1}$) for Carrara Marble. After injection of CO₂, the strain rate increases similarly with increasing grain size for the Merck reagent (Figure 2.5a), however no clear trends could be identified

for crushed Carrara Marble (Figure 2.5b).

The effect of applied stress on the compaction creep rates measured in the Type B tests before injection of CO₂ (Figure 2.5c and d) is shown in Figure 2.7, for both Merck

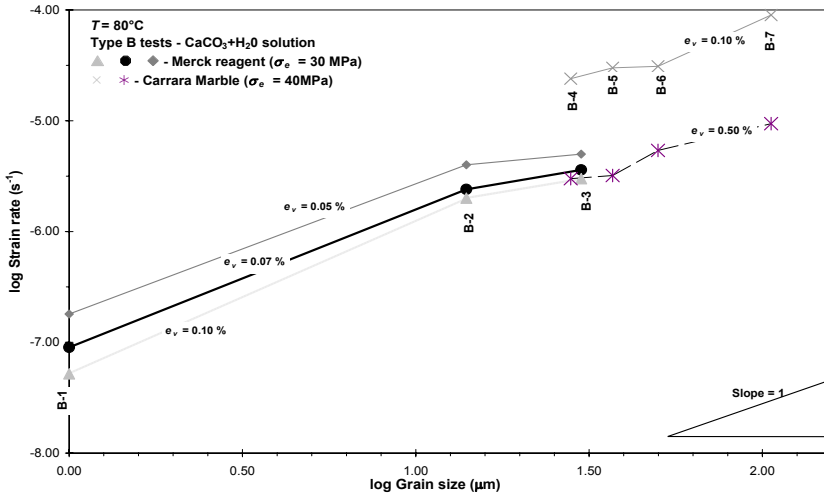


Figure 2.6. Log strain rate ($\dot{\epsilon}$) versus log initial grain size (d). Data for Merck reagent and crushed Carrara Marble compacted in presence of saturated solution, at 80°C and 30 MPa (Merck reagent) or 40 MPa (Carrara Marble) applied effective stress - Type B experiments, before addition of CO₂. The plot shows that the strain rate increases with increasing grain size in near a nearly linear manner.

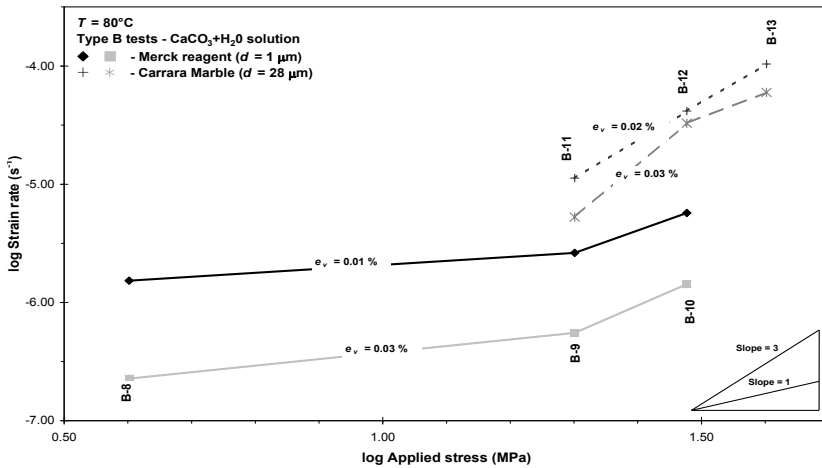


Figure 2.7. Log strain rate ($\dot{\epsilon}$) versus log applied effective stress (σ_e) for Merck reagent ($d = 1 \mu\text{m}$) and crushed Carrara Marble samples ($d = 28 \mu\text{m}$) compacted in the presence of CaCO₃-saturated solution at 80°C - Type B experiments, before CO₂ addition. The strain rate increases with increasing applied effective stress showing an apparent n -value of 0.8 at low stress (Merck reagent) and 3.5 at high stress (Carrara Marble).

reagent and Carrara Marble. Using a power law ($\dot{\epsilon} \propto \sigma_e^n$) to describe the variation of the strain rate with effective stress before CO₂ addition yields an n - value of 0.8 ± 0.2 for

Merck reagent and 3.5 ± 0.3 for crushed Carrara Marble at fixed strains (0.01 - 0.03 %). After addition of CO₂, the large jump in strain and the rapid decrease in strain rate with strain seen in Figure 2.5c and 2.5d prevent assessment of the stress sensitivity of creep rate other than to note qualitatively that this is positive.

2.4.1.3 Type C experiments

Type C tests on crushed Carrara Marble, with CO₂ added from the start of the test, displayed rapid compaction in the pre-compaction phase (at ~ 50 MPa effective stress) attaining 25 % starting porosity (ϕ_0) in 2 hours. In the subsequent compaction creep phase, all samples showed steadily decelerating time-dependent compaction (e.g. Figure 2.8a). For similar applied stresses, grain sizes and volumetric strains, the Type C samples crept at much slower strain rates in the presence of supercritical CO₂ than Type B samples tested in the absence of CO₂.

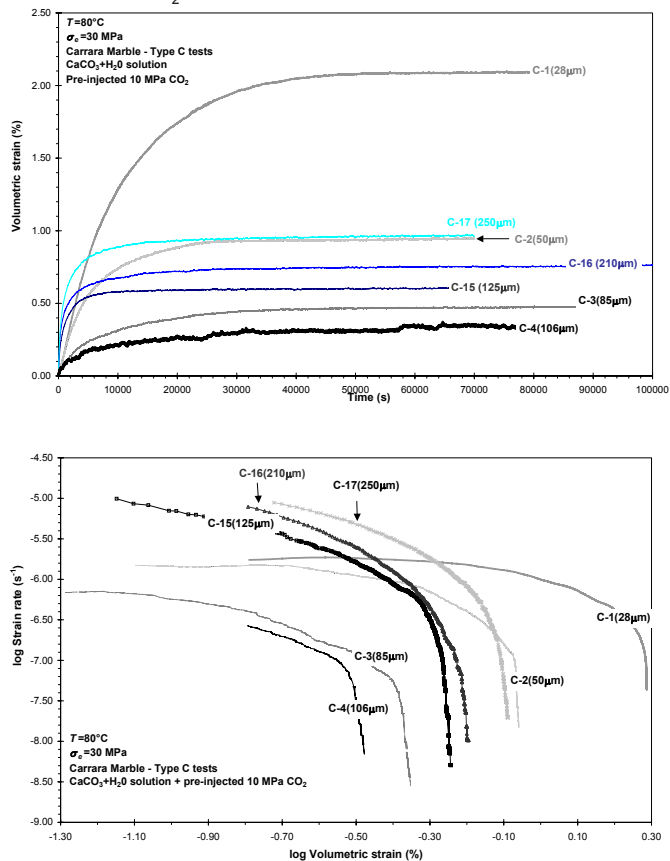


Figure 2.8. Typical creep data for Type C tests on crushed Carrara Marble. a) Creep curves for samples with grain sizes in the range 28-250 μm compacted in the presence of supercritical CO₂ at 80°C and 30 MPa, b) Plot of log strain rate ($\dot{\epsilon}$) versus log volumetric strain (e_v) constructed from the creep data shown in (a).

For example, at $d = 28 \mu\text{m}$, $\sigma_e = 30 \text{ MPa}$ and $e_v = 0.5 \%$ ($\log e_v = -0.3$), crushed Carrara

Marble crept at a strain rate of $\sim 1.4 \cdot 10^{-5} \text{ s}^{-1}$ ($\log \dot{\epsilon} = -4.85$) in test B-12, and at a strain rate of $\sim 1.6 \cdot 10^{-6} \text{ s}^{-1}$ ($\log \dot{\epsilon} = -5.79$) in test C-1 (cf. Figures 2.5d and 2.8b). In the presence of supercritical CO_2 , the strain rates ($\dot{\epsilon}$) obtained for crushed Carrara Marble in tests C also appear to be much slower than the ones observed in Type B tests; at a volumetric strain (e_v) of 1.7 % ($\log e_v = 0.23$), at $d = 28 \mu\text{m}$, $\sigma_e = 30 \text{ MPa}$ Type B samples crept at a strain rate of $\sim 8.9 \cdot 10^{-5} \text{ s}^{-1}$ ($\log \dot{\epsilon} = -4.05$) in test B-12, while in Type C test C-1 it crept at a strain rate $\sim 3.1 \cdot 10^{-7} \text{ s}^{-1}$ ($\log \dot{\epsilon} = -6.50$) (cf. Figures 2.5d and 2.8b). However, it is difficult to compare the strain rate in Type B and Type C tests after addition of CO_2 , as these decrease rapidly with volumetric strain, approaching similar strain rate of $\sim 10^{-8} \text{ s}^{-1}$ ($\log \dot{\epsilon} = -7$) at strains of $\sim 1.9 \%$ ($\log e_v = 0.28$).

In the Type C experiments, two-grain size regimes emerge (Figure 2.9). For grain sizes smaller than $106 \mu\text{m}$, an inverse dependence of creep rate on grain size was found at stresses of 30 MPa and a PCO_2 of 10 MPa (Figure 2.8b and 2.9), compared with a direct dependence in Type B tests before addition of CO_2 (Merck and crushed Carrara Marble samples) and after addition of CO_2 (Merck samples) - see Figure 2.6. However, as in the Type B tests, Type C experiments showed that at grain sizes of $106 - 250 \mu\text{m}$ the strain rate increases with increasing initial grain size (Figure 2.9).

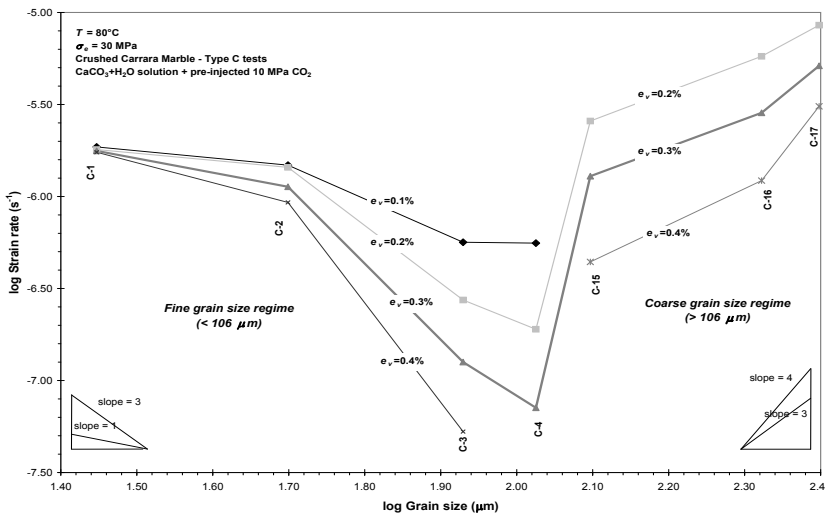


Figure 2.9. Plot of log strain rate ($\dot{\epsilon}$) versus initial grain size (d) for wet samples of crushed Carrara Marble constructed from the Type C test data presented in Figure 8b. Note the two regimes of behavior exhibited. For $d < 106 \mu\text{m}$ (C-4), the strain rate decreases with increasing grain size at fixed volumetric strain (e_v), while the coarser samples ($d > 106 \mu\text{m}$) exhibit a direct dependence of strain rate upon grain size.

In the fine grain size regime of Figure 2.9 ($d < 106 \mu\text{m}$), a power law relation can be used to describe the data roughly ($\dot{\epsilon} \propto 1/d^m$). At the beginning of the experiments, i.e. $e_v \leq 0.20\%$, the sensitivity of the strain rate to grain size is low (slope $m \approx 1$), whereas towards the end of the experiments ($e_v \geq 0.30 \%$) the sensitivity is much higher (slope $m \approx 3$) (see

Figure 2.9). At the beginning of the experiments, i.e. $e_v \leq 0.20\%$, the sensitivity of the strain rate to grain size is low (slope $m \approx 1$), whereas towards the end of the experiments ($e_v \geq 0.30\%$) the sensitivity is much higher (slope $m \approx 3$) (see Figure 2.9). At these fine grain sizes, our data on crushed Carrara Marble samples (tests C-5 to C-9, with a grain size of $28 \mu\text{m}$ tested at different stresses) showed that increasing the applied effective stress (at $e_v = 0.02 - 0.5\%$) strongly increased creep rate, equivalent to a power law stress sensitivity n of 6 – 15, as shown in Figure 2.10. Similarly, increasing the injected CO₂ pressure from 6 to 10 MPa (tests C-7, C-10, C-11) in the fine-grained regime ($d = 28 \mu\text{m}$) led to a significant increase (~ 50 times) in strain rate, as shown in Figure 2.11. By contrast, increasing the temperature from 28 to 100°C (tests C-7, C-12, C-13, C-14) led to a marked decrease in strain rate and in total volumetric strain achieved, especially in the temperature interval from 28 to 60°C (Figure 2.12a, b). We have not investigated the effects of applied effective stress, CO₂ pressure or temperature in the coarse-grained creep regime ($d > 106 \mu\text{m}$) seen in the Type C experiments.

2

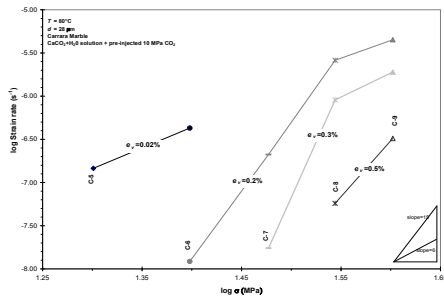


Figure 2.10. Plot of log strain rate vs. log applied effective stress for crushed Carrara Marble samples of $28 \mu\text{m}$ grain size, compacted in presence of supercritical CO₂ - Type C tests. The plot shows that strain rate increases with increasing applied effective stress at fixed volumetric strain.

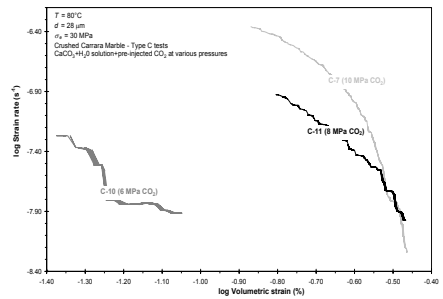


Figure 2.11. Plot of log strain rate versus log volumetric strain for crushed Carrara Marble in Type C tests at various CO₂ pressures. Fine grain size regime ($d=28 \mu\text{m}$) with $T=80^\circ\text{C}$, $\sigma_e=30 \text{ MPa}$. The strain rate increases with increasing CO₂ pressure. Note the steps in the data are artifacts resulting from the data processing.

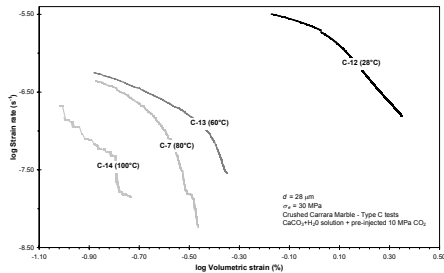


Figure 2.12a. Effect of temperature on compaction creep of crushed Carrara Marble samples with $d = 28 \mu\text{m}$, Type C tests. The strain rate decreases with increasing temperature. Log strain rate versus log volumetric strain for samples tested at 28, 60, 80 and 100°C.

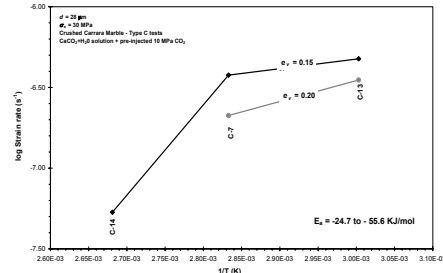


Figure 2.12b. Effect of temperature on compaction creep of crushed Carrara Marble samples with $d = 28 \mu\text{m}$, compacted at $\sigma_e = 30 \text{ MPa}$ and 10 MPa CO_2 - Type C tests. Log strain rate versus $1/T$ (Arrhenius type plot).

2.4.2 Microstructural observations

Optical and SEM observations on uncompacted (i.e. “as separated”) grain size fractions of crushed Carrara Marble and of Merck reagent show mainly rhombohedral and sub-rhomboidal grains of relatively uniform size. Around 60% of the Carrara Marble grains show swarms of thin twins. Scanning Electron Microscope (SEM) images of Merck reagent samples compacted under dry (test A-1*) and wet (test A-2*) conditions, identical to the conditions employed in the control experiments performed on Carrara Marble (Type A tests), are shown in Figures 2.13a and b.

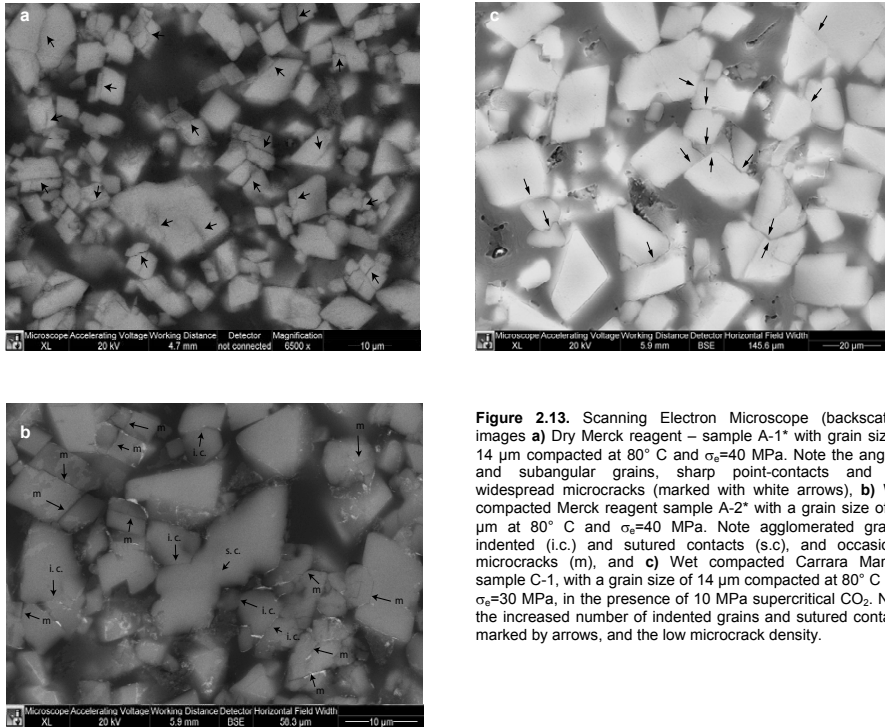


Figure 2.13. Scanning Electron Microscope (backscatter) images **a)** Dry Merck reagent – sample A-1* with grain size = 14 μm compacted at 80° C and $\sigma_c=40$ MPa. Note the angular and subangular grains, sharp point-contacts and the widespread microcracks (marked with white arrows). **b)** Wet compacted Merck reagent sample A-2* with a grain size of 14 μm at 80° C and $\sigma_c=40$ MPa. Note agglomerated grains, indented (i.c.) and sutured contacts (s.c.), and occasional microcracks (m), and **c)** Wet compacted Carrara Marble, sample C-1, with a grain size of 14 μm compacted at 80° C and $\sigma_c=30$ MPa, in the presence of 10 MPa supercritical CO₂. Note the increased number of indented grains and sutured contacts marked by arrows, and the low microcrack density.

Dry compacted control material (sample A-1*) shows a granular microstructure, again with (sub) rhombohedral grains (Figure 2.13a). Many of the contacts between the grains are sharp-point contacts (30 %). Note the frequent fractured grains (m) and rare aggregated grains. The control sample compacted under wet conditions without CO₂ (A-2* test - Figure 2.13b) shows (sub) rhombohedral grains with occasional indented (i.c.) and sutured contacts (s.c.). In comparison with the dry compacted material, fewer crushed or fractured grains (m) can be observed, though they are still present. The wet material shows larger numbers of agglomerated grains (Figure 2.13b) displaying interlocking or tightly fitting contacts. The wet compacted samples also show lower porosities in the SEM images than the dry-compacted ones. Linear intercept analysis showed that overall; the grain size distribution of wet samples is little affected by deformation. Injection of CO₂ from the beginning of

the Type C experiments on crushed Carrara Marble (Test C-1) resulted in an increased number of indented grains and tightly fitting contacts (Figure 2.13c), compared with the samples compacted in presence of CaCO₃-saturated solution only (A-2* sample). Optical study of Carrara Marble samples compacted in Type B tests (Test B-6) demonstrates the presence of numerous cracked grains, together with widespread fines, crushed contacts (c.c) and rare tightly fitting or indented contacts (i.c) (Figure 2.14a). Twins are visible in similar amounts as in the starting material. Confirming the SEM observations on Type C samples, optical microscopy showed fewer microcracks and fewer crushed contacts (test C-2) than in the samples obtained from Type B tests (Figure 2.14a), but markedly more indented grains, more sutured contacts and truncated grains (Figure 2.14b).

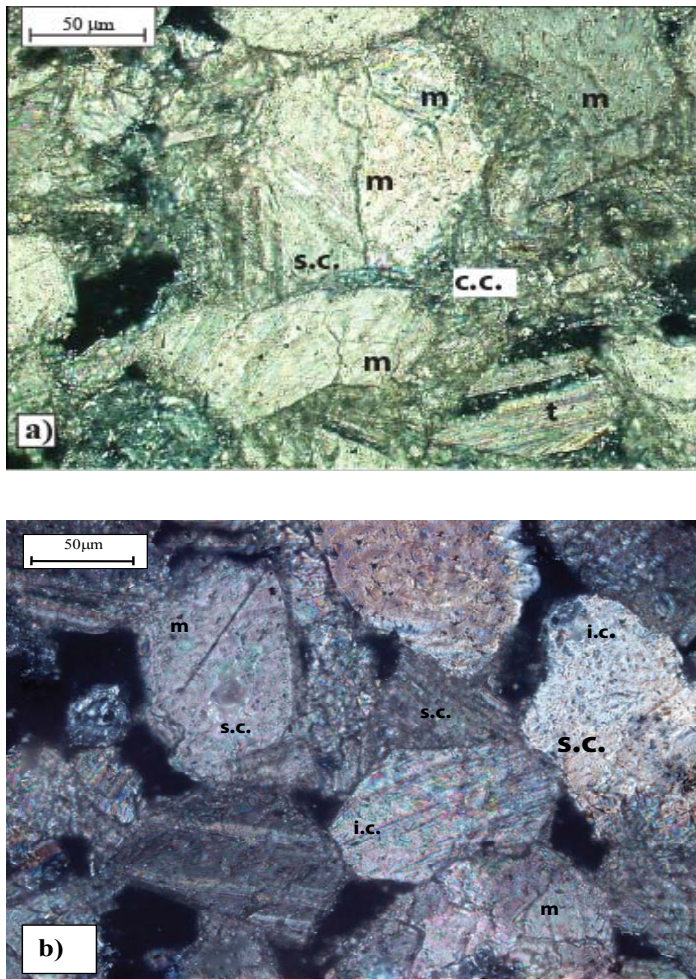


Figure 2.14. **a)** Micrograph of crushed Carrara Marble, sample B-6 (grain size = 50 μm) uniaxially compacted in the presence of saturated CaCO₃ solution at 80° C and 40 MPa effective stress. Note the widespread presence of microcracks (m), the occasional sutured contacts (s.c) and the crushed contacts (c.c). **b)** Micrograph of crushed Carrara Marble, sample C-2 (grain size = 50 μm) uniaxially compacted at 80° C and 30 MPa effective stress in the presence of saturated CaCO₃ solution and 10 MPa supercritical CO₂. Note the increased number of sutured contacts and tightly fitting contacts. Microcracks (m) are far less widespread than in (a).

2.5 Discussion

2.5.1 Deformation mechanism in dry compacted samples

The compaction data obtained in the dry control test (A-1, Figure 2.3) suggest a time-independent deformation process, as $\sim 0.02\%$ volumetric strain was achieved almost instantaneously in the first few minutes of the tests, while for the remainder of the test further strain was below the resolution of the LVDT. This implies that compaction creep, if any occurred in this stage, proceeded at rates slower than 10^{-9} s^{-1} . The corresponding microstructures (sample A-1*) show crushed and fractured grains (Figure 2.13a). On the basis of the microstructures, we infer that the dry pre-compaction, which accounted for significant strain before the creep stage of the dry tests, occurred by grain crushing/fracturing and presumably grain rearrangement. Subsequent time-independent compaction of the dry calcite samples was probably largely elastic. It also accounted for significant strain before the creep stage of the dry tests, and. Since little or no creep was observed during the dry-compaction control test, time-dependent crystal plastic flow mechanisms (i.e. dislocation creep) are ruled out as significant compaction mechanisms in dry material.

2.5.2 Deformation mechanisms under wet conditions

In this section, we will first summarize the results and then discuss the mechanisms of compaction of our wet calcite samples, i.e. Merck and Carrara samples loaded in the presence of CaCO_3 -saturated solution only.

Wet compaction of our calcite samples (the A-2 test and the first part of the Type B tests) showed time-dependent creep not seen in dry compacted material, at rather rapid rates ($10^{-5} - 10^{-7} \text{ s}^{-1}$ for Merck reagent samples and $10^{-3} - 10^{-6} \text{ s}^{-1}$ for crushed Carrara Marble samples, as shown in Figures 2.5a and b). The microstructure of wet-compacted samples, both Merck reagent and crushed Carrara marble, shows cracked grains and crushed contacts, together with occasional indented grains, sutured or truncated contacts and rare aggregated grain clusters (Figure 2.13b and Figure 2.14a). The initial grain size distribution was not much modified. The mechanical data obtained for the wet samples show a direct, near - linear dependence of creep rate on initial grain size, as depicted in Figure 2.6. Finally, the dependence of the strain rate on the effective stress can be roughly described by a power law equation $\dot{\epsilon} \propto \sigma_e^n$ with $n = 0.8 \pm 0.2$ for Merck reagent and $n = 3.5 \pm 0.3$ for Carrara Marble (Figure 2.7).

Deformation mechanisms such as pure intergranular sliding, rotation and rearrangement can be excluded as candidates controlling the compaction creep behaviour seen in our wet samples, as such processes were eliminated in the pre-compaction stage and are intrinsically time-independent. As time-dependent compaction of our samples was enabled by the addition of the solution phase (Figure 2.3), pressure solution creep might be a possible candidate. However, the observed positive relation between strain rate and grain size is inconsistent with the intergranular pressure solution creep models presented in equations (2.3) - (2.6). Hence, some other mechanism must have controlled

the compaction creep rate in our wet samples. Other possible candidates are some kind of fluid-enhanced dislocation glide/creep or twinning, or fluid enhanced microcracking. We rule out dislocation glide/creep processes involving intracrystalline water weakening, since there is a clear positive dependence of strain rate on grain size, and since the temperatures at which our tests were performed are too low to expect such crystal plastic flow processes or to expect any diffusion of water into the calcite lattice to promote dislocation motion. Coupled plasticity-dissolution or “marginal dissolution” mechanisms such as that proposed by *Pharr and Ashby* [1983] can also be rejected, as these are characterized by a negative dependence of strain rate on grain size, like pressure solution creep. Twinning, on the other hand, is a mechanism that is promoted in calcite by increasing grain size [*Schmid*, 1982; *Rowe and Rutter*, 1990; *Ferrill et al.*, 2004]. However, the microstructure of our wet compacted samples did not show any increase in twinning, which could account for the 20 times or more increase in strain seen in wet samples compared with dry material. Therefore, we rule out twinning as the mechanism responsible for the observed time-dependent compaction of our wet samples.

As the only remaining alternative, we now consider stress corrosion cracking (SCC) as a possible mechanism of grain and/or grain - contact failure, hence of compaction in our wet samples. Stress corrosion cracking is a time-dependent mechanism of deformation recognized in glasses and in minerals and rocks, such as quartz, calcite and granite [*Atkinson*, 1984; *Barnett and Kerrich*, 1980; *Scholz*, 1990; *Lockner*, 1998; *Karner et al.*, 2003]. It is best envisaged as a process of subcritical crack growth enhanced by the presence of aqueous phases, which lowers the barrier for crack propagation and promotes weakening [*Atkinson*, 1984; *Atkinson and Meredith*, 1989; *Dunning et al.*, 1994]. SCC is fully consistent with the enhancement of creep observed in our wet samples compared with the dry ones. In addition, previous work indicates that deformation of granular materials by grain scale SCC can lead to a direct dependence of strain rate on grain size, as well as on applied effective stress [*Brzesowsky*, 1995; *Chuhan et al.*, 2002].

Considering first the effect of grain size, it is well known in the literature that it is easier to start new fractures in coarser grains than in finer ones, and that the critical stress for compaction by grain crushing decreases with increasing grain size and porosity [*Wojtal and Mitra*, 1986; *Zhang et al.*, 1990; *Chuhan et al.*, 2002]. Such grain size effects have been attributed to increasing numbers and/or sizes of grain surface flaws with increasing grain size, and to the sharp, angular contacts that characterize coarser materials, compared with finer grained material [*Zhang et al.*, 1990; *Chuhan et al.*, 2002]. Sharp contacts result in an increase in stress at grain-to-grain contacts, leading to more effective microcracking in coarser grains than in finer ones [*Brzesowsky*, 1995; *Chuhan et al.*, 2002].

In addition to these theoretical considerations, uniaxial compaction experiments performed on quartz sand by *Brzesowsky* [1995] have shown that microcracking can indeed lead to a positive dependence of strain rate on grain size, though the observed sensitivity of strain rate to grain size ($\dot{\epsilon} \sim d^{6 \rightarrow 9}$, $m = -6 \rightarrow -9$) was somewhat higher than in our wet Type B tests. Contrary to the findings of *Brzesowsky* [1995], and to the above

theoretical predictions, *Chester et al* [2007] recently reported an inverse grain size dependence of strain rate, with a grain size sensitivity $m \sim 1$, which they attributed to SCC. However, no theoretical argument was presented to underpin this statement. Furthermore the sensitivity of strain rate to grain size was derived from comparison of samples with very different initial porosities ($\sim 10\%$). We scrapped samples with initial porosities varying by more than $\pm 2\%$, as this proved to have large effects on the strain rate due to differences in the grain-contact structure of the samples.

Turning now to the stress dependence of creep rate, our wet samples show a stress sensitivity that can roughly be described by a power law n -value of 0.8 ± 0.2 for Merck reagent and 3.5 ± 0.3 for Carrara Marble (Figure 2.7). These values are similar to or higher than expected for pressure solution creep at low stress, where $n = 1$ [*Rutter*, 1976; *Gratier and Guiget*, 1986; *Lehner*, 1990; *Spiers et al.*, 1990; *Paterson*, 1995; *De Meer and Spiers*, 1995; *De Meer and Spiers*, 1997], and similar to or lower than those reported for creep of wet sands or sandstone by microcracking, which show n values ranging from 3 to 15 [*Brzesowsky*, 1995; *Ngwenya et al.*, 2001].

Overall, then our experimental data for wet samples, together with our microstructural evidence, suggest that SCC most likely controlled the overall rate of compaction. The occasional indentation and interlocking agglomerate microstructures (Figure 2.13b and 2.14a) suggest that IPS might have occurred at the same time. IPS seems to be often associated with microcracking and/or SCC occurring at grain contacts [*Zhang et al.*, 1990; *Dewers and Hajash*, 1995; *Le Guen et al*, 2007; *Yasuhara and Elsworth*, 2008] and interactions between pressure solution and microcracking have been observed in many experimental studies [*Den Brok and Spiers*, 1991; *Den Brok*, 1998; *Gratier et al.*, 1999; *Yasuhara et al.*, 2006; *Van Noort et al.*, 2008] and in natural samples [*Gratier et al.*, 1999]. Similar interactions may have occurred in our wet tests, with grain contact cracking enhancing IPS [*Gratier et al.*, 1999], but our results indicate that strain rate in our wet tests was controlled by SCC.

2.5.3 Deformation mechanisms in wet compacted samples with added CO₂

We now discuss the deformation mechanisms responsible for controlling creep in the second stage of the Type B experiments, where CO₂ was injected after one hour of compaction creep, and in the Type C experiments whereby CO₂ was present from the start of the tests.

2.5.3.1 Type B Experiments

Injection of supercritical CO₂ at 10 MPa pressure during the second stage of the Type B tests on both Merck and Carrara samples resulted in an acceleration of compaction rate from 10^{-5} to 10^{-7} s⁻¹ before injection to strain rates up to 10^{-4} s⁻¹ after injection (Figure 2.5a and 2.5b). However, compaction slowed down to rates as low as 10^{-7} or 10^{-8} s⁻¹ during the following 24 hours of compaction. In this second stage of the Type B experiments, our Carrara samples showed no systematic dependence of creep rate on grain size whereas the Merck material ($d = 1 - 30 \mu\text{m}$) showed a direct dependence similar to that seen before

CO₂ injection. The microstructures seen in samples extracted from the Type B experiments display microcracks, crushed contacts and rare, tightly fitting or indented contacts or truncated grains (see Figure 2.14a). The lack of consistent, quantitative trends in the grain size and stress dependence observed after CO₂ injection (Figures 2.5a-d) means it is difficult to draw firm conclusions regarding the details of the compaction mechanisms under these conditions. We can, therefore, only infer that the compaction rate of calcite increases in the presence of CO₂ by typically 1 - 3 orders of magnitude (Figures 2.5a-d).

We are left with the question of what causes this dramatic increase in compaction rate. An important factor affecting our mechanical data probably resides in the different strain or porosity, and therefore different structure, of each sample at the moment of CO₂ injection. Even allowing for the differences in strain and structure of Type B samples upon CO₂ injection, the dramatic increase in creep rate is unlikely to be due to a simple acceleration of pressure solution, as such a large acceleration would cause IPS to dominate the mechanical behaviour (grain size and stress dependence) clearly and consistently for both materials tested. The same argument applies to a simple acceleration of grain scale microcracking by processes such as SCC. Possible alternatives include:

1. A decrease in mean grain contact area, and an increase in porosity, caused by simple dissolution of grain surfaces upon addition of CO₂-producing grain rearrangement, faster cracking and/or faster IPS at grain contacts on reloading, followed by a rapid increase in contact area and hence rapidly decelerating strain rates.

1. On-going dissolution due to equilibrium not being reached after addition of CO₂.

The first alternative (a) is the most likely explanation for the observed increase in compaction rates after CO₂ injection and reloading, as it accounts for the observation that strain rates later decelerated rapidly. The positive dependence of strain rate on grain size seen in the Merck samples after CO₂ addition is consistent with this explanation and suggests that contact cracking may have been the main process accelerated by grain surface dissolution. The second alternative (b) is less likely to produce the observed results, as simple on-going dissolution of grain surfaces would result in a clear, inverse dependence of strain rate on grain size, in particular immediately after reloading.

2.5.3.1 Deformation mechanism in Type C Experiments

In contrast to dry sample A-1, compaction of crushed Carrara Marble in the Type C experiments (wet, with CO₂ added from the start) showed time-dependent creep (Figure 2.8a) as did all wet tests, providing evidence for some kind of fluid enhanced creep mechanism. The creep rates measured in the Type C experiments with PCO_2 of 10 MPa were about 2 to 3 orders of magnitude lower than in Type B before and after addition of CO₂, at similar stress, grain size, and temperature conditions, to strains up to ~1.7 %. However, beyond this, strain rates converged becoming similar by 1.9 % strain (cf. Figure 2.5d and 2.8b).

We note here, that the starting porosities (ϕ_0) were also much lower in the Type C than Type B tests. As mentioned previously, the strain rate was very sensitive to the starting

porosity of the samples. Samples with higher porosities crept at much faster strain rates at otherwise similar conditions, which makes a direct comparison of Type B and C tests very difficult, obscuring whether CO₂ accelerates or inhibits creep and/or to what extent. Nonetheless, the microstructures of fine-grained Type C samples show far more sutured contacts, truncations and indentations than the Type B samples, and fewer microcracks (cf. Figures 2.13c and 2.14b). Moreover, at 80°C and at grain sizes between 28 and 106 μm (Figure 2.9), strain rates decreased with increasing initial grain size, according to a power law similar to the IPS models given in equations (2.3)-(2.6), with a grain size exponent m varying from ~ 1 at volumetric strains below 0.2% to ~ 3 at higher volumetric strains. On the other hand, at coarser grain sizes ($d > 106 \mu\text{m}$), strain rates displayed a direct dependence on grain size, as seen in the first stage of the Type B experiments but with a higher grain size sensitivity ($m = -3$ to -4 , cf. Figures 2.6 and 2.9).

Let us now examine the fine-grained regime of the Type C experiments in more detail. In our view, taking into account the work by *Brzesowsky*, [1995]; *Zhang et al.* [1990] and *Chuhan et al.* [2002], the negative dependence of $\dot{\epsilon}$ on grain size means that SCC could not have controlled the creep rate in the fine grained Type C tests. The inverse grain size dependence of strain rate seen in this regime, plus the widespread indentation/truncation microstructures, suggest that IPS might have been the dominant compaction mechanism. If so, the grain size sensitivity (m) suggests that deformation was reaction controlled at the beginning of the experiments (strains $< 0.2\%$, $m \approx 1$), gradually changing towards diffusion controlled IPS ($m \approx 3$) at higher volumetric strain (cf. equations 3-7). On the other hand, our results for fine-grained Type C samples (Figure 2.10) show a relatively high stress sensitivity of strain rate, corresponding to a power law stress exponent $n \sim 6$ to 15. Such a high stress exponent might imply a dislocation glide or creep mechanism [*De Bresser and Spiers*, 1990; *Renner et al.*, 2002; *Xu et al.*, 2009]. However, the fact that no such behaviour occurred in dry samples, plus the dependence of strain rate on grain size and the low temperatures at which our tests were conducted, exclude such a mechanism. Superficially, the observed high n values would also seem to exclude IPS, as this is characterized by $n \approx 1$ at low stresses. However, it will be recalled from our analysis of IPS theory in Section 2.2 that, for high grain-contact stresses and large molar volume materials, the strain rate is exponentially dependent on stress as described by equation (2.6). Our Type C experiments on stress dependence cover the largest stresses investigated in our study. Considering a simple cubic packing model, using the stress term $\exp\left(\frac{B(\phi_0, \phi) \cdot \sigma_e \Omega}{RT}\right) - 1$ in equation (2.6), and taking B values of 5-10 appropriate for sample porosities of 24-25 % pertaining to the Type C tests (following *Niemeijer et al.* [2002]) allowed us to predict equivalent power law n -values corresponding to IPS at the stresses shown in Figure 2.10. The values obtained were $n \approx 9-12$, in reasonable agreement with the data shown in Figure 2.10, supporting IPS as dominant mechanism, in fine-grained regime (Figure 2.9).

Besides the effect of grain size and applied stress on the strain rates, we also investigated

the effect of PCO_2 and temperature in the fine grain size regime (Figures 2.11 and 2.12a). Our data show that compaction rates decrease strongly when the CO₂ pressure was decreased from 8 MPa to 6 MPa, but much less in the interval from 10 to 8 MPa pressure, i.e. in the region where CO₂ is supercritical. Indeed, in the supercritical region at volumetric strains ≥ 0.3 %, the strain rate vs. volumetric strain profiles obtained for CO₂ pressures of 8 and 10 MPa merge (Figure 2.11). Interestingly, geochemical data on the bulk dissolution rate of calcite show it is sensitive to CO₂ pressure only at PCO_2 values up to ~5 MPa, with dissolution being diffusion (transport)-controlled [Pokrovsky *et al.*, 2005]. This effect is attributed mainly to pH changes and [H⁺] diffusion rates in solution with increasing CO₂ pressure [Pokrovsky *et al.*, 2005]. However, debate is on-going as to whether dissolution rates are independent of pH when CO₂ pressure is increased. Furthermore there is a lack of experimental dissolution data under our specific experimental conditions. Nonetheless, our results imply that in the fine-grained regime, of Type C experiments, the creep rate was drastically decreased by decreasing CO₂ partial pressure. The implication is that the inferred mechanism of IPS in the fine-grained regime is strongly accelerated by increasing PCO_2 in the range 6-10 MPa. The effect of CO₂ at lower partial pressures is unclear, as we cannot directly compare Type B and C experiments, because of the difference in the initial porosities.

Increasing the temperature from 28°C to 100°C in the fine-grained regime of the Type C tests ($d = 28 \mu\text{m}$) led to a strong decrease in compaction creep rate at fixed strain (Figure 2.12a). Using our results for temperatures and pressures above the critical point of CO₂ at 31°C and 7.38 MPa (tests C-7, C-13, C-14 at 60-100°C) we calculated the apparent activation energy for compaction and obtained negative values of -24 to -55 kJ/mol (Figure 2.12b). The negative sign presumably reflects the competing effects that temperature has on parameters such as the diffusion coefficient and solubility of calcite, its dissolution and precipitation rate constants, relevant equilibrium constants, and perhaps other thermally activated quantities in the solid phase. In most materials, IPS is accelerated through the positive effect of temperature on reaction rate coefficients, or on grain boundary diffusion coefficient and solid phase solubility. However, in the case of calcite, an increase in temperature decreases its solubility [Segnit *et al.*, 1962], while increasing the diffusivity of ions in the grain boundary fluid. Considering the effect of temperature on the kinetic parameters that in theory determine the absolute rate of dissolution- precipitation- or diffusion-controlled IPS (eq. 2.3-2.6) we now compare the apparent activation energy for each of these parameters with the ones obtained from our data. We used the following parameters for calcite: 1) the dissolution rate coefficient I_s [Sjoberg and Rickard, 1984; Alkattan *et al.*, 1998], 2) the precipitation rate coefficient I_p [Shiraki and Brantley, 1995] and 3) the product of diffusion coefficient D [Dysthe *et al.*, 2002], the solubility of calcite C in the H₂O-CO₂ system [Segnit *et al.*, 1962] and the grain boundary thickness S . The lack of data covering our pressure, temperature and driving force conditions makes this comparison difficult. However, the apparent activation energy values for the dissolution of calcite range from 8.4 kJ/mol [Plummer *et al.*, 1978] or 16 kJ/mol [Sjoberg and Rickard, 1984] to 20

kJ/mol at low pH conditions [Alkattan *et al.*, 1998], while for precipitation the activation energy is ~ 11 kJ/mol [Shiraki and Brantley, 1995]. In contrast, taking the activation energy for diffusion in the water film as equal to 15kJ/mol [Nakashima *et al.*, 1995; Dysthe *et al.*, 2002], and using the solubility data extrapolated to our experimental pressure and temperature conditions from Segnit *et al.* [1962], then the product *DCS* decreases with increasing temperature, with a negative apparent energy of around -12.1 kJ/mol versus -1.8 kJ/mol. This is similar at least in sign to the values obtained from our data ($E_a \approx -24$ to -55 kJ/mol). Comparable apparent activation energy values have also recently been obtained from uniaxial compaction experiments performed on calcite aggregates at 20-150°C ($E_a \approx -9.7$ to -29.9 kJ/mol) [Zhang and Spiers, in prep.].

In summary, the apparent activation energy values obtained from our Type C tests on fine material ($d = 28 \mu\text{m}$) are most consistent with compaction by diffusion-controlled compaction by IPS, with the retrograde solubility of calcite resulting in the observed negative sensitivity of strain rate to temperature. This result fits partially with our data on the grain size dependence of strain rate, which suggest that at volumetric strain of $\geq 0.2\%$, occurs by diffusion controlled IPS.

We now move on to consider the behaviour seen in our Type C experiments in the coarser grain size regime (Figure 2.9). In this regime (between $106 \mu\text{m}$ and $300 \mu\text{m}$), a direct relation exists between strain rate and grain size, similar to the trend observed in the compacted wet samples in absence of CO_2 (Type B experiments, Figure 2.9). This similarity in mechanical results leads us to conclude that compaction of calcite aggregates in the coarse grained regime of our Type C experiments ($d > 106 \mu\text{m}$) was mainly controlled by the same mechanism, i.e. by subcritical cracking occurring at the grain scale.

From the two trends in strain rate as a function of grain size seen in our Type C tests, we can now summarize the proposed controlling mechanisms as follows. First, compaction in the fine-grained regime (below $106 \mu\text{m}$) is mainly due to pressure solution creep presumably accompanied by intergranular rearrangement. At coarser grain sizes (above $106 \mu\text{m}$), compaction occurs mainly by time-dependent microcracking i.e. by grain (contact) failure involving SCC, plus grain rearrangement. As these (parallel) mechanisms do not exclude each other, we assume that both contribute to the compaction of our samples, with IPS controlling creep at fine grain size and SCC controlling creep at coarse grain size. Our results are thus consistent with previous observations that IPS is favored in fine-grained material, while microcracking is easier in coarse material [Wojtal and Mitra, 1986; Brzesowsky, 1995; Chuhan *et al.*, 2002].

Nonetheless, the chemistry of the aqueous solution clearly plays an important additional role in promoting one mechanism or the other. For instance, we can infer that in the fine-grained material, at elevated CO_2 pressures ($P_{\text{CO}_2} \geq 6\text{MPa}$), and associated low pH values (i.e. $\text{pH} \approx 3-4$) (Type C tests), IPS becomes more important relative to microcracking through increased solubility of calcite, while at nearer neutral pH (Type B tests, before CO_2 injection), IPS is relatively slower. However, we observed that creep of calcite due to IPS (Type C tests, $d < 106 \mu\text{m}$) proceeded at much slower rates than creep

due to microcracking (Type B tests). We believe this is due to the fact that the absolute rates of creep are dominated by the values of initial porosity, thus initial structure of the grain contacts, rather than to the chemistry of the pore fluid. Unfortunately, the differences in initial structure of the aggregate obscures whether pressure solution is speeded up, and to what extent, due to the presence of supercritical CO₂. Nevertheless, a clear indication to support the idea that CO₂ partial pressure influences the IPS rates comes from the Type C tests, which showed that in the fine-grained material, decreasing the CO₂ partial pressure reduces drastically the creep rate, therefore the overall IPS rate.

We conclude that the presence of CO₂ accelerates compaction of calcite aggregates by both IPS and SCC in Type C experiments, with the two processes operating in parallel. In fine-grained material (< 106 μm) this effect is sufficient to make pressure solution creep the dominant mechanism, whereas at coarser grain size SCC controlled creep remains dominant. Our data suggest IPS is diffusion controlled, especially at $e_v \geq 0.3\%$. Moreover, it is clear that IPS accelerates with increasing CO₂ partial pressure.

2.6 Comparison with previous studies and implications for CO₂ storage

Several experimental studies have recently attempted to identify and quantify the pressure solution creep mechanism in carbonate rocks deformed with and without CO₂ present at high pressure [Zhang and Spiers, 2005; Le Guen et al., 2007]. Pressure solution creep was identified by Zhang and Spiers, [2005a,b] as the main compaction mechanism in wet calcite aggregates uniaxially compacted under ambient conditions, in the absence of added (e.g. supercritical) CO₂. The fact that we inferred microcracking to dominate our Type B tests before CO₂ addition, in contrast to the findings of Zhang and Spiers, [2005] is probably due to the much higher stresses (i.e. 4-40 MPa in our study versus 1-4 MPa) and higher temperatures (i.e. 28-80°C versus room temperature) employed in our study. Since subcritical cracking processes are very stress sensitive [Zhang et al., 1990; Brzesowsky, 1995; Den Brok, 1998; Chuhan et al., 2002], especially the higher applied stresses could be held responsible for promoting microcracking in our experiments.

In line with our findings, the experimental study of the effect of supercritical CO₂ on natural carbonate samples by Le Guen et al. [2007] points to the fact that creep is accelerated by injection of supercritical CO₂, in this case by up to a factor of 5. In the absence of a systematic investigation of the compaction mechanism, Le Guen et al. [2007] concluded that accelerated dissolution, pressure solution and possibly microcracking are the mechanisms responsible for the enhanced deformation of such materials. The smaller increase in compaction rates obtained by Le Guen et al. [2007] for natural samples compared with our Type B tests might be due to the fact that the samples used in our study (Merck reagent and Carrara Marble) contain fewer impurities than the ones in the study of Le Guen et al. [2007]. It is well known that the presence of impurities such as Mg²⁺, SO₄²⁻ or PO₄³⁻ strongly inhibits calcite dissolution and precipitation [Zuddas and Mucci, 1998; Zhang et al., 2002a, b] so that lower compaction rates are to be expected in impure carbonates when deformation involves dissolution-precipitation phenomena.

In their numerical modelling study, *Renard et al.* [2005] examined the effect of long term storage of CO₂ on pressure solution creep of carbonate rocks, under the assumption that compaction of calcite (with and without added CO₂) is fully due to pressure solution creep. A comparison of the predicted IPS rate in calcite without added CO₂ with values predicted for PCO₂ = 10, 20 and 30 MPa at 40°C, led to the conclusion that compaction rates are accelerated by a factor of 50 – 75 [*Renard et al.*, 2005]. This is comparable to the effects observed in our Type B tests and in the Type C tests, the latter of which showed that decreasing the CO₂ pressure from 10 MPa to 6 MPa reduces creep rate by about 50 times. However, the numerical model of *Renard et al.* [2005] is based on the assumption that pressure solution creep is the main mechanism of compaction under both wet, and wet/CO₂ conditions, whereas microcracking dominated in our wet experiments without CO₂ (Type B tests, before CO₂ injection). Nevertheless, all studies do point to the fact that injection of CO₂-rich fluids enhances compaction rates of carbonate.

Beside the initial poro-elastic expansion caused by the injection of supercritical CO₂, our results imply that enhanced dissolution processes, stress corrosion cracking and pressure solution can be expected to play an important role in the overall deformation of porous carbonate reservoirs. The findings of our study, together with previous ones [*Renard et al.*, 2005; *Le Guen et al.*, 2007], imply that injection and long-term storage of CO₂ will accelerate compaction rates, with microcracking and/or intergranular pressure solution being the main mechanisms. However, this acceleration depends strongly on the initial conditions present in the reservoir, i.e. mean grain size, porosity, pH of the formation fluid, temperature, effective stress and CO₂ pressure.

Direct extrapolation of our experimental results to predict effects of CO₂ storage on creep in carbonate reservoirs is problematic because of all these factors. In addition, because of the complex interplay between IPS and microcracking it is difficult for us to construct a useful creep law for either mechanism or even at an empirical level. However, with the possible exception of chalk, creep rates in carbonate reservoirs with and without injected CO₂ will be generally much slower than the absolute rates measured in our experiment, because of the generally much lower porosities, larger grain contact areas (lower B-values), relatively low effective stresses and CO₂ pressures [*Benson et al.*, 2002; *Bachu and Bennion*, 2007]. In particular, the presence of Mg²⁺, PO₄³⁻, SO₄²⁻, Mn²⁺ ions are known to drastically slow down solution/precipitation processes in calcite and are commonly present in residual formation fluids [*Zuddas and Mucci*, 1998; *Zhang et al.*, 2002a, b]. Residual hydrocarbons that can wet calcite grain surfaces may have similar retarding effects on creep rates [*Zhang et al.*, 2002a, b].

This means that predicting compaction creep rates in depleted carbonate reservoirs and in reservoirs used for CO₂ storage is not possible on the basis of our data. However, our results do imply that in rare cases where a depleted reservoir exhibits measurable compaction creep before injection of CO₂, then subsequent injection could potentially speed up the process by 50-75 times, if creep is due to diffusion-controlled, pressure solution, or by even 3 orders of magnitude if grain scale cracking is involved. Carbonate

reservoirs, which show measurable creep during and after depletion, are therefore best avoided for CO₂ storage, as the active creep process will likely be accelerated.

2.7 Summary and Conclusions

Carrara Marble (grain size = 28 - 250 μm) and Merck reagent (grain size = 1 - 30 μm) aggregates were uniaxially compacted under reservoir conditions (4 - 40 MPa, 28 - 80°C, ± 10 MPa CO₂) in order to investigate the effect of CO₂ on the compaction behaviour of granular carbonate rocks. The main conclusions can be summarized as follows:

1. Time-independent compaction occurs in the dry samples due to microcracking, grain rearrangement and grain crushing, while addition of water results in faster strain rates, showing significant time-dependent compaction and suggesting a water-enhanced deformation mechanism.
2. Compaction creep experiments on calcite aggregates at 80°C without added CO₂ display a direct dependence of strain rate on grain size and effective stress. Microstructural features, including widespread microcracks, indented grains and occasional sutured contacts, together with the mechanical results, imply that a combination of pressure solution creep and microcracking is responsible for creep. Addition of CO₂ at 10MPa after ~1 hour of creep resulted in an acceleration of strain rate up to 1-3 orders of magnitude and in an increase in the number of sutured contacts and grain truncations and indentations.
3. Compaction of calcite aggregates in the presence of supercritical CO₂ from the start of the experiments leads to time-dependent deformation, with strain rates being grain size, stress, CO₂ partial pressure and temperature dependent. The strain rates vary inversely with grain size, for grains smaller than 106μm, while for bigger grains than 106μm, the strain rates increase with increasing grain size. This behavior together with microstructural evidence, such as sutured contacts, truncated or indented grains as well as microcracks, suggests that microcracking and intergranular pressure solution creep are operating in parallel and that the fastest mechanism controls the overall deformation of carbonate rocks. In the fine-grained material, pressure solution creep rates are faster than microcracking, while microcracking is favored at coarser grain size (above 106 μm).
4. In the pressure solution region (grain size below 106 μm) the strain rates are sensitive to increasing applied stress, in a similar manner to that predicted for pressure solution creep (see eq. 2.6), with a stress concentration factor at the grain contacts around 5 - 10. Compaction rates vary inversely with temperature, similarly to the trend shown by the effect of temperature on solubility of calcite. The observed T-sensitivity is comparable, at least in sign, to that calculated for diffusion-controlled transport. In the same regime, an increase in PCO_2 from 6 to 10 MPa was found to strongly increase the strain rates (by 50 times).
5. Site-specific factors have to be considered for CO₂ sequestration assessment

in carbonate reservoirs, such as in-situ pressure and temperature conditions, grain size, porosity, presence of impurities, or CO₂ injection pressures. However, with the possible exception of chalk, creep rates in carbonate reservoirs with and without injected CO₂ will be generally much slower than the absolute rates measured in our experiment, because of the generally much lower porosities, larger grain contact areas (lower B-values), relatively low effective stresses and CO₂ pressures. Our results imply that in rare cases if a depleted reservoir exhibits measurable compaction creep before injection of CO₂, then subsequent injection could potentially speed up the process by 50-75 times, if creep is due to diffusion-controlled, pressure solution, or by even 3 orders of magnitude if grain scale cracking is involved.

Acknowledgements:

We would like to thank Peter van Krieken, Gert Kastelein and Eimert de Graaff for the technical support provided in the laboratory and Saskia ten Grotenhuis. The research was sponsored by the Utrecht Center for Geoscience, TNO and the Dutch national research program on CO₂ Capture, Transport and Storage (CATO).

REFERENCE LIST

- Alkattan, M., E. H. Oelkers, J. – L. Dandurand and J. Schott (1998), An experimental study of calcite and limestone dissolution rates as a function of pH from -1 to 3 and temperature from 25 to 80C, *Chem. Geol.* 151, 199-214.
- Atkinson B.K. and R.G. Meredith (1989), The theory of subcritical crack growth with applications to minerals and rocks. In: B.K. Atkinson: *Fracture mechanics of rock*, Academic Press, London, pp. 111–166.
- Atkinson, B.K. (1984), Subcritical crack-growth in geological-materials, *Journal of Geophysical Research* 89(B6), 4077-4114.
- Ambrose, W.A., S.Lakshminarasimhan, M.H. Holtz, V. Nunez-Lopez, S.D. Hovorka, and I. Duncan (2008), Geologic factors controlling CO₂ storage capacity and permanence: case studies based on experience with heterogeneity in oil and gas reservoirs applied to CO₂ storage, *Environ. Geol.*, 54, 1619-1633.
- Bachu, S., and B. Bennion (2007), Effects of in-situ conditions on relative permeability characteristics of CO₂-brine systems, *Environ Geol*, DOI 10.1007/s00254-007-0946-9, in pres.
- Bachu, S. (2003), Screening and ranking of sedimentary basins for sequestration of CO₂ in geological media in response to climate change, *Environmental Geology*, 44, 227-289
- Barnet R.L., and R. Kerrich (1980), Stress corrosion cracking of biotite and feldspar, *Nat.*, 283, 185-187.,
- Bathurst, R. G. C. (1975), Carbonate sediments and their diagenesis, *Develop. in sedim.* 12, 2nd edition, Elsevier, Amsterdam, New York, 658 pp.
- Benson, S. M, R. Hepple, J. Apps, C.-F. Tsang, and M. J. Lippmann (2002) Lessons learned from natural and industrial analogues for storage of carbon dioxide in deep geological formations, Lawrence Berkeley National Laboratory Report LBNL 51170, <http://www.co2captureproject.org/reports/reports.htm>
- Brzesowsky, R.H. (1995), Micromechanics of Sand Grain Failure and Sand Compaction, Ph.D. dissertation, Universiteit Utrecht, Nederlands.
- Buhmann, D., and W. Dreybrodt (1985), The kinetics of calcite dissolution and precipitation in geological relevant situations of karst areas: 1. Open system. *Chem. Geol.* 48, 189-211.
- Cailly, B., P. Le Thiez, P. Egermann, A. Audibert, S. Vidal-Gilbert and X. Longaygue (2005), Geological storage of CO₂: A-state-of-the-art of the injection processes and technologies, *Oil & Gas Sci. and Tech. – Rev IPF*, 60(3), 517-525.
- Chester, F.M., J.S. Chester, A.K. Kronenberg, and A. Hajash, (2007), Subcritical creep compaction of quartz sand at diagenetic conditions: Effects of water and grain size. *J. of Geophys. Res.* 112, B06203.
- Chuhan, F.A., A. Kjeldstad, K. Bjorlykke, and K. Hoeg (2003) Experimental compression of loose sands: relevance to porosity reduction during burial in sedimentary basins, *Can. Geotech. J.* 40, 995–1011.
- De Bresser, J.H.P. (1996) Steady state dislocation densities in experimentally deformed calcite materials: Single crystals versus polycrystals, *J. Geophys. Res.* 101(B10), 22189- 22201.
- De Meer, S., and C.J. Spiers (1999), Influence of pore fluid salinity on pressure solution creep in gypsum, *Tectonophysics*, 308, 311-330.
- De Meer, S. and C.J. Spiers (1995), Creep of wet gypsum aggregates under hydrostatic loading conditions, *Tectonophysics* 245, 171-183.
- De Meer, S., C.J. Spiers, and C.J. Peach (1997), Pressure solution creep in gypsum: Evidence for precipitation reaction control, *Phys. Chem. Earth* 22(1-2), 33-37.
- De Meer, S., C.J. Spiers, and C.J. Peach (2000), Kinetics of precipitation of gypsum and implications for pressure-solution creep, *J. Geol. Soc. Lond.* 157, 269-281
- Den Brok, S.W.J. (1990): Solution-precipitation creep and microcracking in water-weakened quartzite. Symposium on Deformation Processes and the Structure of the Lithosphere, Inter-union Commission on the Lithosphere, Potsdam GDR, May 3rd-10th, 1990, Abstracts volume, page 9.
- Den Brok, S.W.J., and C.J. Spiers (1991), Experimental evidence for water weakening of quartzite by microcracking plus solution-precipitation creep; *J. Geol. Soc. London*, 148, 541-548.
- Den Brok, S.W.J., (1998), Effect of microcracking on pressure solution strain rate: the Gratz grain-boundary model. *Geology* 26, pp. 915–918.
- Dewers, T. A. and A. Hajash (1995), Rate laws for water-assisted compaction and stress-induced water-rock interaction in sandstones, *J. Geophys. Res.*, 100, (B7), 13 093-13 112.
- Dewers , T.A. and P. Ortoleva, (1990), A coupled reaction/transport/mechanical model for intergranular pressure solution, stylolites, and different compaction and cementation in clean sandstones, *Geochim Cosmochim Acta* 54, pp. 1609–1625
- Dove, P. M., and F. M. Platt, (1996), Compatible real-time rates of mineral dissolution by Atomic Force Microscopy (AFM), *Chem. Geol.*, 127 (4), 329-336.
- Dunning, J., B.J. Douglas, M. Miller, and S.K. McDonald, (1994) The role of the chemical environment in

frictional deformation stress corrosion cracking and comminution, *Pure and Appl. Geophys.*, 143, 151-178.

Dysthe D.K., F. Renard, F. Porcheron and B. Rousseau (2002), Fluid in mineral interfaces-molecular simulations of structure and diffusion, *Geophys. Res. Lett.* 29, 13(1)-13(4).

Ellis, A., (1959), The solubility of calcite in carbon dioxide solutions. *Am J Sci* 257:354-365

Emberley, S., I. Hutcheon, M. Shevalier, K. Durocher, B. Mayer, W.D. Gunter, and E.H. Perkins (2005), Monitoring of fluid-rock interaction and CO₂ storage through produced fluid sampling at the Weyburn CO₂-injection enhanced oil recovery site, Saskatchewan, Canada, *Appl. Geochem.* 20 (6), 1131-1157.

Ennis-King, J., and L. Paterson (2003), Role of Convective Mixing in the Long-Term Storage of Carbon Dioxide in Deep Saline Formations. SPE 84344, paper presented at the SPE Annual Technical Conference and Exhibition held in Denver, Colorado, U.S.A., 5-8 October 2003.

Ferrill, D.A., A.P. Morris, M.A. Evans, M. Burkhard, R.H. Groshong, Jr., and C.M. Onasch. (2004), Calcite twin morphology: A low temperature deformation geothermometer. *J. of Struct. Geol.*, 26 (8), 1521-1529

Gaus L, M. Azaroual, and I. Czernichowski-Lauriol (2002), Preliminary modeling of the geochemical impact of CO₂ injection on the caprock at Sleipner. *BRGM Report BRGM/RP-52081-FR*, 43.

Gillfillan, S.M.V., L. B. Sherwood, G. Holland, D. Blagburn, S. Stevens, M. Schoell, M. Cassidy, Z. Ding, Z. Zhou, G. Lacrampe-Couloume, and C.J. Ballentine (2009), Solubility trapping in formation water as dominant CO₂ sink in natural gas fields. *Nature*, 458(7238): 614-618.

Gledhill, D.K., Morse, J.W., 2006. Calcite solubility in Na-Ca-Mg-Cl brines. *Chem. Geol.* 233 (3-4), 249-256.

Gozalpour, F., S. R. Ren, and B. Tohidi (2005), CO₂ EOR and storage in oil reservoirs. *Oil and Gas Science and Technology – Rev IFP* 60 (3), 537-546.

Grasso, J.R. (1992), Mechanics of Seismic Instabilities Induced by the Recovery of Hydrocarbons, *Pure & Appl. Geophys.* 139, 507.

Gratier, J.P., and R. Guiguet (1986), Experimental pressure solution deposition on quartz grains: the crucial effect of the nature of the fluid, *J. of Struct. Geol.* 8, 845- 856.

Gratier, J. P., F. Renard, and P. Labaume (1999) How pressure solution creep and fracturing processes interact in the upper crust to make it behave in both brittle and viscous manner, *J. of Struct. Geol.*, 21, 1189-1197.

Gundersen, E., F. Renard, D. K. Dysthe, K. Bjørlykke, and B. Jamtveit (2002), Coupling between Pressure Solution and Mass Transport in Porous Rocks, *J. of Geophys. Res.*, 107 (B11), 2317, doi:10.1029/2001JB000287.

Hellmann, R., P. Renders, J.P. Gratier, and R. Guiguet (2002), Experimental Pressure Solution Compaction of Chalk in Aqueous Solutions. Part 1. Deformation Behavior and Chemistry. In: *Water-Rock Interactions, Ore Deposits, and Environmental Geochemistry* (Hellmann, R. and Wood, S.A. eds.), Special Publication Series, The Geochemical Society, 129-152.

Heggheim, T. Madland, M.V., Risnes R and Austad, T., (2005), A chemical induced enhanced weakening of chalk by seawater, *J. Pet. Sci. Eng.* 46 pp. 171-184

Hickman, S. H. and B. Evans (1991), Experimental pressure solution in halite: the effect of grain/interphase boundary structure, *J. Geol. Soc. Lond.*, 148, 549-560.

International Panel on Climate Control (IPCC) (2005), Carbon Dioxide Capture and Storage. Special Report. Prepared by Working Group III of the Intergovernmental Panel on Climate Change [Metz, B., O. Davidson, H. C. de Coninck, M. Loos, and L. A. Meyer (eds.)]. Cambridge University Press, Cambridge, United Kingdom and New York, NY, USA, 442.

Izgec, O., B. Demiral, H. Bertin, and S. Akin (2008), CO₂ injection into saline carbonate aquifer formations II: Comparison of numerical simulations to experiments, *Transp. in Por. Media* 73, 57-74.

Karner S., F.M. Chester, A.K. Kronenberg, and J.S. Chester (2003), Subcritical compaction and yielding of granular quartz sand, *Tectonophysics* 337, 357-381.

G. Kaufmann and W. Dreybrodt (2007), Calcite dissolution kinetics in the system CaCO₃-H₂O-CO₂ at high undersaturation, *Geochim. Cosmochim. Acta* 71, 1398-1410.

Le Guen, Y., F. Renard, R. Hellmann, E. Brosse, M. Collombet, D. Tisserand and J.-P. Gratier (2007), Enhanced deformation of limestone and sandstone in the presence of high pCO₂ fluids, *J. of Geophys. Res.*, 112, B05421, doi:10.1029/2006JB004637.

Li, Z., Dong, M., Li, S., and Huang, S. (2006) CO Sequestration in Depleted Oil and Gas Reservoirs-Caprock Characterization and Storage Capacity, *En. Convers. and Man.*, 47, 1372-1382.

Liu, Z. and Dreybrodt, W (1997), Dissolution kinetics of calcium carbonate minerals in H₂O-CO₂ solutions in turbulent flow: the role of the diffusion boundary layer and the slow reaction H₂O+CO₂→H⁺+HCO₃⁻, *Geochim. et Cosmochim. Acta*, 61, 14, 2879-2889

Lockner, D.A. (1998), Brittle deformation law for Westerly Granite, *J. Geophys. Res.*, 103, 5107-5103.

Lehner, F. K. (1990), Thermodynamics of rock deformation by pressure solution. In: *Deformation processes in minerals, ceramics and rocks* (D.J. Barber & P.G. Meredith eds), Unwin Hyman, London, 296-333.

Madland M., A. Finsnes, A. Alkafadgi, R. Risnes, T. Austad (2006), The influence of CO₂ gas and carbonate water on the mechanical stability of chalk, *J. of Petrol. Sci. and Eng.*, 51, 149-168.

Nakashima S., H. Matayoshi, T. Yuko, K. Michibayashi, T. Masuda, N. Kuroki, H. Yamagishi, Y. Ito and A. Nakamura (1995), Infrared microspectroscopy analysis of water distribution in deformed and metamorphosed rocks. In: C.J. Spiers and T. Takeshita, Editors, *Influence of Fluids on Deformation Processes in Rocks Tectonophysics* 245, 263–276.

Nakatani, M., and C. H. Scholz (2004), Frictional healing of quartz gouge under hydrothermal conditions: 1. Experimental evidence for solution transfer healing mechanism, *J. Geophys. Res.*, 109, B07201, doi:10.1029/2001JB001522.

Niemeijer, A.R., C.J. Spiers and B. Bos (2002), Compaction creep of quartz sand at 400–600 °C: experimental evidence for dissolution-controlled pressure solution, *Earth and Planetary Science Letters* 195, 261–275.

Niemeijer, A., C. Marone, and D. Elsworth (2008), Healing of simulated fault gouges aided by pressure solution: Results from rock analogue experiments, *J. Geophys. Res.*, 113, B04204, doi:10.1029/2007JB005376.

Ngwenya, B.T., I.G. Main and S.C., Elphick (2001), A constitutive law for low-temperature creep of water-saturated sandstones, *J. Geophys. Res.*, 21811-21826, 2001JB000403.

Paterson, M. S. (1995), A theory for granular flow accommodated by material transfer via an intergranular fluid. *Tectonophysics* 245, 135–151.

Pharr, G. M. and M.F. Ashby (1983), On creep enhanced by a liquid phase. *Acta Metall.*, 31, 129-138.

Pokrovsky, O. S., S. V. Golubev and J. Schott (2005), Dissolution kinetics of calcite, dolomite and magnesite at 25 °C and 0 to 50 atm CO₂, *Chem. Geol.* 217, 239–255

Pokrovsky, O.S., and J. Schott (2002), Surface Chemistry and Dissolution Kinetics of Divalent Metal Carbonates, *Environ. Sci. and Tech.*, 36, 426-432.

Pokrovsky, O.S., S.V. Golubev, and J. Schott (2005), Dissolution kinetics of calcite, dolomite and magnesite at 25 °C and 0 to 50 atm CO₂, *Chem. Geol.*, 217, 239–255.

Plummer, L.N., and E. Busenberg (1982), The solubilities of calcite, aragonite and vaterite in CO₂-H₂O solutions between 0 and 90°C, and an evaluation of the aqueous model for the system CaCO₃-CO₂-H₂O. *Geochim. Cosmochim. Acta*, 46, 1011-1040.

Plummer, L. N., T. L. M. Wigley, and D. L. Parkhurst (1978), The kinetics of calcite dissolution in CO₂-water systems at 5° to 60°C and 0.0 to 1.0 atm CO₂, *Am. J. Sci.*, 278, 179–216.

Portier, S. and C. Rochelle (2005), Modeling CO₂ solubility in pure water and NaCl-type waters from 0 to 300° C and from 1 to 300 bar. Application to the Utsira Formation at Sleipner, *Chem. Geol.* 217, 187–199.

Preston, C., M. Monea, W. Jazrawi, K. Brown, S. Whittaker, D. White, D. Law, R. Chalaturnyk, and B. Roston (2005), IEA GHG Weyburn CO₂ monitoring and storage project. *Fuel Process. Tech.* 86 (15), 1547-1568.

Renard, F., J. Schmittbuhl, J.-P. Gratier, P. Meakin, and E. Merino (2004), Three-dimensional roughness of stylolites in limestones, *J. Geophys. Res.*, 109, B03209, doi:10.1029/2003JB002555

Renard, F., E. Gundersen, R. Hellmann, M. Collombet, and Y. Le Guen (2005), Numerical modeling of carbon dioxide sequestration on the rate of pressure solution creep in limestone: Preliminary results. *Oil, Gas Sci. & Tech.*, 60, 381-389.

Renner, J., B. Evans, and G. Siddiqi (2002), Dislocation creep of calcite. *J. of Geophys. Res.* 107, B12, 2364 ECV 6 1-16

Rickard D. and E.L. Sjöberg (1983), Mixed kinetic control of calcite dissolution rates, *Am. J. Sci.* 283, 815–830.

Roehl, P.O., and P.W. Choquette (1985), Carbonate Petroleum Reservoirs: Springer- Verlag, 622 pp.

Rowe K.J. and E.H. Rutter (1990), Paleostress estimation using calcite twinning: experimental calibration and application to nature, *J. Struct. Geol.*, 12, 1–17.

Rutter, E. H. (1976), The kinetics of rock deformation by pressure solution, *Philos. Trans. R. Soc. London*, 283, 203– 219

Rutter, E. H., (1983), Pressure solution in nature, theory and experiment. *J. of Geol. Soc.* 140, 725–740.

Schmid, S. M. (1982), Laboratory experiments on rheology and deformation mechanisms in calcite and their application to studies in the field. Mitt. Geol.Inst. ETH University of Zurich. 241, 1-105

Scholz, C.H. (1990), The Mechanics of Earthquakes and Faulting, Cambridge University Press, New York, USA, 1990.

Segnit, E. R., H. D. Holland and C. J. Biscardi (1962), The solubility of calcite in aqueous solutions; I, The solubility of calcite in water between 75 degrees and 200 degrees at CO₂ pressures up to 60 atm. *Geochim. Cosmochim. Acta* 26, 1301–1331.

Segnit, E.R., H.D. Holland, and C.J. Biscardi (1962), The solubility of calcite in aqueous solutions; I, The solubility of calcite in water between 75 degrees and 200 degrees at CO₂ pressures up to 60 atm, *Geochim. et*

Cosmochim. Acta 26, 1301–1331.

Shiraki R. and Brantley S. (1995) Kinetics of near-equilibrium calcite precipitation at 100°C: An evaluation of elementary reaction-based and affinity-based rate laws. *Geochim. Cosmochim. Acta* 59, 1457–1471.

Sjöberg, E.L. (1978), Kinetics and mechanism of calcite dissolution in aqueous solutions at low temperatures, *Stockholm Contribution in Geology* 32, 1–96.

Sjöberg, E.L., and D.T. Rickard (1984), Temperature Dependence of Calcite Dissolution Kinetics between 1 and 62°C at pH 2.7 to 8.4 in Aqueous Solutions. *Geochim. Cosmochim. Acta* 48, 485–493.

Spiers, C. J., and R. H. Brzesowsky (1993), Densification behaviour of wet granular salt: Theory versus experiment, In: *Seventh Symp. on Salt*, 1. Elsevier, Amsterdam, 83–91.

Spiers, C.J., and P.M.T.M. Schutjens (1990), Densification of crystalline aggregates by fluid phase diffusional creep. In: Barber, D.J., Meredith, P.G. (Eds.), *Deformation Processes in Minerals, Ceramics and Rocks*. Unwin Hyman, London, pp. 334–353

Spiers, C.J., P. T. M. Schutjens, R. H. Brzesowsky, C. J. Peach, J. L. Liezenberg, and H.J. Zwart (1990), Experimental determination of constitutive parameters governing creep of rocksalt by pressure solution. In: Nipke, R.J., Rutter, E.H. (Eds.), *Deformation Mechanisms, Rheology and Tectonics*. Special Publication-Geological Society. The Geological Society, London, pp. 215–227.

Spiers, C.J., S. De Meer, A.R. Niemeijer, and X. Zhang (2004), Kinetics of rock deformation by pressure solution and the role of thin aqueous films. In: S. Nakashima, Editor, *Physicochemistry of Water in Geological and Biological Systems*, Universal Academy Press, 129–158.

Svensson, U., and W. Dreybrodt (1992), Dissolution kinetics of natural calcite minerals in CO₂–water system approaching equilibrium, *Chem Geol* 100, 129–145

Tada, R., and R. Siever (1986), Experimental knife-edge pressure solution of halite. *Geochim. Cosmochim. Acta* 50(1), 29–36.

Tondi, E., M. Antonellini, A. Aydin, L. Marchegiani and G. Cello (2006), The role of deformation bands, stylolites and sheard stylolites in fault development in carbonate grainstones of the Majella Mountain, Italy. *J. of Struct. Geol.*, 28, 376–391.

Van Noort, R., C. J. Spiers, and G. M. Pennock (2008), Compaction of granular quartz under hydrothermal conditions: Controlling mechanisms and grain boundary processes, *J. Geophys. Res.*, 113, B12206, doi:10.1029/2008JB005815.

Van Noort, R., H. J. M. Visser, and C. J. Spiers (2008), Influence of grain boundary structure on dissolution controlled pressure solution and retarding effects of grain boundary healing, *J. Geophys. Res.*, 113, B03201, doi:10.1029/2007JB005223.

Wojtal S., and G. Mitra (1986), Strain Hardening and Strain Softening in Fault Zones from Foreland Thrusts, *Geol. Soc. Am. Bull.* 97, 674–687.

Xu, T, J. A. Apps, and K. Pruess (2004), Numerical simulation of CO₂ disposal by mineral trapping in deep aquifers, *App. Geochem.*, 19, 917–936.

Xu, T, J.A. Apps, K. Pruess, and H. Yamamoto (2007), Numerical modelling of injection and mineral trapping of CO₂ with H₂S and SO₂ in a sandstone formation, *Chem. Geol.*, 242 (3–4), 319–346

Xu, L., J. Renner, M. Herwegh, and B. Evans (2009), The effect of dissolved magnesium on creep of calcite II: transition from diffusion creep to dislocation creep, *Contrib Mineral Petrol.*, 157, 3390358. DOI 10.1007/s00410-008-0338-5

Yasuhara, H., and Elsworth, D. (2008) Compaction of a fracture moderated by competing roles of stress corrosion and pressure solution. *Pure and App. of Geophys.*, 165, (7), 1289 – 1306.

Yasuhara, H., A. Polak, Y. Miotani, A., Grader, P. Halleck, and Elsworth, D. (2006), Evolution of fracture permeability through fluid-rock reaction under hydrothermal conditions, *Earth Planet. Sci. Lett.* 244, 186–200.

Zhang, X. and Spiers, C.J., (2005, a) – Compaction of granular calcite by pressure solution at room temperature and effects of pore fluid chemistry, *Int. J. of Rock Mech. and Min. Sci.*, 42, 950–960.

Zhang, X.M. and Spiers, C.J., (2005, b)– Effect of phosphate ions on intergranular pressure solution in calcite :an experimental study *Geochim. et Cosmochim. Acta*, 69, 5681–5691.

Zhang, X.M. and Spiers, C.J., in prep - Pressure Solution Creep of Wet Calcite Aggregate at Temperatures up to 150 °C and Effects of Pore Fluid Chemistry

Zhang, J., T.-f. Wong and D. M. Davis, Micromechanics of pressure-induced grain crushing in porous rocks, *J. Geophys. Res.*, 95, 341–352, 1990.

Zoback, M.D., and J.C. Zinke (2002), Production-induced normal faulting in the Valhall and Ekofisk oil fields, *Pure and App. Geophys.*, 159, 403–420.

Zubtsov, S., F. Renard, J-P. Gratier, D.K. Dysthe, and V. Traskine (2005), Single-contact pressure solution creep on calcite monocrystals. *Geol. Soc., London, Spec. Publ.* 243(1), 81 - 95.

Zuddas, P., and A. Mucci (1994), Kinetics of calcite precipitation from seawater: A classic chemical kinetics description for strong electrolyte solutions. *Geochim. Cosmochim. Acta* 58, 4353–4362.

Chapter 3

ABSTRACT

We have performed uniaxial compaction experiments on simulated porous carbonate rocks (crushed and sieved Carrara Marble), using pore fluids of varying salinity saturated with CO_2 , in order to investigate the long term, chemically coupled effects of CO_2 on creep of such rock materials. Experiments were performed at reservoir conditions equivalent to 3 km depth, that is up to 30 MPa effective pressure and a temperature of 80°C, on samples with mean grain sizes of 28, 37, 50 and 106 μm . The tests were carried out using saline pore fluid solutions containing 0, 0.6, 1, 2 and 3 M NaCl or 0, 1 and 2 M MgCl_2 with and without supercritical CO_2 at a pressure of 10 MPa. Addition of either salt (NaCl or MgCl_2) to the pore fluid in samples compacted with CO_2 caused a reduction in compaction creep rate at low salt concentrations (0.6-1 M). As salt concentration was increased to values of 2-3 M, creep rates increased to approach or exceed values obtained in salt-free experiments. By comparison of our data on the compaction creep of carbonate aggregates in the presence of added salts and supercritical CO_2 with microphysical models and previous work on fluid-enhanced deformation mechanisms, we suggest that the effect of increasing salt concentration in samples tested with supercritical CO_2 is the net result of progressive inhibition of pressure solution and enhancement of the role of subcritical crack growth. The present results imply that storage of CO_2 in highly porous carbonate formations increase creep rates by up to ten times, depending on the salt concentration. However, it remains difficult to quantify the rate of compaction creep of specific carbonate reservoirs in the context of CO_2 storage, as compaction behavior is strongly influenced by porosity and other microstructural and compositional factors, as well as by salinity.

Based on:

Liteanu E., Spiers C.J. - Influence of pore fluid salt content on compaction creep of calcite aggregates in the presence of supercritical CO_2 , Based on *Chemical geology* (2008)-doi:10.1016/j.chemgeo.2008.12.010, including corrections on Figure 3.3 and Table 1

3.1 Introduction

There is now widespread interest in the possibility of CO₂ capture at fossil fuel power stations, coupled with storage in geological formations [Wawersik *et al.*, 2001]. Potential geological storage systems include depleted oil and gas reservoirs [Bachu, 2000; *International Panel on Climate Control*, 2005], saline aquifers and coal beds [Damen *et al.*, 2005; White *et al.*, 2005]. However, numerous questions must be addressed in assessing the performance and integrity of such systems [Ambrose *et al.*, 2008; Benson, 2000; Ennis-King and Paterson, 2003]. A key point, in the case of reservoirs and aquifers for example, is how will the porosity and permeability of the host rock evolve during CO₂ injection, as a result of coupled dissolution, transport and precipitation phenomena [Ambrose *et al.*, 2008; Gaus *et al.*, 2002; Zoback and Zinke, 2002]. Will this evolution promote or impede injection? Will rock matrix dissolution result in reservoir compaction by pore collapse or other deformation mechanisms? And will such deformation effects be large enough to influence caprock and fault seal integrity [Chiaramonte *et al.*, 2008; Zoback and Zinke, 2002]?

Due to their high solubility in the CO₂-water system, carbonate reservoir rocks are expected to be particularly prone to chemically induced porosity-permeability changes [Izgec *et al.*, 2008; Le Guen, 2007; Renard *et al.*, 2005; Xu *et al.*, 2007] and compaction [Le Guen, 2007; Madland *et al.*, 2006; Portier and Rochelle, 2005]. There is, nonetheless, widespread interest in using depleted carbonate reservoirs for CO₂ storage. First, this is because of the vast capacity available. Around 60% of known oil reserves and 40% of gas reserves are located in carbonate reservoirs, many of which already contain significant amounts of CO₂ [Fischer *et al.*, 2006; Lewicki *et al.*, 2007]. Second is the possibility that CO₂ can be used in Enhanced Oil or Gas Recovery (EOR/EGR) operations in carbonates, liberating valuable hydrocarbons while trapping much of the injected CO₂ in the reservoir [Gozalpour *et al.*, 2005]. Almost 50% of current CO₂ flooding operations in EOR research and production involve carbonate reservoirs, for example in the Weyburn Field in Canada or the U.S. Permian Basin, both of which are key sites in EOR and CO₂ storage research [Ambrose *et al.*, 2008; Emberlery, 2005; Gozalpour *et al.*, 2005; Preston, 2005]. Significantly, no major adverse effects have been observed at such sites to date.

Nonetheless, to assess the long term effects of CO₂ injection and storage on carbonate reservoirs, their coupled geochemical and geomechanical response must be understood. Much work has already been done on the geochemical effects of CO₂ on carbonates, including numerous studies of calcite solubility and dissolution rates in the presence of CO₂ [Busenberg and Plummer, 1986; Ellis, 1959; Gledhill and Morse, 2006; He and Morse, 1993; Morse and Mackenzie, 1990; Plummer *et al.*, 1978; Plummer and Busenberg, 1982; Pokrovsky *et al.*, 2005; Segnit *et al.*, 1962]. A limited number of other studies have addressed the coupled chemical-mechanical effects. In particular, the long-term effects of CO₂-water-rock interaction on time-dependent compaction of porous limestones have been investigated by means of both numerical modeling [Renard *et al.*, 2005] and rock mechanics experiments [Le Guen, 2007; Liteanu *et al.*, in prep.]. These studies point to an acceleration of creep in the presence

of CO_2 by 1 to 3 orders of magnitude, due to acceleration of intergranular pressure solution [Renard *et al.*, 2005] and stress corrosion cracking phenomena [Atkinson, 1982; Liteanu *et al.*, in prep.] – independently of direct dissolution effects. This is attributed to the increased acidity of the carbonated pore fluid and hence increased solubility and dissolution rate of calcite.

However, besides the effects of pure water and CO_2 on limestone dissolution and creep, the pore fluid salinity is also expected to play an important role under reservoir conditions. The salinity of pore waters typically ranges from 72 $\text{g}\cdot\text{l}^{-1}$ Total Dissolved Solid (TDS) for meteoric water to 600 $\text{g}\cdot\text{l}^{-1}$ TDS for saline aquifers [Case, 1945; Hanor, 1994]. Increasing salinity results in a significant decrease in the solubility of CO_2 in water [Duan and Sun, 2003; Enick and Klara, 1990; Rosenbauer and Koksalan, 2002] due to the “salting-out” effect. On the other hand, the solubility of calcite increases with salinity in solutions in equilibrium with the atmosphere [Gledhill and Morse, 2006; He and Morse, 1993]. The effect of salinity on calcite dissolution and precipitation kinetics remains unclear [Alkattan *et al.*, 2002; Gledhill and Morse, 2006; Gutjhar *et al.*, 1996; Pokrovsky *et al.*, 2005; Portier and Rochelle, 2005; Sjöberg, 1978; Sjöberg and Rickard, 1984].

Work on compaction of calcite rocks and aggregates, in the presence of supercritical CO_2 , has not yet addressed the influence of pore fluid salinity. From the foregoing, however, significant effects can be expected when deformation is controlled by pressure solution or stress corrosion cracking processes. Pore fluid composition certainly plays a key role in controlling compaction of wet carbonate and other rock systems in the absence of added CO_2 [Austad *et al.*, 2005; de Meer and Spiers, 1999; Le Guen, 2007; Noiriel *et al.*, 2005; Zhang and Spiers, 2005a; Zhang and Spiers, 2005b].

The aim of this paper is to address the above knowledge gap by investigating the effect of pore fluid salt content on the compaction creep behavior of a simulated porous limestone (i.e. a granular calcite aggregate) in the presence of supercritical CO_2 . We focus in particular on the effect of pore fluid salinity on the mechanism of compaction with and without supercritical CO_2 . Our experiments consisted of uniaxial compaction creep tests performed on ground Carrara Marble aggregates, using saline solutions with different NaCl and MgCl_2 concentrations as pore fluid. The tests were conducted under conditions resembling those expected in reservoirs situated at a depth of 2.5 - 3 km, namely at a temperature of 80°C, an effective vertical pressure (axial stress) of 30 MPa, and in the presence or absence of supercritical CO_2 at a pressure of 10 MPa. No attempt was made to investigate purely chemical reaction kinetics on solution chemistry evolution, as the high pressure conditions and mechanical testing method used do not lend themselves to reliable fluid sampling or to *in-situ* analysis.

3.2 Compaction creep of carbonate rocks: Theory and previous experiments

To provide sufficient background for interpreting our results on the chemical effects of salts on compaction creep of carbonates in the context of CO_2 storage, we here review some basic concepts of rock mechanics [Jaeger *et al.*, 2007; Paterson and Wong, 2005]

as well as results on salt-free compaction of calcite aggregates obtained in a separate experimental study by [Litanu *et al.*, in prep.].

3.2.1 Mechanics and mechanisms of compaction

Compaction of rocks, i.e. physical densification or reduction in volume (ΔV) due to porosity loss or mineral reactions at constant solid mass, is generally expressed in terms of a finite volumetric strain defined as

$$e_v = \Delta V/V_0 \quad (3.1)$$

where V_0 is the initial volume. If compaction is accommodated by compressive displacements (ΔL) occurring in one direction only, as is usually the case in simple piston-cylinder (“oedometer”) experiments or under the action of vertical overburden pressure in the upper crust (see Figure 3.1), the volumetric or compaction strain undergone by a representative volume of original thickness L_0 is written:

$$e_v = \Delta L/L_0 \quad (3.2)$$

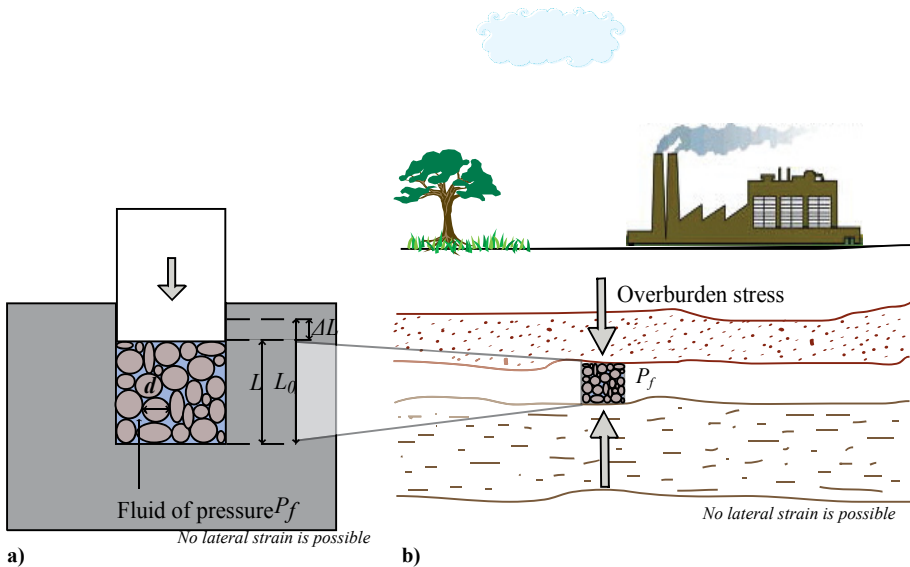


Figure 3.1. Schematic illustration of one-dimensional or uniaxial compaction occurring a) in a simple piston-cylinder apparatus, and b) in a representative volume of upper crustal reservoir rock under the action of overburden pressure. Note that in both cases lateral constraints mean that only vertical displacement or strain (vertical compaction) is possible. No lateral strain is possible, though lateral stresses may change. Note that axial strain is calculated as $e_v = \Delta L/L_0 = \Delta V/V_0$, and effective axial stress $\sigma_e = \sigma - P_f$.

In rocks systems where mineral changes are unimportant, such as relatively pure quartz or carbonate sediments, compaction is driven by the effective stress σ_e (applied normal stress σ minus pore fluid pressure P_f) and may be time-independent (i.e. strain depends only on applied stress at fixed P_f and temperature) or time-dependent (strain depends on stress and time). Time-dependent compaction under constant stress conditions is referred to as compaction creep, and proceeds at an instantaneous rate described in terms of the compaction strain rate $\dot{\epsilon} = -\dot{L}/L$

$$(3.3)$$

(see Figure 3.1). Note that a list of all the symbols used in this paper is provided in Table 3.1.

Symbol	Description	S.I. unit
$A_\alpha(T)$	Geometric constant – subscript $\alpha = p, d, s$ (s=dissolution, d = diffusion, p = precipitation)	-
$B(\phi_0, \phi)$	Measure of the stress concentration at grain contacts due to aggregate structure (function of porosity)	-
C	Solubility of the solute in the grain boundary fluid	$\text{m}^3 \cdot \text{m}^{-3}$
D	Diffusion coefficient in the grain boundary fluid	$\text{m}^2 \cdot \text{s}^{-1}$
d	Grain size	m
e_v	Volumetric strain ($e_v = \Delta V/V_0$)	%
$g_\alpha(\phi_0, \phi)$	Function of porosity (expresses changes in grain contact area, length of transport path, pore wall area during compaction), where $\alpha = p, d, s$ (s=dissolution, d = diffusion, p = precipitation).	-
$K_\alpha(T)$	Reaction rate expressed as velocity of dissolution or precipitation for unit driving force	$\text{m} \cdot \text{s}^{-1}$
L_0	Initial length of the sample	m
\dot{L}	Rate of change of the length of the sample	$\text{m} \cdot \text{s}^{-1}$
ΔL	Sample shortening	m
P_f	Pore fluid pressure	MPa
R	Universal gas constant	$\text{J} \cdot \text{K}^{-1} \cdot \text{mol}^{-1}$
S	Mean grain boundary fluid thickness	m
T	Temperature	K
t	Time	s
Δt	Time interval	s
V_0	Initial sample volume	m^3
ΔV	Sample volume reduction	m^3
$\dot{\epsilon}_\alpha$	Volumetric strain rate-subscript $\alpha = p, d, s$ (s=dissolution, d = diffusion, p = precipitation) $\dot{\epsilon}_\alpha \approx \dot{L}/L$	s^{-1}
ϕ_0	Initial porosity	%
ϕ	Instantaneous porosity ($\phi = [\phi_0 - e_v] / [1 - e_v]$)	%
μ	Chemical potential of the solid	$\text{J} \cdot \text{mol}^{-1}$
$\Delta\mu$	Chemical potential drop between source and sink sites ($\Delta\mu \approx \Delta\sigma_e \cdot \Omega$)	$\text{J} \cdot \text{mol}^{-1}$
Ω	Molar volume of solid phase	$\text{m}^3 \cdot \text{mol}^{-1}$
ρ	Density of solid phase	$\text{kg} \cdot \text{m}^{-3}$
σ_e	Effective axial stress ($\sigma_e = \sigma - P$)	MPa

Table 3.1. List of symbols used in this paper.

Time-independent compaction of porous rocks such as granular limestones or sandstones can occur by reversible processes such as poro-elastic compression [Lockner and Stanchits, 2002; Wang, 1993; Wang, 1997], as well as irreversibly by grain fracture, contact de-bonding and accompanying grain rearrangements [David *et al.*, 2001; Wong *et al.*, 1997; Wong and Baud, 1999]. In calcite rocks, crystal plastic process such as deformation twinning can also play a role [Xiao and Evans, 2003; Zhu *et al.*, 1999; Zubtsov *et al.*, 2005]. Time-dependent compaction creep is irreversible and controlled by thermally activated kinetic processes. Under upper crustal conditions, these include grain failure and de-bonding by slow (sub-critical) crack growth [Atkinson, 1984; Fredrich and Wong, 1986; Fredrich *et al.*, 1989], as well as stress-induced dissolution-precipitation processes

or intergranular pressure solution [Dewers and Hajash, 1995; Niemeijer et al., 2002; Rutter, 1983; Spiers et al., 1990; Tada and Siever, 1986].

3.2.2 Compaction creep by microcracking

Compaction creep of porous rock due to progressive grain or grain framework failure through subcritical crack growth is significantly accelerated in the presence of a chemically active fluid or saturated solution phase, due to stress-induced chemical attack at the crack tip i.e. stress corrosion cracking [Atkinson, 1982; 1984; Chester et al., 2007; Chester et al., 2004; Kerner et al., 2005]. No general theory for compaction creep by this mechanism has yet appeared in the literature. However, preliminary models and most experimental observations [Brzesowsky, 1995; Chuhan et al., 2003; Ngwenya et al., 2001] on compacting by grain scale brittle behaviour imply a strong positive dependence of creep rate ($\dot{\epsilon}$) on both stress (σ_e) and mean grain size (d).

3.2.3 Compaction creep by intergranular pressure solution

This has been more extensively studied from a theoretical point of view. Intergranular pressure solution (IPS) is a key mechanism of compaction creep and porosity/permeability reduction in carbonate and clastic rocks under upper crustal conditions [Dewers and Ortoleva, 1990; Dewers and Hajash, 1995; Niemeijer et al., 2002; Rutter, 1976; Rutter, 1983; Spiers et al., 1990; Tada and Siever, 1986]. Microstructurally, it is characterized by grain-to-grain indentations and overgrowths, grain truncations and micro-stylolites or grain contact suturing [Den Brok and Spiers, 1991; Hellmann et al., 2002; Rutter, 1976]. For IPS to operate in a given rock material, an intergranular fluid must be present in the pores and in grain boundary films or micro-channel networks [Gratier and Guiguet Irigm, 1986; Hickman and Evans, 1995; Rutter, 1976; Spiers et al., 1990]. IPS is driven by the differences in effective normal stress (σ_n^e) around grain boundaries, which set up a difference in chemical potential

$$\Delta\mu \approx \Delta\sigma_n^e \times \Omega \quad (3.4)$$

of the solid with a molar volume (Ω) between highly stressed grain contacts and low stress interfaces or free pore walls [Lehner, 1990]. In a chemically closed system (no long range transport of solid mass via the pore fluid phase), IPS involves three serial steps: 1) dissolution of material at grain contacts under high normal stress, 2) diffusive transport through the grain boundary fluid film or channel network and 3) precipitation at grain contacts and pore walls under low stress, thus effecting local mass transfer and hence creep [de Meer and Spiers, 1999; Gundersen et al., 2002; Hellmann et al., 2002; Lehner, 1990; Rutter, 1976]. The overall rate of IPS is accordingly controlled by the kinetics of the slowest of these steps.

Theoretical rate equations for pressure solution creep have been derived in numerous previous studies, more recently using a non-equilibrium thermodynamic approach [Lehner, 1990; Niemeijer et al., 2002; Spiers et al., 1990]. Considering a regularly packed aggregate formed of spherical grains, the result obtained for the case of uniaxial compaction creep can be written:

$$\dot{\epsilon}_\alpha = A_\alpha \cdot K_\alpha \cdot \exp\left(\frac{B(\phi_0, \phi) \cdot \sigma_e \cdot \Omega}{R \cdot T}\right) g_\alpha(\phi_0, \phi) d^m \quad (3.5)$$

Here the subscript α stands for the dissolution (s), diffusion (d) or precipitation (p) controlled cases, A_α is a geometric constant and $g_\alpha(\phi_0, \phi)$ is a function of the initial and instantaneous porosity of the aggregate (ϕ_0, ϕ), which expresses the changes in the grain contact area, length of transport path and pore wall area during compaction. $B(\phi_0, \phi)$ is a grain contact stress concentration factor, that depends on the initial and instantaneous aggregate porosities and accounts for the evolution of grain contact area during compaction [Dewers and Hajash, 1995; Niemeijer et al., 2002; Spiers et al., 2004]. The instantaneous aggregate porosity is itself of course related to volumetric strain

$$\phi = [\phi_0 - \epsilon_v] / [1 - \epsilon_v] \quad (3.6)$$

The coefficients K_s and K_p incorporate the temperature-dependent dissolution and precipitation reaction rate coefficients of the solid, while K_d is the product DCS , where D is the diffusivity of the solute in the grain boundary fluid phase, C the solubility of the solid, and S is the mean grain boundary fluid thickness. R is of course the gas constant, T is absolute temperature and Ω is the solid molar volume. The grain size sensitivity of strain rate (exponent m) is 1 for dissolution and precipitation controlled IPS and 3 for diffusion control [Niemeijer et al., 2002; Spiers et al., 2004].

3.3 Previous experiments on calcite

In recent years, several experimental studies have attempted to determine which deformation mechanisms control compaction creep of wet calcite in the absence of injected CO_2 . In room temperature uniaxial compaction experiments on finely ground limestone and reagent grade calcite, [Zhang and Spiers, 2005a; Zhang and Spiers, 2005b] found rough qualitative agreement with equation 3.5 and inferred that compaction was controlled by diffusion limited IPS, depending on pore fluid impurity content. To investigate the effects of supercritical CO_2 on compaction creep of calcite aggregates under non-saline reservoir conditions, [Liteanu et al., in prep.] performed in a separate study, similar tests using crushed Carrara Marble of various grain size (i.e. $d = 28 \div 250 \mu\text{m}$) and reagent grade CaCO_3 ($d = 1 - 30 \mu\text{m}$) at temperature up to 80°C in the presence or absence of CO_2 at pressure up to 10 MPa. Since no salts were added, these experiments can be regarded as “salt-free” reference experiments with respect to the present study.

For this reason, we briefly describe here the results obtained for crushed Carrara Marble by [Liteanu et al., in prep.]. All samples were initially pre-compacted under laboratory-dry conditions to a fixed starting porosity. Dry samples showed no creep. Addition of calcium carbonate-saturated solution (in the absence of supercritical CO_2), led to rapid creep, proving a fluid enhanced deformation mechanism. The creep rate was found to depend directly on grain size and on the applied effective stress (Type B tests – see [Liteanu et al., in prep.]). Note that here m is not accordingly to the values expected for IPS compaction creep (cf. equation 3.5, $m \sim -1$), however the value is similar to the theory for

compaction by stress corrosion cracking. Coupling this positive dependence on the grain size with microstructural evidence, the dominant deformation mechanism was inferred to be one of subcritical microcracking (see Section 3.1.1.). The findings of this study are different from those of [Zhang and Spiers, 2005a; Zhang and Spiers, 2005b] that found compaction creep of calcite in the presence of CaCO₃ saturated solution to be controlled by IPS. However, note that our study was performed at higher stress values and higher temperatures, differences that might explain the different compaction-controlling mechanisms. Some experiments (Type B tests) were halted midway and then restarted after injection and equilibration of CO₂ at 10 MPa pressure (Figure 3.2; see also [Litanu et al., in prep.]). Injection of CO₂ accelerated creep by 1 to 3 orders of magnitude.

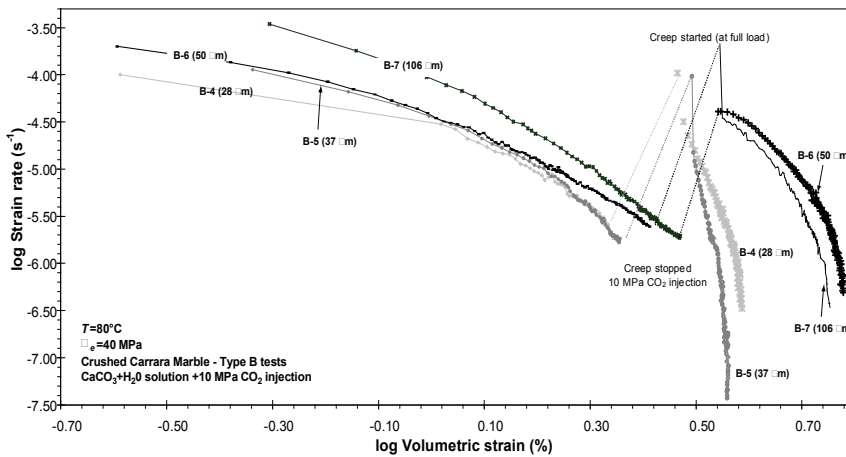


Figure 3.2. Log of axial strain rate ($\dot{\epsilon}$) versus log of volumetric strain (e_v) data obtained for wet samples of crushed Carrara Marble of various grain size. Addition of 10 MPa CO₂ typically resulted in an increase of the strain rate from $\sim 10^{-6} \text{ s}^{-1}$ to $\sim 10^{-4} \text{ s}^{-1}$.

Experiments performed in the presence of 10 MPa CO₂ pressure added from the start also showed accelerated creep (Type C tests, see Figure 3.3), and revealed two regimes of behaviour: a fine grain size regime ($d \leq 106 \mu\text{m}$) characterized by an inverse dependence of strain rate on grain size consistent with models for IPS (equation 3.5), and a coarse grain size regime ($d > 106 \mu\text{m}$), where the strain rate increases with increasing grain size (Figure 3.3). In the fine grain size regime ($d \leq 106 \mu\text{m}$), the increase in grain size sensitivity of strain rate (m) from 1 to 3, cf. equation 3.5 (see Figure 3.3, m calculated from the slope of strain rate versus grain size data) indicates that deformation may be reaction-controlled at the beginning of the experiments, followed by a switch to diffusion controlled creep at higher strain [Lehner, 1990; Spiers et al., 1990; Spiers et al., 2004]. Microstructural observations of widespread indented and sutured grain contacts in the fine grain samples, and of more extensive microcracking in

the coarser regime, led to the inference that both IPS- and microcracking-controlled creep are accelerated in the presence of CO_2 , with IPS becoming dominant at fine grain size and microcracking remaining more important in coarser material.

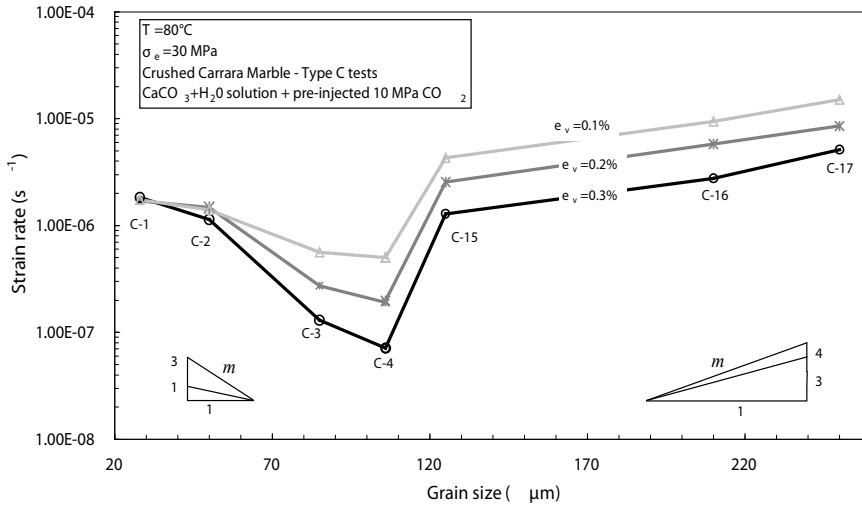


Figure 3.3. Log strain rate vs. grain size for crushed Carrara Marble of various grain sizes, compacted in presence of supercritical CO_2 . Note the two regimes of behaviour. For grain sizes smaller than 106 μm , the strain rate decreases with increasing grain size ($m \sim 1$ for $e_v < 0.2\%$, and $m \sim 3$ for $e_v > 0.2\%$), while the coarser samples exhibit a direct dependence of strain rate upon grain size ($m \sim 4$). These types of dependence suggest that IPS is controls compaction at small grain size, whereas at coarser grain size, microcracking is faster and controls the mechanism of compaction of the calcite aggregates.

The main conclusion of the above study was that aside from poro-elastic deformation, storage of CO_2 in high porosity carbonate reservoirs can lead to enhanced compaction creep due to an acceleration of subcritical microcracking and IPS, through increased solubility and or interfacial reaction rates. These mechanisms are known to be influenced by the pore fluid impurity content and salinity [Atkinson, 1982; 1984; Chester *et al.*, 2007; Dunning *et al.*, 1994; Zhang and Spiers, 2005a]. This formed the motivation for the present investigation of the influence of pore fluid salts content on compaction of calcite aggregates in presence of supercritical CO_2 .

3.4 Experimental method

The present experiments consisted of 1-dimensional compaction creep tests (constant load experiments) performed on pre-compacted samples of granular calcite of specific grain size and porosity ($\sim 25\%$). We used simulated samples instead of natural porous limestones in order to be able to control and systematically vary the sample microstructure. All creep experiments were performed at a temperature of 80°C , an applied effective stress of 30 MPa and a pore fluid ($\text{CO}_2\text{-H}_2\text{O}$) pressure of 10 MPa. We chose grain sizes ≤ 106

μm, corresponding to the IPS regime identified in the salt-free experiments (see Section 3.3 and [Liteanu *et al.*, in prep.]).

3.4.1 Sample and pore fluid preparation

The starting material used in the experiments consisted of crushed Carrara Marble with grain size fractions of $28 \pm 3 \mu\text{m}$, $37 \pm 10 \mu\text{m}$, $50 \pm 7 \mu\text{m}$, $106 \pm 10 \mu\text{m}$. These fractions were obtained by sieving the crushed material, followed by cleaning in an ultrasonic bath to eliminate very fine particles. Grain size distributions were measured using a Malvern particle sizer and more than 80% fell into the ranges stated. X-ray diffraction (XRD) and X-ray fluorescence spectroscopy (XRF) analysis showed that the marble consists of ~ 98% pure CaCO₃ in the form of calcite, while the main impurities were MgO (< 0.30%), K₂O (< 0.13%), SiO₂ (< 0.06%), Fe₂O₃ (< 0.05%). No measurements of the surface area of the calcite grains were made.

Calcite pre-saturated pore fluid was prepared following the procedures presented by [Sjöberg and Rickard, 1984], and by [Pokrovsky and Schott, 2002] who showed that 48 hours is sufficient to produce an equilibrated calcium carbonate solution under ambient laboratory conditions (see also Liteanu *et al.*, in prep.). The method consists of adding excess calcite grains, of the same composition and granulometry as the material to be mechanically tested, to boiled, distilled water (to eliminate any traces of CO₂). The solution is then stirred for 48 hours in an open flask at room temperature. CaCO₃ – saturated saline pore fluid solutions, with molar NaCl concentrations of 0.6, 1, 2, 3 M and MgCl₂ concentrations of 1 and 2 M were prepared by adding analytical grade NaCl (Merck nr. 6404) or MgCl₂ (Merck nr. 5832) to saturated CaCO₃ solution, along with excess calcite grains. The solutions were mixed and allowed to equilibrate for another 48 hours. Measurements of the pH or alkalinity of the resulting solutions were not performed. *In-situ* measurements are not possible at the pressures and temperatures employed in our experiments.

3.4.2 Experimental set-up and data acquisition

The compaction tests were performed using an Instron 8562 servo –controlled, mechanical testing machine equipped with a 10 kN load cell (accuracy 0.1%) plus a 1-D compaction vessel (hardened stainless steel, Remanit – 4122) (see Figure 3.4). The vessel is lined with a titanium insert, to prevent contamination of the sample. The diameter of the liner, in which the granular calcite sample is placed, is 10 mm. The sample is loaded by means of closely fitting titanium pistons driven by Remanit loading frame sealed against the steel vessel with Viton-O rings. The vessel and its contents are heated by an external furnace controlled by a Eurotherm temperature controller (within 0.5°C) connected to a type K control thermocouple that measures the external temperature of the vessel. Sample temperature is measured using a second thermocouple embedded in the vessel next to the sample (Figure 3.4). The displacement obtained during uniaxial loading is measured using the Linear Variable Differential Transducer (LVDT) located in the Instron drive unit, and an external Sangamo LVDT with a range of ± 1 mm for more accurate measurements (0.05% resolution). The Sangamo LVDT measures the relative displacement between the piston and the top part of the main vessel during the

compaction tests (Figure 3.4).

Pre-saturated solution was introduced into the sample prior to assembly of the vessel, as described in Section 3.3. Carbon dioxide pressure was applied to the fluid-filled sample using high purity CO₂ (99.9%), boosting its pressure up to 10 MPa using a CO₂-Ar separator backed by a high-pressure argon buffer (Figure 3.4). The applied CO₂ pressure, which is approximately equal to the CO₂ partial pressure at the test temperature of 80°C, was measured using an MSI US 175 pressure transducer. Note that the argon buffer system maintained constant fluid pressure in the sample and pore fluid system during the experiments with CO₂, despite advancement of the loading piston. In experiments at atmospheric pressure, the sample and pore fluid system were simply vented to air.

The experimental data were logged using a PC and standard Instron software. Raw data collected included time (t), applied axial stress (σ), Sangamo LVDT displacement, temperature (T) and pore fluid pressure (P_f).

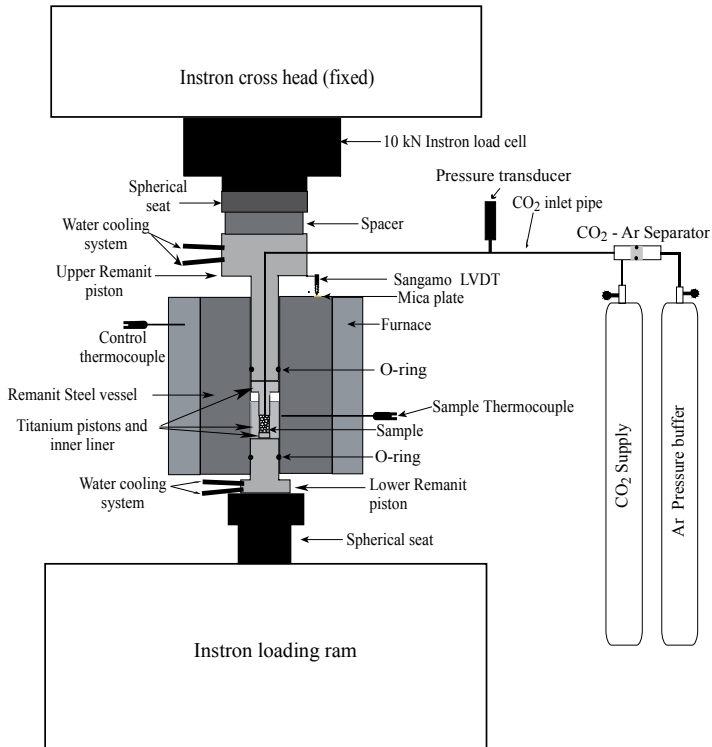


Figure 3.4. Semi-schematic representation of the central elements of the present experimental setup, including the steel vessel, titanium inner vessel/liner and pore fluid system.

First, the displacement data were corrected for temperature fluctuations and apparatus distortion (based on calibration tests performed on a Remanit 4122 stainless steel dummy sample), followed by smoothing out of signal noise using a moving average method.

The corrected displacement $x(t)$ data were then processed to yield sample length and finite shortening, instantaneous porosity, volumetric strain and axial compaction strain rate.

The instantaneous strain rate was calculated from the x vs. t data using the relation:

$$\dot{\epsilon} \approx \frac{1}{L} \cdot \frac{\Delta x}{\Delta t} \quad (3.7)$$

This was applied using a moving window (central difference) method spanning a constant displacement interval (Δx) and a varying time interval, such that the maximum error in $\dot{\epsilon}$ was 5%. The porosity of the sample was calculated using the sample mass, cross-section, and length, along with the density of pure calcite ($\rho = 2710 \text{ kg}\cdot\text{m}^{-3}$). The effective axial stress applied in each experiment was obtained from its definition (see Table 3.1), correcting for minor seal friction whenever necessary.

The experiments reported in this paper are listed in Table 3.2 along with the corresponding experimental variables and conditions at which the tests were performed.

Run / Sample ID	d [μm]	Pore fluid phase [M]	σ_0 [MPa]	P_i [MPa]	T [°C]	Φ_0 [%]	Final e_v [%]
NaCl - 1	28	CaCO ₃ +H ₂ O+1 M NaCl	30	-4·10 ⁻⁵	80	25.75	0.48
NaCl - 2	37	CaCO ₃ +H ₂ O+1 M NaCl	30	-4·10 ⁻⁵	80	25.8	1.27
NaCl - 3	50	CaCO ₃ +H ₂ O+1 M NaCl	30	-4·10 ⁻⁵	80	25.6	1.39
NaCl - 4	106	CaCO ₃ +H ₂ O+1 M NaCl	30	-4·10 ⁻⁵	80	25.43	1.38
CO ₂ NaCl - 0	28	CaCO ₃ +H ₂ O+0 M NaCl+CO ₂	30	10	80	25.93	2.15
CO ₂ NaCl - 1	28	CaCO ₃ +H ₂ O+1 M NaCl+CO ₂	30	10	80	25.33	0.35
CO ₂ NaCl - 2	37	CaCO ₃ +H ₂ O+1 M NaCl+CO ₂	30	10	80	25.47	0.49
CO ₂ NaCl - 3	50	CaCO ₃ +H ₂ O+1 M NaCl+CO ₂	30	10	80	25.43	1.31
CO ₂ NaCl - 4	28	CaCO ₃ +H ₂ O+2 M NaCl+CO ₂	30	10	80	25.34	1.50
CO ₂ NaCl - 5	28	CaCO ₃ +H ₂ O+3 M NaCl+CO ₂	30	10	80	25.34	2.23
CO ₂ NaCl - 6	28	CaCO ₃ +H ₂ O+0.6 M NaCl+CO ₂	30	10	80	25.55	0.21
CO ₂ MgCl ₂ - 1	28	CaCO ₃ +H ₂ O+1 M MgCl ₂ +CO ₂	30	10	80	24.18	0.43
CO ₂ MgCl ₂ - 2	28	CaCO ₃ +H ₂ O+2 M MgCl ₂ +CO ₂	30	10	80	25.27	2.43

Table 3.2. List of the experiments reported in this paper and the experimental conditions at which the tests were conducted.

3.4.3 Experimental procedure

We conducted three new types of experiments to investigate the effect of salts on compaction creep of wet, CO₂-bearing calcite aggregates:

1. Compaction in the presence of NaCl (1 M solution), without CO₂ (Runs NaCl-y),
2. Compaction in the presence of NaCl (0.6 - 3 M solution), with pre-injected CO₂ at 10 MPa (Runs - CO₂NaCl-y),
3. Compaction in the presence of MgCl₂ (1 - 2 M solution) with pre-injected CO₂ at 10 MPa (Runs - CO₂MgCl₂-y).

In addition, we performed a single control experiment on a sample compacted in the presence of pure carbonate solution plus pre-injected CO₂ at 10 MPa with no added salts. This is denoted in Table 3.1 as CO₂NaCl-0.

For all types of experiments, we followed the same basic procedure. First 1 g of powder was funneled into the titanium insert. Subsequently, ~ 0.40 ml of the desired pore fluid solution was added. This volume of solution was added to completely fill the pore volume typically obtained after pre-compaction to standard starting porosity ϕ_0 of ~ 25% (see Table 3.2). Pilot tests showed that at least 95 % pore saturation was obtained.

The titanium vessel was next inserted in the 1-D compaction vessel, between the loading pistons. The main compaction vessel was subsequently located in the Instron loading frame (Figure 3.4) and a small load was applied to the sample. The vessel and the sample were then heated. In the experiments performed with CO₂, when the desired temperature was reached, 10 MPa CO₂ pressure was applied to the sample, maintaining the small additional load previously applied. The CO₂ and the pore fluid were allowed to reach equilibrium for one hour, following equilibration times measured independently in an *in-situ* Fourier Transform Infrared Reflectance (FTIR) cell of similar dimensions. In experiments performed without CO₂, the added solution phase was simply maintained at 1 atmosphere pressure by venting the pore fluid system to air. Note that compaction in our experiments led only to expulsion of pore fluid from the sample chamber at constant pressure (no flow through the sample).

After reaching thermal and chemical equilibrium state, all samples were pre-compacted to a porosity of 25 ± 1 %. Subsequently, the sample was unloaded and reloaded at the effective stress. The compaction creep test was then run for 2 to 3 days. The experiments were ended by removing the load, the CO₂ pressure and cooling down the vessel. The sample was removed and dried, followed by resin impregnation and thin sectioning. The samples were sectioned axially. The epoxy impregnated thin sections were examined using optical microscopy and Scanning Electron Microscope (SEM).

3.5 Results

3.5.1 Mechanical data

The data presented here are describing the constant load (creep) experiments performed on our pre-compacted samples (initial porosity $\phi_0 \approx 25$ %).

3.5.1.1 NaCl Runs

Samples loaded in the presence of NaCl-bearing pore fluid without supercritical CO₂ (Table 3.2) showed substantial, on-going compaction creep (Figure 3.5a), reaching final volumetric strains between 0.48 % for samples with 28 μm grain size compacted for 58 hours, and 1.38 % for 106 μm material compacted for ~16 hours (Figure 3.5a). The data obtained for increasing grain size in this range show a systematic increase both in strain achieved at a given time and in strain rate at fixed strain. This direct dependence of strain rate on grain size is illustrated in Figures 3.5b and 3.5c. From the log-log plot of Figure 3.5c, it is clear that at grain sizes in the range 37-106 μm , the strain rate increases with grain size in a roughly linear manner. At lower grain sizes, the strain rate is much more sensitive to grain size (Figure 3.5c).

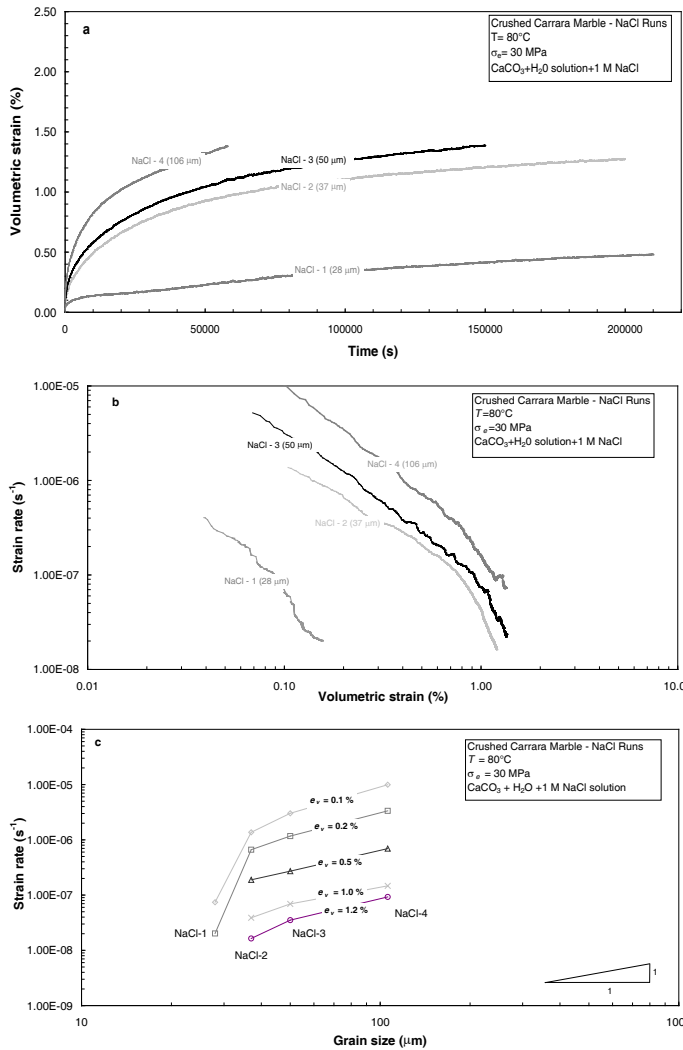


Figure 3.5. Results of the NaCl Runs on crushed Carrara Marble compacted at 80°C and 30 MPa effective applied stress. The samples were compacted in the presence of calcite-equilibrated solution containing 1 M NaCl (no CO_2). a) Volumetric strain versus time plot shows significant time-dependent compaction or creep. The volumetric strain achieved at any time clearly increases with increasing grain size. b) Log-log plot of strain rate versus volumetric strain for the NaCl Runs showing a systematic increase of strain rate with grain size at any given volumetric strain. c) Log-log plot of strain rate versus grain size illustrating that the strain rate increases in a roughly linear manner in the grain size range 37-106 μm (slope \sim 1).

3.5.1.2 CO₂NaCl Runs

These runs, i.e. samples compacted in the presence of NaCl-bearing solution and supercritical CO_2 , also showed substantial creep (see Figure 3.6). Two trends are present in the corresponding strain rate data. First, a direct dependence of the strain rate on grain size is observed in samples tested with fixed salt content (Figure 3.7a), similar to that seen in the NaCl Runs without CO_2 (Figure 3.5c).

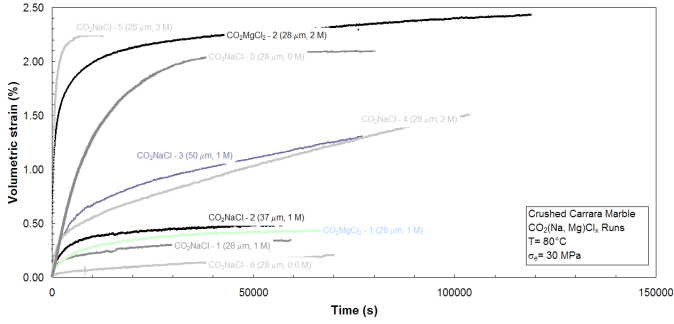


Figure 3.6. Volumetric strain versus time data obtained for the CO_2/NaCl and $\text{CO}_2/\text{MgCl}_2$ Runs. The experiments were performed on crushed Carrara Marble (grain size=28-50 μm), at 80°C and 30 MPa effective applied stress, in the presence of calcite-equilibrated solution with the salt concentrations indicated. The samples exhibit significant time-dependent compaction or creep. The volumetric strain achieved at any time clearly increases with increasing grain size and with increasing salts concentration. The single 28 μm control experiment performed with CO_2 , but no salt in solution (CO_2/NaCl -0) does not conform to this trend – it shows much more creep than similar samples with 0.6 – 1 M NaCl in the pore fluid (e.g. CO_2/NaCl -6).

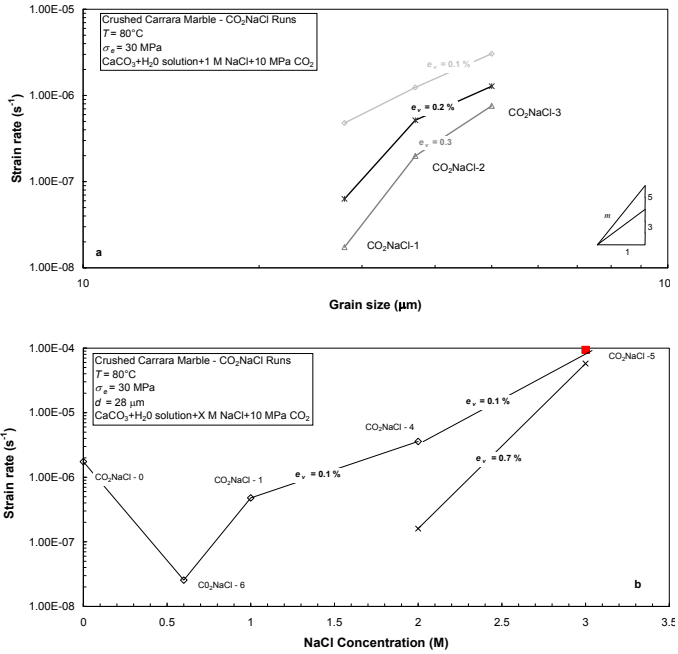


Figure 3.7. Results of the CO_2/NaCl Runs on crushed Carrara Marble aggregates compacted at 80°C and 30 MPa effective applied stress in the presence of calcite-equilibrated solution (1 M NaCl) and supercritical CO_2 (10 MPa). a) Log-log plot of strain rate versus grain size showing that the strain rate increases with increasing grain size at a fixed NaCl concentration (1M) and fixed strain (e_v). b) Log-log plot of strain rate versus NaCl concentration, for 28 μm samples showing that compaction creep rates first decrease and then increase with NaCl concentration at fixed strain (e_v). (■ Data point extrapolated from trend shown by CO_2/NaCl -5, Figure 3.8).

Second, tests performed on 28 μm grain size samples, but at different initial NaCl concentrations show that compaction creep rates decrease with the first addition of NaCl (0-0.6 M) and then increase strongly with concentration in the range 0.6-3 M (Figure 3.7b). For comparison with the NaCl Runs performed without CO₂ (Figure 3.5b), Figure 3.8 shows the log strain rate vs. log strain data derived from Figure 3.6 for the samples compacted in the presence of salts (NaCl and MgCl₂) plus CO₂.

In the finest grained NaCl-bearing samples, creep was clearly enhanced by the presence of CO₂ (compare the 28 μm grain size samples in Figure 3.8 vs. Figure 3.5b), while at coarser grain sizes CO₂ addition had little effect or even decreased the strain rate (compare the 37 μm and 50 μm samples in Figure 3.8 vs. Figure 3.5b). Particularly noteworthy in Figure 3.8 is the log $\dot{\epsilon}$ vs log e_v curve for the 28 μm control sample CO₂NaCl-0, which was compacted with CO₂ but without NaCl in solution. This curve is quite different from those obtained for samples with added NaCl, suggesting a different deformation mechanism in this control sample.

3.5.1.3 CO₂MgCl₂ Runs

Only two compaction creep experiments were performed on calcite samples in the presence of MgCl₂ and supercritical CO₂ (the CO₂MgCl₂ Runs, Figure 3.6). These 28 μm grain size samples showed a similar salt concentration effect to the samples compacted in the presence of NaCl and CO₂ (CO₂NaCl Runs), i.e. the strain rate first decreased compared with the salt-free control experiment (CO₂NaCl-0) and then increased with increasing MgCl₂ concentration (Figure 3.8).

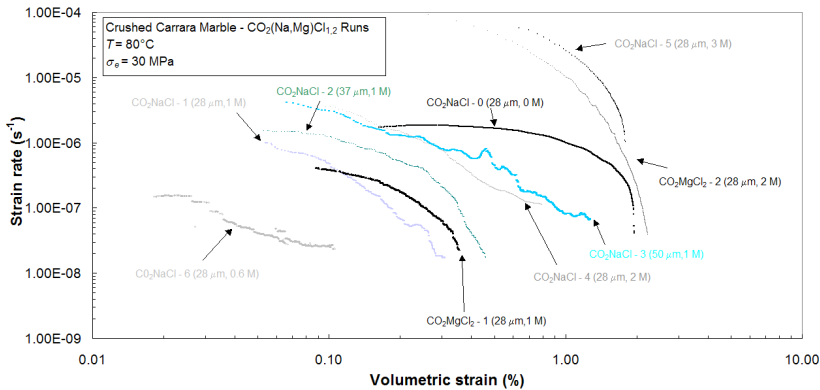


Figure 3.8. Log-log plot of strain rate versus volumetric strain for the samples compacted in the presence of added salts plus CO₂ (see Table 3.2). Comparison with Figure 6a shows that 28 μm samples creep some 3-8 times faster with CO₂ than without. However, creep of coarser material is not much affected by the presence of CO₂ (Figure 3.8 vs. Figure 3.5b).

However, the effect was much larger in the CO₂MgCl₂ Runs, with an increase in MgCl₂ concentration from 1 M to 2 M causing a 3-order of magnitude increase in strain rate as opposed to the 1-order of magnitude increase observed in the CO₂NaCl Runs, for the same change in NaCl concentration (Figure 3.8).

3.5.2 Microstructural observations

Optical examination of the starting (uncompacted) material fractions showed them to consist of angular and subangular grains of quite uniform size, displaying sparse deformation twins and intergranular cracks. Micrographs of control sample $\text{CO}_2\text{NaCl-0}$ compacted in the presence of supercritical CO_2 , but without added salts (Figure 3.9a), show a homogeneous granular microstructure with no obvious mean grain size reduction in comparison with the initial grain size of $28\ \mu\text{m}$. Thin twins and cracks can be observed, similar to the starting material with no apparent increase in their frequency. Indented and sutured grain-grain contacts typical of IPS are the most conspicuous microstructures observed (Figure 3.9a).

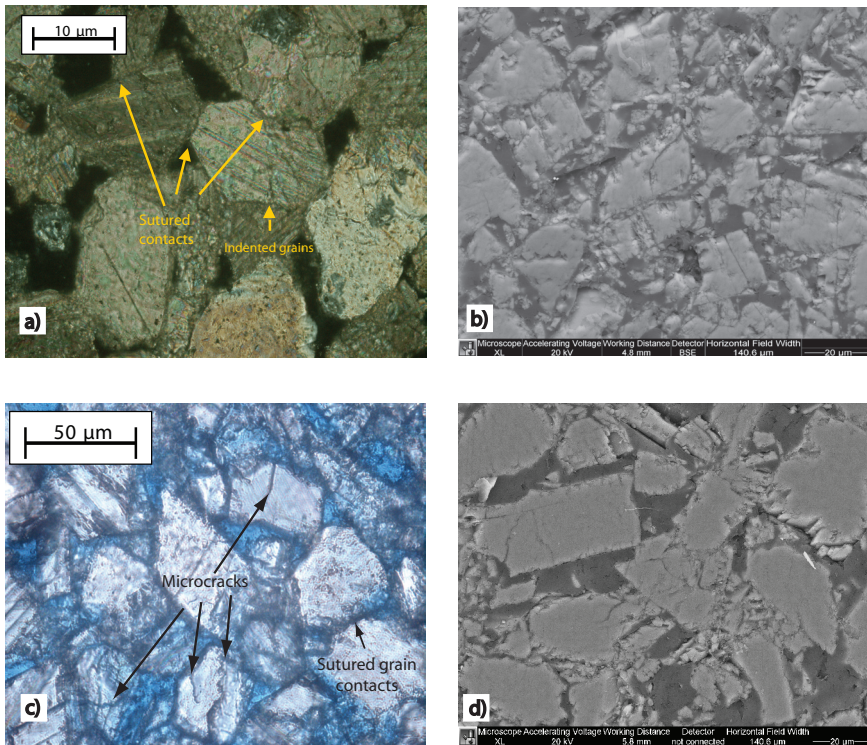


Figure 3.9. Microstructures of crushed Carrara Marble aggregates, uniaxially compressed at 30 MPa and 80°C . a) Optical micrograph of control sample $\text{CO}_2\text{NaCl-0}$, with mean grain size of $28\ \mu\text{m}$, compacted in the presence of 10 MPa CO_2 , without added salts. Note the indented grains and sutured grain-grain contacts typical of intergranular pressure solution. b) SEM backscatter image of sample NaCl-1 (crushed Carrara Marble, $d=28\ \mu\text{m}$), compacted with 1 M NaCl in solution but without CO_2 . Notice the subangular grains, crushed material and microcracks. c) Optical micrograph of sample $\text{CO}_2\text{NaCl-3}$ ($d=50\ \mu\text{m}$, compacted in the presence of NaCl and 10 MPa CO_2). Some sutured contacts are present, while transgranular and intragranular microcracks are widespread. d) Secondary electron SEM image of sample $\text{CO}_2\text{NaCl-2}$ ($d=28\ \mu\text{m}$), showing widespread grain size fracture/crushing.

SEM images of samples retrieved from the NaCl Runs, i.e. samples compacted in the presence of NaCl-bearing pore fluid but without supercritical CO_2 ; show a more

heterogeneous, bi-modal, granular microstructure (Figure 3.9b). Fractured large (original) grains with interfering fines provide clear evidence for grain size reduction by brittle grain failure and contact crushing (Figure 3.9b). Transgranular, intragranular and grain margin microcracks are widespread. Little evidence is visible for grain-to grain indentations of the type found in the salt-free control sample (CO₂NaCl-0 – Figure 3.9a).

Samples retrieved from the CO₂NaCl Runs, i.e. samples compacted in the presence of both NaCl-bearing fluid and supercritical CO₂, showed a granular microstructure intermediate in character between the control Run CO₂NaCl-0 (CO₂, no NaCl) and the NaCl Runs (NaCl, no CO₂) – see Figures 3.9c, d for optical and SEM images, respectively. The microstructure showed grain scale cracking and contact crushing, along with intergranular fines and a reduction of mean grain size, e.g. from 28 to 24 μm (Figures 3.9c, d). At the same time, occasional grain contacts showed indentation and suturing features (Figure 3.9c) resembling those seen in the control sample (CO₂, no NaCl).

Samples retrieved from the CO₂MgCl₂ experiments showed a microstructure that was visually indistinguishable from those of the CO₂NaCl Runs.

3.6 Discussion

The above experiments have investigated the effects of adding salts (NaCl, MgCl₂) and supercritical CO₂ to the pore fluid phase, on the compaction creep behavior of wet granular calcite samples at 80°C and 30 MPa. Samples with grain sizes in the range 28-106 μm were used. Independent experiments on wet samples of the same grain size, loaded in the presence of CO₂ but without added salts, showed compaction creep due mainly to pressure solution [Liteanu *et al.*, in prep.]. The present control experiment (CO₂NaCl-0), performed on 28 μm grain size material under the same conditions showed similar creep rates (Figure 3.8) and similar microstructural evidence such as grain-to-grain indentations and suturing (Figure 3.9a) for pressure solution.

In the following, we examine how the addition of salts to the pore fluid phase influences compaction creep, with and without CO₂, and we attempt to explain the mechanisms responsible for creep. We go on to consider briefly the possible implications of long term CO₂ injection and storage on the creep of carbonate-rich reservoirs.

3.6.1 Effect of added NaCl on creep in the absence of supercritical CO₂ (NaCl Runs)

Comparison of our data obtained in the NaCl Runs (no supercritical CO₂ added, see Figure 3. 5b) with data on creep of wet samples compacted without added salt or CO₂ (Figure 3. 2, first stage) with similar grain size shows that addition of 1 M NaCl to the pore fluid results in a decrease in strain rate at otherwise fixed conditions. However, both sets of data show an increase in strain rate with increasing initial mean grain size (Figures 3.5c and 3.2). This trend is inconsistent with creep by IPS (equation 3.1), but consistent with most previous works on compaction by grain scale brittle failure [Brzesowsky, 1995; Liteanu *et al.*, in prep.; Wong *et al.*, 1997; Wong and Baud, 1999]. The present NaCl Runs (as well as the samples represented in Figure 3. 2) also show widespread microstructural evidence for grain scale

crushing or fracture. Though some of these microstructures may have originated in the pre-compaction stage, we infer that subcritical cracking at the grain scale was probably the main creep mechanism in our NaCl Runs (Figure 3. 9c), as well as in our earlier experiments without added salts or CO₂ (Figure 3. 2, first stage; [Litanu *et al.*, in prep.]). The implication is that addition of 1 M NaCl to the pore fluid in the NaCl Runs decelerated this creep process. Subcritical crack growth is known to be dominated in aqueous systems by fluid-solid interactions, such as crack tip dissolution, giving rise to subcritical crack growth mechanism known as stress corrosion cracking. Possible explanations for the deceleration of creep by this type of mechanism due to increased NaCl concentration include decelerated activity of water at crack tip or a reduction in crack tip dissolution rate coefficient.

3.6.2 Effect of added NaCl on creep in the presence of supercritical CO₂ (CO₂NaCl Runs)

Our earlier experiments outlined in Section 2.2 indicate that the addition of supercritical CO₂, in the absence of salts, enhances compaction creep of wet calcite aggregates by promoting pressure solution, in fine grained material, and subcritical (stress-corrosion) cracking in coarser samples (Figure 3.3). The present CO₂NaCl Runs also show faster creep than our NaCl Runs at fine grain size – 28 μm (Figure 3.8), though in coarser material there is no clear effect of CO₂ (cf. Figures 3.5b, 3.8). The positive dependence of strain rate on grain size seen in both NaCl and CO₂NaCl Runs suggests that creep is dominated by subcritical crack growth [Brzesowsky, 1995; Wong *et al.*, 1997; Wong and Baud, 1999]; see also Section 2.1.1). However, the microstructure of the CO₂NaCl samples shows evidence for both microcracking and subordinate pressure solution (indentation microstructures, Figures 3.9c, d). It seems likely, then, that creep in the CO₂NaCl Runs is enhanced relative to the NaCl Runs, at fine grain size, by a similar effect of CO₂ to that seen in NaCl free system (Section 2.2). The increase in creep rate might be a CO₂-induced acceleration of creep due to IPS and/or stress corrosion, seen only at fine grain sizes. The most likely reason for acceleration of such mechanisms is an increase in the solubility or dissolution rate of calcite accompanying dissolution of supercritical CO₂ in the pore fluid (Renard *et al.*, 2005). However, there is insufficient data on such effects under conditions of elevated pressure and temperature to warrant further speculation on this.

Compared with the control experiment CO₂NaCl-0, the CO₂NaCl Runs showed slower creep rates (Figure 3.8). The effect of adding NaCl to the Runs conducted in the presence of CO₂ was therefore similar to the effect of adding NaCl to Runs performed without CO₂ (see Section 3.5.1). The positive dependence of strain rate on grain size, and the brittle microstructural signatures seen in the present CO₂NaCl experiments, once again suggest that subcritical crack growth and time-dependent grain failure controlled compaction creep in these Runs.

However, the effect of NaCl concentration on creep rate at the fixed CO₂ pressure of 10 MPa in the CO₂NaCl Runs raises questions. We note from Figure 3.7b that increasing the

NaCl content of the pore fluid from 0 to 0.6 M leads to a decrease in strain rate at fixed strain. Further increase in NaCl concentration produced an increase in strain rate (Figure 3.7b). Since our CO₂NaCl-0 control sample exhibited a microstructure consistent with dominant IPS (and falls in the IPS creep regime inferred from our earlier experiments, see Figure 3.3), and since the NaCl bearing CO₂NaCl Runs showed microcracking with only minor evidence for intergranular dissolution, as well as positive grain size dependence of creep rate, we suggest that increasing the NaCl content in the CO₂NaCl Runs first slows down pressure solution (first step in Figure 3.7b) but ultimately speeds up microcracking sufficiently to become the dominant mechanism (increasing strain rate portion, Figure 3.7b).

It remains hard to explain in detail why the addition of NaCl to the pore fluid in the presence of 10 MPa CO₂ might slow down pressure solution and speed up microcracking. Possibilities include the following competing effects: a) the decrease in solubility of CO₂ in increasingly saline solutions [Duan and Sun, 2003], b) the increase in solubility of calcite with addition NaCl concentration [Gledhill and Morse, 2006; He and Morse, 1993] and c) the effects of CO₂ and NaCl on the dissolution and precipitation coefficient rate for calcite. Data on the effects of CO₂ and NaCl on calcite dissolution/precipitation kinetics under relevant conditions are few, conflicting and subject to debate. Dissolution rates have been reported to increase due to the addition of salts [Gledhill and Morse, 2006], whereas other studies suggest little importance [Buhmann and Dreybrodt, 1987; Pokrovsky et al., 2005]. A considerable amount of data exists in the literature on the effects of temperature and salinity at ambient conditions. However, none of the previous studies investigated the dissolution rate of calcite, at conditions similar to our experiments. Up to date the only investigation of calcite dissolution at high CO₂ partial pressure [Pokrovsky et al., 2005] suggests that increasing CO₂ pressure led to an increase of calcite dissolution. However it has a limited effect on the rate of dissolution, only up to 5 MPa CO₂ pressure. Moreover, the salinity of the solution was found to have only a minor effect at a constant pH. The presence of NaCl and an increase of the ionic strength of the solution effects on the precipitation of calcite, are also subject to debate [Bischoff, 1968; He and Morse, 1993; Walter, 1986; Zhang and Dawe, 2000; Zuddas and Mucci, 1994]. To explain our data, it seems that new geochemical data are needed on the effects of NaCl and CO₂ on calcite solubility and dissolution/precipitation kinetics at upper crustal pressure and temperature.

3.6.3 Effect of added MgCl₂ on creep in the presence of supercritical CO₂ (CO₂MgCl₂ Runs)

As observed in the case of NaCl, addition of MgCl₂ to the pore fluid, in the presence of supercritical CO₂ resulted in a decrease of strain rate at small MgCl₂ concentration (1 M), in comparison with the control Run. However, increasing the concentration to 2 M lead to a significant increase in the strain rate (Figure 3.8), in comparison with the same salt-free control Run CO₂NaCl-0. The microstructural evidence for microcracking, with limited grain contact dissolution, suggests that compaction creep of the samples CO₂MgCl₂ occurred mainly by subcritical crack growth.

Literature data indicate that the presence of magnesium ion leads to a decrease in calcite

dissolution rate at circumneutral conditions [Berner, 1975; Buhmann and Dreybrodt, 1987; Gutjhar et al., 1996]. However, its effect is unclear under acidic conditions [Alkattan et al., 2002]. Moreover, previous studies investigating the compaction creep of CO₂-free calcite aggregates [Zhang and Spiers, 2005b] found that pressure solution creep is slowed down by addition of MgCl₂ to the pore fluid. Our samples seem to reflect such a decrease in creep rate at low MgCl₂ concentrations. However, the creep rate increases with increasing MgCl₂ concentrations, while the observed microstructures suggest that the compaction of the samples occurred by grain scale fracturing, i.e. by stress corrosion cracking.

From these findings we can only conclude that the presence of MgCl₂ at small concentrations (~ 1 M) in the pore fluid produces a decrease in the compaction rate of calcite aggregates, possibly by reducing the contribution of IPS to creep. At higher concentrations, MgCl₂ addition seems to speed up compaction by stress corrosion cracking. We are not aware of any independent data that could be used to test this hypothesis further.

3.7 Implications

Injection of CO₂ into carbonate reservoir rocks will initially lead to vertical poroelastic expansion of the formation, as a result of the increase in pore pressure ($\sigma_e = \sigma - P_p$). This will be followed by some degree of compaction caused by straightforward dissolution of the rock formation as the system attempts to re-equilibrate chemically. Our results provide insight into the additional creep effects that can be expected during long-term CO₂ storage in depleted reservoirs with pore fluids of various salinities.

Pore fluids in sedimentary rocks show a wide range of salinities, and vary by as much as 5 orders of magnitude in salts content, from dilute waters to brines with salinities up to 600 g·l⁻¹ [Case, 1945; Gledhill and Morse, 2006]. Formation brines are generally a mixture of salts, mainly NaCl and MgCl₂. Current CO₂ injection projects, such as Sleipner, Norway [Portier and Rochelle, 2005] and Weyburn, Canada [Emberlery, 2005], contain reservoir brines with NaCl and MgCl₂ concentrations varying from 0.5 M to 1 M, and 0.01 M to 0.03 M, respectively. From our results for NaCl and MgCl₂-bearing fluids with concentrations up to 1 M, (cf. Figure 3.5b and Figure 3.8), we infer that injection of CO₂ into carbonates with similar formation fluid salinities might increase creep rates by up to ten times, as a result of accelerated microcrack growth and grain failure. This ten-fold increase is relative to background creep rates under the same conditions without CO₂. In the short term, this will be affected by poroelastic expansion, but in long term may lead to significant creep strains. Our findings also indicate that the increase in compaction rates expected for CO₂ injection into salt-free systems (i.e. 1 to 2 orders of magnitude, see Figure 3.2), is reduced by about ten times as a result of pore fluid salinity around 1 M NaCl, probably due to inhibition of contributions to creep by pressure solution. Overall, modest salt concentrations up to 1 M will likely reduce the long-term deformation effects of CO₂ storage in carbonates. However, it remains difficult to quantify the absolute rate of compaction creep of specific carbonate reservoirs in the context of CO₂ storage, as compaction behaviour is a strong function of variables such as porosity and other microstructural and compositional factors, as well as

pore fluid salinity. This means that site-specific investigations of the response of the local rocks will always be necessary. Nonetheless our results do help illuminate what creep processes can be activated and/or inhibited in carbonate reservoirs or aquifers as a consequence of CO₂ storage, or in other carbonate formations in which CO₂ might unwantedly leak.

3.8 Conclusions

We have performed compaction creep tests on wet granular calcite aggregates with grain sizes in the range of 28 – 106 μm, under simulated reservoir conditions (80°C and 30 MPa) in the absence or in the presence of supercritical CO₂, with various salt (NaCl and MgCl₂) concentrations (0.6-3 M). Our main findings can be summarized as follows:

1. Addition of NaCl to the pore fluid in samples compacted both without and with supercritical CO₂ causes a reduction in compaction creep rate at low concentrations (0.6-1 M NaCl).
2. In samples tested with supercritical CO₂, this effect is most marked at fine grain size resulting in a reduction in creep rate of up to 10 times in material with 28 μm grain size. As NaCl concentration is increased to values of 2-3 M, creep rate increase to approach and surpass NaCl-free levels.
3. From the grain size dependence of creep rate seen in samples tested with and without CO₂, and from our microstructural observations, we suggest that the effect of increasing NaCl concentration in samples tested with supercritical CO₂ is one of reducing IPS contribution to deformation at low NaCl concentrations while increasing the role of subcritical crack growth and grain scale failure/crushing at higher concentrations. Neither mechanism dominates totally in our CO₂ experiments, but the relative importance seems to change with changing NaCl content.
4. The presence of MgCl₂ in concentrations around 1 M in the pore fluid phase was also found to result in a decrease of the compaction rate in calcite aggregates, compacted in the presence of supercritical CO₂, again higher concentrations speeded up the compaction. We infer a similar effect of MgCl₂ on the relative importance of IPS and subcritical cracking as attributed to NaCl.
5. Under in-situ conditions, excluding the initial poroelastic expansion and straightforward dissolution, injection of CO₂ into highly porous carbonate reservoirs with pore fluid salinities up to 1 M can potentially increase the long term creep rates by up to ten times compared with injecting CO₂-free fluid. Predicting the absolute rate of creep in a given carbonate reservoir remains highly problematic, and site specific studies of host rock mechanical behaviour will always be necessary.

Acknowledgements:

We thank Dr. Catherine Noiriel and two anonymous reviewers for their constructive comments and suggestions for improving this article. We would also like to thank Colin Peach for much advice in conducting the experiments and also Peter van Kreiken, Gert Kastelein and Eimert de Graaff for the technical support provided in the laboratory.

REFERENCE LIST

- Alkattan, M., et al. (2002), An experimental study of calcite dissolution rates at acidic conditions and 25 °C in the presence of NaPO₃ and MgCl₂, *Chemical Geology*, 190(1-4), 291-302.
- Ambrose, W. A., et al. (2008), Geologic factors controlling CO₂ storage capacity and permanence: case studies based on experience with heterogeneity in oil and gas reservoirs applied to CO₂ storage, *Environmental Geology* 54, 1619-1633.
- Atkinson, B. K. (1982), Subcritical crack propagation in rocks: theory, experimental results and applications. , *Journal of Structural Geology* 4, 41-56.
- Atkinson, B. K. (1984), Subcritical crack growth in geological materials., *Journal of Geophysical Research*, 89, 4077-4114.
- Austad, T., et al. (2005), Seawater as IOR fluid in fractured chalk. , in *Oilfield Chemistry Symposium*, edited, PE Paper 93000, Houston, TX.
- Bachu, S. (2000), Sequestration of CO₂ in geological media: criteria and approach for site selection in response to climate change, *Energy Conversion Management* 41, 953-970.
- Benson, S. M. (2000), Advances in geologic sequestration: identifying and addressing key issues., *Geological Society of America* 32(A200).
- Berner, R. A. (1975), The role of magnesium in the crystal growth of calcite and aragonite from sea water, *Geochimica et Cosmochimica Acta*, 39(4), 489-494, IN483, 495-504.
- Bischoff, J. L. (1968), Kinetics of Calcite Nucleation: Magnesium Ion Inhibition and Ionic Strength Catalysis, *J. Geophys. Res.*, 73.
- Brzesowsky, R. H. (1995), Micromechanics of sand grain failure and sand compaction, 180 pp, Universiteit Utrecht, The Netherlands, Utrecht.
- Buhmann, D., and W. Dreybrodt (1987), Calcite dissolution kinetics in the system H₂O---CO₂---CaCO₃ with participation of foreign ions, *Chemical Geology*, 64(1-2), 89-102.
- Busenberg, E., and L. N. Plummer (1986), A comparative study of the dissolution and crystal growth kinetics of calcite and aragonite., in *Studies in Diagenesis*. , edited by M. F.A., pp. 139-168., U.S. Geological Survey Bulletin Case, L. C. (1945), Exceptional Silurian brine near Bay City, Michigan., *American Association Petroleum Geology Bulletin* 29, 567-570.
- Chester, F. M., et al. (2007), Subcritical creep compaction of quartz sand at diagenetic conditions: Effects of water and grain size, *J. Geophys. Res.*, 112.
- Chester, J. S., et al. (2004), Mechanisms of compaction of quartz sand at diagenetic conditions, *Earth and Planetary Science Letters*, 220(3-4), 435-451.
- Chiaromonte, L., et al. (2008), Seal integrity and feasibility of CO₂ sequestration in the Teapot Dome EOR pilot: Geomechanical site characterization. , *Journal of Environmental Geology* 54, 1667-1675.
- Chuhan, F. A., et al. (2003), Experimental compression of loose sands: relevance to porosity reduction during burial in sedimentary basins, *Canadian Geotechnical Journal* 40, 995-1011.
- Damen, K., et al. (2005), Identification of early opportunities for CO₂ sequestration-worldwide screening for CO₂-EOR and CO₂-ECBM projects. , *Energy* 30, 1931-1952.
- David, C., et al. (2001), Mechanical compaction, microstructures and permeability evolution in sandstones, *Physics and Chemistry of the Earth, Part A: Solid Earth and Geodesy*, 26(1-2), 45-51.
- de Meer, S., and C. J. Spiers (1999), Influence of pore-fluid salinity on pressure solution creep in gypsum, *Tectonophysics*, 308(3), 311-330.
- Den Brok, S. W. J., and C. J. Spiers (1991), Experimental evidence for water weakening of quartzite by microcracking plus solution-precipitation creep, *Journal of the Geological Society*, 148(3), 541-548.
- Dewers, T., and P. Ortoleva (1990), A coupled reaction/transport/mechanical model for intergranular pressure solution, stylolites, and differential compaction and cementation in clean sandstones, *Geochimica et Cosmochimica Acta*, 54(6), 1609-1625.
- Dewers, T., and A. Hajash (1995), Rate laws for water-assisted compaction and stress-induced water-rock interaction in sandstones, *J. Geophys. Res.*, 100(B7), 13093-13112. .
- Duan, Z., and R. Sun (2003), An improved model calculating CO₂ solubility in pure water and aqueous NaCl solutions from 273 to 533 K and from 0 to 2000 bar, *Chemical Geology*, 193(3-4), 257-271.
- Dunning, J., et al. (1994), The role of the chemical environment in frictional deformation: Stress corrosion cracking and comminution, *Pure and Applied Geophysics*, 143(1), 151-178.
- Ellis, A. (1959), The solubility of calcite in carbon dioxide solutions, *American Journal of Science*, 257, 354-365.
- Emberlery, S., Hutcheon, I., Shevalier, M., Durocher, K., Mayer, B., Gunter, W.D., Perkins, E.H. (2005),

Monitoring of fluid-rock interaction and CO₂ storage through produced fluid sampling at the Weyburn CO₂-injection enhanced oil recovery site, Saskatchewan, Canada., *Applied geochemistry* 20(6), 1131-1157.

Enick, R. M., and S. M. Klara (1990), CO₂ solubility in water and brine under reservoir conditions, *Chemical Engineering Communications*, 90(1), 23 - 33.

Ennis-King, J., and L. Paterson (2003), Role of convective mixing in the long-term storage of carbon dioxide in deep saline formations. , in *SPE Annual Technical Conference and Exhibition*, edited, SPE, Denver, Colorado, U.S.A.

Fischer, M., et al. (2006), Origins of CO₂ in permian carbonate reservoir rocks (Zechstein, Ca2) of the NW-German Basin (Lower Saxony), *Chemical Geology*, 227(3-4), 184-213.

Fredrich, J., and T.-f. Wong (1986), Micromechanics of thermally induced cracking in three crustal rocks, *Journal of Geophysical Research*, 91(B12), 12 743-712 764.

Fredrich, J. T., et al. (1989), Micromechanics of the Brittle to Plastic Transition in Carrara Marble, *J. Geophys. Res.*, 94(B4), 4129-4145.

Gaus, L., et al. (2002), Preliminary modeling of the geochemical impact of CO₂ injection on the caprock at Sleipner, *BRGM Report BRGM/RP-52081-FR*, 43.

Gledhill, D. K., and J. W. Morse (2006), Calcite solubility in Na-Ca-Mg-Cl brines, *Chemical Geology*, 233(3-4), 249-256.

Gozalpour, F., et al. (2005), CO₂ EOR and storage in oil reservoirs. , *Oil and Gas Science and Technology - Rev IFP*, 60(3), 537-546.

Gratier, J. P., and R. Guiguet Irigm (1986), Experimental pressure solution-deposition on quartz grains: the crucial effect of the nature of the fluid, *Journal of Structural Geology*, 8(8), 845-856.

Gundersen, E., et al. (2002), Coupling between pressure solution creep and diffusive mass transport in porous rocks, *J. Geophys. Res.*, 107.

Gutjhar, A., et al. (1996), Studies on the growth and dissolution kinetics of the CaCO₃ polymorphs calcite and aragonite: I. Growth and dissolution rate in water., *Journal of Crystal Growth* 158, 269-309.

Hanor, J. S. (1994), Origin of saline fluids in sedimentary basins, in *Geofluids: Origin, Migration, and Evolution of Fluids in Sedimentary Basins.*, edited by J. Parnell, pp. 151-174, Geological Society Publishing House, Bath.

He, S., and J. W. Morse (1993), The carbonic acid system and calcite solubility in aqueous Na-K-Ca-Mg-Cl-SO₄ solutions from 0 to 90°C, *Geochimica et Cosmochimica Acta*, 57(15), 3533-3554.

Hellmann, R., et al. (2002), Experimental pressure solution of chalk in aqueous solutions: Part 1. Deformation behaviour and chemistry., in *Water-Rock Interactions, Ore Deposits, and Environmental Geochemistry: A Tribute to David A. Crerar*, edited by T. G. Society.

Hickman, S. H., and B. Evans (1995), Kinetics of pressure solution at halite-silica interfaces and intergranular clay films, *J. Geophys. Res.*, 100, 13,113-113,132.

International Panel on Climate Control, I. (Ed.) (2005), *Carbon Dioxide Capture and Storage. Special Report.* , 442 pp., Cambridge University Press, Cambridge, United Kingdom and New York, NY, USA.

Izgec, O., et al. (2008), CO₂ injection into saline carbonate aquifer formations II: Comparison of numerical simulations to experiments. , *Transport in Porous Media*, 73, 57-74. .

Jaeger, C. J., et al. (2007), *Fundamentals of rock mechanics*, Wiley-Blackwell.

Karner, S. L., et al. (2005), Laboratory deformation of granular quartz sand: Implications for the burial of clastic rocks, *American Association of Petroleum Geology Bulletin*, 89, 603-625.

Le Guen, Y., F. Renard, R. Hellmann, E. Brosse, M. Collombet, D. Tisserand, and J.-P. Gratier (2007), Enhanced deformation of limestone and sandstone in the presence of high Pco₂ fluids, *Journal of Geophysical Research*, 112(B05421).

Lehner, F. K. (1990), Thermodynamics of rock deformation by pressure solution., in *Deformation processes in minerals, ceramics and rocks*, edited by D. J. Barber, Meredith, P.G., pp. 296-333, Unwin Hyman, London.

Lewicki, J., et al. (2007), Natural and industrial analogues for leakage of CO₂ from storage reservoirs: identification of features, events, and processes and lessons learned, *Environmental Geology*, 52(3), 457-467.

Liteanu, E., et al. (in prep.), The effect of CO₂ on creep of wet calcite aggregates, *Journal of Geophysical Research*.

Lockner, D. A., and S. A. Stanchits (2002), Undrained poroelastic response of sandstones to deviatoric stress change, *J. Geophys. Res.*, 107.

Madland, M. V., et al. (2006), The influence of CO₂ gas and carbonate water on the mechanical stability of chalk, *Journal of Petroleum Science and Engineering*, 51(3-4), 149-168.

Morse, J. W., and F. T. Mackenzie (1990), *Geochemistry of Sedimentary Carbonates*, 707 pp., Elsevier, Amsterdam.

Ngwenya, B. T., et al. (2001), A constitutive law for low-temperature creep of water-saturated sandstones, *J. Geophys. Res.*, 106.

- Niemeijer, A. R., et al. (2002), Compaction creep of quartz sand at 400-600°C: experimental evidence for dissolution-controlled pressure solution, *Earth and Planetary Science Letters*, 195(3-4), 261-275.
- Noiriel, C., et al. (2005), Évolution des paramètres hydrauliques et de la microgéométrie d'un calcaire pendant sa dissolution par une eau acide, *Oil & Gas Science and Technology - Rev. IFP*, 60(1), 177-192.
- Paterson, M. S., and T.-f. Wong (2005), *Experimental Rock Deformation - The Brittle Field.*, 2nd Edition ed., Springer-Verlag, New York.
- Plummer, L. N., et al. (1978), The kinetics of calcite dissolution in CO₂-water systems at 5 degrees to 60 degrees C and 0.0 to 1.0 atm CO₂, *Am J Sci*, 278(2), 179-216.
- Plummer, L. N., and E. Busenberg (1982), The solubilities of calcite, aragonite and vaterite in CO₂-H₂O solutions between 0 and 90°C, and an evaluation of the aqueous model for the system CaCO₃-CO₂-H₂O, *Geochimica et Cosmochimica Acta*, 46(6), 1011-1040.
- Pokrovsky, O. S., and J. Schott (2002), Surface Chemistry and Dissolution Kinetics of Divalent Metal Carbonates, *Environmental Science & Technology*, 36(3), 426-432.
- Pokrovsky, O. S., et al. (2005), Dissolution kinetics of calcite, dolomite and magnesite at 25 °C and 0 to 50 atm pCO₂, *Chemical Geology*, 217(3-4), 239-255.
- Portier, S., and C. Rochelle (2005), Modelling CO₂ solubility in pure water and NaCl-type waters from 0 to 300 °C and from 1 to 300 bar: Application to the Utsira Formation at Sleipner, *Chemical Geology*, 217(3-4), 187-199.
- Preston, C., Monea, M., Jazrawi, W., Brown, K., Whittaker, S., White, D., Law, D., Chalaturnyk, R., Roston, B. (2005), IEA GHG Weyburn CO₂ monitoring and storage project, *Fuel Processing Technology*, 86(15), 1547-1568.
- Renard, F., et al. (2005), Numerical modeling of carbon dioxide sequestration on the rate of pressure solution creep in limestone: Preliminary results, *Oil & Gas Science and Technology*, 60, 381-399
- Rosenbauer, R. J., and T. Koksalan (2002), Experimental determination of the solubility of CO₂ in electrolytes: application to CO₂ sequestration in deep-saline aquifers, in *Geological Society of America annual meeting*, edited, Denver, Colorado.
- Rutter, E. H. (1976), The kinetics of rock deformation by pressure solution, *Philosophical Transactions of the Royal Society of London*, 283, 203- 219.
- Rutter, E. H. (1983), Pressure solution in nature, theory and experiment, *Journal of the Geological Society*, 140(5), 725-740.
- Segnit, E. R., et al. (1962), The solubility of calcite in aqueous solutions—I The solubility of calcite in water between 75° and 200° at CO₂ pressures up to 60 atm, *Geochimica et Cosmochimica Acta*, 26(12), 1301-1331.
- Sjöberg, E. L. (1978), Kinetics and mechanism of calcite dissolution in aqueous solutions at low temperatures, *Stockholm Contribution in Geology*, 32, 1-96.
- Sjöberg, E. L., and D. T. Rickard (1984), Temperature dependence of calcite dissolution kinetics between 1 and 62°C at pH 2.7 to 8.4 in aqueous solutions, *Geochimica et Cosmochimica Acta*, 48(3), 485-493.
- Spiers, C. J., et al. (1990), Experimental determination of constitutive parameters governing creep of rock salt by pressure solution, *Geological Society, London, Special Publications*, 54(1), 215-227.
- Spiers, C. J., et al. (2004), Kinetics of rock deformation by pressure solution and the role of thin aqueous films, in *Physicochemistry of Water in Geological and Biological Systems-Structures and Properties of Thin Aqueous Films*, edited by S. Nakashima, pp. 129-158, Universal Acad. Press, Tokyo.
- Tada, R., and R. Siever (1986), Experimental knife-edge pressure solution of halite, *Geochimica et Cosmochimica Acta*, 50(1), 29-36.
- Walter, L. M. (1986), Relative efficiency of carbonate dissolution and precipitation during diagenesis: A progress report on the role of solution chemistry. , *Journal of Sedimentary Petrology*, 56, 1-11.
- Wang, H. F. (1993), Quasi-static poroelastic parameters in rock and their geophysical applications, *Pure and Applied Geophysics*, 141(2), 269-286.
- Wang, H. F. (1997), Effects of deviatoric stress on undrained pore pressure response to fault slip, *Journal of Geophysical Research*, 102(17), 943-950.
- Wawersik, W. R., et al. (2001), Terrestrial sequestration of CO₂: An assessment of research needs, *Advances in Geophysics*, 43, 97-177.
- White, C. M., et al. (2005), Sequestration of carbon dioxide in coal with enhanced coalbed methane recovery—a review, *Energy and Fuels* 19, 659-724.
- Wong, T.-f., et al. (1997), The transition from brittle faulting to cataclastic flow in porous sandstones: Mechanical deformation, *J. Geophys. Res.*, 102.
- Wong, T.-f., and P. Baud (1999), Mechanical Compaction of Porous Sandstone, *Oil & Gas Sci. and Tech. - Rev. IFP*, 54(6), 715-727.
- Xiao, X., and B. Evans (2003), Shear-enhanced compaction during non-linear viscous creep of porous calcite-quartz aggregates, *Earth and Planetary Science Letters*, 216(4), 725-740.

Xu, T., et al. (2007), Numerical modeling of injection and mineral trapping of CO₂ with H₂S and SO₂ in a sandstone formation, *Chemical Geology*, 242(3-4), 319-346.

Zhang, X., and C. J. Spiers (2005a), Effects of phosphate ions on intergranular pressure solution in calcite: An experimental study, *Geochimica et Cosmochimica Acta*, 69(24), 5681-5691.

Zhang, X., and C. J. Spiers (2005b), Compaction of granular calcite by pressure solution at room temperature and effects of pore fluid chemistry, *International Journal of Rock Mechanics and Mining Sciences*, 42(7-8), 950-960.

Zhang, Y., and R. A. Dawe (2000), Influence of Mg²⁺ on the kinetics of calcite precipitation and calcite crystal morphology, *Chemical Geology*, 163(1-4), 129-138.

Zhu, W., et al. (1999), Densification and permeability reduction in hot-pressed calcite: A kinetic model, *J. Geophys. Res.*, 104.

Zoback, M. D., and J. C. Zinke (2002), Production-induced normal faulting in the Valhall and Ekofisk oil fields, *Pure and Applied Geophysics*, 159, 403-420.

Zubtsov, S., et al. (2005), Single-contact pressure solution creep on calcite monocrystals, *Geological Society, London, Special Publications*, 243(1), 81-95.

Zuddas, P., and A. Mucci (1994), Kinetics of calcite precipitation from seawater: A classic chemical kinetics description for strong electrolyte solutions., *Geochim. Cosmochim. Acta*, 58, 4353-4362.

Chapter 4

ABSTRACT

Reduction of compressive strength by injection of water into chalk is a well-known mechanism responsible for increased compaction in chalk reservoirs. This raises the question of whether such effects might be enhanced in the context of long-term storage of CO₂ or of CO₂ injection for enhanced oil and gas recovery (EOR/EGR) purposes. Therefore, data regarding the effect of supercritical CO₂ on the mechanical behaviour of chalk are needed. The effect of supercritical CO₂ on the short-term failure behaviour of chalk was accordingly investigated by means of conventional triaxial deformation experiments, performed on Maastrichtian chalk cores under dry conditions, in the presence of saturated chalk solution and using CO₂-saturated solution at temperatures simulating reservoir conditions (20–80°C) and effective confining pressures up to 7 MPa. Increasing temperature from 20 to 80°C did not show any significant effects on the strength of the dry samples. Addition of aqueous solution to the samples led to drastic weakening of the chalk, the effect being more pronounced at high effective confining pressures ($P_{\text{eff}} > 3$ MPa). Addition of 10 MPa supercritical CO₂ to wet samples did not produce any significant additional effect in comparison with the wet samples. All samples showed a yield strength envelope characterized by shear failure at low effective mean stresses giving way to a compaction cap at high mean stresses. The weakening effect of aqueous solution was explained in terms of a reduction in frictional resistance of the material, due to water-enhanced grain-contact cracking, and perhaps pressure solution, with a possible contribution by disjoining pressure effects caused by water adsorption. While CO₂ does not seem to reduce short-term failure strength of chalk, processes such as intergranular pressure solution have to be considered for assessing mechanical stability of chalk in the context of long-term CO₂ storage or EOR/EGR operations.

Based on:

Liteanu E., Spiers C.J., Bresser J.H.P. - The influence of water and supercritical CO₂ on the failure behaviour of chalk. *Tectonophysics* (submitted)

4.1 Introduction

Carbonate rocks form important hydrocarbon reservoirs, hosting some 40-60 % of known oil and gas reserves worldwide [Roehl, 1985]. Chalks such as those found in the Cretaceous of the North Sea represent a particularly interesting type of carbonate reservoir rock, as they are typically characterized by high intergranular porosity (35-45 %) and low permeability (a few mD or less) [Teufel et al., 1991; Gutierrez et al., 2000; Homand and Shao, 2000; Risnes, 2001; Risnes et al., 2005; Madland et al., 2006]. This means that chalks have a high oil and gas capacity, but are relatively difficult to produce from. In recent years, the possibility of injecting CO₂ into depleted chalk reservoirs has been considered as a potential means of achieving enhanced oil and gas recovery (EOR and EGR) from such reservoirs [Jensen et al., 2000; Schroeder et al., 2001; Gozalpour et al., 2005; Meyer, 2007; Ambrose et al., 2008]. This in turn points to the possibility of using depleted chalk reservoirs for geological storage of CO₂, either in combination with EOR/EGR or independently. However, many chalks show marked weakening when water is injected, leading to water-enhanced compaction [Teufel et al., 1991; Risnes and Flaageng, 1999; Homand, 2000; Risnes, 2001; Risnes et al., 2005]. Such effects are well known from the Ekofisk and Valhall fields in the North Sea, where subsidence of about 10 m occurred as a consequence of water injection for EOR purposes [Teufel et al., 1991; Risnes, 2001]. This raises the question of what might be the coupled chemical-mechanical effects of CO₂ injection be on chalk reservoirs or on chalk formations into which CO₂ might migrate from deeper CO₂ storage systems.

Previous work on water-weakening of chalk has led to hypotheses of chemical weakening related to enhanced dissolution [Newman, 1983], physical weakening due to capillary or surface forces acting at wetted grain contacts [Delage et al., 1996; Strand et al., 2006; Korsnes et al., 2008], or coupled physico-chemical effects related to intergranular pressure solution or water-enhanced grain-scale microcracking [Hellmann et al., 2002a; Hellmann et al., 2002b; Madland et al., 2006]. Studies concerning the effects of CO₂ on the mechanical strength of chalk suggest no significant short term effect of supercritical CO₂ [Schroeder et al., 2001]. Other indicate long-term weakening and creep of chalk by CO₂-enriched water [Madland et al., 2006; Korsnes, 2008; Korsnes et al., 2008]. However, systematic investigations on the effect of supercritical CO₂ on the failure behaviour of chalks are lacking, as are detailed microstructural studies of operative deformation mechanisms in wet and wet/CO₂ samples. The mechanism of water-weakening in chalk thus remains controversial, and the possible effects of supercritical CO₂ unclear.

This paper aims to clarify the effect of supercritical CO₂ on the compressive strength of chalk by means of triaxial compression experiments performed on cylindrical chalk cores. The main questions addressed are: a) does injection of supercritical CO₂ into wet chalks weaken the material beyond the weakening effect of water alone? and b) if so, what is the responsible mechanism? The experiments were performed on dry, wet and wet/CO₂-saturated Maastrichtian chalk samples at temperatures of 20 and 80°C, effective confining

pressures in the range 0.5 to 7 MPa and pore fluid pressures up to 10 MPa. The data were used to construct failure envelopes, which provide a basis for assessing mechanical integrity of chalks during CO₂ storage and EOR operations.

4.2 Experimental method

4.2.1 Material

All of the present triaxial tests were performed on Maastrichtian age chalk retrieved from the Sibbergroeve underground quarry, operated by ENCI near Maastricht, The Netherlands. The chalk appears to be relatively homogeneous on the cm to m scale. At the microscopic level, it is mainly composed of bioclastic coccospheres (~100 μm diameter) consisting of micron-sized coccolith fragments, which are densely bound together to form the large grains. The material consists of ~98.5 % calcite and ~ 1.5 % silica [Hjuler and Fabricius, 2009]. Measurements based on the weight difference between water-saturated and dried cylindrical samples, showed the porosity of the material to be ~ 42 %. Permeability tests performed on undeformed samples at room temperature and at a reference confining pressure of 1 MPa, using a constant pressure difference of 0.2-0.3 MPa yielded values in the range of $2 \times 10^{-15} \text{ m}^2$ to $5 \times 10^{-15} \text{ m}^2$. The material was chosen as being representative of the Maastrichtian chalk formations present in the stratigraphic sequence overlying the older clastic reservoirs considered for long-term CO₂ storage in The Netherlands, though recent very recent work [Hjuler and Fabricius, 2009] suggests that it may have suffered more meteoric diagenesis than most such chalks.

4.2.2 Preparation of samples and pore fluids

Cores measuring 35 mm in diameter were drilled from a large chalk block and cut to a length of 75 mm to obtain right cylindrical samples. The samples were then oven dried at 105°C for 24 hours [Gutierrez *et al.*, 2000], until a constant weight was obtained. This was considered as being the dry state of the samples, although it has been previously shown that despite such drying procedures, a small amount of water (around 0.2 %) is generally still present in the chalk [Risnes *et al.*, 2005].

The samples were deformed dry and using the following pore fluids: a) aqueous solution in equilibrium with the samples (“wet tests”) and b) CO₂-saturated solution in equilibrium with the samples (“wet/CO₂ tests”). The samples employed in the dry experiments were stored after drying, in airtight containers, until they were used in the triaxial tests. In the wet tests, the chalk cores were pre-saturated under vacuum with chalk solution and then stored, submerged in the fluid phase, in airtight containers. The solution was prepared by stirring crushed chalk with water for 48 hours, which is known to be sufficient to produce a solution that is saturated with CaCO₃ [Pokrovsky and Schott, 2002]. Prior to testing in the triaxial cell, additional pore fluid was added to the wet samples, to ensure complete saturation and to prevent drying out during test assembly. In the wet/CO₂ tests, the pre-saturated cores were injected with supercritical CO₂ upon emplacement in the triaxial cell, until constant CO₂ pressure (10 MPa) and constant pore fluid volume were attained at the

desired experimental conditions. This equilibration process generally took ~ 4 hours.

4.2.3 Experimental apparatus and data acquisition

A conventional, triaxial deformation apparatus, designed for axi-symmetric compression of cylindrical samples was used in this study. The apparatus is shown schematically in Figure 4.1 and is described in detail by *Peach* [1991] and *Peach and Spiers* [1996]. It consists of an externally heated pressure vessel, which uses silicone oil as confining medium, connected via high-pressure tubing to an auxiliary pressure vessel, such that the system volume is nominally constant. Axial load is applied to the sample by means of a pressure-balanced piston assembly, located between the two pressure vessels. During loading of the sample, the confining pressure is maintained constant by a servo-controlled volumetric pump or volumometer.

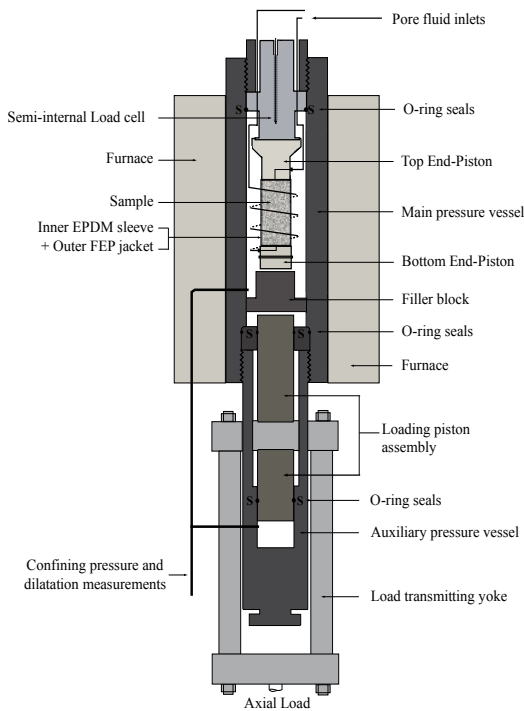


Figure 4.1. Semi-schematic representation of the triaxial testing machine used in this study.

Confining pressure is measured using a Jensen pressure transducer (100 MPa range, resolution ± 0.02 MPa). Axial load on the sample is measured using a DVRT-based, semi-internal load cell located at the top of the vessel (400 kN range, resolution ± 35 N, DVRT = differential variable reluctance transformer). Piston displacement is measured externally (at the yoke in Figure 4.1) using a high-precision LVDT (linear variable differential transformer, 100 mm range, resolution ± 0.8 μm). Aqueous pore fluid is introduced into the sample at fixed pressure via a pore pressure system, which is controlled by an independent servo-pump. The pore fluid pressure is measured using a second Jensen pressure transducer

(50 MPa pressure range, resolution ± 0.02 MPa). Supercritical CO_2 is introduced into solution-flooded samples at a pressure up of 10 MPa, using an ISCO 65 D servo-controlled syringe-pump, fitted with a Honeywell TJE pressure transducer (150 MPa range, resolution ± 0.012 MPa). The temperature of the external furnace is controlled by a proportional-integral-derivative, or PID, controller (400°C range, resolution $\pm 0.02^\circ\text{C}$) plus sheathed, type K thermocouple located in the windings. The temperature of the sample is measured using similar thermocouples located at the top and at the bottom of the sample.

In the present study, the signals corresponding to axial load, piston displacement, confining pressure, sample temperature, oil volume change, pore fluid pressure, pore fluid volume, CO_2 pressure and CO_2 volume change were logged by means of a PC equipped with a 12-bit National Instruments VI logger system. The raw displacement and volume-change data were accurately corrected for both axial and volumetric apparatus distortion and for thermal expansion/contraction effects in the confining and pore fluid systems, using pre-determined calibrations. Final processing yielded differential stress ($\sigma_1 - \sigma_3$), axial strain (ϵ), volumetric strain (ϵ_v) and axial strain rate ($\dot{\epsilon}$) values as functions of time (t).

4.2.4 Sample assembly and testing procedure

The experiments were performed at a constant displacement rate yielding a near constant strain rate ($\dot{\epsilon}$) of $\sim 5 \times 10^{-5} \text{ s}^{-1}$, using samples subjected to four different sets of conditions:

1. Dry samples deformed at 20°C , at confining pressures (P_c) in the range 0.5-7 MPa.
2. Dry samples deformed at 80°C , at confining pressures (P_c) in the range 0.5-5 MPa.
3. Wet samples deformed at 80°C , at a pore fluid pressure (P_f) of 5 MPa and effective confining pressures (P_{eff}) in the range 0.5-5 MPa (wet tests).
4. Samples deformed wet at 80°C with the pore fluid in equilibrium with supercritical CO_2 at a pressure (P_f) of 10 MPa, and at effective confining pressures (P_{eff}) in the range 0.5-5 MPa (wet/ CO_2 tests).

Prior to testing, each sample was jacketed in an inner, CO_2 -resistant Ethylene Propylene Diene, M-class (EPDM) rubber sleeve, and an outer Fluorinated Ethylene Propylene (FEP) Teflon jacket to prevent leakage of the confining medium into the sample assembly. The sample was then located between the top and bottom end-pistons shown in Figure 4.1. Each piston face is radially and concentrically grooved and features a central bore connected to the pore fluid system, to allow fluid injection and to promote distribution of pore fluid over the sample ends. Perforated Teflon sheets with were placed between the end-pistons and the sample to reduce friction. The sample assembly was sealed against the end-pistons using a wire tournique method with underlying EPDM band countersunk in the end-piston surfaces. The completed sample assembly was subsequently connected to the removable load cell and pore fluid pipes, and the whole assembly inserted into the main pressure vessel (Figure 4.1). The setup was then heated up by means of the external furnace at an effective confining pressure of 0.5 MPa. When the desired temperature was reached (20 or 80°C), the (effective) confining pressure and pore fluid pressure assigned

for each test were applied.

In the experiments on dry samples, the pore fluid system was maintained open so that the samples were drained to air. In the wet experiments, when the samples reached the desired temperature, the pre-saturated cores were re-saturated with solution in equilibrium with chalk by briefly evacuating and then applying the pore fluid pressure (P_f) via the pore fluid system and a servo-pump. The confining pressure (P_c) was simultaneously increased such that the effective confining pressure ($P_{eff} = P_c - P_f$) exerted on the sample remained constant. In the wet/CO₂ experiments, supercritical CO₂ pressure was applied to the pre-saturated samples at a pressure of to 10 MPa, again adjusting the confining pressure so that the effective value remained fixed. When equilibrium was reached, the tests were started by loading the samples at the chosen constant displacement rate of 1.1 $\mu\text{m}/\text{sec}$, which resulted in a near-constant strain rate of $\sim 5 \times 10^{-5} \text{ s}^{-1}$.

The tests were run until shortly after the samples failed in a brittle manner, or until a strain of $\sim 2\text{-}2.5\%$ was reached in cases where samples showed semi-brittle or ductile strain-hardening behaviour. The tests were terminated by unloading the samples, by releasing the pore fluid pressure and the confining pressure, followed by cooling down of the machine and the sample. Finally, the samples were extracted from the testing machine, carefully removed from the jacket-piston assembly, oven dried at 60°C, vacuum impregnated with epoxy resin and thin-sectioned. The thin sections were subsequently polished for study using Scanning Electron Microscopy (SEM) and optical microscopy.

4.3 Results

All experiments reported here are listed in Table 4.1 along with the corresponding experimental variables and key data obtained from each experiment. Note that compressive stresses, compressive axial strains (ϵ), compressive strain rate () and dilatant volume changes (ϵ_v) are taken as positive throughout this paper. The principal compressive stresses are denoted as σ_i with $\sigma_1 > \sigma_2 = \sigma_3$. Axial differential stress is defined as the principal stress difference ($\sigma_1 - \sigma_3$). The peak strength (σ^*) is defined as the maximum differential stress ($\sigma_1 - \sigma_3$) supported by the sample. Failure is defined as the loss of strength of a given sample beyond the peak strength, while the yield stress (σ_y) is taken as the point of departure of the stress-strain curves from linearity, i.e. from (quasi-) elastic behaviour in the initial loading stage [Fredrich *et al.*, 1989]. Sample strength at 1 % axial strain ($\sigma_{1\%}$) was also recorded, as a method of representing the near steady-state strength of the samples attained either after failure or else after yield plus strain hardening. The (apparent) Young's modulus (E) of each sample was calculated using the linear, (quasi) elastic portion of the stress-strain curve.

4.3.1 Mechanical data and failure modes

4.3.1.1 Dry samples deformed at 20°C

The complete set of differential stress and volumetric strain versus axial strain curves

Sample ID	T [°C]	P_c [MPa]	P_{eff} [MPa]	P_f [MPa]	Pore fluid	σ_y [MPa]	σ^* [MPa]	$\sigma_{1\%}$ [MPa]	Final ax. strain [%]	Final e_v [%]	E [GPa]
<i>Dry samples deformed at 20°C</i>											
CDRY-0.5	20	0.5	0.5	-	Dry	4.29	4.67	-	0.95	-0.12	0.81
CDRY-1.5	20	1.5	1.5	-	Dry	4.89	5.81	4.79	2.13	-1.39	0.91
CDRY-3	20	3	3	-	Dry	4.27	5.44	5.30	2.93	-1.07	0.98
CDRY-5	20	5	5	-	Dry	3.31	†	4.59	2.89	-5.96	0.98
CDRY-7	20	7	7	-	Dry	0.66	†	1.41	3.60	-6.06	0.66
<i>Dry samples deformed at 80°C</i>											
HDRY-0.5	80	0.5	0.5	-	Dry	4.11	4.34	-	0.91	-0.27	0.72
HDRY-1	80	1	1	-	Dry	5.08	5.33	4.56	1.00	-2.15	0.77
HDRY-1.5	80	1.5	1.5	-	Dry	5.26	†	6.25	1.89	-1.93	0.95
HDRY-4	80	4	4	-	Dry	3.54	†	4.53	2.53	-5.60	0.93
HDRY-5	80	5	5	-	Dry	2.86	†	3.86	2.41	-4.84	0.91
<i>Wet samples deformed at 80°C</i>											
HWET-0.5	80	5.5	0.5	5	Wet	3.49	4.82	3.52	1.05	-3.53	1.49
HWET-1.5	80	6.5	1.5	5	Wet	3.29	†	5.02	2.06	-5.16	1.36
HWET-3	80	8	3	5	Wet	2.63	†	3.44	2.48	-6.71	0.80
HWET-5	80	10	5	5	Wet	0.99	†	1.49	1.61	-6.60	0.48
<i>Wet/CO₂ bearing samples deformed at 80°C</i>											
HCO ₂ -0.5	80	10.5	0.5	10	Wet/CO ₂	3.24	4.01	2.96	1.02	-0.96	0.83
HCO ₂ -1.5	80	11.5	1.5	10	Wet/CO ₂	3.70	4.48	3.52	1.85	-3.63	0.84
HCO ₂ -2.5	80	12.5	2.5	10	Wet/CO ₂	2.43	3.03	3.02	2.21	-3.35	0.75
HCO ₂ -3	80	13	3	10	Wet/CO ₂	1.73	†	3.24	2.52	-2.36	0.65
HCO ₂ -5	80	15	5	10	Wet/CO ₂	0.98	†	1.90	2.46	-4.40	0.63

Table 4. 1. List of the experiments reported within the present report and the experimental conditions at which the tests were conducted. Here T denotes the temperature at which the tests were conducted, P_c is the confining pressure, P_{eff} is the effective confining pressure, P_f is the pore fluid pressure, σ_y is the yield stress taken as the departure of the stress-strain curves from linearity (departure from quasi-elastic behaviour), σ^* is the peak strength at which the samples failed, $\sigma_{1\%}$ is the strength of the sample at 1 % axial strain, E is the Young's modulus obtained from a linear fit to the linear (elastic) part of the stress-strain curve.

Note: † Samples showing strain hardening, with no peak strength.

obtained for the samples tested under dry conditions at room temperature is presented in Figure 4.2. At confining pressures up to 3 MPa, the stress versus axial strain curves showed initial quasi-elastic behaviour and a clear peak in differential stress marking failure at 4.7 to 5.8 MPa. The post-peak part of the stress-strain curves showed residual stresses in the range 2.5-5.4 MPa. Failure occurred at 0.7-0.8 % axial strain. At higher confining pressures, i.e. at 5-7 MPa, the stress-strain curves showed initial, near-linear loading up to 0.1-0.3 % axial strain followed by continuous strain hardening. The sample deformed at 5 MPa confining pressure showed near steady state deformation beyond ~0.7 % axial

strain, at a differential stress similar to the residual strength of samples tested at lower pressures. In contrast, the sample deformed at 7 MPa confining pressure was much weaker but showed higher strain hardening rates (Figure 4.2). The volumetric strain vs. axial strain plots showed continuous compaction (i.e. volume reduction) in the first 0.6 % axial strain, for all samples. At the lowest confining pressure employed (0.5 MPa, sample CDRY-0.5), this was followed by minor dilatation (i.e. volume increase), which marked the failure event. At confining pressures of 1.5 MPa up to 7 MPa, the data indicate more or less continuous compaction, with the volumetric strain decreasing in a nearly linear manner with increasing axial strain (Figure 4.2). The rate of compaction is slow and constant at 1.5-3.0 MPa.

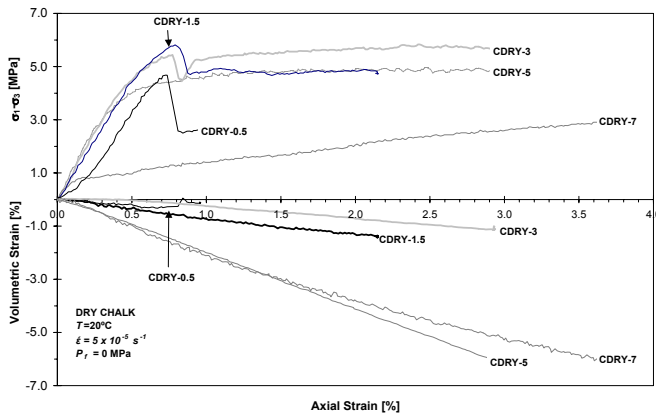


Figure 4.2. Differential stress ($\sigma_1 - \sigma_3$) and volumetric strain versus axial strain curves for chalk samples tested under dry conditions at 20°C.

However, it is much higher at 5.0-7.0 MPa, reaching rates of around -2 % volumetric strain (ϵ_v) per 1 % axial strain (ϵ) and thus demonstrating shear-induced lateral compaction at these confining pressures.

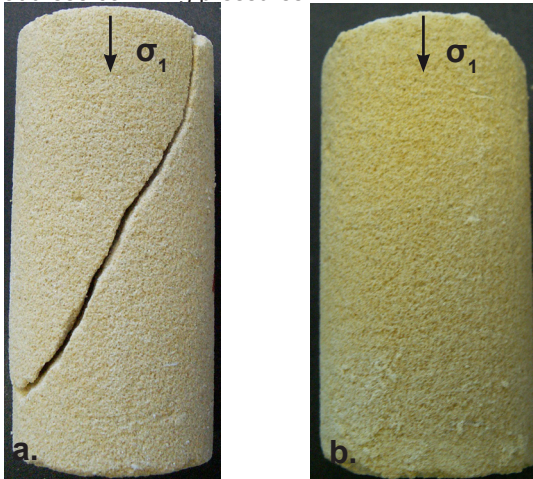


Figure 4.3. Photographs of chalk samples deformed dry at 20°C, compression direction vertical. a) Sample CDRY-1.5 (confining pressure 1.5 MPa) showing a single macroscopic shear fracture, with the failure plane orientated at an angle of approximately 30° to the σ_1 direction. b) Sample CDRY-5 (confining pressure 5 MPa) deformed without any fracturing to strains up to 3%.

Apparent Young's modulus (E) values determined from the linear portion of the stress-strain curves increased with increasing confining pressure (5 MPa) and decreased at higher

confining pressure. The E -values varied between 0.8 to 1.0 GPa at confining pressures of 0.5 to 5.0 MPa (Table 4.1), and decreased again to 0.6 GPa at 7.0 MPa confining pressure.

At low confining pressures (0.5-1.5 MPa), post-test inspection of the cores indicated that the material failed along a single, macroscopic, shear fracture, with the failure plane orientated at an angle of around 30° to the σ_1 direction (Figure 4.3a).

At confining pressures in the range 3 to 7 MPa the samples do not show shear fractures nor macroscopic compaction bands, but shortened and compacted in a macroscopically uniform, distributed manner (Figure 4.3b), presumably by pore collapse.

4.3.1.2 Dry samples deformed at 80°C

The differential stress and volumetric strain versus axial strain data for the dry experiments performed at 80°C are shown in Figure 4.4. The behaviour observed is broadly similar to that seen at 20°C , at least up to the maximum confining pressure of 5 MPa investigated at 80°C . The differential stress versus axial strain curves for samples deformed at confining pressures of 0.5 (sample HDRY-0.5) and 1 MPa (sample HDRY-1) show initial quasi-elastic loading behaviour to axial strains of $\sim 0.6\%$, followed by departure from linearity and failure, marked by well-defined peak stresses at 4.3 and 5.3 MPa respectively. The peak was followed by a sharp load drop to a residual strength of 2.3 and 4.4 MPa, respectively. At higher confining pressures (1.5 MPa to 5 MPa), the differential stress versus axial strain curves showed linear loading behaviour up to $\sim 0.3 - 0.5\%$ axial strain, followed by strain hardening towards a steady-state plateau, where the differential stress remains nearly constant. Sample strength increased with confining pressure in the range 0.5-1.5 MPa and then decreased with confining pressure.

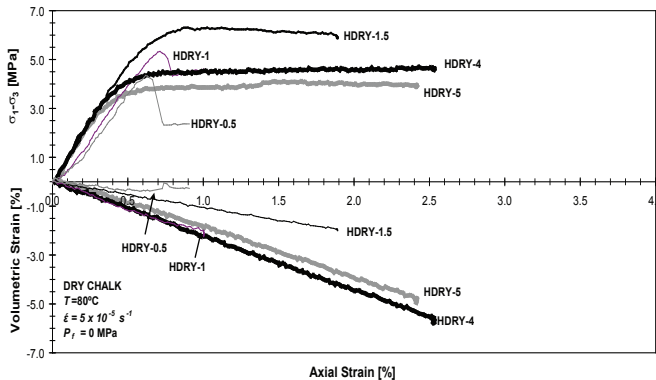


Figure 4.4. Differential stress ($\sigma_1 - \sigma_3$) and volumetric strain versus axial strain for chalk samples tested under dry conditions at 80°C .

The volumetric strain versus axial strain plots show ongoing compaction for all samples, with the exception of sample HDRY-0.5, which was deformed at the lowest confining pressure investigated (0.5 MPa). This showed initial compaction to axial strain around 0.6%, followed by dilatant behaviour through failure up to the final axial strain of 0.9% (Figure 4.4). The remaining (higher pressure) samples showed marked compaction at a rate of around -2% volumetric strain per 1% axial strain, or about half this in the case of sample HDRY-1.5 deformed at 1.5 MPa confining pressure.

Apparent E -values determined from the linear portion of the stress-strain curves increased with increasing confining pressures from around 0.7 GPa at 0.5 and 1 MPa confining pressure to 0.9 GPa at 1.5 to 5.0 MPa confining pressure (Table 4.1).

Macroscopically, the samples which showed a peak stress and load drop (HDRY-0.5 and HDRY-1) exhibited failure on a single shear fracture, with the fracture plane orientated at an angle of approximately 35° to the σ_1 direction. The failure mode was thus similar to that seen in dry samples deformed at low confining pressures at 20°C (see Fig. 4.3a). Samples tested at higher confining pressure (1.5-5.0 MPa) showed no localized failure plane, but shortened and compacted in a pervasive manner similar to dry samples deformed at 20°C at 3.0-7.0 MPa confining pressure, again suggesting pore collapse (see Fig. 4.3b).

4.3.1.3 Wet samples deformed at 80°C

Figure 4.5 shows the differential stress and volumetric strain vs. axial strain data for the wet chalk samples deformed at effective confining pressures varying from 0.5-5.0 MPa and at a pore fluid pressure of 5 MPa. These samples showed behaviour resembling that seen in the dry experiments at 80°C, except for generally lower strength notably at 5 MPa effective confining pressure, and for a generally slightly higher rate of compaction with respect to axial strain, especially at the effective confining pressure of 5 MPa (cf. Figures 4.5 vs. 4.4). At low effective confining pressure (0.5 MPa), sample HWET-0.5 showed initial quasi-elastic loading up to 0.2 % axial strain, followed by a peak stress (4.8 MPa) and failure of the sample at an axial strain of ~0.5 %. At higher effective confining pressures (up to 5 MPa), the samples showed initial quasi-elastic loading to strains up to 0.2 or 0.3 %, followed by a gradual decrease in hardening rate until steady state was reached at an axial strain of ~0.8 %. The steady state strength decreases systematically with increasing effective confining pressure in the range 1.5-5.0 MPa.

The volumetric strain versus axial strain plot (Fig. 4.5) shows straightforward compaction for all wet samples, at a mean rate of around -2.5 % volumetric strain per 1 % shortening strain at 0.5-3.0 MPa effective confining pressure, and at about -3 % volumetric strain per 1 % shortening at 5 MPa effective confining pressure (Fig. 4.5).

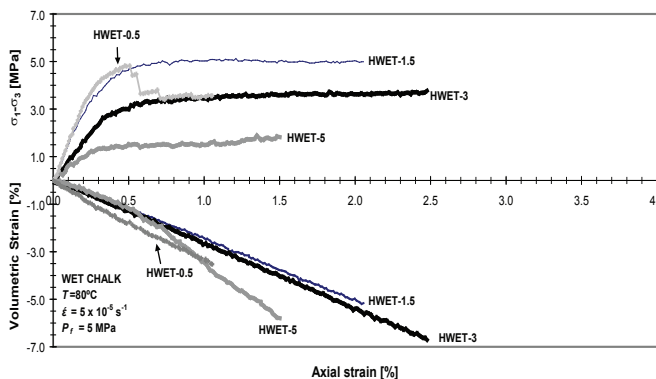


Figure 4.5. Differential stress and volumetric strain versus axial strain for chalk samples deformed under wet conditions at 80°C.

Apparent Young's modulus values determined from the linear portion of the stress-strain

curves decrease with increasing effective confining pressures from 1.5 to 0.5 GPa (Table 4.1).

Macroscopically, the samples show the same type of failure behaviour as the dry chalk, with the samples failing on a single shear fracture at 0.5 MPa effective confining pressure while shortening and compacting in a distributed manner without any macroscopically visible fractures or compaction bands at higher effective confining pressures.

4.3.1.4 Wet/CO₂ samples deformed at 80°C

The results obtained for wet chalk samples deformed at 80°C in the presence of supercritical CO₂ are depicted in Figure 4.6. The differential stress vs. axial strain data for the samples deformed at low effective confining pressures (0.5 to 1.5 MPa) showed initial quasi-elastic loading to axial strains up to ~0.2, followed by the failure of the samples. Failure at these effective confining pressures (0.5 and 1.5 MPa) is marked by peak-stresses at 4.0 and 4.5 MPa followed by a stress drop to residual stresses of 2.8 and 3.7 MPa respectively. At 2.5 MPa effective confining pressure, sample HCO₂-2.5 showed very similar behaviour but failed at a peak stress of only 3 MPa, i.e. well below the value of 4 MPa obtained at an effective confining pressure of 0.5 MPa. At higher effective confining pressures (3 and 5 MPa), our samples showed initial near-linear loading to strains up to only 0.1 %, followed by strain hardening at a gradually decelerating hardening rate.

The volumetric vs. axial strain plots showed straightforward compaction for all samples at rates ranging from -1 % to -2 % volumetric strain per 1 % to axial strain, but with little systematic dependence upon effective confining pressure.

Apparent *E*-values decrease with increasing effective confining pressure from 0.8 to 0.6 GPa (Table 4.1).

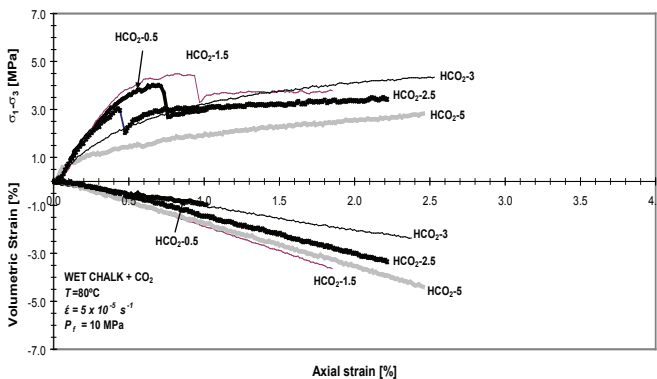


Figure 4.6. Differential stress and volumetric strain versus axial strain for chalk samples deformed under wet conditions in the presence of supercritical CO₂ at a partial pressure of 10 MPa at 80°C.

In comparison with the wet samples deformed at similar temperature, injection of supercritical CO₂ clearly had little further effect on strength (cf. Figures 4.6, 4.5 and 4.4). No systematic weakening was observed due to the presence of supercritical CO₂ in comparison with the wet chalk.

However, whereas the wet samples deformed in a homogeneous, distributed manner without load drops at effective confining pressures of 1.5 MPa and above, samples deformed

in the presence of CO₂ showed peak stresses and load drops at effective confining pressures up to 2.5 MPa (cf. Figure 4.5 vs. Figure 4.6). Macroscopic observation showed that this (load-drop) behaviour was accompanied by shear failure, while pervasive, compactional flow dominated at effective confining pressures above 2.5 MPa.

4.3.2 Microscopic observations

The thin sections made from our samples were studied using a Philips XL30FEG SEM, operated in backscatter electron imaging mode, as well as a Leica DMRX optical microscope. Both undeformed and deformed samples were qualitatively examined in order to identify microstructural changes occurring during the triaxial deformation tests performed with different pore fluids.

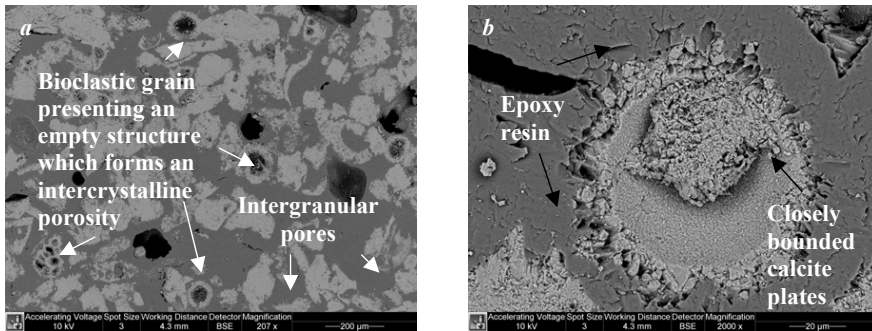


Figure 4.7. Backscatter electron image of **a)** the chalk starting material, showing relatively rounded, sub-angular and elongated bioclastic grains (remains of coccospheres or other microfossils) with a mean grain size of around 100 μm . **b)** A single coccosphere in the starting material. The internal spherical chamber surface shows a regular structure of $\sim 1 \mu\text{m}$ thick plates of calcite or coccoliths closely bound together in a radiating structure.

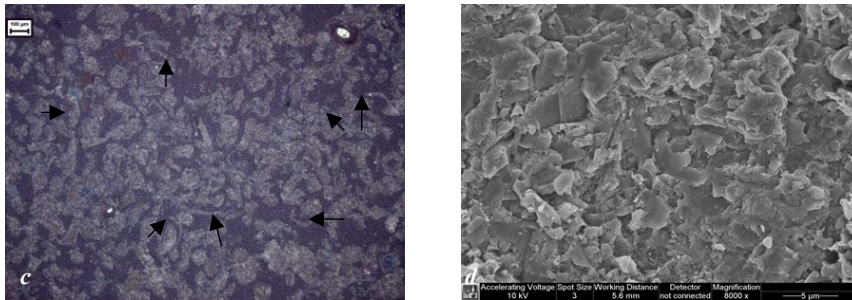


Figure 4.7. Optical micrograph showing microstructure of sample CDRY-1.5 (sample deformed under dry conditions at 20°C and 1.5 MPa confining pressure); compression direction is vertical. **c)** The deformation of the sample brought about a reduction of the intergranular and chamber porosity. Note that the arrows point to broken, concavo-convex fragments of coccospheres. **d)** Secondary Electron image. Note that the chamber porosity appears to collapse during deformation, producing un-organized structures formed of coccoliths.

The undeformed chalk consists of a highly porous aggregate (porosity $\sim 42 \%$) of rounded, sub-angular and elongated bioclastic grains, with sizes varying from ~ 50 to $500 \mu\text{m}$, as shown in Figure 4.7a. About 40 % of the grains are coccospheres showing a hollow, spherical structure. Close inspection of individual bioclastic coccosphere grains reveals that the outer spherical shell consists of small calcite plates or coccoliths ($\sim 1 \mu\text{m}$ thick), densely bound

together but with a fine-scale, intercrystalline microporosity (Figure 4. 7b.). The remaining bioclastic grains consist mainly of poorly preserved coccospheres not displaying an organized internal structure. A few percent of the bioclastic grains present are chambered microfossils such as foraminifera, also composed of finely crystallized calcite. In line with the various types of grains observed in the microstructure, three different types of pores were identified in the undeformed samples: a) large intergranular pores that account for the main porosity, located between the bioclastic grains, b) chambers within the bioclastic grains and c) micropores between the fine calcite grains making up the biogenic shell structures. These will be referred to, henceforth as intergranular porosity, chamber porosity and shell microporosity.

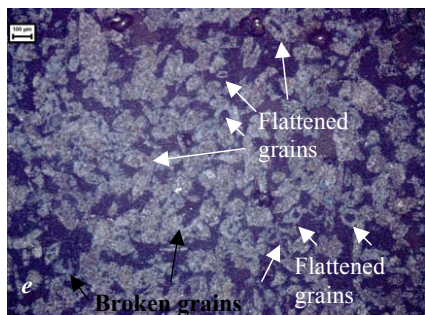


Figure 4.7. e) Optical micrograph showing microstructure of sample HWET-1.5 (sample deformed under wet conditions at 80°C and 0.5 MPa effective confining pressure); compression direction is vertical. The deformation of the sample leads to reduction of the pore space. The bioclastic grains often appear flattened rather than broken, and the proportion of elongated and sub-angular grains is lowered.

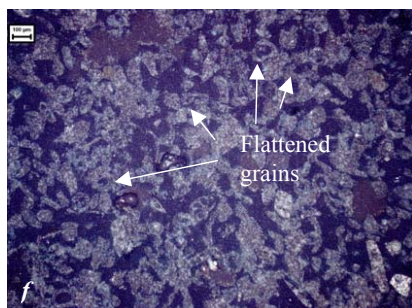
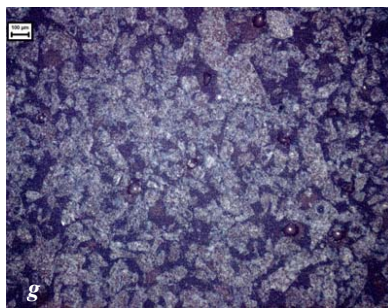


Figure 4.7. f) Optical micrograph showing microstructure of sample HCO₂-1.5 (sample deformed under wet conditions in the presence of added CO₂ at 80°C and 1.5 MPa effective confining pressure); compression direction is vertical. The deformation of the sample brought about a reduction of intergranular and chamber porosity, as a large proportion of the bioclastic coccospheres appears intact and/or flattened. **g)** Optical micrograph showing microstructure of sample HCO₂-5 (sample deformed under wet conditions in the presence of added CO₂ at 80°C and 5 MPa effective confining pressure); compression direction is vertical. The deformation of the sample brought about a drastic reduction of the intergranular and chamber pore space. Individual (hollow) coccospheres can no longer be easily distinguished.



Deformation of the samples under dry conditions at 20°C resulted in a marked reduction of the main intergranular porosity and of the chamber pore space in the body of both fractured and unfractured samples (Figure 4.7c). The relatively large bioclastic grains often retain the initial elongated or sub-angular grain shapes (cf. Figure 4.7a and b). However, the percentage of well preserved coccospheres showing a hollow spherical, or chambered structure is drastically reduced, from ~40 % to about 10 %. Most such structures and the associated chamber porosity appear to collapse during deformation,

with some producing ruptured, concavo-convex fragments of bioclastic grains (Figure 4.7c). The microcrystalline shell wall structures show a less organized, disrupted structure of coccoliths (Figure 4.7d). The shear fractures developed at low effective confining pressure showed an increased number of fragmented bioclastic grains, in comparison with the body of the samples. Increased testing temperature (80°C) produced no additional changes in the microstructure of the dry chalk samples.

The microstructure typifying the body of the wet deformed chalk samples is depicted in Figure 4.7e. Away from the fractures and in unfractured samples, wet deformation led to a similar reduction of intergranular and chamber pore space in comparison with the dry deformed samples (Figure 4.7e). However, upon addition of pore fluid, the bioclastic grains often became flattened rather than broken.

Material in the region of the fracture developed at low effective confining pressure show an increase in the number of fragmented bioclastic grains in comparison with the body of the samples. No visible difference in microstructure could be observed in wet samples with added CO₂ (Figure 4.7f). Deformation of all samples at higher effective confining pressures ($P_{eff} > 3$ MPa) resulted in much lower intergranular and chamber porosity, than seen at low confining pressures (Figure 4.7g). Note that fewer intact coccospheres can be identified at higher effective confining pressures.

4.4 Discussion

The present results for Maastrichtian chalk samples deformed under dry conditions at 20 and 80°C show a transition from brittle shear failure at very low (effective) confining pressure (0.5 to 1.5 MPa) to pervasive, macroscopically homogeneous flow plus marked compaction at higher (effective) confining pressures up to 7 MPa. Despite the high initial porosity of our samples and significant reduction of the pore volume at the end of the tests, notably in the higher pressure regime, no compaction bands were observed during post-test inspection of the samples. Compaction seems to have involved more pervasive pore/grain collapse. Experiments performed at 80°C in the presence of chalk-saturated pore fluid, showed similar behaviour but with a significant reduction of about 15 - 65 % in the compressive strength of the samples (cf. Table 4.1, Figures 4.4 and 4.5). Addition of CO₂ to the pore fluid had no further systematic effect on the (yield) strength of the samples (see Table 4.1).

In the following, the compressive strength data obtained under the various conditions investigated are analyzed by constructing appropriate failure or strength envelopes. This approach allows more detailed assessment of any effects of temperature on strength present in our data on dry samples, as well as the effects of adding aqueous pore fluid and CO₂. We go on to attempt to explain the observed effects and to consider some of the practical implications of our data.

4.4.1 Strength envelopes and comparison with previous data

The failure behaviour of our complete set of samples is plotted in Figure 4.8, making

use of the modified Mohr-Coulomb or P - Q plot [Wong and Baud, 1999; Baud et al., 2000; Risnes et al., 2003] applied to our data on yield strength (σ_y) and strength measured at 1 % strain ($\sigma_{1\%}$).

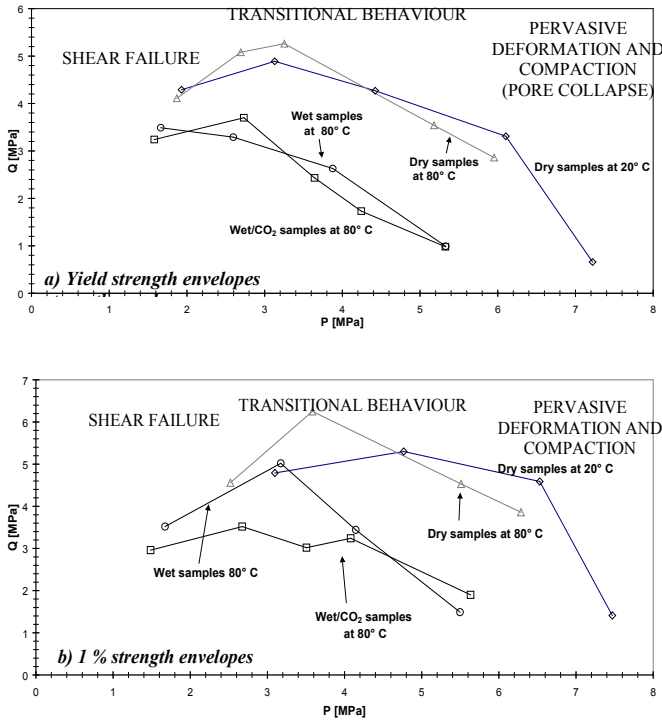


Figure 4.8. Modified Mohr-Coulomb diagram obtained for the tests presented in the present paper. **a)** Strength envelopes constructed for yield stresses (σ_y) determined from the departure of the stress-strain curves from linearity. **b)** Envelopes constructed for stresses supported by the samples at 1 % axial strain ($\sigma_{1\%}$). Macroscopic observation of sample failure modes showed that at low mean stresses shear failure characterized our samples, whereas at higher mean stresses macroscopically uniform deformation and pervasive compaction dominated the deformation behaviour of our samples.

The P - Q plot is widely used to represent the yield/failure behaviour of granular materials in soil and rock mechanics and represents stress space defined in terms of the mean effective stress (P) and equivalent shear stress (Q) defined as

$$P = \frac{\sigma_1 + \sigma_2 + \sigma_3}{3} - P_f \tag{4.1}$$

$$Q = (\sigma_1 - \sigma_3) \tag{4.2}$$

Taken together with our sample-scale and microstructural observations, our P - Q plots show three regimes of behaviour (Figures 4.8a and b). At low mean effective stresses ($P < 3$ MPa) the envelopes plotted show a mainly positive slope. The samples deformed at these low effective stresses failed in shear failure mode characterized by a macroscopic shear fracture. At higher mean effective stresses ($P > 4$ MPa), our envelopes show a steep negative slope, while the corresponding samples showed pervasive strain hardening or steady state flow plus marked compaction due to a reduction in intergranular and chamber porosity, through collapse of the bioclastic grains. At intermediate mean stresses ($3 \leq P \leq 4$ MPa), transitional behaviour is observed between the shear and compactional regimes. These three regimes of shear, transitional and compactional behaviour are commonly seen in P - Q plots constructed for highly porous limestones and chalks [Risnes and

Flaageng, 1999; Homand, 2000; Scott Jr. et al., 2001; Collin et al., 2002] or highly porous sandstones [*Baud et al., 2000; Olsson and Holcomb, 2000; Wong et al., 2001*]. Indeed, the strength properties of most highly porous materials (i.e. with a porosity of 30-45 %) can be described by a positively sloping shear failure envelope at relatively low mean stresses, giving way at higher mean stresses to a negatively sloping, elliptical end-cap that represents a transition to pore collapse and/or compaction band formation [*Mollema and Antonellini, 1996; Olsson, 1999; Issen and Rudnicki, 2001*]. Our yield strength envelopes plotted for dry samples in Figure 4.8a demonstrate that the increase in temperature from 20°C to 80°C resulted in little or no change in the yield strength. However, addition of aqueous solution in the wet experiments led to a 25 % decrease in the yield stresses in the shear failure field, increasing to a 65 % reduction of yield stress in the compaction or pore collapse field. In comparison with the wet samples, addition of CO₂ led to little further change in the yield envelope (Figure 4.8a).

Our 1 % strength data for the dry samples (20 and 80°C) and the wet samples (Figure 4.8b) show similar trends and behaviour to those seen in the *P-Q* diagrams based on the strength at yield (cf. Figures 8a and b). The water weakening effect is again visible in all regimes, especially at mean effective stresses above 3.5 MPa. The addition of CO₂ appears to produce a weakening at mean effective stresses up to 4 MPa, while at higher mean stresses it led to minor strengthening of the samples. Given the contradictory trends in either yield or 1 % strength envelopes (cf. Figure 4.8a and b), we do not consider the effects of CO₂ to be significant compared with likely sample variability.

We now briefly compare our yield strength envelopes with those obtained previously for dry and wet chalk samples tested in hydrostatic and triaxial compression tests performed at room temperature. We focus on data obtained for both dry and wet Lixhe chalks (Upper Campanian, Belgium), which have similar porosity to our samples, i.e. around 42 % [*Homand, 2000; Collin et al., 2002; Risnes et al., 2005*]. We also consider data on dry samples of Danian Chalk (Denmark) with a porosity of 35 % [*Scott Jr. et al., 2001*]. The dry Lixhe chalks mean stresses giving way to a compaction cap at high mean stresses and dry Danian chalk [*Scott Jr. et al., 2001*] show 1.3 to 4 times higher yield strength in the shear failure regime than our dry material deformed at room temperature (Figure 4.9).

The wet Lixhe and Danian chalks are also far stronger in the compaction regime (Figure 4.9). The wet Lixhe chalks [*Risnes and Flaageng, 1999; Homand, 2000; Collin et al., 2002*] exhibit similar yield strengths to our wet and wet/CO₂ samples in the shear failure regime, at low mean stresses (Figure 4.9). However, moving towards higher mean stresses our samples weaken much more quickly, reaching strengths some 2 to 7 times smaller than the Lixhe chalks at a mean effective stress of ~5 MPa, and showing closure of the yield cap at *P*-values some 30-50 % lower than the Lixhe chalks. Overall, comparison of the various data implies considerable variation between chalk types, though similar water-weakening effects are observed. The differences in yield strength observed between our samples and the Lixhe samples, which have similar porosities, are difficult to explain in detail at this stage.

One of the most likely possibilities is the degree of meteoric weathering. Very recently, ENCI chalks have been reported to be characterized by extreme meteoric diagenesis [Hjuler and Fabricius, 2009], which lowers the cohesion of the material, due to weakening of intergranular bonds, thus reducing compressive strength of the material.

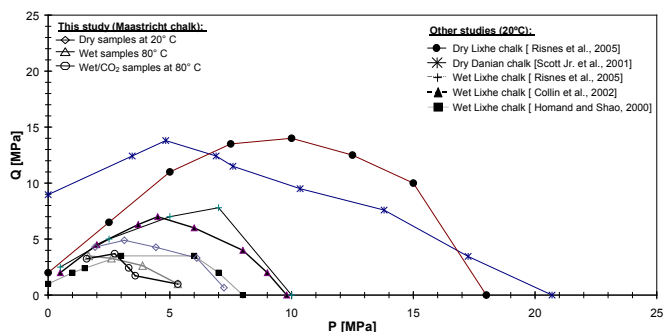


Figure 4.9. Comparison of the yield envelopes resulting from the present study with the yield envelopes obtained in previous studies on Lixhe and Danian chalks (Collin et al., 2002; Homand, 2000; Risnes, et al., 2005, Scott Jr. et al., 2001). Our data for dry Maastricht chalk at 80°C are omitted, as they are similar to those obtained at 20°C.

4.4.2 Effects of water and CO₂ on strength: Mechanistic considerations

Our yield and failure envelopes for the Maastricht Chalk at 80°C have shown that addition of a pore fluid composed of a saturated chalk solution leads to a major reduction of compressive strength, typically by about 50 %. Equilibration, or near-equilibration, of the pore fluid with supercritical CO₂ before loading produces no further weakening effect – at least no major, systematic effect. As already discussed, numerous authors have reported similar results for the effects of adding water or brine to chalks. These authors have attempted to explain the observed weakening in terms of capillary forces [Delage et al., 1996; Papamichos et al., 1997], surface forces [Austad et al., 2005; Korsnes et al., 2008], enhanced dissolution [Newman, 1983], pressure solution [Hellmann et al., 2002a; Hellmann et al., 2002b; Madland et al., 2006] and fluid enhanced microcracking [Risnes et al., 2005]. However, none of these mechanisms seems to explain the water-weakening effect well, and the topic remains highly controversial [Gutierrez et al., 2000; Risnes et al., 2005; Korsnes et al., 2008].

In the following, we consider briefly each of the mechanisms proposed previously in relation to our results, taking into account the additional information from our tests and from those of [Madland et al., 2006] on the effects of CO₂. We conclude by comparing our mechanical and microstructural findings for chalk with the results of our earlier compaction creep experiments on synthetically prepared granular carbonates [Liteanu and Spiers, 2009; Liteanu et al., in prep.] – Chapters 2 and 3, to establish whether the “water-weakening” effects observed in these experiments (i.e. subcritical crack growth and pressure solution) can help explain the effects of water and CO₂ on the compressive strength of chalks.

4.4.2.1 Capillary forces

Previous workers investigating the weakening of chalks by water have suggested that at small degrees of saturation, water is bound in small pores, giving rise to water bridges or

menisci between the calcite plates within the bioclastic grains, pulling the plates together via a Laplace force [Han *et al.*, 2002; Risnes *et al.*, 2005], which imparts strength to the bioclastic grains and/or to their contacts. When the chalk is water flooded, such menisci are destroyed, resulting in a drastic weakening of the material [Piau and Maury, 1994; Delage *et al.*, 1996; Papamichos *et al.*, 1997; Risnes, 2001; Risnes *et al.*, 2003; Risnes *et al.*, 2005]. This means that chalk should be very weak, when fully dry. However, it has been shown that chalks, dried at 120°C still contain about 0.2 weight % water, which has the potential to form capillary menisci binding the chalk grains [Risnes *et al.*, 2005]. In our dry tested chalks at both 20 and 80°C, the small degree of water present could give rise to capillary forces binding the chalk grains thus leading to its cohesiveness. A rise in temperature from 20 to 80°C is not expected to affect these forces, as capillary menisci are believed to be stable to temperatures up to 300°C [Papamichos *et al.*, 1997; Lord *et al.*, 1998]. Hence capillary forces might play a role in controlling the strength of our samples (Figure 4.8a). However, estimates of the maximum Laplace force $L_f \approx \pi D \gamma$, arising between chalk grains of 0.5 μm diameter (D) due to a water meniscus with a (γ) surface tension of 0.07 N/m² predict a cohesive strength of about 0.2 MPa for our dry samples, when integrated over a cubic pack of grains, following Risnes *et al.* [2003]. Assuming that, when water is added, such forces will disappear, this means that the mean yield envelope for our dry samples, would be shifted by 0.2 MPa towards the compactional field, which in turn would lead a decrease in strength of ~ 0.2 MPa in the shear failure regime, but to an increase in strength at high mean effective stresses. This effect is not consistent with our results, which indicate a 0.6 to 2 MPa weakening of our wet samples in comparison with the dry samples tested at similar temperatures (Figure 4.8). We infer that the capillary forces and associated surface tension changes can not explain more than a fraction of the water-weakening effect observed in our experiments or those of others [Risnes *et al.*, 2003; Risnes *et al.*, 2005; Madland *et al.*, 2006].

4.4.2.2 Surface charge and surface force effects

Changes in surface charges of chalk grains related to the presence of surface-potential-determining ions have also been considered as a possible explanation for the water weakening observed in chalks. [Pierre *et al.*, 1990; Risnes *et al.*, 2005; Strand *et al.*, 2006; Korsnes, 2008; Korsnes *et al.*, 2008]

It has been previously shown that the strong adherence of water to the surface of chalk grains (i.e. most of the chalks are strongly water-wet) or the presence of potential-determining ions such as Ca²⁺, Mg²⁺, CO₃²⁻ or SO₄²⁻ will give rise to a surface charge in such materials [Pierre *et al.*, 1990; Risnes *et al.*, 2005; Strand *et al.*, 2006; Korsnes, 2008; Korsnes *et al.*, 2008], which in turn creates repulsive forces at the grain-grain contact areas [Israelachvili, 1985]. Based on the fact that the magnitude of such surface charges is reflected in the zeta potential, Risnes *et al.* [2005] estimated that intergranular repulsive forces arising in chalk materials in the presence of water (zeta potential = 20 mV) are about $5 \cdot 10^{-11}$ N. As concluded by Risnes *et al.* [2005] for Lixhe chalk, such forces are far

too low to explain the observed weakening effect of adding solution to our samples.

The decrease of yield strength in the presence of aqueous solution has also been suggested to be due to hydration forces related to the polar nature of the water molecules [Risnes *et al.*, 2005]. These forces represent an adsorption or disjoining which has been estimated to be around 2 MPa by Risnes *et al.* [2005]. Such a reduction of effective stress due to this effect would be sufficient to explain the water-weakening observed in chalks (Figure 4.8) and is hard to eliminate. However, the basis for this calculation involves many poorly constrained assumptions so its validity is unclear.

4.4.2.3 Dissolution, pressure solution and subcritical crack growth

Dissolution, pressure solution and subcritical or stress corrosion cracking of the bioclastic grains or at the micrograin contacts within them have all been proposed as mechanisms for water weakening of chalks [Risnes and Flaageng, 1999; Hellmann *et al.*, 2002a; Hellmann *et al.*, 2002b; Heggheim *et al.*, 2005; Madland *et al.*, 2006]. We consider each here with reference to our own experiments on compaction creep of simulated calcite aggregates (Chapters 2 and 3).

Dissolution of grain-to-grain cement bridges between the bioclastic grains or between the finest grains within, might explain the water-weakening effect seen in chalks such as ours [Newman, 1983]. However, the low solubility and slow dissolution rate of calcite in water makes this mechanism seem unlikely, as drastic water weakening is often observed to occur in chalk on very short time scales. More importantly, in our wet experiments we added a pore fluid solution phase to our chalk samples, which was pre-saturated with respect to the solid material at room temperature. During heating to the test temperature of 80°C, this would have become supersaturated with calcite as the solubility of calcite decreases with increasing temperature [Segnit *et al.*, 1962; Plummer and Busenberg, 1982]. Thus, cement bridges would more likely form than dissolve. Moreover, injection of 10 MPa supercritical CO₂ into wet chalk samples produced no further weakening in our experiments, despite the fact that the solubility of calcite increases with CO₂ pressure by up to two orders of magnitude under our test conditions [Segnit *et al.*, 1962]. We accordingly infer that simple dissolution of cement bridges between either the large or ultrafine bioclastic grains in our chalk, cannot explain the observed water-weakening effect.

Pressure solution has also been put forward as a mechanism to explain the water weakening observed in chalk, notably by Hellmann *et al.*, [2002a]; Hellmann *et al.*, [2002b]; Madland *et al.*, [2006]. Pressure solution is a time dependent process involving intergranular dissolution, diffusion of the dissolved material through wetted grain boundaries and precipitation on pore walls. It is considered as one of the most important deformation processes occurring in carbonate rocks in the upper crust, both at the intergranular level and in pressure solution seams or stylolites [Rutter, 1976; Dewers and Ortoleva, 1990; Graham *et al.*, 2003; Tondi *et al.*, 2006]. Through stress-enhanced dissolution at grain-to-grain contacts, rapid pressure solution may offer a means of reducing intergranular cohesive and/or frictional resistance, resulting in lower shear strength of the material.

Pressure solution creep has been inferred in calcite (rich) aggregates or chalk samples loaded under laboratory conditions on time scales ranging from hours to 700 days, with final volumetric strains varying from 0.1 to 6 % [Hellmann *et al.*, 2002a; Hellmann *et al.*, 2002b; Zhang and Spiers, 2005a; Zhubtsov *et al.*, 2005; Le Guen *et al.*, 2007; Liteanu and Spiers, 2009], see also Chapters 2 and 3. When supercritical CO₂ is injected into chalk, the pH of the pore fluid is reduced to values as low as 3 [Madland *et al.*, 2006], which enhances dissolution/precipitation processes in calcite rocks, and is expected to speed up intergranular pressure solution creep [Renard *et al.*, 2005a; Le Guen *et al.*, 2007; Liteanu and Spiers, 2009]. Drastic weakening associated with CO₂ injection into wet chalk, at stress levels beyond the yield point, was observed in experimental investigations performed on Aalborg chalk and attributed to pressure solution at grain contacts, i.e. between the calcite plates forming the bioclastic grains [Madland *et al.*, 2006]. Other experimental and numerical investigations have also shown that the presence of supercritical CO₂ increases rates of compaction in carbonate aggregates by at least two orders of magnitude [Renard *et al.*, 2005b; Le Guen *et al.*, 2007; Liteanu and Spiers, 2009; Liteanu *et al.*, in prep.]. However, in the present experiments on chalk, introduction of supercritical CO₂ was found to have little effect on the compressive strength of wet samples certainly with regards to initial yield strength (Figure 4.8a). This suggests that pressure solution is not the main factor controlling the compressive strength of our chalk sample. In the long term, however, enhanced intergranular pressure solution might be a key factor controlling creep of carbonate reservoirs (see Chapters 2 and 3).

Other mechanisms that can cause water-weakening in silicate and carbonate rocks include subcritical crack growth, or stress corrosion cracking, and water-enhanced Griffith or equilibrium crack extension [Barnett and Kerrich, 1980; Atkinson, 1984; Atkinson and Meredith, 1987; Atkinson and Meredith, 1989; Dewers and Hajash, 1995; Chester *et al.*, 2004; Chester *et al.*, 2007; Le Guen *et al.*, 2007; Liteanu and Spiers, 2009]. According to Griffith theory [Griffith, 1921; Brzesowsky, 1995; Wong and Baud, 1999] fracture occurs when local stress concentration at flaws present in the structure of the material exceeds the critical stress intensity factor or fracture toughness of the material [Atkinson, 1982]. Crack propagation can be enhanced either by promoting bond-breaking reactions at the crack tip at subcritical stress intensities, or by lowering the surface energy of the material. In the first case, compaction through failure of the material by subcritical crack growth is significantly accelerated in the presence of a chemically active fluid or saturated solution phase, due to stress-induced chemical attack at the crack tip, i.e. stress corrosion cracking [Atkinson, 1982; 1984; Chester *et al.*, 2004; Karner *et al.*, 2005; Chester *et al.*, 2007]. In the second case, the stress required for failure to occur depends on the surface energy of the material via the Griffith crack extension criterion, in which strength depends on the square root of the crack surface energy [Shah and Wong, 1997]. If the surface energy of the material is lowered, e.g. by addition of water, the fracture toughness is lowered accordingly. Such mechanisms have been proposed for chalk by Risnes *et al.* [2003], and have been recognized in experiments on compaction creep of granular calcite and on the

failure behaviour of wellbore cement, which like chalk shows a strong water-weakening effect of ~50 % (see Chapter 5). We now specifically compare our findings for chalk with the findings of our experiments on granular calcite.

The compaction experiments on granular calcite aggregates reported by Liteanu and co-workers (Chapters 2 and 3) show that creep is very strongly accelerated upon addition of saturated solution to the samples, while there is a large, but much smaller effect of CO₂ when direct dissolution effects are eliminated, i.e. when CO₂ is added prior to starting the deformation tests. These effects, which are observed in the calcite aggregates under similar conditions to those of the present experiments on chalk, were explained in terms of grain-scale, stress corrosion cracking and pressure solution creep, depending on the experimental conditions and on the grain size of the aggregates. At fine-grained sizes (grains < 106 μm), pressure solution dominated the compaction creep of the samples, whereas at coarser grain sizes stress corrosion cracking became more important. On this basis, it seems likely that addition of chalk-saturated solution to our chalk samples produced enhanced grain-scale microcracking and/or dissolution at grain contacts, which reduced their cohesive and frictional strength. Such local effects will in turn enhance rotation and sliding of the bioclastic and coccolith grains. The mechanical results and microstructural evidence presented for our chalk tests suggests that addition of saturated solution caused increased internal deformation (flattening) of the bioclastic grains. By contrast, in the dry samples, the higher fraction of fragmented bioclastic grains suggests that the main deformation mechanism was grain breakage and cracking. Based on experiments investigating the hydromechanical properties of fractures present in chalk, [Gutierrez *et al.*, 2000] suggested similar enhanced grain rotation and sliding due to a reduction of frictional resistance, by water-enhanced grain contact cracking or dissolution.

Combining all our observations and arguments and noting the small effect of addition of CO₂ compared with that of water, we infer that the “water weakening” effects observed in our chalk samples can be attributed to a reduction in cohesive strength and frictional resistance of the material, due to water-enhanced grain-contact cracking and perhaps pressure solution within the bioclastic grains, with possibly a contribution from disjoining pressure effects caused by water adsorption. Nonetheless, further work is still needed to unambiguously identify the water-weakening mechanism(s).

4.4.3 Implications - CO₂ storage or EOR/EGR activities in chalk reservoirs.

Our results are relevant for evaluating CO₂ storage integrity and CO₂-enhanced oil and gas recovery operations in chalk reservoirs, and to assessing the effects of CO₂ migration into chalk formations overlying CO₂ storage reservoirs. It was found that while solution-flooding of dry chalks drastically reduces their yield strength, further addition of supercritical CO₂ has little effect. Based on these results, we infer that on the short term, injection of CO₂ into water-wet chalk formations will not lead to enhanced brittle/frictional failure or compaction. However, aside from initial poro-elastic expansion caused by the injection of supercritical CO₂, dissolution-enhanced processes, stress corrosion cracking

and pressure solution can be expected to play an important role in the overall deformation of chalks on long time scales (years) [Hellmann *et al.*, 2002a; Renard *et al.*, 2005b; Safaric and Davison, 2005; Madland *et al.*, 2006; Le Guen *et al.*, 2007; Liteanu and Spiers, 2009]. Such processes occur due to changes in the chemistry of the pore fluid coupled with the changes in the state of stress in the reservoir. Increased calcite solubility has the potential of accelerating mechanisms such as intergranular pressure solution creep or stress corrosion cracking on long term scales, which in turn can alter the transport properties of the chalk formations, through the dissolution, transport, precipitation or formation of microcracks. In time, such processes may affect the brittle/frictional strength also. Based on the results on compaction creep in granular calcite, reported by Liteanu and Spiers [2009] - Chapters 2 and 3, creep effects related to pressure solution or subcritical crack growth will depend on the initial conditions present in the reservoir, including the mean grain size, the porosity, the pH of the pore fluid, the temperature, the effective stress, and the CO₂ partial pressure. Furthermore, in the presence of Mg²⁺, PO₄³⁻, SO₄²⁻, Mn²⁺ ions, commonly present in residual formation fluids, solution/precipitation processes can be drastically slowed down in carbonate rich formations [Dove and Hochella Jr, 1993; Zuddas and Mucci, 1994; Zhang and Spiers, 2005b; Zhang and Spiers, 2005a]. Residual hydrocarbons may have similar retarding effects on creep rates especially if they compete with water in wetting the surface of the carbonate grain in the rock [Zhang and Spiers, 2005a; Zhang and Spiers, 2005b]. This means that the importance of creep effects in chalk is difficult to predict. However, the effects of dissolution/precipitation retardants raise several interesting questions. For example, an interesting possibility is that the addition of Mg²⁺ or PO₄³⁻ before or during EOR/EGR or CO₂ storage may reduce the weakening effects of water injection as well as the effects of creep phenomena such as pressure solution and subcritical crack growth. Based on the results of Zhang and Spiers [2005a; 2005b], which show major retardation effects of these ions, this deserves future attention.

4.5 Conclusion

In this study, we aimed to determine the effect of chalk-saturated water and of CO₂-saturated solution on the mechanical strength and failure behaviour of Maastrichtian chalk. To this end, we performed conventional triaxial compression experiments on chalk cores under dry conditions at 20 and 80°C, under wet conditions at 80°C and wet with added supercritical CO₂ at 80°C. The tests were carried out at effective confining pressures of 0.5 to 7 MPa and at a near constant strain rate of 5x10⁻⁵ s⁻¹. The main findings can be summarized as follows:

1. At low mean effective stresses (<3 MPa), most of the samples failed in shear failure mode characterized by localization in a macroscopic shear fracture. In a conventional P-Q plot, this was followed by a transition towards compaction and pore collapse at higher mean effective stresses (> 4 MPa). The compaction regime was microstructurally characterized by a reduction in intergranular and microfossil chamber porosity, through intergranular pore collapse and deformation of the

bioclastic coccosphere grains. In dry samples hollow coccospheres showed wider mechanical evidence for brittle failure, whereas wet and wet/CO₂ samples showed increased numbers of coccosphere flattening.

2. Increasing testing temperature did not produce any marked effects on the strength or failure behaviour of our samples.
3. Addition of pore fluid to the chalk samples resulted in a drastic reduction of the strength, in the shear, transitional and compactional regimes. Further addition of supercritical CO₂ to our wet samples at 10 MPa pressure led to yield strengths similar to those of wet chalk.
4. The short-term weakening effects due to the addition of water (chalk solution) and CO₂-saturated fluid seen in our samples can be best explained as a result of solution-enhanced stress corrosion cracking and perhaps pressure solution creep, occurring between and especially within the biogenic coccospheres making up most of the chalk. Disjoining pressure, caused by water adsorption onto the coccolith surfaces, may also play a role. On the long-term compaction creep mechanisms such as intergranular pressure solution will likely become important for CO₂ storage in chalk reservoirs and it has the potential to enhance compaction creep.

Acknowledgments:

We thank Peter van Krieken, Gert Kastelein and Eimert de Graaff for technical support provided in the laboratory. This project was jointly funded by TNO Bouw and Ondergrond and Utrecht Center of Geosciences (UCG), and was conducted in the framework of the Dutch national programme on Carbon Capture and Storage (CATO).

REFERENCE LIST

- Ambrose, W. A., S. Lakshminarasimhan, M. H. Holtz, V. Nunez-Lopez, S. D. Hovorka, and I. Duncan (2008), Geologic factors controlling CO₂ storage capacity and permanence: case studies based on experience with heterogeneity in oil and gas reservoirs applied to CO₂ storage, *Environmental Geology* 54, 1619-1633.
- Atkinson, B. K. (1982), Subcritical crack propagation in rocks: theory, experimental results and applications. , *Journal of Structural Geology* 4, 41-56.
- Atkinson, B. K. (1984), Subcritical crack growth in geological materials., *Journal of Geophysical Research*, 89, 4077-4114.
- Atkinson, B. K., and P. G. Meredith (1987), The theory of subcritical crack growth with applications to minerals and rocks, in *Fracture Mechanics of Rock*, edited by A. B.K., pp. 111-166, Academic Press.
- Atkinson, B. K., and R. G. Meredith (1989), The theory of subcritical crack growth with applications to minerals and rocks, in *Fracture mechanics of rock*, edited by B. K. Atkinson, pp. 111-166, Academic Press, London.
- Austad, T., S. Strand, E. J. Høgenesen, and P. Zhang (2005), Seawater as IOR fluid in fractured chalk. , in *Oilfield Chemistry Symposium*, edited, PE Paper 93000, Houston, TX.
- Barnett, R. L., and R. Kerrich (1980), Stress corrosion cracking of biotite and feldspar, *Nature*, 283(5743), 185-187.
- Baud, P., W. Zhu, and T.-f. Wong (2000), Failure mode and weakening effect of water on sandstone, *Journal of Geophysical Research*, 105(12), 16371-16390.
- Brzesowsky, R. H. (1995), Micromechanics of sand grain failure and sand compaction, 180 pp, Universiteit Utrecht, The Netherlands, Utrecht.
- Chester, F. M., J. S. Chester, A. K. Kronenberg, and A. Hajash (2007), Subcritical creep compaction of quartz sand at diagenetic conditions: Effects of water and grain size, *J. Geophys. Res.*, 112.
- Chester, J. S., S. C. Lenz, F. M. Chester, and R. A. Lang (2004), Mechanisms of compaction of quartz sand at diagenetic conditions, *Earth and Planetary Science Letters*, 220(3-4), 435-451.
- Collin, F., Y. J. Cui, C. Schroeder, and R. Charlier (2002), Mechanical behaviour of Lixhe chalk partly saturated by oil and water: experiment and modelling, *International Journal for Numerical and Analytical Methods in Geomechanics*, 26(9), 897-924.
- Delage, P., C. Schroeder, and Y. J. Cui (1996), Subsidence and capillary effects in chalks, in *EUROCK '96, Prediction and performance on rock mechanics and rock engineering - ISRM International symposium*, edited, Torino, Italy.
- Dewers, T., and P. Ortoleva (1990), A coupled reaction/transport/mechanical model for intergranular pressure solution, stylolites, and differential compaction and cementation in clean sandstones, *Geochimica et Cosmochimica Acta*, 54(6), 1609-1625.
- Dewers, T., and A. Hajash (1995), Rate laws for water-assisted compaction and stress-induced water-rock interaction in sandstones, *J. Geophys. Res.*, 100(B7), 13093-13112. .
- Dove, P. M., and M. F. Hochella Jr (1993), Calcite precipitation mechanisms and inhibition by orthophosphate: In situ observations by Scanning Force Microscopy, *Geochimica et Cosmochimica Acta*, 57(3), 705-714.
- Fredrich, J. T., B. Evans, and T.-F. Wong (1989), Micromechanics of the Brittle to Plastic Transition in Carrara Marble, *J. Geophys. Res.*, 94(B4), 4129-4145.
- Gozalpour, F., S. R. Ren, and B. Tohidi (2005), CO₂ EOR and storage in oil reservoirs. , *Oil and Gas Science and Technology - Rev IFP*, 60(3), 537-546.
- Graham, B., M. A. Antonellini, and A. Aydin (2003), Formation and growth of normal faults in carbonates within a compressive environment, *Geology*, 31(1), 11-14.
- Griffith, A. A. (1921), The phenomenon of rupture and flow in solids, *Philosophical Transactions of the Royal Society*, 221(Series A), 163-198.
- Gutierrez, M., L. E. Oino, and K. Hoeg (2000), The effect of fluid content on the mechanical behaviour of fractures in chalk, *Rock Mech Rock Eng*, 33(2), 93-117.
- Han, G., M. B. Dusseault, and J. Cook (2002), Quantifying Rock Capillary Strength Behavior in Unconsolidated Sandstones, in *SPE/ISRM Rock Mechanics Conference*, edited, Irving, Texas.
- Heggheim, T., M. V. Madland, R. Risnes, and T. Austad (2005), A chemical induced enhanced weakening of chalk by seawater, *Journal of Petroleum Science and Engineering*, 46(3), 171-184.
- Hellmann, R., P. J. N. Renders, J.-P. Gratier, and R. Guiguet (2002a), Experimental pressure solution of chalk in aqueous solutions. Part 2. deformation examined by SEM, porosimetry, synthetic permeability, and X-ray computerized tomography, in *Water-rock interactions, ore deposits, and environmental geochemistry: a tribute to David A. Crerar*, edited, The Geochemical Society
- Hellmann, R., P. J. N. Renders, G. J.-P., and R. Guiguet (2002b), Experimental pressure solution of chalk in

aqueous solutions: Part 1. Deformation behaviour and chemistry., in *Water-Rock Interactions, Ore Deposits, and Environmental Geochemistry: A Tribute to David A. Crerar*, edited by T. G. Society.

Hjuler, M. L., and I. L. Fabricius (2009), Engineering properties of chalk related to diagenetic variations of Upper Cretaceous onshore and offshore chalk in the North Sea area, *Journal of Petroleum Science and Engineering*, 68(3-4), 151-170.

Homand, S., and J. F. Shao (2000), Comportement mécanique d'une craie poreuse et effets de l'interaction eau/craie. Première partie : Résultats expérimentaux, *Oil & Gas Science and Technology*, 55(6), 591-598.

Homand, S., Shao, J. F. (2000), Mechanical behaviour of a porous chalk and effect of saturating fluid, *Mechanics of Cohesive-frictional Materials*, 5(7), 583-606.

Israelachvili, J. N. (1985), *Intermolecular and Surface Forces*, New York.

Issen, K. A., and J. W. Rudnicki (2001), Theory of compaction bands in porous rock, *Physics and Chemistry of the Earth, Part A: Solid Earth and Geodesy*, 26(1-2), 95-100.

Jensen, T. B., K. J. Harpole, and A. Osthus (2000), EOR Screening for Ekofisk, in *SPE European Petroleum Conference*, edited, Paris, France.

Karner, S. L., J. S. Chester, F. M. Chester, A. K. Kronenberg, and A. Hajash (2005), Laboratory deformation of granular quartz sand: Implications for the burial of clastic rocks, *American Association of Petroleum Geology Bulletin*, 89, 603-625.

Korsnes, R. I., M. V. Madland, T. Austad, S. Haver, and G. Røslund (2008), The effects of temperature on the water weakening of chalk by seawater, *Journal of Petroleum Science and Engineering*, 60(3-4), 183-193.

Korsnes, R. I., Madland M.V., Vorland, K.A.N., Hildebrand-Habel, T., Kristiansen, T.G., Hiorth, A. (2008), Enhanced chemical weakening of chalk due to injection of CO₂ enriched water, in *International Symposium of the Society of Core Analysts*, edited, SCA, Abu Dhabi, UAE.

Le Guen, Y., F. Renard, R. Hellmann, E. Brosse, M. Collombet, D. Tisserand, and J.-P. Gratier (2007), Enhanced deformation of limestone and sandstone in the presence of high PCO₂ fluids, *Journal of Geophysical Research*, 112(B05421).

Liteanu, E., and C. J. Spiers (2009), Influence of pore fluid salt content on compaction creep of calcite aggregates in the presence of supercritical CO₂, *Chemical Geology*, 265(1-2), 134-147.

Liteanu, E., C. J. Spiers, C. J. Peach, and J. H. P. De Bresser (in prep.), The effect of CO₂ on creep of wet calcite aggregates, *Journal of Geophysical Research*.

Lord, C. J., C. L. Johlman, and D. W. Rhett (1998), Is Capillary Suction a Viable Cohesive Mechanism in Chalk? , in *SPE/ISRM Rock Mechanics in Petroleum Engineering*, edited, p. 7, SPE, Trondheim, Norway.

Madland, M. V., A. Finsnes, A. Alkafadgi, R. Risnes, and T. Austad (2006), The influence of CO₂ gas and carbonate water on the mechanical stability of chalk, *Journal of Petroleum Science and Engineering*, 51(3-4), 149-168.

Meyer, J. P. (2007), State-of-the-art of carbon dioxide enhanced oil recovery (CO₂EOR) injection well technology, Contek Solutions LLC, Plano, Texas, USA.

Mollema, P. N., and M. A. Antonellini (1996), Compaction bands: a structural analog for anti-mode I cracks in aeolian sandstone, *Tectonophysics*, 267(1-4), 209-228.

Newman, G. H. (1983), The effect of water chemistry on the laboratory compression and permeability characteristics of some North Sea Chalks, *J. Pet. Technol.* , 35, 976-980.

Olsson, W. A. (1999), Theoretical and experimental investigation of compaction bands in porous rock, *J. Geophys. Res.*, 104(B 4).

Olsson, W. A., and D. J. Holcomb (2000), Compaction localization in porous rock, *Geophys. Res. Lett.*, 27, 3537-3540.

Papamichos, E., M. Brignoli, and F. J. Santarelli (1997), An experimental and theoretical study of a partially saturated collapsible rock, *Mechanics of Cohesive-frictional Materials*, 2(3), 251-278.

Peach, C. J. (1991), Influence of deformation on the fluid transport properties of salt rocks. , Universiteit Utrecht, Utrecht.

Peach, C. J., and C. J. Spiers (1996), Influence of crystal plastic deformation on dilatancy and permeability development in synthetic salt rock. , *Tectonophysics*, 256, 101-128.

Piau, J. M., and V. Maury (1994), Mechanical effects of water injection in chalk reservoirs, paper presented at Eurock '94, SPE/ISRM, Delft, Netherland

Pierre, A., J. M. Lamarche, R. Mercier, A. Foissy, and J. Persello (1990), Calcium as potential determining ion in aqueous calcite suspensions, *Journal of Dispersion Science and Technology*, 11(6), 611 - 635.

Plummer, L. N., and E. Busenberg (1982), The solubilities of calcite, aragonite and vaterite in CO₂-H₂O solutions between 0 and 90°C, and an evaluation of the aqueous model for the system CaCO₃-CO₂-H₂O, *Geochimica et Cosmochimica Acta*, 46(6), 1011-1040.

Pokrovsky, O. S., and J. Schott (2002), Surface Chemistry and Dissolution Kinetics of Divalent Metal Carbonates, *Environmental Science & Technology*, 36(3), 426-432.

Renard, F., E. Gundersen, R. Hellmann, M. Collombet, and Y. Le Guen (2005a), Numerical modeling of carbon dioxide sequestration on the rate of pressure solution creep in limestone: Preliminary results, *Oil & Gas Science and Technology*, 60, 381-399

Renard, F., E. Gundersen, H. R., M. Collombet, and Y. Le Guen (2005b), Numerical modeling of carbon dioxide sequestration on the rate of pressure solution creep in limestone: Preliminary results, *Oil & Gas Science and Technology*, 60, 381-399

Risnes, R., and O. Flaageng (1999), Propriétés mécaniques de la craie : interactions fluide-craie et aspects micro-mécaniques, *Oil & Gas Science and Technology*, 54(6), 751-758.

Risnes, R. (2001), Deformation and yield in high porosity outcrop chalk, *Physics and Chemistry of the Earth, Part A: Solid Earth and Geodesy*, 26(1-2), 53-57.

Risnes, R., H. Haghghi, R. I. Korsnes, and O. Natvik (2003), Chalk-fluid interactions with glycol and brines, *Tectonophysics*, 370(1-4), 213-226.

Risnes, R., M. V. Madland, M. Hole, and N. K. Kwabiah (2005), Water weakening of chalk - Mechanical effects of water-glycol mixtures, *Journal of Petroleum Science and Engineering*, 48, 21-36.

Roehl, P. O., and P.W. Choquette (1985), Carbonate Petroleum Reservoirs, 622.

Rutter, E. H. (1976), The kinetics of rock deformation by pressure solution, *Philosophical Transactions of the Royal Society of London*, 283, 203- 219.

Safaricz, M., and I. Davison (2005), Pressure solution in chalk, *AAPG Bulletin*, 89(3), 383-401.

Schroeder, C., S. Houyou, P. Illing, P. Mathieu, and A. Monjoie (2001), Combination of enhanced oil recovery and near zero CO₂ emission power plants in 1th European Symposium On Improved Oil Recovery, edited, Amsterdam, The Netherlands.

Scott Jr., T. E., Y. Aboulseiman, and M. Zaman (2001), Acoustical Imaging and Mechanical Properties of Soft Rock and Marine Sediments 56 pp, Rock Mechanics Institute, Oklahoma.

Segnit, E. R., H. D. Holland, and C. J. Biscardi (1962), The solubility of calcite in aqueous solutions--I The solubility of calcite in water between 75° and 200° at CO₂ pressures up to 60 atm, *Geochimica et Cosmochimica Acta*, 26(12), 1301-1331.

Shah, K. R., and T. F. Wong (1997), Fracturing at contact surfaces subjected to normal and tangential loads, *International Journal of Rock Mechanics and Mining Sciences*, 34(5), 727-739.

Strand, S., E. J. Høgenesen, and T. Austad (2006), Wettability alteration of carbonates--Effects of potential determining ions (Ca²⁺ and SO₄²⁻) and temperature, *Colloids and Surfaces A: Physicochemical and Engineering Aspects*, 275(1-3), 1-10.

Teufel, L. W., D. W. Rhett, and H. E. Parrel (1991), Effect of reservoir depletion and pore pressure drawdown in in-situ stress and deformation in the Ekofisk field, North Sea, paper presented at 32nd U.S. Rock Mechanics Symposium.

Tondi, E., M. Antonellini, A. Aydin, L. Marchegiani, and G. Cello (2006), The role of deformation bands, stylolites and sheared stylolites in fault development in carbonate grainstones of Majella Mountain, Italy, *Journal of Structural Geology*, 28(3), 376-391.

Wong, T.-f., and P. Baud (1999), Mechanical Compaction of Porous Sandstone, *Oil & Gas Sci. and Tech. - Rev. IFP*, 54(6), 715-727.

Wong, T.-f., P. Baud, and E. Klein (2001), Localized failure modes in a compactant porous rock, *Geophysical Research Letters*, 28, 2521-2524.

Zhang, X., and C. J. Spiers (2005a), Effects of phosphate ions on intergranular pressure solution in calcite: An experimental study, *Geochimica et Cosmochimica Acta*, 69(24), 5681-5691.

Zhang, X., and C. J. Spiers (2005b), Compaction of granular calcite by pressure solution at room temperature and effects of pore fluid chemistry, *International Journal of Rock Mechanics and Mining Sciences*, 42(7-8), 950-960.

Zubtsov, S., F. Renard, J.-P. Gratier, D. K. Dysthe, and V. Traskine (2005), Single-contact pressure solution creep on calcite monocrystals, *Geological Society, London, Special Publications*, 243(1), 81-95.

Zuddas, P., and A. Mucci (1994), Kinetics of calcite precipitation from seawater: A classic chemical kinetics description for strong electrolyte solutions., *Geochim. Cosmochim. Acta*, 58, 4353-4362.

Chapter 5

ABSTRACT

Maintaining mechanical integrity of wellbore cements, during CO₂ injection and storage into depleted oil and gas reservoirs, is needed to ensure long-term storage safety and efficiency. In this paper, we evaluate the effects of supercritical CO₂ on the mechanical behaviour of wellbore cement (Class A, Portland cement) and construct strength envelopes for this type of material, which is typically present as a cement sheath or plug in many reservoirs considered for CO₂ storage. This was done by means of conventional triaxial deformation experiments, which were employed at simulated reservoir conditions, i.e. temperature of 20-80°C, confining pressures in the range of 1.5-30 MPa and pore fluid pressures of 0-10 MPa. Increasing temperature from 20 to 80°C in dried samples was found to result in a small strengthening effect. Drastic strength reduction was observed in samples deformed under wet conditions, whereas the addition of supercritical CO₂ produce a small strengthening effect in comparison with the wet samples, especially at high effective confining pressures ($P_{eff} > 15$ MPa). The weakening effect of water was attributed to a lowering of the surface energy of the cement-fluid interface, which promotes equilibrium crack extension, and to water-enhanced subcritical crack growth. The small strengthening effect determined by CO₂ injection most likely occurred most likely as a direct result of an increase in the net surface energy, compared to the wet samples, and to a decrease in subcritical crack growth rates upon addition of supercritical CO₂. Combining our strength envelopes with calculations on the stress development in wellbore cement plugs suggest that stress changes in Class A cement plugs, associated with CO₂ injection into depleted gas or oil reservoirs overlain by a typical caprock, pose little risk for loss of CO₂ storage integrity through wellbore leakage.

Based on:

Liteanu E., Spiers C.J., Peach C. J. - Mechanical failure of wellbore cement and the influence of supercritical CO₂. *Cement and concrete research* (submitted)

5.1. Introduction

Storage of captured CO₂ in depleted oil and gas reservoirs is currently seen as one of the most feasible ways of reducing greenhouse gas emissions to the atmosphere [Bachu, 2003; Gozalpour *et al.*, 2005; *International Panel on Climate Control*, 2005; Bachu, 2008]. Key to evaluating this concept, and to storage site selection, is the assessment of system integrity – in other words, of the potential for CO₂ leakage. Possible leakage paths include natural faults and fractures present in the reservoir and/or caprock [*International Panel on Climate Control*, 2005; Pruess, 2005; Ambrose *et al.*, 2008], but also man-made paths such as wells drilled through the caprock. Indeed, leakage via abandoned exploration, production and injection wells is widely seen as posing the most significant risk to system integrity [Gasda *et al.*, 2004; *International Panel on Climate Control*, 2005; Pruess, 2005; Carey *et al.*, 2007; Hofstee *et al.*, 2008; Bachu and Bennion, 2009]. Depleted oil and gas reservoirs are perforated by a large number of production and exploration wells, especially on-shore. More than 300 000 such wells are present throughout the province of Alberta, Canada, reaching a local density of up to 4 wells/km² [Gasda *et al.*, 2004]. Around 1800 wells perforate SACROC Unit (Texas, USA) at a mean density of 8-9 wells/km² [Meyer, 2007]. Respectively 51 and 5 wells penetrate the relatively small De Lier gas field and Barendrecht/Barendrecht-Zeidewij fields in The Netherlands [Hofstee *et al.*, 2008].

Wellbores are usually lined with a steel casing, surrounded by a cement sheath to prevent fluid migration along the annular region between the casing and surrounding rock (Figure 5.1). They are generally sealed and plugged with cement upon abandonment, in order to block the vertical migration of fluids (Figure 5.1). However, wellbores may still pose a leak risk due to poor completion or abandonment procedures, due to geochemical degradation of the cement or casing, or due to geomechanical failure of the cement, of the casing, or of the caprock-cement or cement-casing interfaces [Bonett and Pafitis, 1996; Mainguy *et al.*, 2007]. To assess the potential for CO₂ leakage and to design mitigation measures, data concerning the long-term chemical and mechanical behaviour of wellbore cements are therefore needed.

To date, most investigations into the long-term CO₂ sealing capacity of wellbore systems have consisted of laboratory experiments on geochemical degradation of the cement and the effect of this on porosity and permeability [Duguid *et al.*, 2005; Barlet-Gouédard *et al.*, 2006; Kutchko *et al.*, 2006; Barlet-Gouédard *et al.*, 2007; Carey *et al.*, 2007; Kutchko *et al.*, 2007; Kutchko *et al.*, 2008; Rimmelé *et al.*, 2008; Bachu and Bennion, 2009; Barlet-Gouédard *et al.*, 2009]. The results for typical wellbore cements, such as Portland Class G or H, are often highly variable. Porous degradation fronts penetrating a drastic 20 - 25 mm have been reported to develop after one year of immersion in large volumes of (freely convecting) CO₂-water solutions at a pressure (P) of 28 MPa and temperature (T) of 90°C [Barlet-Gouédard *et al.*, 2006]. Similar fronts, but less than 1 mm thick, have been reported to form on comparable time scales at 50°C and pressures ranging from 0.1-30 MPa [Duguid *et al.*, 2005; Kutchko *et al.*, 2008]. By contrast, flow-through experiments

conducted on confined samples by *Bachu and Bennion*, [2009] at an external confining pressure (P_c) of 29 MPa and a mean internal fluid pressure of 15 MPa at 65°C, showed a decrease in permeability to CO₂-saturated water from 10⁻¹⁹ m² to 10⁻²⁰ m² after 90 days. In addition, Class A wellbore cement samples recovered from the well-known SACROC Unit in the Permian Basin of West Texas, after exposure to supercritical CO₂ over 30 years of enhanced oil recovery (EOR), operations retain their sealing capacity despite clear evidence of carbonation [*Carey et al.*, 2007].

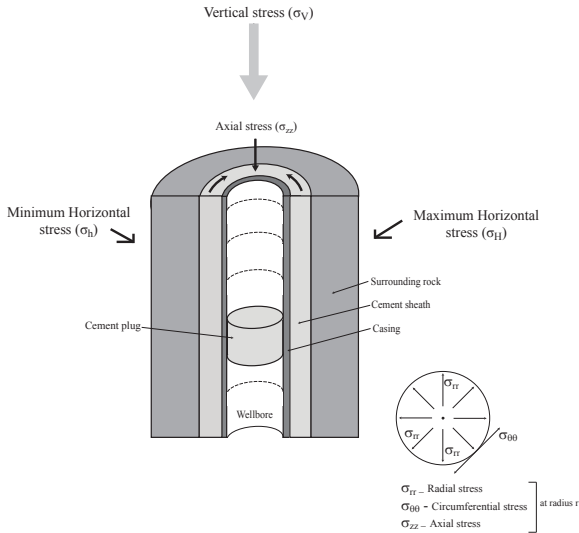


Figure 5.1. Semi-schematic representation of a wellbore, including the steel casing, cement sheath and cement plug.

On this basis, and since the potential for free convection of fluid is generally limited under *in-situ*, wellbore conditions, it seems unlikely that geochemical degradation of wellbore cement will prove problematic. However, little attention has been paid to the effects of CO₂ injection on mechanical behaviour. Indeed, virtually no data are available on how injection of supercritical CO₂ may affect the failure behaviour of cement through coupled chemical-mechanical effects, or on how stress changes in the reservoir may affect mechanical integrity in the presence of CO₂. This is surprising, as mechanical failure of wellbore cement has been widely identified as a potential cause of fluid leakage from reservoirs [*Bonett and Pafitis*, 1996; *Dusseault et al.*, 2000; *Kutchko et al.*, 2006; *Mainguy et al.*, 2007; *Bachu and Bennion*, 2009].

Focusing now on these mechanical aspects, it is well known that reservoir pressure changes, due to depletion or fluid injection, can lead to deformation and/or failure of the wellbore casing, of the cement sheath and of internal cement plugs [*Bonett and Pafitis*, 1996; *Dusseault et al.*, 2000]. As the pore fluid pressure decreases during depletion of a reservoir, the effective vertical stress increases, causing both compaction of the reservoir and associated surface subsidence [*Dusseault et al.*, 2000; *Hettema et al.*, 2002; *Settari*, 2002; *Mainguy et al.*, 2007]. Re-injection will in turn cause a decrease in the effective stress in the reservoir, with part of the compaction strain being recovered. Such changes

induce shear stresses at the interface between the wellbore system and the surrounding reservoir rock and caprock, as well as tensile stresses in the wellbore plug or cement sheath, which can potentially lead to failure of the cement [Dusseault *et al.*, 2000]. For a reliable assessment of wellbore integrity in the context of CO₂ storage, this means that data are needed on the compressive and tensile strengths of wellbore cement, on the possible effects of CO₂ on these, and on stress path evolution during fluid depletion and injection.

This study aims to provide new data on the failure behaviour of wellbore cement and on the effects of water and supercritical CO₂ on its compressive strength under down-hole conditions. We investigate the mechanisms responsible for weakening seen in the presence of these pore fluids and look into the implications of such effects for the integrity of subsurface CO₂ storage systems. These issues were addressed by means of conventional triaxial compression tests performed on standard Class A wellbore cement, cured for 6 months as opposed to the immature curing times employed in most previous studies [Philippacopoulos and Berndt, 2000; Barlet-Gouédard *et al.*, 2007; Xie *et al.*, 2008; Barlet-Gouédard *et al.*, 2009]. The tests were carried out on dried, wet and water/CO₂-saturated samples at temperatures of 20 and 80°C, at confining pressures of 1.5-30 MPa and at pore fluid pressures up to 10 MPa, thus approaching reservoir P- T conditions at 2-3 km depth. The data are used to construct failure envelopes, which are then coupled with previous geomechanical modeling work to assess wellbore integrity in the context of CO₂ storage.

5.2. Experimental method

5.2.1 Sample preparation and curing

The present experiments were performed on cylindrical samples of Class A Portland cement (ENCI, The Netherlands), prepared using a water:cement (w:c) ratio of 0.5. This material is representative for the wellbore cement used in oil and gas fields throughout The Netherlands prior to 1980. This type of cement has also been widely used elsewhere in the world, for example in some of the wells penetrating the SACROC Unit of West Texas [Carey *et al.*, 2007].

The cement slurry was prepared in accordance with American Petroleum Institute specifications (ISO/API 10B, section 5) using fresh water. After mixing the cement with water, the slurry was degassed under vacuum and slowly poured into cylindrical molds of 85 mm length and 35 mm diameter. It was then cured for 48 hours in a water bath at 58°C at atmospheric pressure. The cured cylindrical samples were subsequently removed from the molds and furthered cured for 6 months at room temperature, in water-filled, airtight containers, to avoid exposure to atmospheric CO₂. Most previous studies on the effects of CO₂ on wellbore cement were mainly performed on samples cured for only 7 to 31 days [Jacquemet *et al.*, 2005; Barlet-Gouédard *et al.*, 2006; Kutchko *et al.*, 2006; Barlet-Gouédard *et al.*, 2007; Barlet-Gouédard *et al.*, 2009]. While cements employed

in laboratory testing are usually characterized by 28-day compressive strength values, curing over 6 months results in at least a 20 % strength increase, which much more closely approximates long-term values [Çolak, 2006]. This compressive strength increase is due to ongoing precipitation of hydration products such as calcium silicate hydrate (C-S-H or $3\text{CaO}\cdot 2\text{SiO}_2\cdot 4\text{H}_2\text{O}$), which results in a progressively denser and homogeneous matrix. Indeed, porosity measurements on our samples showed that the 6-months curing led to a reduction of porosity from 42 % to 36 %. Our long-term curing approach thus provided us with cement cores as similar as possible to the material present in many abandoned wells in The Netherlands (e.g. de Lier Field) and in the USA (e.g. the SACROC Unit).

Following the 6-month wet-curing period, the samples were cut to length, to obtain cylinders measuring 75 mm in length by 35 mm in diameter. Prior to conducting triaxial tests on dry cement samples, the cylinders were dried in air at 60°C until a constant weight was obtained, which took approximately 6 days. This drying method was chosen to minimize the formation of microcracks and the dehydration of ettringite ($(\text{CaO})_6(\text{Al}_2\text{O}_3)(\text{SO}_3)_3\cdot 32\text{H}_2\text{O}$) present in the samples [Taylor, 1992; Yurtdas et al., 2006]. The dried samples were then tested immediately. In experiments performed on wet samples, with and without CO_2 , undried cylinders were cut to length and returned to the wet curing environment before use. Once loaded into the triaxial testing machine, pore fluid pressure was applied, ensuring re-saturation. The pore fluid used consisted of a chemically saturated solution obtained by stirring crushed, cured samples with water, while boiling for 48 hours to prevent carbonation.

5.2.2 Experimental apparatus and data acquisition

Our experiments were performed using a conventional, triaxial deformation apparatus, designed for axi-symmetrical compression of cylindrical samples. The apparatus is shown schematically in Figure 5.2 and is described in detail by [Peach, 1991] and [Peach and Spiers, 1996]. It consists of an externally heated pressure vessel, which uses silicone oil as confining medium, connected via high-pressure tubing to an auxiliary pressure vessel, such that the system volume is nominally constant. Axial load is applied to the sample by means of a pressure-balanced piston assembly, located between the two pressure vessels. During loading of the sample, the confining pressure is maintained constant by a servo-controlled volumetric pump or volumometer. Confining pressure is measured using a Jensen pressure transducer (100 MPa range, resolution ± 0.02 MPa). Axial load on the sample is measured using a DVRT-based, semi-internal load cell located at the top of the vessel (400 kN range, resolution ± 35 N, DVRT = differential variable reluctance transformer).

Piston displacement is measured externally (at the yoke in Figure 5.2) using a high-precision LVDT (linear variable differential transformer, 100 mm range, resolution ± 0.8 μm). Aqueous pore fluid is introduced into the sample at fixed pressure via a pore pressure system, which is controlled by an independent servo-pump. The pore fluid pressure is measured using a second Jensen pressure transducer (50 MPa pressure range, resolution

± 0.02 MPa). Supercritical CO₂ is introduced into solution-flooded samples at pressures up to 10 MPa, using an ISCO 65 D servo-controlled syringe-pump, fitted with a Honeywell TJE pressure transducer (150 MPa range, resolution ± 10µl). The temperature of the external furnace is controlled by a proportional-integral-derivative or PID controller (400°C range, resolution ± 0.02°C) plus sheathed, type K thermocouple located in the windings. The temperature of the sample is measured using similar thermocouples located at the top and at the bottom of the sample.

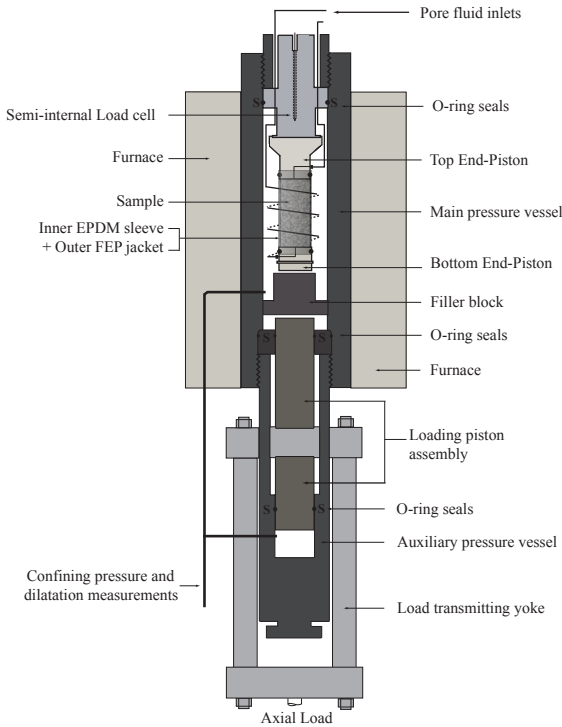


Figure 5.2. Semi-schematic representation of the central elements of the conventional, triaxial testing machine used in this study, including the main and auxiliary pressure vessels, the sample assembly and the pore fluid inlets.

In the present study, the signals corresponding to axial load, piston displacement, confining pressure, sample temperature, oil volume change, pore fluid pressure, pore fluid volume, CO₂ pressure and CO₂ volume change were logged by means of a PC equipped with a 12-bit National Instruments VI logger system. The raw displacement and volume-change data were accurately corrected for both axial and volumetric apparatus distortion and for thermal expansion/contraction effects in the confining and pore fluid systems, using pre-determined calibrations. Final processing yielded differential stress ($\sigma_1 - \sigma_3$), axial strain (ϵ), volumetric strain (ϵ_v) and axial strain rate ($\dot{\epsilon}$) values as functions of time (t).

5.2.3 Sample assembly and testing procedure

The experiments were performed at a displacement rate yielding a near constant strain rate ($\dot{\epsilon}$) of $\sim 5 \times 10^{-5} \text{ s}^{-1}$, using samples subjected to four different sets of conditions:

1. Dried samples deformed at 20°C, at confining pressures (P_c) in the range 1.5 - 30

- MPa,
2. Dried samples deformed at 80°C, at confining pressures (P_c) in the range 1.5 - 30 MPa,
 3. Wet samples deformed at 80°C, at a pore fluid pressure (P_f) of 5 MPa and effective confining pressures (P_{eff}) in the range 1.5-30 MPa,
 4. Samples deformed wet with supercritical CO₂ at a CO₂ pressure (P_f) of 10 MPa, at 80°C and at effective confining pressures (P_{eff}) in the range 1.5-30 MPa. These experiments will be referred to throughout as the wet/CO₂ tests.

Prior to testing, each sample was jacketed in an inner, CO₂ resistant, Ethylene Propylene Diene, M-class rubber (EPDM) sleeve, and an outer Fluorinated Ethylene Propylene (FEP) jacket to prevent leakage of the confining medium into the sample assembly. The jacketed sample was then located between the top and bottom end-pistons shown in Figure 5.2. Each piston face is radially and concentrically grooved and features a central bore connected to the pore fluid system. This allows fluid injection and promotes distribution of pore fluid over the sample ends. Perforated Teflon sheets were placed between the end-pistons and the sample to reduce friction. The outer FEP jacket was sealed against the end-pistons using a wire tourniquet method with underlying EPDM band countersunk in the end-piston outer surfaces. The completed sample assembly was subsequently connected to the removable load cell and pore fluid pipes, and the whole assembly inserted into the main pressure vessel.

Dried samples were then heated by means of the external furnace, to the required temperature (~3 hours), while maintaining the confining pressure below the value assigned for each test, with the pore fluid system drained to air. When the desired temperature was reached, the confining pressure assigned for each test was applied. In the case of wet and wet/CO₂ experiments, the samples were heated under undrained conditions, maintaining the confining pressure at a value around 1 MPa, while the pore fluid pressure remained at around 0.1 MPa through buffering by the small amount of air trapped in the pore fluid system. When the test temperature was reached, the confining and pore fluid pressures were simultaneously increased until the desired effective pressure was attained. In the wet/CO₂ tests, the CO₂ and the solution within the sample were then allowed to reach equilibrium for ~4 hours before testing (i.e. until the CO₂ volume ceased to change).

The samples were subsequently deformed at constant confining pressure, temperature, pore fluid pressure and piston displacement rate. The tests were run until shortly after the samples failed in a brittle mode, or until a strain of ~5-10 % was reached in cases where samples showed semi-brittle or ductile strain-hardening behavior. In the case of selected CO₂-bearing samples, a deform-hold-deform procedure was employed to investigate post-yield or post-failure re-strengthening or healing behavior. These samples were held at fixed position for 3 days after yield or failure, and allowed to stress-relax in the presence of supercritical CO₂. After the 3-day period, the deformation test was restarted and continued until additional strains up to 5 % were reached.

The tests were terminated by unloading the samples, releasing the pore fluid pressure,

and then the confining pressure, followed by cooling down the apparatus and finally extracting the sample assembly. The samples were then carefully removed from the jacket-piston assembly and oven dried at 60°C prior to resin impregnation and thin sectioning.

5.3. Results

All experiments reported are listed in Table 5.1 along with the conditions at which the tests were performed and key parameters measured. Compressive stresses (σ_j), compressive axial strains (ϵ), compressive strain rate ($\dot{\epsilon}$) and dilatant volume changes (e_v) are taken as positive throughout this paper.

Sample ID	T [°C]	P [MPa]	P _f [MPa]	P _{eff} [MPa]	Pore fluid	σ_y [MPa]	$\sigma_{1\%}$ [MPa]	σ^* [MPa]	E [GPa]	Final ϵ [%]	Final e_v [%]
Dry samples deformed at 20°C											
CEM-1	20	1.5	-	1.5	Dry	41.65	30.26	45.20	6.01	1.43	0.15
CEM-2	20	5	-	5	Dry	32.68	38.76	40.00	5.03	3.47	-0.20
CEM-3	20	10	-	10	Dry	37.36	41.47	51.78	4.67	5.37	-1.42
CEM-4	20	20	-	20	Dry	24.50	34.90	†	4.71	9.66	-3.90
CEM-5	20	30	-	30	Dry	31.14	44.10	†	5.77	3.87	-3.02
Dry samples deformed at 80°C											
CEM-6	80	1.5	-	1.5	Dry	29.30	31.51	32.00	3.91	1.25	-1.19
CEM-7	80	5	-	5	Dry	36.79	42.63	47.71	4.78	2.01	-1.68
CEM-8	80	10	-	10	Dry	39.46	48.35	61.47	5.64	3.02	-4.78
CEM-9	80	20	-	20	Dry	33.75	42.49	†	5.11	5.66	-5.94
CEM-10	80	30	-	30	Dry	25.98	37.15	†	5.00	5.89	-7.83
Wet samples deformed at 80°C											
CEMs-1	80	6.5	5	1.5	Wet	19.29	24.82	26.22	2.92	3.13	-2.67
CEMs-2	80	10	5	5	Wet	22.34	23.22	26.30	2.43	5.82	-5.38
CEMs-3	80	25	5	20	Wet	9.83	16.01	†	1.89	4.80	-7.13
Wet/CO₂ bearing samples deformed at 80°C											
CEMCO ₂ -1*	80	11.5	10	1.5	Wet/CO ₂	18.56	21.33	22.42	3.37	5.09	-0.08
CEMCO ₂ -2	80	15	10	5	Wet/CO ₂	19.35	23.40	28.18	2.89	3.29	-2.36
CEMCO ₂ -3*	80	30	10	20	Wet/CO ₂	20.02	24.78	†	3.18	4.04	-4.45
CEMCO ₂ -4	80	40	10	30	Wet/CO ₂	12.91	20.32	†	2.67	3.65	-4.84

Table 5.1. List of the experiments reported and the experimental conditions at which the tests were conducted.

T denotes the temperature at which the tests were performed, P_c is the confining pressure, P_f is the pore fluid pressure, P_{eff} is the effective confining pressure, σ_y is the yield stress taken at the departure of the stress-strain curves from linearity (departure from quasi-elastic behaviour), $\sigma_{1\%}$ is the differential stress supported by the samples at 1 % axial strain, σ^* is the peak differential stress at which the samples failed, E is the apparent Young's modulus obtained from a linear fit to the linear (elastic) part of the stress-strain curve.

Note: † Samples showing strain hardening with no peak strength.

* Samples tested using a deform-load-deform procedure to investigate post-yield or post-failure re-strengthening or healing behaviour.

The principal compressive stresses are denoted as σ_j with $\sigma_1 > \sigma_2 = \sigma_3$. Axial differential stress is defined as the principal stress difference ($\sigma_1 - \sigma_3$). The peak strength (σ^*) is defined as the maximum differential stress ($\sigma_1 - \sigma_3$) supported by the sample. Failure is defined as the loss of strength of a given sample beyond the peak strength, while the yield stress (σ_y) is taken as the point of departure of the stress-strain curves from linearity, i.e. from

(quasi-) elastic behaviour in the initial loading stage [Fredrich *et al.*, 1989]. The (apparent) Young's modulus (E) of each sample was calculated using this (quasi)-elastic, linear portion of the stress-strain curve.

5.3.1 Mechanical data

5.3.1.1 Dry samples deformed at room temperature

The complete set of differential stress and volumetric strain versus axial strain curves obtained for the samples tested under dry conditions at room temperature are presented in Figure 5.3. At low confining pressure ($P_c \leq 10$ MPa), the stress versus axial strain curves show initial, near-linear (quasi- elastic) loading behaviour up to yield stresses (σ_y) in the range 32 to 42 MPa, attained at ~ 0.6 . This is followed by strain hardening towards a differential stress peak at 40 to 52 MPa (σ^* , in Table 5.1), marking brittle or semi-brittle failure of the samples. Strain softening towards a residual strength level of 20-45 MPa followed the failure stage. At higher confining pressures, i.e. at 20-30 MPa, the stress-strain curves showed initial, near-linear loading followed at around 0.5% strain by yield at 24-31 MPa, and then by continuous strain hardening.

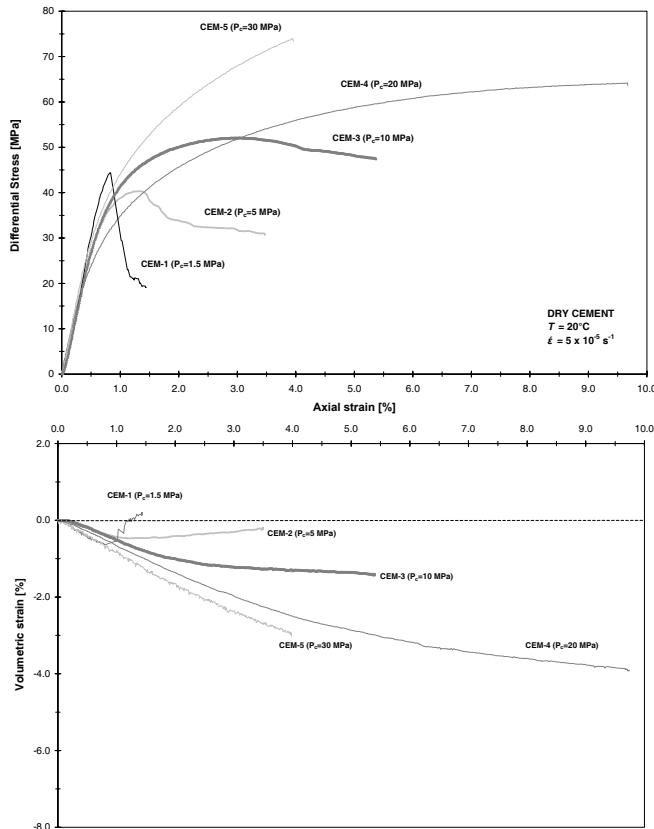


Figure 5.3. Differential stress ($\sigma_T - \sigma_3$) and volumetric strain (e_v) versus axial strain (e) curves for cement samples tested under dry conditions at 20°C. Imposed strain rate $\dot{\epsilon} = 5 \times 10^{-5} \text{ s}^{-1}$.

Across the full range of confining pressures investigated Young's modulus (E) values determined from the linear portion of the stress-strain curves vary between 4.7 to 6.0 GPa. Both yield stress (σ_y) and Young's modulus (E) values tend to decrease with increasing confining pressure, except at 30 MPa (Table 5.1).

The volumetric strain versus axial strain data (Figure 5.3) for all samples tested at 20°C show straightforward compaction (i.e. volume reduction) in the first 0.8 % axial strain. At low confining pressures (1.5-5.0 MPa), this was followed by dilatation (i.e. volume increase), which marked the inception of failure. At confining pressures of 10 to 30 MPa, the data show continuous compaction with increasing axial strain, at a gradually decreasing rate.

5.3.1.2 Dry samples deformed at 80°C

The differential stress and volumetric strain versus axial strain curves for dry samples tested at 80°C are shown in Figure 5.4.

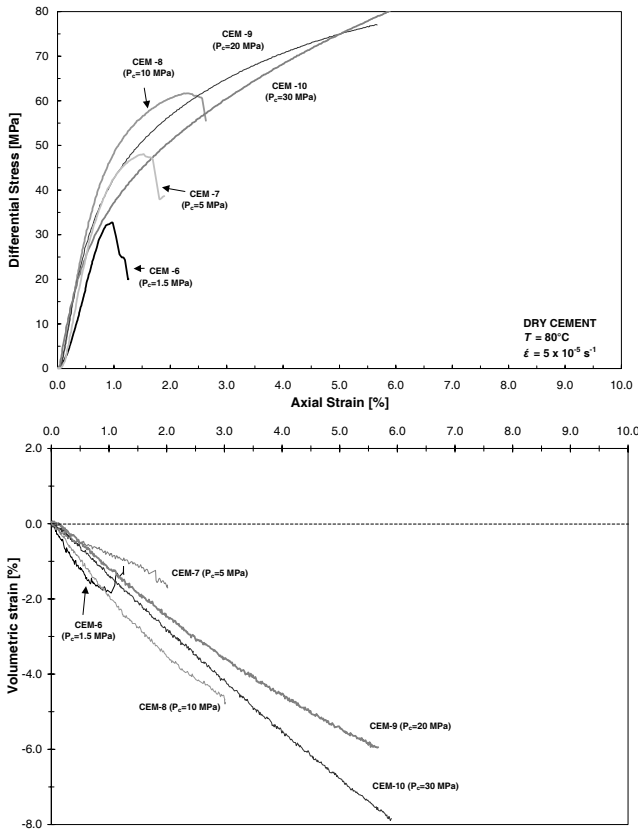


Figure 5.4. Differential stress ($\sigma_j - \sigma_3$) and volumetric strain (e_v) versus axial strain (e) curves for cement samples tested under dry conditions at 80°C. Imposed strain rate $\dot{\epsilon} = 5 \times 10^{-5} \text{ s}^{-1}$.

Samples deformed at confining pressures in the range 1.5-10 MPa show initial quasi-elastic loading followed by precursory yielding at stresses in the range 29-39 MPa, followed by well-defined differential stress peaks at 32 to 61 MPa. Strength drops to residual values

of 23 to 55 MPa follow the peak stress. In contrast, curves obtained for samples deformed at confining pressures of 20 and 30 MPa showed initial elastic loading, followed by yield at ~26-34 MPa, and then continuous strain hardening to final strains up to 5.6 to 6 %. Note that for the sample deformed at a confining pressure of 1.5 MPa, increasing temperature from 20 to 80°C led to a decrease in peak strength from 45 MPa to 32 MPa (Table 5.1), while at higher confining pressures (5-10 MPa) peak strengths were higher at 80°C than at room temperature.

The elastic moduli measured at 80°C fell in the range 3.9 to 5.6 GPa (Table 5.1). Both yield stress and Young’s modulus show an increase then a decrease with confining pressure (Table 5.1).

5.3.1.3 Wet samples deformed at 80°C

Differential stress and volumetric strain versus axial strain plots for the solution-saturated samples tested at 80°C are shown in Figure 5.5.

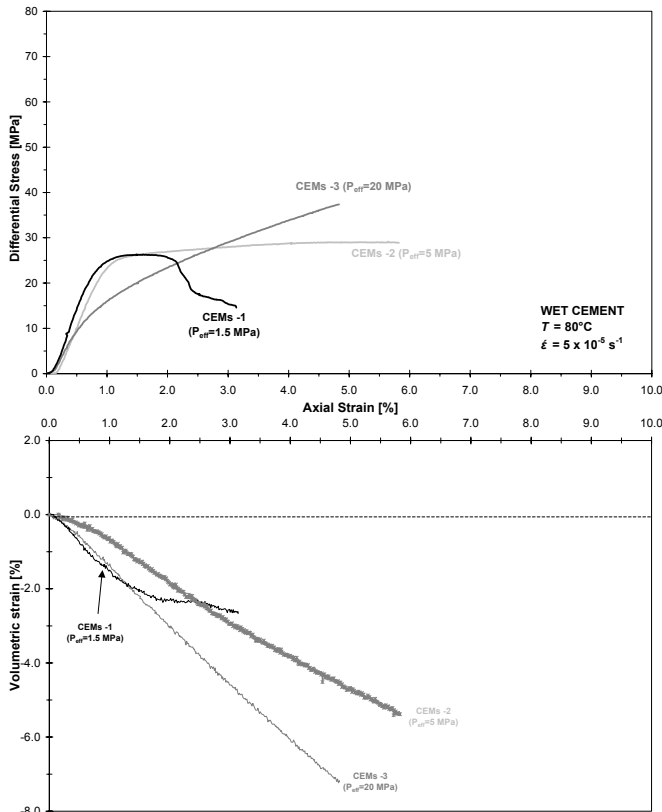


Figure 5.5. Differential stress ($\sigma_1 - \sigma_3$) and volumetric strain (e_v) versus axial strain (e) curves for cement samples tested under wet conditions at 80°C. Imposed strain rate $\dot{\epsilon} = 5 \times 10^{-5} \text{ s}^{-1}$.

At a 1.5 MPa effective confining pressure (CEMs-1), initial quasi-elastic loading was followed by yielding at ~19 MPa and a broad peak stress plateau, in which the sample accumulated an

axial strain of ~1 %. This was followed by marked strain softening towards a residual strength of ~15 MPa at 2-3 % strain. The differential stress versus axial strain curve for cement deformed at 5 MPa effective confining pressure (CEMs-2) showed yielding at ~22 MPa, giving way at ~1 % strain to more or less steady-state flow showing a broad peak strength of ~26 MPa. At 20 MPa effective pressure, continuous strain hardening occurred almost from the onset of loading, with marked yielding at around 10 MPa (CEMs-3). Clearly then, in comparison with the dry samples deformed at the same temperature (80°C) and effective confining pressures, the presence of the pore fluid solution phase resulted in a drastic reduction of both the yield and peak strengths (Table 5.1) - an effect which increased with increasing effective confining pressure (cf. Figure 5.5 and Figure 5.4). The apparent Young's modulus showed similarly lower values (1.8 to 2.9 GPa) in the wet samples (See Table 5.1).

The volumetric strain versus axial strain curves for the wet samples at deformed 80°C (Figure 5.5), show that at 1.5 MPa effective confining pressure, sample CEMs-1 underwent marked compaction up to the peak strength, followed by almost constant volume deformation during strain softening of the sample. At higher effective confining pressures (5-20 MPa), continuous compaction was observed, reaching volumetric strains of -5 to -7 %, at axial strains of around 5 %.

5.3.1.4 *Wet/CO₂ samples deformed at 80°C*

The mechanical data for the wet samples saturated with supercritical CO₂ and deformed at 80°C are shown in Figure 5.6. The sample deformed at 1.5 MPa effective confining pressure (CEMCO₂-1) initially shows near-linear behaviour in the stress vs. axial strain curve, followed by yielding at ~19 MPa and reaching a peak stress at around 22 MPa, similar to the value of 26 MPa obtained for wet material without CO₂. Strain softening followed the peak stress reading a steady value of ~19 MPa at 1.2 % axial strain. The sample deformed at 1.5 MPa effective confining pressure (CEMCO₂-1) initially shows near-linear behaviour in the stress vs. axial strain curve, followed by yielding at ~19 MPa and reaching a peak stress at around 22 MPa, similar to the value of 26 MPa obtained for wet material without CO₂. Strain softening followed the peak stress reading a steady value of ~19 MPa at 1.2 % axial strain.

The sample deformed at 1.5 MPa effective confining pressure (CEMCO₂-1) initially shows near-linear behaviour in the stress vs. axial strain curve, followed by yielding at ~19 MPa and reaching a peak stress at around 22 MPa, similar to the value of 26 MPa obtained for wet material without CO₂. Strain softening followed the peak stress reading a steady value of ~19 MPa at 1.2 % axial strain. Reloading of the sample (CEMCO₂-1), after 3 days of stress relaxation from 19 to 8 MPa at ~1.5 % axial strain, again led to a quasi-elastic response, giving way to more or less steady state flow at a stress level of 17 MPa, i.e. about 90 % of the post-peak residual strength. Increasing the effective confining pressure to 5 MPa led to similar yield behaviour at ~19 MPa, followed by ductile strain hardening flow, reaching a more or less steady state at 2 % strain. At higher effective confining pressures (20 and 30 MPa), yielding occurred at stresses varying from 20 to 13 MPa (CEMCO₂-3 and -4) and higher rates of post-yielding strain hardening were observed.

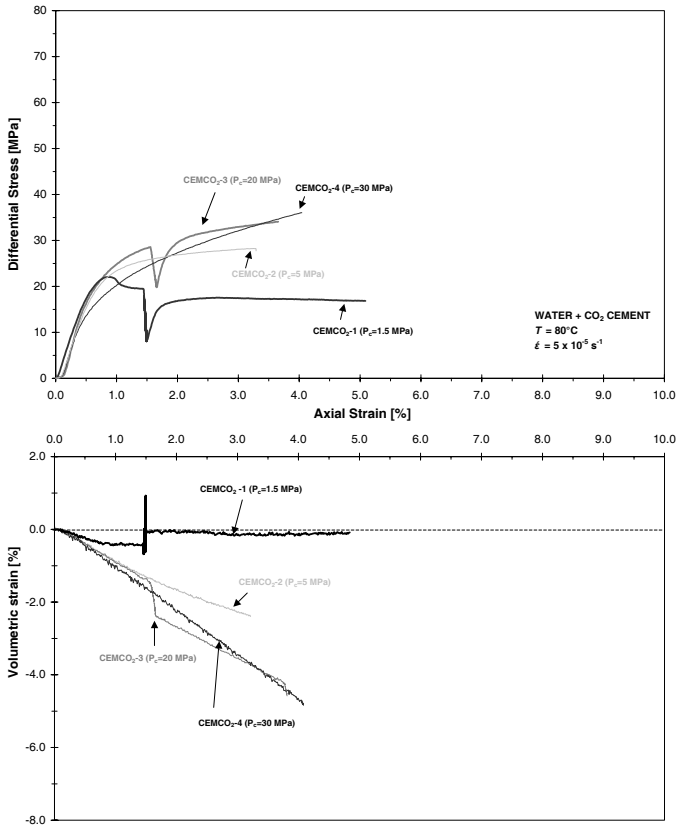


Figure 5.6. Differential stress ($\sigma_1 - \sigma_3$) and volumetric strain (e_v) versus axial strain (e) curves for wet/CO₂ samples deformed at 80°C. Imposed strain rate $\dot{\epsilon} = 5 \times 10^{-2} \text{ s}^{-1}$.

The data obtained for sample CEMCO₂-3 ($P_{eff} = 20 \text{ MPa}$) showed that it regained full strength upon reloading after 3 days of stress relaxation at $\sim 1.5 \%$ axial strain. In comparison with the samples compacted wet but without CO₂, the data obtained for the wet/CO₂ samples suggest minor weakening at low confining pressures, versus significant strengthening at higher confining pressure (cf. Figures 5.5 and 5.6, Table 5.1). Young's modulus increased due to the addition of CO₂ to values around 2.6 to 3.4 GPa.

The volumetric strain versus axial strain plots for the wet/CO₂ samples (Figure 5.6) show that at low confining pressure ($P_{eff} = 1.5 \text{ MPa}$), around 0.5 % compaction occurred prior to failure, followed by constant volume deformation beyond the peak strength. Stress relaxation at $\sim 1.5 \%$ axial strain led to a volume increase, followed by compaction to a nearly constant volumetric strain of -0.1 % after re-loading. At higher confining pressures (5-30 MPa), the samples showed continuous compaction to volumetric strains varying from -2.4 up to -4.8 % at axial strains in the range 3.3 to 4.0 %. Relaxation and reloading of sample CEMCO₂-3 ($P_{eff} = 20 \text{ MPa}$) at 1.5 % axial strain were respectively accompanied by minor dilatation and then sharp compaction.

5.3.2 Macroscopic failure mode

The dry samples deformed at 20 and 80°C and at confining pressures in the range 1.5-10 MPa showed brittle to semi-brittle failure evidenced by distributed axial cracks and localized, cohesive shear-fractures orientated at 35-40° to the compression direction (see Figure 5.7a).



Figure 5. 7. Photographs of the samples tested under various conditions. a) Sample CEM-1, deformed dry at 1.5 MPa confining pressure at 20°C, showing both axial cracks and shear fractures. b) Sample CEM-5 deformed dry at 30 MPa confining pressure at 20°C, showing compacted macro-pores. c) Sample CEMs-1 deformed wet at 1.5 MPa effective confining pressure at 80°C, showing brittle failure characterized by a single, cohesionless fracture. d) Sample CEMs-2 deformed wet at 5 MPa effective confining pressure at 80°C, showing failure through distributed shear fracture. e) Sample CEMCO₂-1 deformed wet in the presence of supercritical CO₂ at 1.5 MPa effective confining pressure and at 80°C, showing failure marked by discrete conjugate but cohesive shear-fractures. f) Sample CEMCO₂-4 deformed wet in the presence of supercritical CO₂ at 30 MPa effective confining pressure at 80°C, showing macroscopically uniform shortening and pore flattening.

The latter formed conjugate sets in some samples. Macropores observed in these samples retained the spherical shape and size exhibited by those seen in the undeformed material. By contrast, macroscopically homogeneous, ductile behaviour characterized dry samples deformed at confining pressures of 20 and 30 MPa. At these higher pressures,

we observed marked flattening of many of the visible macropores, suggesting local strains well in excess of the imposed axial shortening of 5-10 % (Figure 5.7b). However no macroscopic fractures or localized compaction bands were visible.

Wet material deformed at 80°C and at low effective confining pressure (sample CEMs-1, $P_{eff} = 1.5$ MPa) was characterized by strain localization and brittle failure on a single, cohesionless shear-fracture cross-cutting the sample at $\sim 30^\circ$ (Figure 5.7c). At 5 MPa effective pressure, pervasive conjugate shear cracks developed in the center of the sample, at $\sim 45^\circ$ to the compression direction, producing clear barreling (Figure 5.7d). With increasing confinement (i.e. $P_{eff} \sim 10$ -20 MPa), this mode of deformation gave way to macroscopically homogeneous ductile flow, again characterized by flattening of visible macropores (cf. Figure 5.7b). No evidence for pore flattening was found at 1.5-5 MPa effective confining pressure.

Turning now to the wet/CO₂ tests, sample CEMCO₂-1 deformed at 1.5 MPa effective pressure showed discrete, cohesive, conjugate shear fractures, as well as less prominent subvertical (axial) cracks, typical of brittle to semi-brittle behaviour (Figure 5.7e). Samples deformed with CO₂ at higher effective confining pressures again showed macroscopically homogenous ductile shortening, plus macropore flattening (Figure 5.7f).

5.3.3 Microstructural observations

Scanning Electron Microscopy (SEM) and energy-dispersive X-ray spectroscopy (EDX) analysis were used to investigate respectively the microstructure and mineralogical composition of the cement samples. Imaging was carried out in backscatter mode applied to polished thin sections. Immature cement, sampled for control purposes after only 48 hours of curing at the temperature of 58°C used for the initial preparation of our samples, showed a heterogeneous microstructure consisting of dense, ovoid clusters of intergrown portlandite ($\text{Ca}(\text{OH})_2$), aluminate ferrite ($\text{Ca}_4(\text{Al},\text{Fe})_2\text{O}_5$ or C_4AF) and calcium aluminate (CaAl_2O_4 or CA), embedded in a porous matrix of C-S-H gel, ettringite ($(\text{CaO})_6(\text{Al}_2\text{O}_3)(\text{SO}_3)_3 \cdot 32\text{H}_2\text{O}$) and portlandite grains and/or blebs (50 – 100 μm) (Figure 5.8a). Generally, the samples showed a relatively high porosity (42 % estimated from the difference in weight of dried vs. wet material), with pore sizes ranging from micrometer dimensions (micropores) up to hundreds of micrometers (macropores). The irregular pattern of microcracks seen in this material (Figure 5.8a), notably at the interface between the ovoid mineral clusters and matrix, developed during preparation of the sections used for SEM study and probably represents drying cracks.

Microscopic investigation of undeformed reference samples, cured for the full 6-months, showed a much more uniform, homogeneous microstructure (Figure 5.8b), characterized by a lower porosity (~ 36 %). The material consists of portlandite, ettringite and calcium aluminate grains, often with subeuhedral form and showing reaction rims of all three

Our fully (6-month) cured cement samples deformed dry at 20 and 80°C (e.g. sample CEM-6) show a homogeneous microstructure, similar to that of the undeformed reference samples. This is the case for both remote from the fractures developed at low confining pressures (1.5-5 MPa) and throughout the samples deformed at higher confining pressures (Figure 5.8c). Intergranular, intragranular and transgranular cracks oriented parallel to the

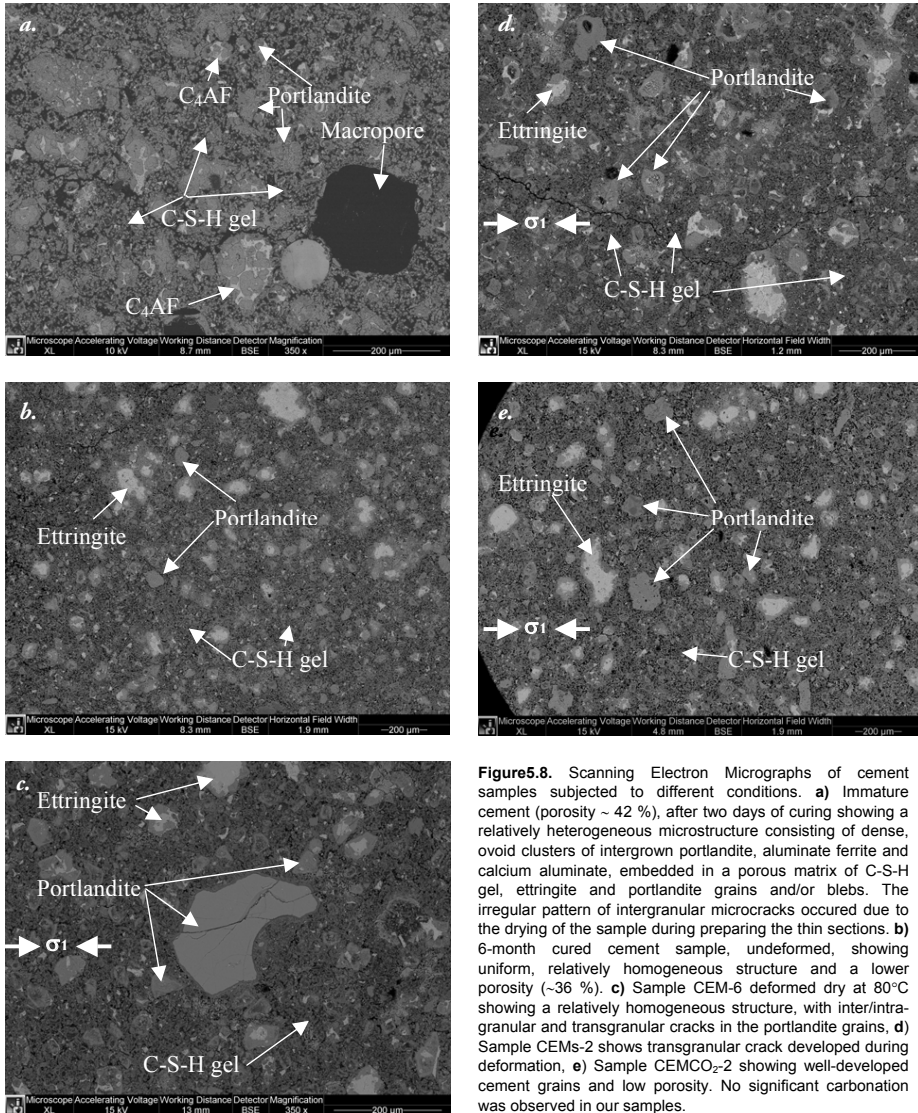


Figure 5.8. Scanning Electron Micrographs of cement samples subjected to different conditions. **a)** Immature cement (porosity ~ 42 %), after two days of curing showing a relatively heterogeneous microstructure consisting of dense, ovoid clusters of intergrown portlandite, aluminat ferrite and calcium aluminat, embedded in a porous matrix of C-S-H gel, ettringite and portlandite grains and/or blebs. The irregular pattern of intergranular microcracks occurred due to the drying of the sample during preparing the thin sections. **b)** 6-month cured cement sample, undeformed, showing uniform, relatively homogeneous structure and a lower porosity (~36 %). **c)** Sample CEM-6 deformed dry at 80°C showing a relatively homogeneous structure, with inter/intra-granular and transgranular cracks in the portlandite grains. **d)** Sample CEMs-2 shows transgranular crack developed during deformation. **e)** Sample CEMCO₂-2 showing well-developed cement grains and low porosity. No significant carbonation was observed in our samples.

direction of the axial stress are common in all samples but not pervasive (Figure 5.8c). Adjacent to the discrete shear fractures in samples deformed dry at low confining pressure, the porosity is visibly increased, defining a damage zone some 200-500 mm thick, but with no obvious gouge development.

Microscopic investigation of the cement samples deformed under wet conditions shows a broadly similar microstructure to the undeformed and dry-deformed samples but with a relatively high frequency of intergranular and transgranular cracks in conjugate orientations (Figure 5.8d). The shear fractures developed in wet samples at the lowest effective confining pressures investigated are bounded by a narrow damage zone of increased porosity and contain a core of fault gouge ~200 μm in thickness. The samples deformed wet in the presence of CO₂ (Figure 5.8e) show closely similar microstructures to

the wet samples deformed at both low and high pressures respectively.

Note that no significant carbonation or other reaction fronts were observed in any of our samples. Most probably the short-term duration of our tests was not enough for such phenomena to become important, though minor carbonation might have occurred during storage.

5.4. Discussion

The present results for maturely cured, Class A cement samples, deformed under dry conditions at 20 and 80°C, have shown a transition from brittle failure at very low (effective) confining pressure (1.5 MPa), through more pervasive semi-brittle behaviour at 5-10 MPa, to macroscopically fully ductile flow at pressures at 10-20 MPa and above. In the presence of cement-saturated pore fluid, similar behaviour occurs but with a 30-65 % reduction of failure and/or flow strength. Addition of CO₂ to the pore fluid has little further effect at low confining pressures. However, at high confining pressure (20 MPa) a major increase in strength was observed. In the following, the strength data obtained under the various conditions investigated are analyzed by constructing appropriate failure envelopes. This approach highlights minor effects of temperature, as well as the effects of pore fluid and adding CO₂ on the strength of the samples. The effects of experimental conditions on elastic stiffness are also considered. We go on to attempt to explain these effects, before considering the practical implications of our data in Section 5.

5.4.1 Strength envelopes and stiffness trends

5.4.1.1 Mohr-Coulomb envelopes

To summarize the compressive strength data obtained for our cement samples under the four sets of conditions investigated (Table 5.1), modified Mohr-Coulomb failure envelopes are presented in a so-called *P-Q* plot in Figure 5.9. Such plots represent stress space defined in terms of the differential stress $Q = (\sigma_1 - \sigma_3)$ versus the mean effective stress $P = \frac{\sigma_1 + \sigma_2 + \sigma_3}{3} - P_f$, and are widely used to represent failure criteria in soil and rock mechanics [Chen, 1984; Wong and Baud, 1999; Baud et al., 2000; Risnes et al., 2003]. The *P* and *Q* values used to construct the present strength diagrams are based on our yield stress data (σ_y) determined from the departure of the stress-strain curves from linearity, and on the differential stresses supported at 1 % axial strain ($\sigma_{1\%}$) – see Figures 5.9a and b respectively. Peak strengths are not plotted, because samples deformed at high (effective) confining pressures were characterized by continuous strain hardening to axial strains of up to 10 %.

The differential stresses supported at 1 % axial strain are introduced as a strength measure, since they fall just at or just before the point of failure for most samples that show a peak strength (Figure 5.9b). Envelopes constructed using the present definitions of *P* and *Q* at yield or at 1 % axial strain should accordingly be referred to as strength envelopes rather than failure envelopes.

Overall, the strength envelopes obtained for our cement samples are relatively flat in P - Q space, mostly showing a gentle positive slope at the lowest effective mean stresses (P -values) investigated, a maximum in strength at mid-range P -values and a negative slope at the highest effective mean stresses investigated (Figure 5.9). The dried samples, tested at 80°C mostly show 6-37 % higher strength than those tested at 20°C, with the exception of the samples tested at 1.5 and 30 MPa confining pressure, which showed 16-30 % lower strength. The wet samples are much weaker than the dry, showing strengths around 30-66 % of those exhibited by dried samples (see also Table 5.1). The wet/CO₂-saturated samples are also much weaker than the dried samples, however they are significantly stronger than the wet ones at high mean stresses.

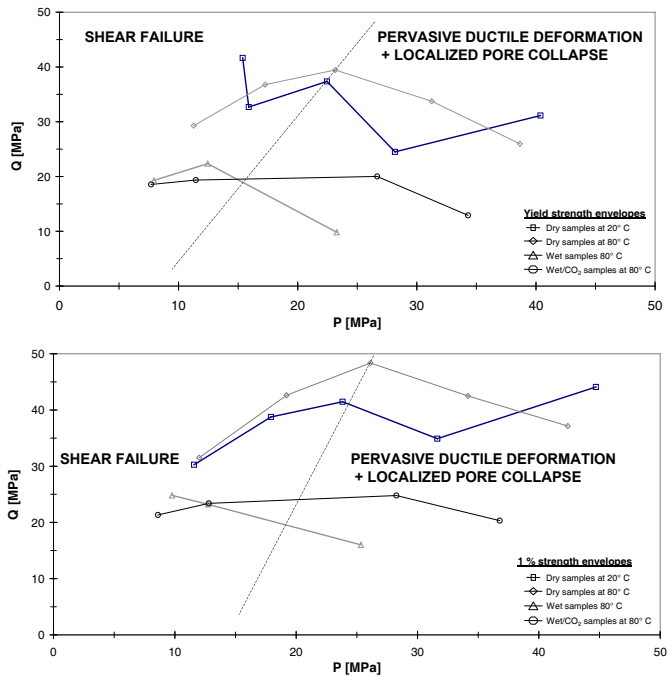


Figure 5.9. Modified Mohr-Coulomb diagram obtained for the tests reported in the present paper. Here, Q is defined as the differential stress ($\sigma_1 - \sigma_3$), while the mean effective stress P is the quantity $\frac{\sigma_1 + \sigma_3}{2}$. Strength envelopes constructed for yield stresses (σ_y) determined from the departure of the stress-strain curves from linearity. b) Envelopes constructed for the differential stresses supported at 1 % axial strain ($\sigma_{1\%}$). Macroscopic observation of sample failure mode shows that at low mean stresses shear failure characterizes our samples, whereas at higher mean stresses macroscopically uniform deformation and localized pore compaction dominate the deformation behaviour of our samples.

Though unusually flat compared with most rocks, our strength envelopes are similar to those obtained for highly porous materials (porosity of 30 to 45 %), such as Class A or G cement [Imran and Pantazopoulou, 2001; Sfer et al., 2002; Stiles, 2006], porous limestones and chalks [Papamichos et al., 1997; Homand and Shao, 2000; Palchik and Hatzor, 2004] or highly porous sandstones [Baud et al., 2000; Olsson and Holcomb, 2000; Wong et al., 2001]. The strength of such materials can generally be described by a

positively sloping shear failure envelope at low mean stresses, giving way at high mean stresses to a negatively sloping, elliptical end-cap that represents a transition to pervasive pore collapse and/or development of localized compaction bands [Mollema and Antonellini, 1996; Olsson, 1999; Issen and Rudnicki, 2001; Rudnicki, 2002].

On this basis, the present envelopes for Class A cement would seem to reflect mainly shear failure at the lowest effective mean stresses studied, i.e. at effective pressures of 1.5-5 MPa, giving way to pore collapse at the higher mean stresses – which is fully consistent with our sample scale observations on failure mode, including the marked flattening of macropores seen only in the high pressure ductile regime (cf. Figures 5.7 and 5.9). The slope of the envelopes for dry and wet samples at 80°C in the shear failure regime suggests cohesions (c) of respectively 8.2 and 8.1 MPa and coefficients of internal friction (μ) of 0.4 and 0.3 and internal friction angles (ϕ) of 21 and 16°. The flattened pores seen in the high-pressure regime are often much more strongly flattened than expected from the total axial strain of the samples (Figure 5.7b). The corresponding samples also show volumetric compaction strains that roughly track the axial strain in magnitude (see Figures 5.4-5.6), suggesting little lateral strain. We infer that samples deformed at high (effective) confining pressures, i.e. in the negatively sloping region of our strength envelopes (ductile field, Figure 5.9), at least in part deformed by compaction band development associated with the observed pore collapse, though discrete compaction bands were not visible in the microstructure.

We now briefly compare our yield strength envelopes for Class A cement (porosity \approx 36 %) with those obtained in previous studies on Class G cement and cement-silica mixtures [Philippacopoulos and Berndt, 2001; Xie et al., 2008]-see Figure 5.10. We found no other triaxial data for Class A cement to compare our results with.

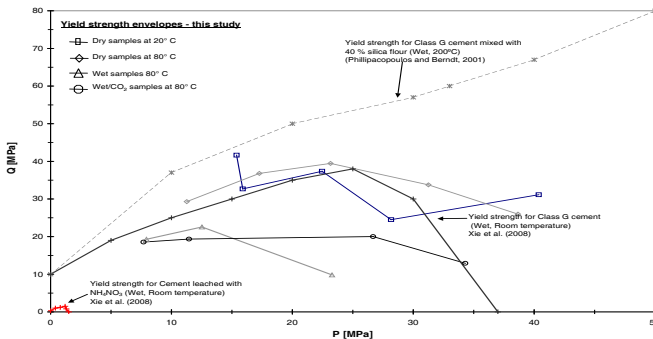


Figure 5.10. Comparison of the yield strength envelopes obtained in the present study on Class A cement, with the yield strength envelopes obtained in previous studies on Class G materials [Philippacopoulos and Berndt, 2001; Xie et al., 2008].

In comparison with the results of triaxial testing of wet Class G cement ($w:c = 0.44$, porosity = 36 %, cured for 27 days) at room temperature [Xie et al., 2008], our wet and wet/CO₂-bearing samples tested at 80°C show slightly lower yield strength at low mean

stresses (~ 20 % weaker), but much lower strength at higher mean stresses (40 to 60 % weaker), especially our wet samples without CO₂. Compared with Class G cement mixed with 40 % silica flour ($w:c = 0.44$, cured for 28 days) and deformed under wet conditions at 200°C [Philippacopoulos and Berndt, 2001], our wet and wet/CO₂ samples deformed at 80°C show a yield envelope that is 50-70 % weaker. Comparing the yield strengths of our samples with the yield envelopes obtained for Class G cement samples leached with ammonium nitrate to a porosity of 60 % [Xie *et al.*, 2008] shows that leaching to such porosities drastically reduces the compressive strength. However, as shown by Liteanu *et al.* [2009] see also Chapter 6, such major leaching will not occur under *in-situ* conditions. Overall, our comparison confirms that the composition of the material, the $w:c$ ratio, and the porosity of wellbore cement significantly influences its strength, and should be taken into careful account in designing and selecting future wellbore sealing materials.

5.4.1.2 Mogi envelopes

Recently, the Mogi failure criterion [Mogi, 1971; Al-Ajmi and Zimmerman, 2005; Al-Ajmi, 2006] has become preferred for wellbore stability analysis over the P - Q or Mohr-Coulomb criterion, as it takes into account the strengthening effect of σ_2 observed in true triaxial tests on rocks when $\sigma_2 > \sigma_3$, and because it generally provides the best fit to experimental data [Al-Ajmi and Zimmerman, 2005]. Similarly, it has been shown that empirically fitted Drucker-Prager criteria generally overestimate the strength of (rock) materials when applied to wellbore stability [Ewy, 1999; Al-Ajmi, 2006]. Mogi criteria thus lead to better results than obtained using the modified Mohr-Coulomb (P - Q) or Drucker-Prager criteria [Mogi, 1971; Wong and Baud, 1999; Vajdova *et al.*, 2004; Al-Ajmi and Zimmerman, 2005; Risnes *et al.*, 2005; Al-Ajmi, 2006; Talesnick and Shehadeh, 2007].

For conventional triaxial tests, where $\sigma_2 = \sigma_3$, Mogi failure criteria are expressed as relationships between the octahedral shear stress (τ_{oct}) written

$$\tau_{oct} = \frac{\sqrt{2}}{3}(\sigma_1 - \sigma_3) \quad (5.1)$$

and Mogi's mean (effective) normal stress ($\sigma_{m,2}$) defined

$$\sigma_{m,2} = \frac{\sigma_1 + \sigma_3}{2} - P_f \quad (5.2)$$

Mogi failure criteria are therefore typically expressed either as a linear relationship such as $\tau_{oct} = a + b\sigma_{m,2}$, where a and b can be expressed in terms of a cohesion and coefficient of internal friction, or as a power law of the form $\tau_{oct} = a\sigma_{m,2}^n$, where a and n are material parameters [Mogi, 1971; Al-Ajmi, 2006; Al-Ajmi and Zimmerman, 2006]. As shown by Al-Ajmi, [2006], a parabolic form of the Mogi criterion is generally the most suitable for weak and porous materials such as our cements. Indeed, we obtained the best fit to our yield stress and 1 % strength data using a parabolic form of the Mogi failure criterion written as $\tau_{oct} = a + b\sigma_{m,2} + c\sigma_{m,2}^2$. Our fits are plotted in Figures 5.11a and b. In this case, a , b and c are fitting parameters, which lose direct physical significance and can not be used to derive the cohesion and the coefficient of internal friction of the material - see Al-Ajmi, [2006]. The Mogi criteria and the values of the fitting parameters obtained for our cement samples

are listed in Table 5.2. Overall, the Mogi criteria show the same trends as the strength envelopes appearing in our P - Q plots.

Type of test	Parabolic Mogi criteria	R ²
Yield strength envelope		
Dry cement – 20°C	$\tau_{\text{oct}} = -0.015 \sigma_{m,2}^2 - 1.157 \sigma_{m,2} + 35.737$	0.335
Dry cement – 80°C	$\tau_{\text{oct}} = -0.029 \sigma_{m,2}^2 + 1.674 \sigma_{m,2} - 5.591$	0.989
Wet cement – 80°C	$\tau_{\text{oct}} = -0.069 \sigma_{m,2}^2 + 2.888 \sigma_{m,2} - 14.653$	1.000
CO ₂ -saturated water cement – 80°C	$\tau_{\text{oct}} = -0.018 \sigma_{m,2}^2 + 0.969 \sigma_{m,2} + 2.397$	0.922
1% strength envelope		
Dry cement – 20°C	$\tau_{\text{oct}} = -0.002 \sigma_{m,2}^2 + 0.317 \sigma_{m,2} + 10.678$	0.553
Dry cement – 80°C	$\tau_{\text{oct}} = -0.023 \sigma_{m,2}^2 + 1.649 \sigma_{m,2} - 6.496$	0.956
Wet cement – 80°C	$\tau_{\text{oct}} = 0.027 \sigma_{m,2}^2 - 1.728 \sigma_{m,2} + 39.204$	1.000
CO ₂ -saturated water cement – 80°C	$\tau_{\text{oct}} = -0.011 \sigma_{m,2}^2 + 0.730 \sigma_{m,2} + 5.643$	0.986

Table 5.2. Parabolic Mogi failure criteria fitted to the data obtained for the present cement samples, along with the associated correlation coefficient R².

The strong weakening effect caused by presence of water is confirmed in Figures 5.11a and b, as is the strengthening effect brought about by the addition of CO₂ to the pore fluid, especially at high mean (effective) normal stress ($\sigma_{m,2}$).

5.4.1.3 Stiffness trends

To evaluate any correlation between yield/failure strength and (apparent) elastic stiffness, we plotted the Young's Modulus values determined from the near-linear portion of our stress-strain curves versus the (effective) confining pressure applied to the samples (Figure 5.12a). The resulting E -plots crudely mirror the trends seen in our P - Q and Mogi envelopes for yield strength (cf. Figures 5.9, 5.11, 5.12a). The relationship between E and σ_y seen in various tests is further illustrated in Figure 5.12b. From Figure 5.12a and b, it is clear that at 80°C the presence of water resulted in 25-63 % reduction of E -values in comparison with the dried samples, whereas the injection of CO₂ brought about a 15-68 % increase of Young's modulus values relative to wet samples. Overall, our E -values lie in the range 4.7 to 6.0 GPa for dry samples deformed at 20°C, between 3.9 and 5.6 GPa for dry samples deformed at 80°C, decreasing to values of 1.9 to 2.9 GPa for wet samples and to between 2.6 and 3.4 GPa for wet/CO₂ samples. These E -values are much lower than literature data for wet Class G cements, which indicate a Young's modulus of 10 GPa [Philippacopoulos and Berndt, 2001], but closely similar to the value of 6 GPa previously reported for Class A cement [Stiles, 2006].

The correlation between our E -values and yield strength data may suggest that permanent deformation processes initiated in our samples during the loading stage [Jeong et al., 2007]. Our data imply that the processes occurring during this stage are water and wet/CO₂ enhanced, as the E -values decrease in these cases. Moreover, our differential stress versus axial strain curves have an S-shaped form, especially in the wet and wet/CO₂ samples (see Figures 5.5 and 5.6), supporting the hypothesis of a strain contribution by inelastic processes, such as early microcracking or pore collapse, during initial loading.

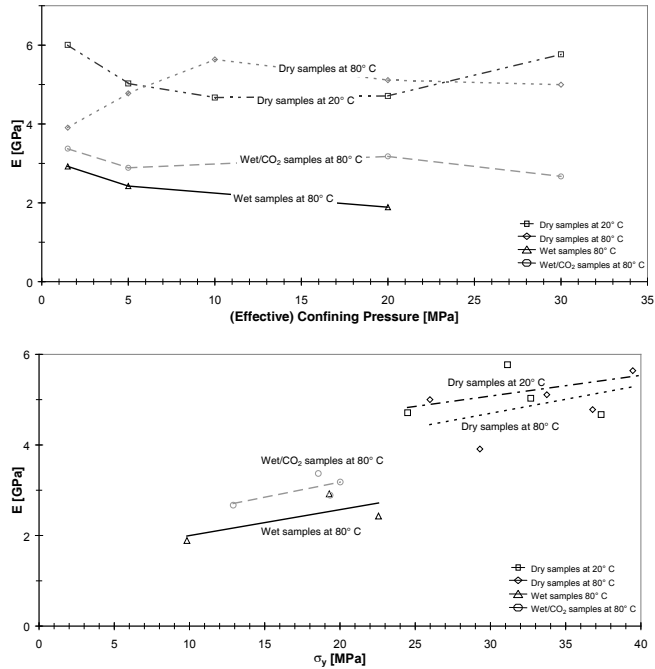


Figure 5.12. a) Young modulus (E) versus effective confining pressure (P_{eff}) for the present Class A cement samples. b) Young's modulus (E) versus yield strength (σ_y) data for all samples.

5.4.1.4 Effect of temperature on the strength of dry samples

The strength data and envelopes presented above show that dried samples deformed at 80°C mostly supported similar or slightly higher stresses than dry material deformed at 20°C, notably at yield, at failure, or at 1 % axial strain (e.g. Figures 5.9a and b). It is well established that water influences the strength of cements [Wittmann, 1973; Schneider *et al.*, 1986; Neville, 1996; Schneider and Chen, 1998], and our own results show that wet samples are much weaker than dried ones (by ~50 %). Moreover, our dry samples were tested with the pore fluid system open to the atmosphere (drained). So that water loss would have been possible at 80°C. It therefore seems likely that the tendency for increased strength in dry samples deformed at 80°C versus those deformed at 20°C might reflect additional drying of the samples at 80°C. The effects of drying are discussed further below.

5.4.2 Effects of water content and drying on strength

5.4.2.1 Background

As a basis for further discussion of the effects of temperature, water and CO₂, we now summarize present knowledge on the composition and the microstructure of cements, and on the water distribution within them.

Before mixing, Class A Portland cement typically consists of four main components in the following proportions: 45 % tricalcium silicate (Ca_3SiO_5 or C_3S), 27 % dicalcium silicate (Ca_2SiO_4 or C_2S), 11 % tricalcium aluminate ($\text{Ca}_3\text{Al}_2\text{O}_6$ or C_3A) and 8 % tetracalcium aluminoferrite ($\text{Ca}_4(\text{Al},\text{Fe})_2\text{O}_5$ or C_4AF), with small quantities of CaSO_4 , MgO and CaO . These components react upon mixing with water to form hydration products. During hydration, the mineralogical composition of the cement changes, forming calcium hydroxide or portlandite, calcium silicate hydrate or C-S-H gel, calcium sulfoaluminate ($\text{AF}_{(m,t)}$) or ettringite, and a range of calcium aluminates (CA) and calcium aluminate ferrite (C_4AF) [Lea, 1970; Mindess and Young, 1981].

The hydration of cement leads not only to the above mineralogical changes but also to the development of a porous and more homogeneous structure in comparison with the unhydrated material [Lea, 1970; Mindess and Young, 1981]. Large portlandite and ettringite crystals form relatively quickly (~1 hour) after mixing the cement with water. C-S-H forms by hydration of C_3S , and has a poorly crystalline, fibrous or platy structure similar to that of jennite or tobermorite. Poorly crystalline C-S-H gel and small crystals of portlandite and ettringite then start filling the intervening pores and growing within the unreacted matrix. Note that typically 70 % of the C_3S and 30 % of the C_2S originally present have reacted after 28 days, while 100 % reaction of all phases present requires about one year [Lea, 1970; Mindess and Young, 1981]. Long-term curing or hydration is thus needed to ensure a cement structure and composition similar to the material typically present in wellbores. After such curing, C-S-H gel makes up around 50-60 % of the material. As mentioned above, this has a poorly crystalline structure, similar to jennite or tobermorite, and is accordingly characterized by a high internal surface area of typically 100-700 m^2/g , with platy crystals being separated by a water film when the material is wet [Lea, 1970; Mindess and Young, 1981]. It is the C-S-H gel that contributes mainly to the strength of the material, due to the covalent and van der Waals bonding within its complex structure. Calcium hydroxide or portlandite is present in proportions of ~20 to 25 % of the hydrated cement and occurs as weak blebs or hexagonal plates [Mehta and Monteiro, 2006]. The C_3A and $\text{AF}_{(m,t)}$ phases contribute further to stiffening and strengthening the material through their needle-like (C_3A) and hexagonal-plate morphology ($\text{AF}_{(m,t)}$), making up to 15-20 % of the volume of hydrated cement [Lea, 1970; Mindess and Young, 1981; Neville, 1996].

Alongside these solid phases, the hydration process forms three different types of pores, termed micropores, capillary pores and macropores or air voids [Neville, 1996]. Micropores or gel pores represent the void space within the platy C-S-H structure and vary between 0.5 and 10 nm in width or diameter. Capillary pores are irregular in shape and may range from 5 nm to 5 μm in diameter. Air voids or macropores are generally spherical in shape, may be as large as 50 to 200 μm , and are formed due to the air trapped in the cement paste during mixing. Water can accordingly be present in the cement structure in the following forms [Feldman and Sereda, 1968; Lea, 1970; Taylor, 1992; Neville, 1996]: a) as chemically bound water in the C-S-H, ettringite or $\text{Ca}(\text{OH})_2$ phases, b) as adsorbed

water bound to the solid phase surfaces and C-S-H micropores by adhesive surface forces, and c) as capillary water or free-water present in the capillary pores and air voids [Feldman and Sereda, 1968; Hewlett, 2004]. Evaporable water is lost during drying [Taylor, 1992]. However, part of the total water content is non-evaporable and is still present in the cement structure even after drying in amounts of 20-25 % by weight of the initial anhydrous material [Taylor, 1992]. Drying the cement increases the degree of silicate polymerization and results in a densification of the C-S-H gel. Moreover, the pore structure become coarser, forming increased capillary porosity [Thomas and Jennings, 2002].

The degree of water saturation it is known to influence the compressive and tensile strength of cements. This effect is believed to be due to lowering by water of the surface energy of the C-S-H gel [Wittmann, 1973], or to disjoining pressures arising due to water sorption between the crystalline sheets within the C-S-H phase [Israelachvili, 1985; Beltzung and Wittmann, 2005]. Reduction of surface energy by water reduces the energy required to propagate cracks and fractures, and has been shown to be at least partially responsible for lowering the compressive strength of French high alumina cement [Wittmann, 1973].

Another possible explanation for weakening by water may lie in the fact that water provides a corrosive environment promoting Si-O bond weakening in the C-S-H gel, through formation of Si-OH:HO-Si bonds, which allow accelerated subcritical crack growth or stress corrosion cracking [Feldman and Sereda, 1968; Schneider et al., 1986; Schneider and Chen, 1998; Imran and Pantazopoulou, 2001]. Non-equilibrium, grain boundary wetting effects, related to on-going reaction involving dissolution-precipitation processes in wet material [Spiers et al., 2004 ; de Meer et al., 2002 ; Ghoussoub et al., 2001], may also influence cohesion and strength. As all of these processes depend on water, drying of cement will lead to an increase in compressive and tensile strength [Wittmann, 1968; Pihlajavaara, 1974; Thomas and Jennings, 2002]. Precipitation of dissolved solid phases in the pore space upon drying can also strengthen porous materials by decreasing the overall porosity of the samples and increasing intergranular cohesion. However, this effect cannot play a significant role in our case, as the solubility of the phases present in cement is too low at the conditions of our tests.

5.4.2.2 *Effect of drying on strength in the present tests*

On the basis of the above, an attempt can now be made to explain the observed tendency for our dry samples tested at 80°C to show higher strength than those deformed at 20°C, and to explain the major difference in yield/peak strength and in (apparent) Young's modulus seen between our wet and dried samples at 80°C (see Figures 5.9 and 5.12, Table 5.1).

In principle, any of the mechanisms mentioned above could be responsible for increased strength due to water loss upon heating or drying, namely:

- a. Surface energy increase.
- b. A reduction of disjoining pressure effects in the C-S-H phase.
- c. Inhibition/exclusion of subcritical crack growth or stress corrosion effects.

d. Inhibition/exclusion of non-equilibrium grain boundary wetting effects.

Note that the effects of water and drying seen in our experiments, and in cement in general, closely resemble the effects of wetting and drying observed in sandstones and chalks, where water has been found to promote deformation and to weaken these materials, through chemically-enhanced processes such as stress-corrosion cracking in sandstone [Atkinson, 1982; Atkinson and Meredith, 1987; Wong and Baud, 1999; Baud et al., 2000] or sub-critical breakage of intergranular cement bridges in chalk [Risnes, 2001; Risnes et al., 2005; Xie and Shao, 2006].

We first assess the possible effect of drying on compressive strength through increasing surface energy due to the loss of water from the surface of the C-S-H gel phase present in our cement samples. Generally, the surface energy of a solid is reduced by the presence of a liquid phase according to Young's equation:

$$\gamma_{s-l} = \gamma_s - \gamma_l \cos \theta \quad (5.3)$$

where γ_{s-l} is the energy of the solid-liquid interface, γ_s is the surface energy of the solid in vacuum [$\text{J}\cdot\text{m}^{-2}$], γ_l is the surface energy of the liquid [$\text{J}\cdot\text{m}^{-2}$], and θ is the contact angle between the solid and liquid phase. As cement is a hydrated material, it is expected that $\theta \approx 0$ for water [Asamoto and Ishida, 2004; Matsushita and Onoue, 2006] so that

$$\gamma_{s-l} \approx \gamma_s - \gamma_l \quad (5.4)$$

Now, the critical stress (σ_c) at which tensile failure of a solid occurs depends on the surface energy of the material via the Griffith crack extension criterion [Griffith, 1921; Matsushita and Onoue, 2006]. For a perfectly elastic material this is written as:

$$\sigma_c = \sqrt{\frac{2E\gamma_c}{\pi l}} \quad (5.5)$$

where E is the Young's modulus [GPa], γ_c is the crack surface energy [$\text{J}\cdot\text{m}^{-2}$] and l is the crack half-length [m]. Consequently, a lower crack surface energy, caused for example by wetting (equation 5.3), leads to a decrease in the stress required for the propagation of tensile microcracks. Even though the Griffith theory is derived for tensile failure by extension of Mode I (opening) cracks, several authors [Orowan, 1949; Haque et al., 1976; Matsushita and Onoue, 2006] have shown that the Griffith principle can be applied to more general states of stress, as local tensile stresses will generally be proportional to the differential stress, and as the normal or shear stresses perpendicular to the edge of the crack will not appreciably influence the failure condition [Wong and Baud, 1999]. Using equation (5.5), the reduction in compressive yield strength of cement due to water adsorption on crack surfaces can therefore be estimated from the associated lowering of crack surface energy, according to the relationship

$$\left(\frac{\sigma_{s-l}}{\sigma_o}\right)^2 = \frac{\gamma_{s-l}}{\gamma_o} \quad (5.6)$$

given by [Haque et al., 1976], where σ_{s-l} is the strength of the material under wet conditions, σ_o it is its strength in vacuum, and where $\gamma_o = \gamma_s$ depicts the surface energy of the solid under vacuum [$\text{J}\cdot\text{m}^{-2}$]. Independent literature data for dry Portland cements (similar to Class A cements), with a $w:c$ ratio of 0.45 to 0.6 and cured at 20°C for 28 days, show

surface energy values in the range 1.37 to 0.657 J·m⁻² [Wittmann, 1968]. We interpolated these data to our w:c ratio of 0.5 and assumed a similar surface energy reduction to that measured in the study of [Haque et al., 1976] for dry versus wet samples, to estimate the strength reduction expected between our dry and wet samples due to surface energy effects. The results predict a reduction in yield strength from 42 MPa measured in dry samples to 22 MPa in wet samples, which is similar to the 20-26 MPa yield strength values measured in our tests. These estimates imply that the surface energy reduction induced by the presence of water plays the dominant role in determining the difference in compressive (yield) strength between our wet and dry samples.

The second possible mechanism that might have caused the strengthening of our dried samples relative to the wet is an increase of grain contact strength via reduction of disjoining pressure in fluid adsorbed into and onto the C-S-H phase. It has been shown that water adsorbed onto the platelets of the C-S-H gel component of cement develops a disjoining pressure, representing an equilibrium between interparticle mechanical forces and surface interaction forces, such as van der Waals forces [Wittmann, 1968; Israelachvili, 1985]. Disjoining pressure developed by adsorption of water between the C-S-H particles tends to reduce the van der Waals forces of attraction between the solid particles, thus lowering the strength of the cement. Disjoining pressures are estimated to be around 1 MPa in wet cementitious materials at room temperature [Beltzung and Wittmann, 2005], nearly disappearing above 80°C. Since their mechanical effect is equivalent to reducing the effective confining pressure by similarly small amounts (i.e. 1 MPa), and since the yield/peak strength of our samples is insensitive to effective confining pressure (Figure 5.9), we infer that disjoining pressure effects are too small to explain the large difference in compressive strength seen between our wet and dry samples.

The third mechanism that might have determined the difference in yield strength between our wet and dry samples is that of water-enhanced, subcritical crack growth or stress corrosion cracking [Bentur et al., 1979; Schneider et al., 1986; Beaudoin, 1987; Thomas and Jennings, 2002]. In this class of processes, small crack grows stably, at stresses below the critical value given in equation (5.5), until the crack length is large enough to satisfy this equation, i.e. the Griffith crack extension criterion, resulting in failure at lower stresses than seen in dry material [Atkinson, 1982; Atkinson and Meredith, 1987; Beaudoin, 1987]. This effect is well known in rocks [Barnett and Kerrich, 1980; Atkinson, 1982; Schneider et al., 1986; Beaudoin, 1987; Atkinson and Meredith, 1989; Dewers and Hajash, 1995; Chester et al., 2007; Liteanu and Spiers, 2009]. It has also been reported in cement, where it is suggested that water weakens the cement a) by attacking the Si-O-Si bonds in the C-S-H phase forming much weaker Si-OH:OH-Si bonds, as described earlier [Schneider et al., 1986; Beaudoin, 1987], or b) by modifying the Ca(OH)₂ structure [Beaudoin, 1987]. We have no specific evidence that this mechanism operated in our wet or room temperature experiments, or that it is responsible for the strength difference seen between the wet and dried samples. On the other hand microcracking is widespread in our samples especially in the wet samples, and subcritical crack growth or stress corrosion

has been reported in cement [Schneider *et al.*, 1986; Beaudoin, 1987]. Therefore, it cannot be excluded from operating in our wet samples and probably did accompany enhanced microcracking due to surface energy reduction in wet material.

The last possible mechanism that might have contributed to the observed differences in yield strength between our wet and dried samples is non-equilibrium wetting of grain boundaries [de Meer *et al.*, 2005], i.e. of the interfaces between reacting phases. Considering the gel-like, partly crystalline (platy) structure of the C-S-H phase, which is the main load-bearing constituent of Portland cement, we believe that such a process is unlikely to have played a role in our tests, as conventional grain boundaries are not present

A similar weakening effect of water was observed in the Young's modulus values estimated for our cement samples. This suggests that cement exhibits only quasi-elastic behaviour, and that permanent deformation is initiated in the loading stage, thus reducing the apparent elastic stiffness [see also Risnes and Nygaard, 1999; Jeong *et al.*, 2007]. As already mentioned, quasi-elastic behaviour of our samples is suggested by the S-shaped form of the differential stress versus axial strain plots obtained for our samples, an effect which is generally attributed to crack formation in the initial loading stage. Thus, if addition of water enhances crack formation, lower values of Young's modulus are to be expected. Disjoining pressure effects may also have contributed to the reduction of elastic stiffness of wet samples versus dry, but are likely to have been minor as argued with respect to yield strength.

We conclude that the most likely mechanism producing the observed difference in yield strength and apparent Young's modulus between wet and dry samples is the reduction of the surface energy of the cement caused when water is present, leading to easier, Griffith-type crack extension in wet samples. In addition, this effect may have been to some extent enhanced by subcritical crack growth or stress corrosion cracking effects, probably affecting the C-S-H phase.

5.4.3 Effect of CO₂ on strength

In our tests at 80°C, the effect on compressive strength of adding CO₂ at 10 MPa pressure to fluid-saturated samples was minor at low effective mean stresses, while at higher effective stresses, the wet/CO₂ samples were significantly stronger than the wet samples (see Figures 5.9, 5.5 and 5.6). Moreover, the apparent Young's modulus increased from 1.9-2.9 GPa in the case of wet samples to 2.6-3.4 GPa for wet/CO₂ samples, depending on effective confining pressure.

Following the same principles used in the previous section, we now investigate the effects brought about by addition of CO₂ to the pore fluid from a consideration of both surface energy and subcritical crack growth phenomena. We ignore disjoining pressure as a possible mechanism explaining the effects observed in our wet/CO₂ samples, as in wet material it has been shown to be too small to be significant especially as the effect virtually disappears at 80°C [Beltzung and Wittmann, 2005].

To our knowledge there are no data on the effect of supercritical CO₂ on the surface energy of Portland cement. However, we can relate the compressive strength of cement to the surface energy of the pore fluid. It has been shown that the compressive strength of concrete decreases with increasing surface tension of the fluid [Matsushita and Onoue, 2006]. This is qualitatively consistent with the predictions of equations 4 and 5, as the net surface energy of wetted cracks decreases with increasing surface energy of the liquid phase (see equation 5.4). In the case of CO₂-saturated water at 80°C and 10 MPa CO₂ pressure, the surface energy has been measured as 0.0363 N/m, while for water at 80°C the value is 0.0628 N/m [Chiquet *et al.*, 2007; Shah *et al.*, 2008; Chalbaud *et al.*, 2009]. The addition of 10 MPa CO₂ thus decreases the surface energy of the liquid phase and increases the solid-liquid interfacial energy, and hence the crack surface energy. Our wet/CO₂ samples should therefore show a higher compressive strength compared with the wet samples. This effect is indeed observed in our samples, at least at high mean stresses (Figure 5.9).

Let us look now in more detail at the subcritical crack growth mechanism in cement, i.e. the attack by H₂O of the Si-O-Si bonds present in the C-S-H gel. It is well known that such mechanisms are strongly affected by pH, in particular by the deviation in pH from the pH point of zero charge or pH_{PZC}, i.e. the pH where the net charge density at the solid surface is zero [Atkinson and Meredith, 1981; Dunning *et al.*, 1994]. Experimental studies have shown that increasing deviation from the pH point of zero charge results in an increase in subcritical crack growth velocity [Atkinson and Meredith, 1981; Dunning *et al.*, 1994]. In the C-S-H phase of cement, the surface charge developed reflects ionization of silanol sites. This occurs through the de-protonation reaction given $\text{>SiOH} \leftrightarrow \text{>SiO}^- + \text{H}^+$, and through the sorption of Ca²⁺ onto silanol sites via the reaction $\text{>SiOH} + \text{Ca}^{2+} \leftrightarrow \text{>SiOCa}^+ + \text{H}^+$ [Pointeau *et al.*, 2006]. At low and neutral pH's, the surface of C-S-H is negatively charged, whereas at high pH values (pH > 12) sorbed Ca²⁺ cations determine the surface potential and the C-S-H surface becomes positively charged. The balance between positive and negative charges, i.e. the point of zero charge occurs at pH ~ 10 for C-S-H gel [Stein, 1968; Viallis-Terrisse *et al.*, 2001; Pointeau *et al.*, 2006]. Experimental studies have shown that the pH decreases from 13.5-12.5 in the cement-water system to about 9 when supercritical CO₂ is added at conditions similar to those of the present experiments [García-González *et al.*, 2008; Xie *et al.*, 2008]. Therefore, for cements exposed to CO₂-rich solutions, one would expect a lower surface charge, hence decreased attack of Si-O-Si bonds by H₂O, hence slower subcritical crack growth by stress corrosion in comparison to samples exposed to water only. This would in turn result in a higher strength of wet/CO₂ samples compared with wet samples, as observed in many of our tests notably at the higher effective mean stresses.

Finally, the apparent Young's modulus values that we report increase upon addition of CO₂ in comparison with the wet only samples. In line with our interpretation on the effects of CO₂ on yield strength, we suggest that this increase in *E*-values reflects a decrease in Griffith microcracks damage due to an increase in cement surface energy in the presence

of supercritical CO₂, as well as a decrease in subcritical crack growth associated with the lowering of the pH.

Taking into account the above discussion of the effects of surface energy and pH on Griffith type crack extension and on stress corrosion cracking, we suggest that both effects play a role in the observed strengthening of our CO₂-bearing samples relative to the wet samples. In addition to these short-term effects of CO₂ injection on surface energy and subcritical crack growth, carbonation of the cement is expected in the long term [Liteanu and Spiers, 2009; See Chapter 6]. Such reactions will either cause cementation and strengthening of the cement [Chi et al., 2002; Chang et al., 2003; Bachu and Bennion, 2009], or else zonation/leaching and weakening. The present load-hold-load tests on samples CEMCO₂-1 and CEMCO₂-3 (Figure 5.6), showed that after 3 days of stress relaxation the samples regained 90-100 % of their pre-relaxation strength. These data are too limited and still too short term to gain insight into the possible healing or weakening effects of carbonation reactions. Moreover, no evidence for carbonation reaction was seen in the microstructure of the samples subjected to relaxation. Further work on the long-term effects of CO₂ on the mechanical behaviour of cement samples is therefore necessary.

5.5. Implications for wellbore integrity

The key objective of geological storage of CO₂ is long-term confinement. In this context, wellbore leakage has been identified as posing a significant risk [Gasda et al., 2004; International Panel on Climate Control, 2005]. Integrity loss of wellbore systems can potentially provide paths for leakage. This may result from chemical degradation of the wellbore cement, de-bonding of the casing-cement-rock interfaces, or mechanical fracturing of the cement sheath or plug components. Therefore, it is important to identify the possible mechanisms of mechanical failure of wellbore cements that may accompany CO₂ injection.

Assuming poroelastic behaviour of the reservoir rock, pore pressure and temperature changes associated with injection of CO₂ into a reservoir, generate a decrease in the effective stress in the reservoir that changes the state of stress and strain within the reservoir and overlying rocks. Shear stresses are bound to develop at the interfaces between the reservoir rock, the caprock and the wellbore system, and between the wellbore components (cement plugs, casing and cement sheath). Tensile and compressive stresses will also develop in the wellbore plugs and in other cement components [Mainguy et al., 2007; Soltanzadeh et al., 2007; Rutqvist et al., 2008a]. Similar changes, but largely opposite in sign, will also occur during depletion of oil and gas reservoirs, being approximately reversed when CO₂ injection follows - provided that the elastic properties of the various rock and wellbore components do not change significantly.

In a previous modeling study, Mainguy et al. [2007] used a finite element model to predict the risk of failure of Class G cement plugs after abandonment of a depleted oil reservoir, using coupled reservoir-geomechanics simulations. Examples of stress path

evolution in the reservoir, caprock and cement plugs, during re-pressurization by natural water influx, were investigated, focusing on the case of a wellbore cement plug present at the level of an impermeable caprock situated at 3 km depth. The rock material properties and geological scenario considered represent a realistic generic model for the case of CO₂ storage in depleted oil and gas reservoirs at similar depths [Rutqvist *et al.*, 2008b; Bildstein *et al.*, 2009]. The post-production stress levels predicted also quite closely resemble those estimated for Dutch gas reservoirs, such as the De Lier field (effective mean stress of ~18 MPa after reservoir depletion) [Hofstee, 2008].

Considering the pressure and temperature changes due to 20 years of oil production followed by 400 years of re-pressurization of the reservoir due to the recharging water influx, Mainguy *et al.* [2007] calculated the stress changes that occur in a wellbore that was plugged with cement at the caprock level immediately after production ceased. The state of stress in the cement plug upon solidification was assumed to be isotropic and in equilibrium with the residual pore pressure in the reservoir. The pore fluid pressure in the cement plug was assumed to be buffered by the fluid pressure in the overlying wellbore column and therefore equal to the residual pore pressure in the reservoir at the moment of abandonment. The effective stress in the plug after solidification and at the onset of re-pressurization was thus assumed to be zero. The cement plug was assumed to be characterized by a Young's modulus of 10 GPa and a Poisson's ratio of 0.18. The model assumed a 25 MPa fluid pressure decrease from 45 to 20 MPa due to production, followed by a 15 MPa increase after abandonment. Minor thermal effects of fluid influx on stress-strain evolution were also taken into account.

For the case of an impermeable caprock, the model predicted that re-pressurization of the reservoir, from 25 to 35 MPa would lead to the development of compressive stresses in the cement plug of a few MPa. This is caused by lateral compression of the plug by the caprock as the caprock arches upwards in response to reservoir re-pressurization and associated decompaction. Compression of the plug from below, by increasing fluid pressure, and penetration of the plug by fluid from the reservoir seem to have been neglected. A comparison of the stress path evolution computed by Mainguy *et al.* [2007] with our wet and wet/CO₂ strength envelopes with is shown in Figure 5.13.

This clearly shows that compressive failure of a Class A cement plug is not likely to occur during re-pressurization of such a reservoir system with CO₂. Since Mainguy *et al.* [2007] assumed a Class G cement plug with a Young's modulus $E = 10$ GPa, the magnitude of the stress changes for Class A cement, with $E \sim 1.9$ -3.4 GPa will be reduced more or less proportionally. In addition, if the effect of the increasing fluid pressure on the lower surface of the plug is taken into account in calculating the stress evolution in the plug, then the mean effective stress P will increase more strongly than calculated by Mainguy *et al.* [2007], depressing the calculated stress path towards the horizontal axis.

Taken together, all of these points indicate that the compressive failure of Class A wellbore cement is exceedingly unlikely during CO₂ injection into depleted reservoirs resembling the generic one modeled by Mainguy *et al.* [2007], and hence highly unlikely

in most practical cases. On the other hand, if the injected CO_2 penetrates the cement plug for any significant distance, reaching pressures within the plug in excess of the compressive stresses of a few MPa generated by the caprock deformation, then the stress path represented in Figure 5.13 can be expected to be diverted sharply towards the tensile field. Thus, if injection pressures are high enough and the plug is permeable enough, extensional failure of the cement plug (or the interfaces with the casing or the caprock) will ensue.

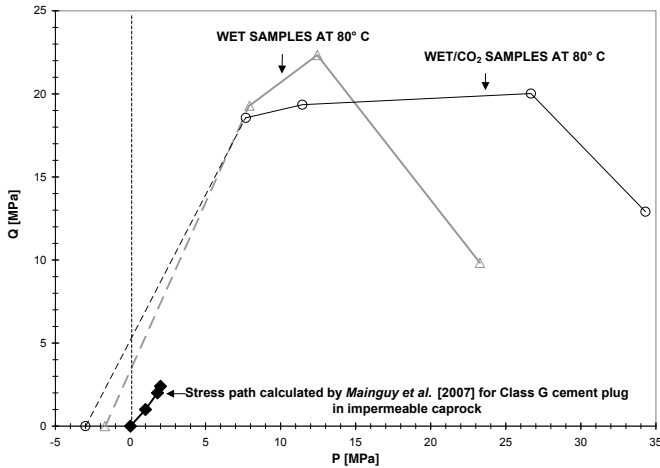


Figure 5.13. Yield strength envelopes for Class A cement deformed under wet and wet/ CO_2 conditions in this study compared with the stress changes occurring in a wellbore cement plug after reservoir depletion and fluid re-injection, upon abandonment calculated by [Mainguy et al., 2007], assuming a cement plug (Class G cement, $E = 10$ GPa) situated in a caprock, subjected to a 25 MPa decrease during production stage, followed by 15 MPa pressure increase during abandonment. Note that our strength envelopes have been extended into the tensile field on the basis of tensile strength of 10 % of the compressive strength [Barlet-Gouédard et al., 2009].

Occurrence of fractures in cement sheath has been reported for the SACROC field [Carey et al., 2007]. However, in this case it is not clear if the fractures developed during the production phase, during cement placement in the wellbore or during CO_2 injection. Regardless of when this fracturing occurred, after exposure to supercritical CO_2 , healing and sealing due to precipitation of calcium carbonate in the fractures occurred [Carey et al., 2007]. This finding is confirmed also by the experimental investigations performed on Class A cement reported by Liteanu et al. 2009 (Chapter 6), which show that if mechanical defects are present in the cement, they will heal, thus maintaining CO_2 storage integrity. Moreover, these experiments show that intact cement rapidly becomes impermeable upon exposure to supercritical CO_2 . On this basis, significant extensional failure of wellbore plugs is highly unlikely.

In disposing of CO_2 in a depleted reservoir at around 3km depth, the maximum pressure for storage is likely to be ~ 10 MPa which is significantly less than the value of 15 MPa used in the calculation of Mainguy et al. [2007]. Coupling this with the information

above, we can safely infer that wellbore compressive failure will not occur in depleted oil and gas reservoirs situated at depths around 3 km and plugged with Class A Portland cement. Extensional failure cannot be eliminated but is unlikely provided that carbonation reduces the cement permeability as observed in experiments [Litanu *et al.* 2009, Chapter 6]. Clearly, to make full use of our strength envelope data, our compressive strength and apparent Young's modulus data for Class A Portland cement should be applied in a numerical model coupling both geochemical and geomechanical effects, as proposed by [Mainguy *et al.*, 2007].

5.6. Conclusions

Triaxial compression tests were performed on wellbore Portland Class A cement prepared with a *w:c* ratio of 0.5 and cured to a mature state over 6 months. Tests were performed at temperatures up to 80°C and (effective) confining pressures in the range 1.5-30 MPa, thus simulating reservoir conditions at 2-3 km depth. The tests were done under dry and wet conditions, as well as wet with added supercritical CO₂. Wet and wet/CO₂ experiments were performed using pore fluid pressures of 5 and 10 MPa respectively. The main findings can be summarized as follows:

1. Regardless of detailed conditions (dry, wet, wet/CO₂) Class A cement samples fail in a brittle manner at low (effective) confining pressures (1.5 to 10 MPa) and in a ductile manner at higher confining pressures.
2. In the brittle field, failure is generally marked by a differential stress peak and dilatation of the sample, along with localized shear fracture. The ductile regime is characterized by pervasive compactional deformation and strain hardening.
3. Strength envelopes constructed for the yield strength and for the stress supported at 1 % axial strain, which is close to the peak strength in samples showing a load drop, mainly display a positive slope consistent with shear failure at low effective mean stress, versus compactional behaviour (a negatively sloping compaction cap) at high (effective) mean stresses (>20-30 MPa).
4. The yield and peak strengths of wet samples are about half those of dried samples deformed at otherwise similar conditions. The relative weakness of the wet material can be explained by a lowering of the surface energy of the cement due to wetting. This promotes equilibrium (Griffith-type) crack extension. The presence of water also promotes subcritical or stress corrosion crack growth in wet cement compared with dry.
5. Addition of supercritical CO₂ to wet Class A cement leads to a strengthening of the material at high confining pressures. This is thought to be due to an increase in the net energy of the cement-fluid interface, compared with wet samples, and to a decrease in subcritical crack growth rates caused by a shift in the pH of the pore fluid towards the point of zero charge for C-S-H.
6. Apparent Young's modulus values decrease from around 3.9 to 5.6 GPa for dry

cement deformed at 80°C, to around 1.9 to 3.4 GPa for wet cement and CO₂-bearing wet cement deformed at the same temperature. This is believed to be due to enhanced microcrack damage occurring during loading of wet samples and of CO₂-bearing wet samples, reflecting the above-mentioned effects of water and CO₂ on surface energy and subcritical crack growth in cement.

7. Combining our yield envelopes with previous calculations on stress development in wellbore cement plugs shows that CO₂ injection into depleted reservoirs will result in increased compressive stresses developing in the plugs. However, such stress changes will not lead to compressive failure of Class A Portland cement plugs. Extensional failure cannot be eliminated but is unlikely, assuming that carbonation seals the cement plug preventing any significant penetration of the cement by CO₂. Any fractures, which do form, are expected to heal. For the case of CO₂ injection into a depleted gas or oil reservoir overlain by a typical caprock, we infer that the stress changes that are expected to occur in the plugs pose little risk for CO₂ storage integrity

Acknowledgments:

We thank Peter van Krieken, Gert Kastelein and Eimert de Graaff for technical support provided in the laboratory. We would also like to thank the Nederlandse Aardolie Maatschappij (NAM) for kindly providing us with advice on sample preparation. This project was jointly funded by TNO Bouw and Ondergrond and Utrecht Center of Geosciences (UCG), and was conducted in the framework of the CATO Dutch national programme on Carbon Capture and Storage.

REFERENCE LIST

- Al-Ajmi, A. M. (2006), Wellbore stability analysis based on a new true-triaxial failure criterion, 138 pp, Stockholm.
- Al-Ajmi, A. M., and R. W. Zimmerman (2005), Relation between the Mogi and the Coulomb failure criteria, *International Journal of Rock Mechanics and Mining Sciences*, 42(3), 431-439.
- Al-Ajmi, A. M., and R. W. Zimmerman (2006), Stability analysis of vertical boreholes using the Mogi-Coulomb failure criterion, *International Journal of Rock Mechanics and Mining Sciences*, 43(8), 1200-1211.
- Ambrose, W. A., S. Lakshminarasimhan, M. H. Holtz, V. Nunez-Lopez, S. D. Hovorka, and I. Duncan (2008), Geologic factors controlling CO₂ storage capacity and permanence: case studies based on experience with heterogeneity in oil and gas reservoirs applied to CO₂ storage, *Environmental Geology* 54, 1619-1633.
- Asamoto, S., and T. Ishida (2004), Microscopic approach to time-dependent deformation mechanism of concrete based on liquid characteristics, *Journal of Materials, Concrete structures, Pavements, JSCE*, 50(760), 159-172.
- Atkinson, B. K. (1982), Subcritical crack propagation in rocks: theory, experimental results and applications. , *Journal of Structural Geology* 4, 41-56.
- Atkinson, B. K., and P. G. Meredith (1981), Stress corrosion cracking of quartz: A note on the influence of chemical environment, *Tectonophysics*, 77(1-2), T1-T11.
- Atkinson, B. K., and P. G. Meredith (1987), The theory of subcritical crack growth with applications to minerals and rocks, in *Fracture Mechanics of Rock*, edited by A. B.K., pp. 111-166, Academic Press.
- Atkinson, B. K., and R. G. Meredith (1989), The theory of subcritical crack growth with applications to minerals and rocks, in *Fracture mechanics of rock*, edited by B. K. Atkinson, pp. 111-166, Academic Press, London.
- Bachu, S. (2003), Screening and ranking of sedimentary basins for sequestration of CO₂ in geological media in response to climate change, *Environmental Geology*, 44(3), 277-289.
- Bachu, S. (2008), CO₂ storage in geological media: Role, means, status and barriers to deployment, *Progress in Energy and Combustion Science*, 34(2), 254-273.
- Bachu, S., and D. B. Bennion (2009), Experimental assessment of brine and/or CO₂ leakage through well cements at reservoir conditions, *International Journal of Greenhouse Gas Control*, 3(4), 494-501.
- Barlet-Gouédard, V., G. Rimmelé, B. Goffé, and O. Porcherie (2006), Mitigation strategies for the risk of CO₂ migration through wellbores, paper presented at IADC/SPE Drilling Conference, SPE 98924-MS, Miami, Florida, February 21-23.
- Barlet-Gouédard, V., G. Rimmelé, B. Goffé, and O. Porcherie (2007), Well technologies for CO₂ geological storage: CO₂-resistant cement, *Oil and Gas Science and Technology, Review IFP*, 62(3), 1-12.
- Barlet-Gouédard, V., G. Rimmelé, O. Porcherie, N. Quisel, and J. Desroches (2009), A solution against well cement degradation under CO₂ geological storage environment, *International Journal of Greenhouse Gas Control*, 3(2), 206-216.
- Barnett, R. L., and R. Kerrich (1980), Stress corrosion cracking of biotite and feldspar, *Nature*, 283(5743), 185-187.
- Baud, P., W. Zhu, and T.-f. Wong (2000), Failure mode and weakening effect of water on sandstone, *Journal of Geophysical Research*, 105(12), 16371-16390.
- Beaudoin, J. J. (1987), Subcritical crack growth in low-porosity cement systems, *Journal of Materials Science Letters*, 6(2), 197-199.
- Beltzung, F., and F. H. Wittmann (2005), Role of disjoining pressure in cement-based materials, *Cement and Concrete Research*, 35, 2371-2383.
- Bentur, A., R. L. Berger, J. H. Kung, N. B. Milestone, and J. F. Young (1979), Structural Properties of Calcium Silicate Pastes: II, Effect of Curing Temperature, *Journal of the American Ceramic Society*, 62(7-8), 362-366.
- Bildstein, O., M. Jullien, A. Crédoz, and J. Garnier (2009), Integrated modeling and experimental approach for caprock integrity, risk analysis, and long term safety assessment, *Energy Procedia*, 1(1), 3237-3244.
- Bonett, A., and D. Pafitis (1996), Getting to the root of gas migration, *Oilfield review*, 8(1), 36-49.
- Carey, J. W., M. Wigand, S. J. Chipera, G. WoldeGabriel, R. Pawar, P. C. Lichtner, S. C. Wehner, M. A. Raines, and J. G. D. Guthrie (2007), Analysis and performance of oil well cement with 30 years of CO₂ exposure from the SACROC Unit, West Texas, USA, *International Journal of Greenhouse Gas Control*, 1(1), 75-85.
- Chalbaud, C., M. Robin, J. M. Lombard, F. Martin, P. Egermann, and H. Bertin (2009), Interfacial tension measurements and wettability evaluation for geological CO₂ storage, *Advances in Water Resources*, 32(1), 98-109.
- Chang, J. J., W. Yeih, R. Huang, and M. Chi (2003), Mechanical properties of carbonated concrete, *Zhōngguó gōngchéng xuékān* 26(4), 513-522.
- Chen, W. F. (1984), Soil Mechanics, Plasticity and Landslides. , in *Mechanics of Inelastic Materials*, edited by G. J.

- a. S. Dvorak, R.T., pp. 31-58, Elsevier, Amsterdam.
- Chester, F. M., J. S. Chester, A. K. Kronenberg, and A. Hajash (2007), Subcritical creep compaction of quartz sand at diagenetic conditions: Effects of water and grain size, *J. Geophys. Res.*, 112.
- Chi, J. M., R. Huang, and C. C. Yang (2002), Effects of carbonation on mechanical properties and durability of concrete using accelerated testing method, *Journal of Marine Science and Technology*, 10(1), 14-20.
- Chiquet, P., J.-L. Daridon, D. Broseta, and S. Thibeau (2007), CO₂/water interfacial tensions under pressure and temperature conditions of CO₂ geological storage, *Energy Conversion and Management*, 48(3), 736-744.
- Çolak, A. (2006), A new model for the estimation of compressive strength of Portland cement concrete, *Cement and Concrete Research*, 36(7), 1409-1413.
- de Meer, S., C. J. Spiers, and S. Nakashima (2005), Structure and diffusive properties of fluid-filled grain boundaries: An *in-situ* study using infrared (micro) spectroscopy, *Earth and Planetary Science Letters*, 232(3-4), 403-414.
- de Meer, S., C. J. Spiers, C. J. Peach, and T. Watanabe (2002), Diffusive properties of fluid-filled grain boundaries measured electrically during active pressure solution, *Earth and Planetary Science Letters*, 200(1-2), 147-157.
- Dewers, T., and A. Hajash (1995), Rate laws for water-assisted compaction and stress-induced water-rock interaction in sandstones, *J. Geophys. Res.*, 100(B7), 13093-13112. .
- Duguid, A., M. Radonjic, and G. Scherer (2005), Degradation of Well Cement Exposed to Carbonated Brine, paper presented at 4th Annual Conference on Carbon Capture and Sequestration, Exchange and Monitor Publications and Forum, Alexandria, VA, 2006.
- Dunning, J., B. Douglas, M. Miller, and S. McDonald (1994), The role of the chemical environment in frictional deformation: Stress corrosion cracking and comminution, *Pure and Applied Geophysics*, 143(1), 151-178.
- Dusseault, M. B., M. N. Gray, and P. A. Nawrocki (2000), Why oilwells leak: Cement behavior and long-term consequences., paper presented at SPE International Oil and Gas Conference and Exhibition in China, SPE Beijing, China, 7-10 November 2000.
- Ewy, R. T. (1999), Wellbore-Stability Predictions by Use of a Modified Lade Criterion, *Journal of petroleum technology*, 14(2), 85-91.
- Feldman, R. F., and P. J. Sereda (1968), A model for hydrated portland cement paste as deduced from sorption-length change and mechanical properties, *Mater. Constr*, 1, 501-519.
- Fredrich, J. T., B. Evans, and T-F. Wong (1989), Micromechanics of the Brittle to Plastic Transition in Carrara Marble, *J. Geophys. Res.*, 94(B4), 4129-4145.
- García-González, C. A., N. el Grouh, A. Hidalgo, J. Fraile, A. M. López-Periago, C. Andrade, and C. Domingo (2008), New insights on the use of supercritical carbon dioxide for the accelerated carbonation of cement pastes, *The Journal of Supercritical Fluids*, 43(3), 500-509.
- Gasda, S. E., S. Bachu, and M. A. Celia (2004), Spatial characterization of the location of potentially leaky wells penetrating a deep saline aquifer in a mature sedimentary basin, *Environmental Geology*, 46(6), 707-720.
- Gozalpour, F., S. R. Ren, and B. Tohidi (2005), CO₂ EOR and storage in oil reservoirs. , *Oil and Gas Science and Technology - Rev IFP*, 60(3), 537-546.
- Griffith, A. A. (1921), The phenomenon of rupture and flow in solids, *Philosophical Transactions of the Royal Society*, 221(Series A), 163-198.
- Haque, M. N., D. J. Cook, and D. R. Morgan (1976), The influence of admixtures on the surface energy of Portland cement paste, *Materiaux et constructions*, 9(52).
- Hettema, M., P. E., and P. Schutjens (2002), Subsidence delay: field observations and analysis., *Oil and Gas Science and Technology - Rev IFP*, 57(5), 443-458.
- Hewlett, P. C. (2004), *Lea's Chemistry of Cement and Concrete, 4th Edition*, Elsevier Butterworth-Heinemann Publishers.
- Hofstee, C., F. Seeberger, B. Orlic, F. Mulders, F. van Bergen, and R. Bisschop (2008), The feasibility of effective and safe carbon dioxide storage in the De Lier gas field, *First break*, 26(1), 53-57.
- Homand, S., and J. F. Shao (2000), Comportement mécanique d'une craie poreuse et effets de l'interaction eau/craie. Première partie : Résultats expérimentaux, *Oil & Gas Science and Technology*, 55(6), 591-598.
- Imran, I., and S. J. Pantazopoulou (2001), Plasticity model for concrete under triaxial compression, *Journal of Engineering Mechanics*, 127(3), 281-290.
- International Panel on Climate Control, I. (Ed.) (2005), *Carbon Dioxide Capture and Storage. Special Report* , 442 pp., Cambridge University Press, Cambridge, United Kingdom and New York, NY, USA.
- Israelachvili, J. N. (1985), *Intermolecular and Surface Forces*, New York.
- Issen, K. A., and J. W. Rudnicki (2001), Theory of compaction bands in porous rock, *Physics and Chemistry of the Earth, Part A: Solid Earth and Geodesy*, 26(1-2), 95-100.
- Jacquemet, N., J. Pironon, and E. Caroli (2005), A new experimental procedure for simulation of H₂S + CO₂

- geological storage. , *Oil Gas Sci. Technol.*, 60(1), 196-206.
- Jeong, H.-s., S.-s. Kang, and Y. Obara (2007), Influence of surrounding environments and strain rates on the strength of rocks subjected to uniaxial compression, *International Journal of Rock Mechanics and Mining Sciences*, 44(3), 321-331.
- Kutchko, B., D. Strazisar, D. A. Dzombak, and G. Lowry (2006), Degradation of well cements under geologic sequestration conditions, in *Wellbore Integrity network Meeting*, edited, Princeton, N.J.
- Kutchko, B. G., B. R. Strazisar, D. A. Dzombak, G. V. Lowry, and N. Thaulow (2007), Degradation of Well Cement by CO₂ under Geologic Sequestration Conditions, *Environmental Science & Technology*, 41(13), 4787-4792.
- Kutchko, B. G., B. R. Strazisar, G. V. Lowry, D. A. Dzombak, and N. Thaulow (2008), Rate of CO₂ Attack on Hydrated Class H Well Cement under Geologic Sequestration Conditions, *Environmental Science & Technology*, 42(16), 6237-6242.
- Lea, F. M. (1970), *The Chemistry of Cement and Concrete*, 3rd ed., Edward Arnold Ltd, London.
- Liteanu, E., and C. J. Spiers (2009), Influence of pore fluid salt content on compaction creep of calcite aggregates in the presence of supercritical CO₂, *Chemical Geology*, 265(1-2), 134-147.
- Mainguy, M., P. Longuemare, A. Audibert, and E. Lecolier (2007), Analyzing the risk of well plug failure after abandonment. , *Oil & Gas Sci. and Tech. - Rev. IFP*, 62(3), 311-324.
- Matsushita, H., and K. Onoue (2006), Influence of surface energy on compressive strength of concrete under static and dynamic loading, *Journal of Advanced Concrete Technology*, 4(3), 409-421.
- Mehta, P., and P. Monteiro (2006), *Concrete: Microstructure, Properties, and Materials* The McGraw-Hill Companies, Inc.
- Meyer, J. P. (2007), State-of-the-art of carbon dioxide enhanced oil recovery (CO₂EOR) injection well technology, Contek Solutions LLC, Plano, Texas, USA.
- Mindess, S., and J. F. Young (1981), *Concrete*, Prentice-Hall, Inc., Englewood Cliffs, New Jersey.
- Mogi, K. (1971), Effect of the Intermediate Principal Stress on Rock Failure, *J. Geophys. Res.*, 72.
- Mollema, P. N., and M. A. Antonellini (1996), Compaction bands: a structural analog for anti-mode I cracks in aeolian sandstone, *Tectonophysics*, 267(1-4), 209-228.
- Neville, A. M. (1996), *Properties of Concrete*, John Wiley and Sons, Inc., New York.
- Olsson, W. A. (1999), Theoretical and experimental investigation of compaction bands in porous rock, *J. Geophys. Res.*, 104(B 4).
- Olsson, W. A., and D. J. Holcomb (2000), Compaction localization in porous rock, *Geophys. Res. Lett.*, 27, 3537-3540.
- Orowan, E. (1949), *Fracture and strength of solids*, Physics Soc., London.
- Palchik, V., and Y. H. Hatzor (2004), The Influence of Porosity on Tensile and Compressive Strength of Porous Chalks, *Rock Mechanics and Rock Engineering*, 37(4), 331-341.
- Papamichos, E., M. Brignoli, and F. J. Santarelli (1997), An experimental and theoretical study of a partially saturated collapsible rock, *Mechanics of Cohesive-frictional Materials*, 2(3), 251-278.
- Peach, C. J. (1991), Influence of deformation on the fluid transport properties of salt rocks. , Universiteit Utrecht, Utrecht.
- Peach, C. J., and C. J. Spiers (1996), Influence of crystal plastic deformation on dilatancy and permeability development in synthetic salt rock. , *Tectonophysics*, 256, 101-128.
- Philippopoulos, A. J., and M. L. Berndt (2000), Characterization and modeling of cements for geothermal well casing remediation, *Geothermal Resources Council Transactions*, 24, 81-86.
- Philippopoulos, A. J., and M. L. Berndt (2001), Mechanical property issues for geothermal well cements, in *Geothermal Resources Council Transactions*, edited, pp. 119-124, San Diego, USA.
- Pihlajavaara, S. E. (1974), A review of some of the main results of a research on the ageing phenomena of concrete: Effect of moisture conditions on strength, shrinkage and creep of mature concrete, *Cement and Concrete Research*, 4(5), 761-771.
- Poiteau, I., P. Reiller, N. Macé, C. Landesman, and N. Coreau (2006), Measurement and modeling of the surface potential evolution of hydrated cement pastes as a function of degradation, *Journal of Colloid and Interface Science*, 300(1), 33-44.
- Pruess, K. (2005), Numerical studies of fluid leakage from a geologic disposal reservoir for CO₂ show self-limiting feedback between fluid flow and heat transfer, *Geophys. Res. Lett.*, 32(L14404).
- Raj, R. (1982), Creep in Polycrystalline Aggregates by Matter Transport Through a Liquid Phase, *J. Geophys. Res.*, 87(B6), 4731-4739.
- Rimmelé, G., V. Barlet-Gouédard, O. Porcherie, B. Goffé, and F. Brunet (2008), Heterogeneous porosity distribution in Portland cement exposed to CO₂-rich fluids, *Cement and Concrete Research*, 38(8-9), 1038-1048.
- Risnes, R. (2001), Deformation and yield in high porosity outcrop chalk, *Physics and Chemistry of the Earth, Part A:*

- Solid Earth and Geodesy*, 26(1-2), 53-57.
- Risnes, R., and V. Nygaard (1999), Elasticity in high porosity outcrop chalk., in *Second Euroconference on Rock Physics and Rock Mechanics*, edited, Heriot-Watt University, Edinburgh, Scotland.
- Risnes, R., H. Haghighi, R. I. Korsnes, and O. Natvik (2003), Chalk-fluid interactions with glycol and brines, *Tectonophysics*, 370(1-4), 213-226.
- Risnes, R., M. V. Madland, M. Hole, and N. K. Kwabiah (2005), Water weakening of chalk - Mechanical effects of water-glycol mixtures, *Journal of Petroleum Science and Engineering*, 48, 21-36.
- Rudnicki, J. W. (2002), Conditions for compaction and shear bands in a transversely isotropic material, *International Journal of Solids and Structures*, 39(13-14), 3741-3756.
- Rutqvist, J., J. T. Birkholzer, and C. F. Tsang (2008a), Coupled reservoir-geomechanical analysis of the potential for tensile and shear failure associated with CO₂ injection in multilayered reservoir-caprock systems, *International Journal of Rock Mechanics and Mining Sciences*, 45, 132-143.
- Rutqvist, J., J. T. Birkholzer, and C.-F. Tsang (2008b), Coupled reservoir-geomechanical analysis of the potential for tensile and shear failure associated with CO₂ injection in multilayered reservoir-caprock systems, *International Journal of Rock Mechanics and Mining Sciences*, 45(2), 132-143.
- Schneider, U., and S.-W. Chen (1998), The chemomechanical effect and the mechanochemical effect on high-performance concrete subjected to stress corrosion
Cement and Concrete Research, 28(4), 509-522.
- Schneider, U., E. Nagele, and F. Dumat (1986), Stress corrosion initiated cracking of concrete, *Cement and Concrete Research*, 16, 535-544.
- Settari, A. (2002), Reservoir compaction, *Society of Petroleum Engineers*(76805), 62-69.
- Sfer, D., I. Carol, R. Gettu, and G. Etse (2002), Study of the behavior of concrete under triaxial compression, *Journal of engineering mechanics* 128(2), 156-163.
- Shah, V., D. Broseta, G. Mournval, and F. Montel (2008), Water/acid gas interfacial tensions and their impact on acid gas geological storage, *International Journal of Greenhouse Gas Control*, 2(4), 594-604.
- Soltanzadeh, H., C. D. Hawkes, and J. S. Sharma (2007), Poroelastic model for production and injection-induced stresses in reservoirs with elastic properties different from the surrounding rock., *International Journal of Geomechanics*, 7, 353-361.
- Spiers, C. J., S. De Meer, A. R. Niemeijer, and X. Zhang (2004), Kinetics of rock deformation by pressure solution and the role of thin aqueous films, in *Physicochemistry of Water in Geological and Biological Systems-Structures and Properties of Thin Aqueous Films*, edited by S. Nakashima, pp. 129-158, Universal Acad. Press, Tokyo.
- Stein, H. N. (1968), Surface charges on calcium silicates and calcium silicate hydrates, *Journal of Colloid and Interface Science*, 28(2), 203-213.
- Stiles, D. (2006), Study of the behavior of concrete under triaxial compression, in *IADC/SPE Drilling conference*, edited by IADC/SPE, Miami, Florida, U.S.A.
- Talesnick, M., and S. Shehadeh (2007), The effect of water content on the mechanical response of a high-porosity chalk, *International Journal of Rock Mechanics and Mining Sciences*, 44(4), 584-600.
- Taylor, H. F. W. (1992), *Cement Chemistry*, Academic Press LTD., London.
- Thomas, J. J., and H. M. Jennings (2002), Effect of Heat Treatment on the Pore Structure and Drying Shrinkage Behavior of Hydrated Cement Paste, *Journal of the American Ceramic Society*, 85(9), 2293-2298.
- Vajdova, V., P. Baud, and T.-f. Wong (2004), Compaction, dilatancy, and failure in porous carbonate rocks, *J. Geophys. Res.*, 109.
- Viallis-Terrisse, H., A. Nonat, and J.-C. Petit (2001), Zeta-Potential Study of Calcium Silicate Hydrates Interacting with Alkaline Cations, *Journal of Colloid and Interface Science*, 244(1), 58-65.
- Wittmann, F. H. (1968), Surface tension shrinkage and strength of hardened cement paste, *Materials and Structures*, 1(6), 547-552.
- Wittmann, F. H. (1973), Interaction of hardened cement paste and water, *Journal of American Ceramic Society*, 56, 409-415.
- Wong, T.-f., and P. Baud (1999), Mechanical Compaction of Porous Sandstone, *Oil & Gas Sci. and Tech. - Rev. IFP*, 54(6), 715-727.
- Wong, T.-f., P. Baud, and E. Klein (2001), Localized failure modes in a compactant porous rock, *Geophysical Research Letters*, 28, 2521-2524.
- Xie, S. Y., and J. F. Shao (2006), Elastoplastic deformation of a porous rock and water interaction, *International Journal of Plasticity*, 22(12), 2195-2225.
- Xie, S. Y., J. F. Shao, and N. Burlion (2008), Experimental study of mechanical behaviour of cement paste under compressive stress and chemical degradation, *Cement and Concrete Research*, 38(12), 1416-1423.

Yurtdas, I., H. Peng, N. Burlion, and F. Skoczylas (2006), Influences of water by cement ratio on mechanical properties of mortars submitted to drying, *Cement and Concrete Research*, 36(7), 1286-1293.

Chapter 6

ABSTRACT

This paper investigates the process and rate of carbonation reaction of Class A wellbore cement exposed to CO₂-saturated solution at confined conditions similar to those employed in geological storage of CO₂. The main goal was to investigate whether reaction improves or degrades the sealing/healing capacity of fractured Type A cement plugs. Batch reaction experiments were performed for up to three months, on both intact and fractured Class A Portland cement cylinders, at a constant confining pressure of 30 MPa, a temperature of 80°C and a CO₂ pressure of 10 MPa. The experiments were carried out on water-saturated samples, exposing them to the supercritical CO₂ at one end. All samples were jacketed in sleeves to seal them from the high pressure confining medium. The results indicate that cement carbonation front advanced in time, leading to a densification of the material. Extrapolation of the reaction rates to 1-year period indicates a carbonation depth of about 1.38 mm, and about 7.56 mm after 30 years of exposure to CO₂-saturated solution. Thermogravimetric analyses, Scanning Electron Microscopy observations and permeability measurements indicate that carbonation of wellbore cement leads to a decrease of the porosity of the material on the reaction front and moreover, has the potential for healing pre-existent fractures and for improving the sealing properties of good-quality cement samples in time, at reservoir conditions.

Based on:

Liteanu E., Spiers C.J. - Healing/sealing and transport properties of wellbore cement in the presence of supercritical CO₂. *Environmental Science and Technology* (submitted)

6.1 Introduction

Long-term geological storage of carbon dioxide is now widely accepted as a potential means of mitigating greenhouse gas emissions to the atmosphere [Holloway, 2001; Gale, 2004; International Panel on Climate Control, 2005; International Panel on Climate Control, 2007; Bachu, 2008]. One of the most important storage options is that of depleted oil and gas reservoirs. The effectiveness of such storage systems mainly depends on trapping CO₂ as a supercritical fluid, or as a dissolved component in the formation water [Xu *et al.*, 2007; Gilfillan *et al.*, 2009]. For structural or stratigraphic trapping of supercritical and dissolved CO₂, the sealing capacity of the caprock is crucial to system integrity. However, depleted oil and gas reservoirs and their associated caprocks are generally perforated by large numbers of production and exploration wellbores [Bachu, 2003; Gasda *et al.*, 2004; International Panel on Climate Control, 2005; Pruess, 2005; Carey *et al.*, 2007; Bachu, 2008]. Although most wellbores are sealed and plugged with cement upon abandonment, chemical degradation and mechanical failure of the cement have the potential to create leakage paths [Barlet-Gouédard *et al.*, 2006; Kutchko *et al.*, 2006; Barlet-Gouédard *et al.*, 2007; Bachu and Bennion, 2009]. Wellbores can accordingly pose a significant risk for CO₂ leakage [Bonett and Pafitis, 1996; Dusseault *et al.*, 2000; Mainguy *et al.*, 2007].

The most commonly used wellbore cements, in the oil and gas industry, are the Class A, G and H, Portland-based cements. Numerous recent studies have addressed chemical degradation of these cements in the presence of CO₂. Interaction between hydrated cement and supercritical (SC) CO₂ involves dissolution of CO₂ in the pore fluid, the formation and dissociation of carbonic acid, and reaction with the Ca(OH)₂ and calcium silicate hydrate (C-S-H) phases present in the cement, thus precipitating calcium carbonate (CaCO₃) and silica gel (SiO₂ · H₂O) [Duguid *et al.*, 2005; Kutchko *et al.*, 2006; Barlet-Gouédard *et al.*, 2007; Carey *et al.*, 2007; Kutchko *et al.*, 2007; García-González *et al.*, 2008; Kutchko *et al.*, 2008; Rimmelé *et al.*, 2008; Bachu and Bennion, 2009; Barlet-Gouédard *et al.*, 2009; Regnault *et al.*, 2009; Wigand *et al.*, 2009]. Early studies of such reactions employed cement samples exposed to large volumes of water and SC CO₂, at temperatures in the range 50 to 90°C, pressures up to 30 MPa, under unconfined conditions allowing advective transport. These studies show heavy degradation in the form of porous reaction fronts reaching 1 to 25 mm in thickness after one year [Duguid *et al.*, 2005; Barlet-Gouédard *et al.*, 2006; Kutchko *et al.*, 2008]. By contrast, more recent studies of confined samples, i.e. samples tested under conditions of positive effective pressure similar to those expected *in-situ*, show that carbonation reactions decrease porosity and permeability and improve sealing capacity [Bachu and Bennion, 2009]. Similar conclusions have been drawn from observations made on cement samples recovered from a wellbore in a caprock horizon within the SACROC Unit, in the Permian Basin of West Texas, following exposure to supercritical CO₂ over 30 years of enhanced oil recovery (EOR) [Carey *et al.*, 2007]. On the other hand, aside from purely geochemical effects on wellbore cement, it is widely recognized that pre-existing mechanical defects, such as fractures or injection voids, have the potential to provide pathways for CO₂ leakage, impairing CO₂ storage safety

[Hofstee *et al.*, 2008; Bachu and Bennion, 2009].

In view of the highly variable results obtained in geochemical degradation experiments under different conditions, it is important to clarify whether carbonation reactions between CO₂ and cement, under realistic (i.e. confined) downhole conditions, degrade the sealing properties of wellbore cements, by increasing their porosity and permeability, or whether they enhance these properties, by decreasing porosity and pore connectivity. It is also important to investigate the potential of supercritical CO₂ for leaching versus healing and sealing of pre-existing mechanical defects (i.e. fractures or cracks) in cemented wellbore systems. Finally, as previous geochemical studies have often used cement samples cured (i.e. hydrated) for only 28 days after mixing, it is important to use not only realistic downhole conditions but also mature cement samples.

This paper reports experiments addressing the effect of CO₂-induced carbonation reactions on the transport properties of both fractured and unfractured cylinders of mature Class A Portland cement, cured for 6 months. This is long enough for the samples to much more closely approach the compositional, microstructural and mechanical properties expected under *in-situ* conditions [Çolak, 2006]. The experiments consisted of batch reaction runs, performed for up to four months, on wet, polymer-jacketed cement samples subjected to a constant hydrostatic confining pressure (P_c) of 30 MPa, a temperature (T) of 80°C, and a CO₂ pressure (P_{CO_2}) of 10 MPa applied to one end of the samples. These conditions were chosen to simulate *in-situ* wellbore conditions relevant to CO₂ storage at a depth of 2-3 km.

6.2 Experimental method

6.2.1 Sample preparation and curing

The experiments were performed on cylindrical samples of Class A Portland cement (ENCI, The Netherlands) prepared with a water-cement or *w:c* ratio of 0.5. This material is similar to that used prior to 1980 in abandoned wellbores present in depleted oil and gas fields throughout The Netherlands (e.g. the De Lier field) and in numerous fields elsewhere around the world. It is also similar in composition to the cement plugs retrieved from the well in the SACROC Unit, Permian Basin, Texas, USA [Carey *et al.*, 2007].

Before mixing and reaction with water, Class A Portland cement contains four main components typically in the following proportions: 45 % tricalcium silicate (Ca₃SiO₅ or C₃S), 27 % dicalcium silicate (Ca₂SiO₄ or C₂S), 11 % tricalcium aluminate (Ca₃Al₂O₆ or C₃A) and 8 % tetracalcium aluminoferrite (Ca₄(Al,Fe)₂O₅ or C₄AF), as well as small quantities of CaSO₄, MgO and CaO. The major products of reaction with water and subsequent curing (i.e. on-going hydration) are calcium hydroxide or portlandite (Ca(OH)₂) in a proportion of about 20-25 %, around 50-60 % of calcium silicate hydrate gel (C-S-H or 3CaO·2SiO₂·4H₂O) formed by hydration of C₃S, around 15-20 % calcium sulfoaluminate (AF_(m,i)) or ettringite ((CaO)₆(Al₂O₃)(SO₃)₃·32H₂O), plus 1-12 % calcium aluminates [Lea, 1970; Mindess and Young, 1981]. It is the C-S-H, which has a platy, partially crystalline, jennite- or tobermorite-like structure, that mainly contributes to the strength of cement [Lea, 1970; Mehta and Monteiro, 2006].

In the present study, cement slurry was prepared in accordance with American Petroleum Institute specifications (ISO/API 10B, section 5, [API, 1997] using fresh water. After mixing the cement and water, the slurry was degassed under vacuum and slowly poured into cylindrical molds of 85 mm length and 35 mm diameter. The cement was then cured for 48 hours in a water bath at 58°C at atmospheric pressure. The cured cement samples were subsequently removed from the molds and furthered cured at room temperature, for 6 months, in a water-saturated, air-tight environment, to avoid exposure to atmospheric CO₂. The 6-months curing time allowed enough time for near completion of the various hydration reactions producing a mature, homogeneous, cement microstructure. Typically 70 % of the C₃S initially present in Class A cement reacts after 28 days, while 100 % reacts within 12 months; similarly, 30 % of the C₂S reacts after 28 days, while 100 % reacts within 12 months [Lea, 1970; Mindess and Young, 1981]. Our long-term curing approach thus provided us with cement cores that are closely similar to the material present in many abandoned wells in The Netherlands (e.g. the de Lier Field) and in the USA (e.g. the SACROC Unit, Permian Basin).

Following curing, the water-saturated cylindrical samples were cut and ground to length, to obtain right cylinders of 17 mm length and 35 mm diameter. Selected samples were fractured along the longitudinal axis by cleaving using a hammer and a chisel, such that “naturally” rough, axial fracture planes were obtained. All samples were subsequently stored in water-saturated, air-tight containers prior to testing.

6.2.2 Healing/reaction experiments: apparatus and procedure

Long-term healing/reaction experiments were performed, under confined conditions, on both intact and fractured samples using an externally heated, hydrostatic pressure vessel employing silicon oil as the pressure medium. The vessel contains up to six jacketed sample assemblies, arranged in pairs connected to three independent CO₂ pressure lines, as shown in Figure 6.1. Sample temperature was measured using a type K (chromel - alumel) thermocouple, placed inside the pressure vessel amidst the various samples. The confining pressure applied to the samples was simply shut in via the access port shown in Figure 6.6.1 and monitored using a Nova Swiss pressure gauge (40 MPa full scale). High purity carbon dioxide was introduced into the samples using an Air Products CO₂ cylinder and shut into the samples using valves in the three independent CO₂ lines (Figure 6.1). The pressure in each CO₂ line was monitored using Swagelok pressure gauges (40 MPa full scale). The CO₂ was initially introduced at pressures up to 5 MPa, and then boosted to higher pressures (up to 10 MPa) using an argon-backed separator plus large volume argon buffer (Figure 6.1).

In the present experiments, each water-saturated sample was jacketed in a CO₂ resistant, Ethylene Propylene Diene, M-class rubber (EPDM) sleeve and outer Fluorinated Ethylene Propylene (FEP) Teflon jacket, the latter being sealed against two steel end-pistons (316 Stainless Steel) to prevent leakage of the silicone oil confining medium into the sample assembly (Figure 6.1). The top piston of each sample assembly featured radial grooves on its face, plus a central bore connected to the pore fluid system, to allow CO₂ injection and to maximize the distribution of supercritical CO₂ over the top end of each sample. The bottom

end-piston consisted of a solid steel blank. Jacket sealing was accomplished by using a wire tourniquette method with underlying EPDM band countersunk in the end-piston surfaces. A small amount of water was added to the samples before sealing, to prevent drying during handling and to ensure saturation of the samples prior to testing.

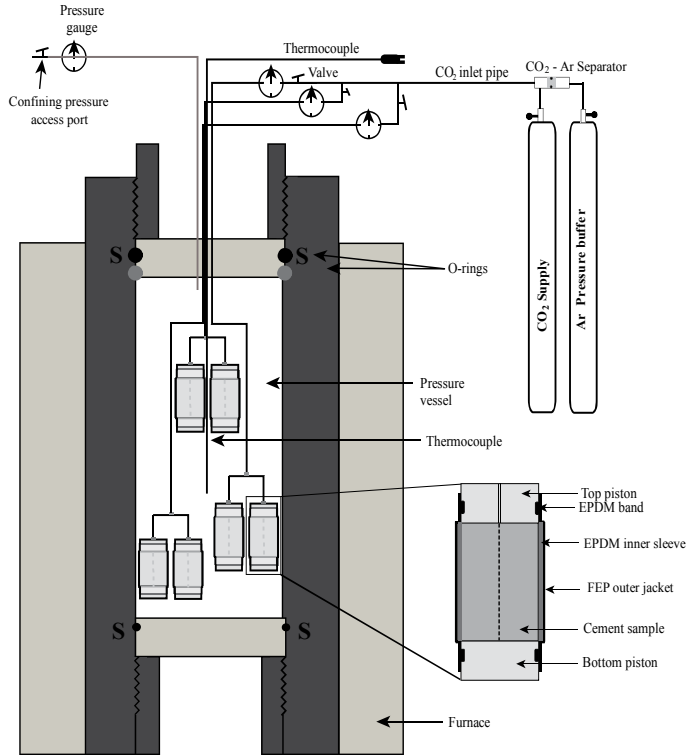


Figure 6.1. Schematic diagram of the high pressure experimental set-up and of the individual sample assemblies used.

In initiating the experiments, six sealed samples (1 intact and 5 fractured) plus supporting pipework were placed in the pressure vessel. This was then pressurized with a confining pressure of 10 MPa. The samples were then heated to a temperature of 80°C by means of the external furnace plus appropriate process controller, maintaining the confining pressure at 10 MPa. Heating was performed with the CO₂ lines closed to prevent drying of the samples. When the desired temperature of 80°C was reached, a confining pressure of 30 MPa was applied, followed by injection of 10 MPa supercritical CO₂ into the top of each sample assembly, such that the CO₂ would gradually diffuse into the aqueous phase present in the sample pores.

Experiments were run in three, 30-day stages, each terminated by venting the CO₂ pressure and then the confining pressure from the system, followed by cooling of the system and removal of the samples from the vessel. After each 30-day (1 month) stage, one fractured sample and a single intact sample were retrieved, removed from their jackets, and their bulk permeability measured. Note that the fractured samples were coherently bonded at this stage.

The intact sample was then re-jacketed and a new fractured sample assembly was prepared to replace that removed. The entire set of six samples was then returned to the pressure vessel for the following 30 days stage of the experiment. This was done with the aim of retrieving fractured samples treated for 30, 60 and 90 days, along with a single intact sample treated for a cumulative total of 90 days.

Following permeability measurement, each fractured sample removed from the vessel was sawn axially, perpendicular to the pre-existent fracture plane, to obtain two identical halves. One half the sample was used for thermogravimetric analysis (TGA) of reaction progress. The remaining half was oven-dried at 60°C for 6 days, impregnated with resin and then sectioned parallel to the axial saw cut. The polished sections were analyzed using Scanning Electron Microscopy and energy-dispersive X-ray spectroscopy (EDX).

In this way, we were able to study the progress of reaction, microstructural development and permeability evolution in a suite of fractured and intact samples, over a period of 3 months reaction time. In practice, however, several leaks occurred so that ultimately only four experiments were successfully completed. These are listed in Table 6.1 along with details on two untreated samples used for control purposes. Note that the control samples were cured for 2 days and 6 months respectively.

6.3 Analytical methods and results

In the following, we describe the detailed observational, analytical and permeability measurement techniques applied to the samples and we present the results obtained per technique. We performed the various measurements and analyses not only on the reacted samples, but also on the unreacted control samples.

Sample ID	Curing time [days]	Sample type	Duration of reaction [days]	Reaction conditions			Reaction front [μm] (top surface)	κ _{mean} [m ²]
				P _c [MPa]	T [°C]	P _{CO₂} [MPa]		
PCEM-R	2	Control	Not reacted	-	-	-	-	-
PCEM-O	180	Control	Not reacted	-	-	-	78.9 - 120.3	1.84 10 ⁻¹⁶
PCEM-U	180	Intact	90	20	80	10	Not measured	8.30 10 ⁻¹⁸
PCEM-1	180	Fractured	30	20	80	10	357.9 - 498.9	1.09 10 ⁻¹⁴
PCEM-2	180	Fractured	60	20	80	10	1110 - 1111.3	1.33 10 ⁻¹⁴
PCEM-3	180	Fractured	90	20	80	10	1156 - 1187	1.32 10 ⁻¹⁴

Table 6.1. List of the healing/reaction experiments reported in this paper, along with the experimental conditions at which the tests were conducted. Samples PCEM-R and PCEM-O are control samples cured for 2 and 180 days respectively. These were not subjected to healing/reaction treatment. Here T denotes the temperature at which the tests were performed, P_c is confining pressure, P_{CO₂} is CO₂ pressure and κ_{mean} is mean permeability value obtained for whole samples.

6.3.1 Sample-scale measurements and observations

Upon removal from the reaction vessel, all reacted samples were visibly still wet and fractured samples were cohesively bonded. A distinct, white, carbonation front had formed at the outer rims of all of the samples, and around the fracture plane in the fractured samples. Reaction front penetration or carbonation depths were measured on low magnification SEM

images, made using the polished, axial sections of the fractured samples, cut perpendicular to the fracture plane. A Phillips XL 30 FEG scanning electron microscope with backscatter electron image (BSE) detector was used for this purpose. Penetration depths were measured at 10 evenly spaced points at the top rim of each sample, i.e. at the surface directly in contact with the injected supercritical CO_2 . The fronts were clearly visible as a bright homogeneous zone, with decreased porosity, and sharp internal boundary. The mean value of the ten penetration depth measurements was taken as the carbonation depth. The values obtained lie in the range of 358-1187 μm and are summarized in Table 6.1. The carbonation fronts developed at the remaining outer surfaces of the reacted samples were much thinner, and fell in the range 210-270 μm , similarly to the carbonation fronts developed on both sides of the fracture plane, which ranged between 120 and 230 μm . The unreacted control sample PCEM-0 showed carbonation fronts with thickness varying between 78.9 and 120.3 μm .

6.3.2 Detailed SEM – EDX observations

The Phillips XL 30 FEG scanning electron microscope (SEM) equipped with was also used to investigate the detailed microstructure of the samples. Samples examined included the immaturely cured control material (PCEM-R, 2 days curing), the unreacted starting material cured for 6 months in a CO_2 free environment (PCEM-0), and the fractured samples reacted for one (PCEM-1), two (PCEM-2) and three (PCEM-3) months (see Table 6.1). The SEM's energy-dispersive X-ray spectroscopy (EDX) system was used to determine the chemical composition of the phases present in the samples, and hence to identify them.

The immature material (PCEM-R) shows a relatively heterogeneous microstructure consisting of ovoid, polymineralic clusters of portlandite ($\text{Ca}(\text{OH})_2$), tricalcium silicate (C_3S), dicalcium silicate (C_2S) and calcium aluminates ($\text{Ca}_3\text{Al}_2\text{O}_6$ or C_3A) embedded in a porous matrix of intergrown C-S-H gel (Figure 6.2). Particle size range from ~ 20 to 100 μm . Generally, the sample shows a relatively high porosity ($\sim 42\%$, measured from the difference in weight of dry vs. wet material) with pore sizes ranging from the micrometer scale (micropores) up to hundreds of micrometers (macropores).

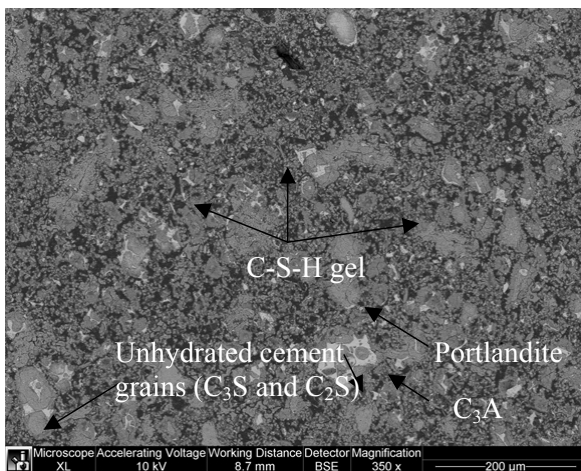


Figure 6.2. Scanning electron microscope image of immature cement sample, cured for two days (PCEM-R) showing a relatively heterogeneous structure, with polymineralic clusters of portlandite, tricalcium silicate (C_3S), dicalcium silicate (C_2S) and calcium aluminate (C_3A) embedded in a porous matrix of intergrown C-S-H gel. The irregular intergranular and transgranular microcracks developed due to the drying of the sample during preparing the thin sections.

The irregular pattern of fine inter- and transgranular microcracks seen in this material, developed during preparation of the sections used for SEM study, and most probably represents drying cracks.

Samples cured for 6 months in a sealed air-tight CO₂-free environment (sample PCEM-0) show a more homogeneous, coarser grained microstructure characterized by a lower porosity (~36 %) than that of sample PCEM-R (Figure 6.3a). The material consists of newly formed, zoned portlandite grains, often with subhedral crystal form, together with residual tricalcium silicate (C₃S) and dicalcium silicate (C₂S) grains undergoing hydration. All of these phases are embedded in a homogeneous, porous C-S-H gel matrix and all show reaction rims. Note that small amounts of calcite were present in the samples as shown by the TGA measurements that were not identified by the SEM observations. The narrow carbonation front developed in sample PCEM-0 is characterized by light grey contrast and has a much lower porosity in comparison with the body of the sample (Figure 6.3b). Combined EDX analysis and secondary electron imaging showed that calcium carbonate precipitated in the carbonation front as a framboidal or nano-crystalline layer on the portlandite grains present in the material (Figure 6.3c). Such calcite-rich layers have been recognized in the literature as passivating layers that develop in the absence of water [Shtepenko *et al.*, 2006]. Their presence thus confirms that the carbonation observed in sample PCEM-0 occurred during preparation of the sample.

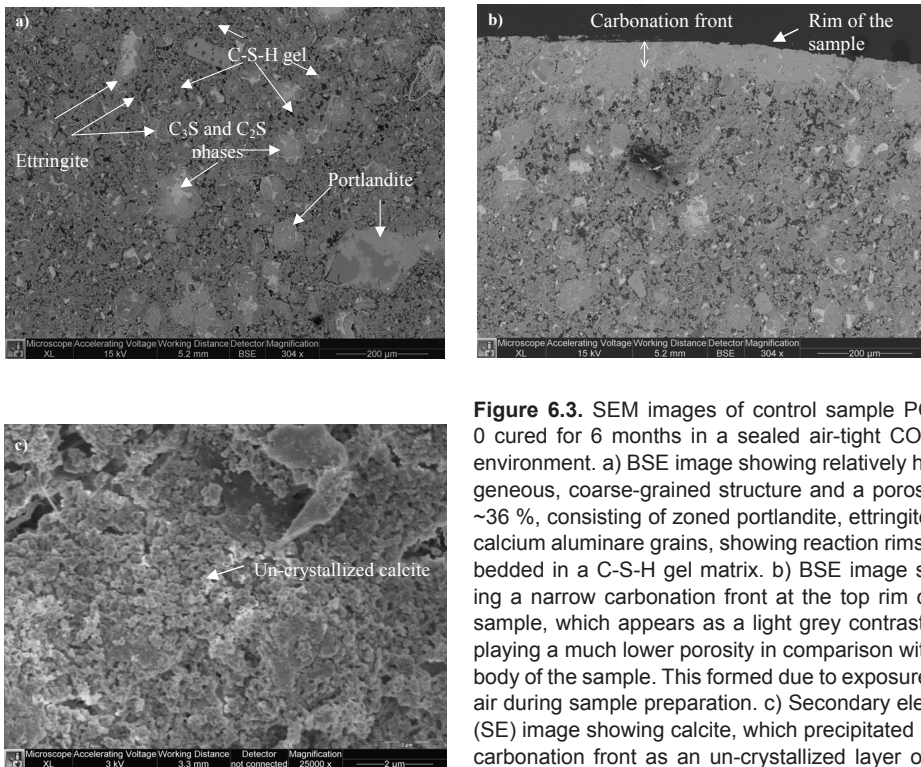


Figure 6.3. SEM images of control sample PCEM-0 cured for 6 months in a sealed air-tight CO₂-free environment. a) BSE image showing relatively homogeneous, coarse-grained structure and a porosity of ~36 %, consisting of zoned portlandite, ettringite and calcium aluminare grains, showing reaction rims, embedded in a C-S-H gel matrix. b) BSE image showing a narrow carbonation front at the top rim of the sample, which appears as a light grey contrast, displaying a much lower porosity in comparison with the body of the sample. This formed due to exposure with air during sample preparation. c) Secondary electron (SE) image showing calcite, which precipitated in the carbonation front as an un-crystallized layer on the surface of portlandite grains present in the material.

The fractured samples exposed to supercritical CO_2 for 1, 2 and 3 months (samples PCEM-1, -2 and -3) showed not only much thicker but also a much denser carbonation fronts at all rims of the samples. We focus first on the development of the carbonation front at the top rim of the samples, i.e. at the surface in contact with injected CO_2 . While the thickness of the front clearly increases with exposure time, especially in the first 60 days (Table 6.1, Figures 6.4a-c), the carbonation process also led to marked densification of the carbonation zone (compare Figures 6.4a-c). Within the fronts, a strong increase in CaCO_3 content was observed, seen as a fine precipitate of crystalline calcite, with grain sizes of typically 0.5 microns and ranging from 0.1 up to 4 microns. Compared with the bulk material, the carbonation front is also depleted in portlandite and calcium aluminate.

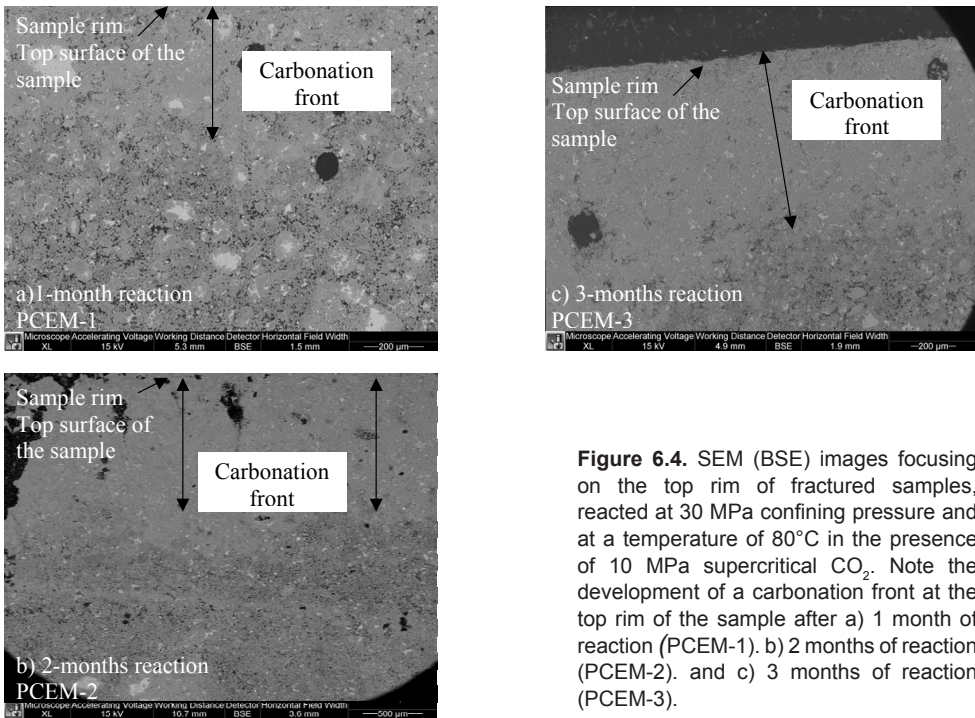


Figure 6.4. SEM (BSE) images focusing on the top rim of fractured samples, reacted at 30 MPa confining pressure and at a temperature of 80°C in the presence of 10 MPa supercritical CO_2 . Note the development of a carbonation front at the top rim of the sample after a) 1 month of reaction (PCEM-1), b) 2 months of reaction (PCEM-2), and c) 3 months of reaction (PCEM-3).

Moving from the upper carbonation front into the “undisturbed” interior of the fractured samples (i.e. into the bulk material remote from either the sample rims or axial fracture), samples PCEM-1, -2, and -3 display a relatively homogeneous microstructure, with a porosity and general microstructure similar to the untreated control sample, PCEM-0, cured for 6-months (Figures 6.5a, b, c). However, it appears that during the reaction experiments, hydration of the interior of the samples continued without detectable carbonation. For example, in the 1-month sample (PCEM-1), C_4AF and C_3A grains are still present (around 5-8 %) and are undergoing hydration to form C-S-H, ettringite and calcium sulfoaluminate (Figure 6.5a), while in the 2- and 3-month samples (PCEM-2 and -3) the C_4AF and C_3A grains are present in a much smaller percentage (~ 2-3 %) and portlandite grains and C-S-H gel are more prevalent (Figures 6.5b and c).

Let us now turn to the microstructures developed near the fracture plane in samples PCEM-1, -2 and -3 (Figures 6.6a, b, c). rims of the samples, though much thinner, especially with respect to the top rim.

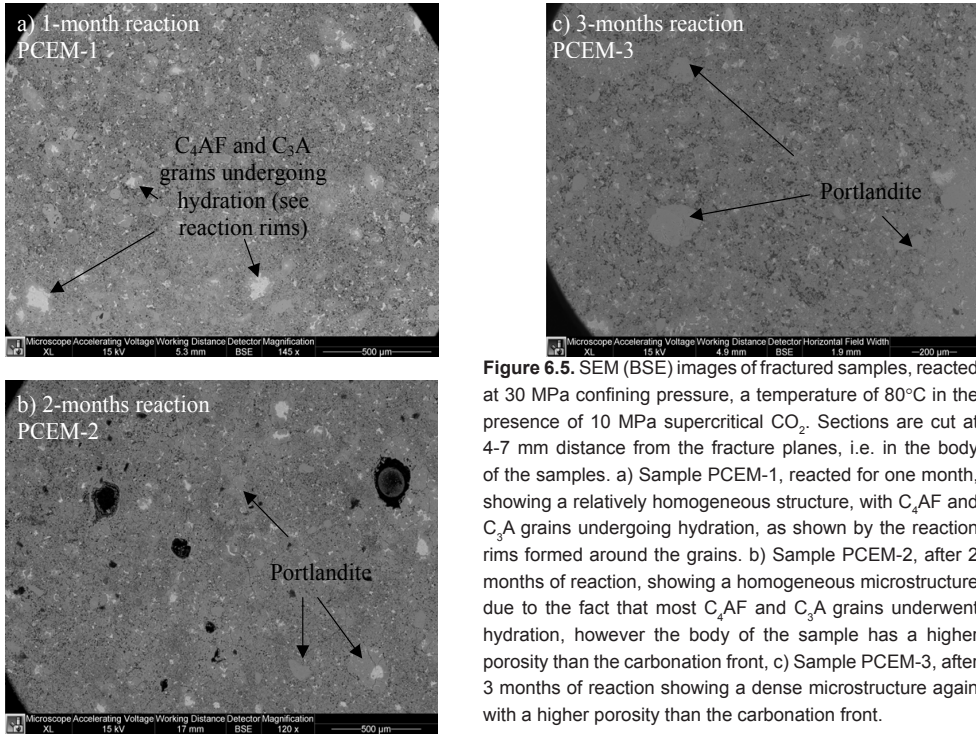


Figure 6.5. SEM (BSE) images of fractured samples, reacted at 30 MPa confining pressure, a temperature of 80°C in the presence of 10 MPa supercritical CO₂. Sections are cut at 4-7 mm distance from the fracture planes, i.e. in the body of the samples. a) Sample PCEM-1, reacted for one month, showing a relatively homogeneous structure, with C₄AF and C₃A grains undergoing hydration, as shown by the reaction rims formed around the grains. b) Sample PCEM-2, after 2 months of reaction, showing a homogeneous microstructure due to the fact that most C₄AF and C₃A grains underwent hydration, however the body of the sample has a higher porosity than the carbonation front, c) Sample PCEM-3, after 3 months of reaction showing a dense microstructure again with a higher porosity than the carbonation front.

SEM study of the fractures, in sections cut perpendicular to them, showed the development of carbonation fronts similar to the ones observed at the On each side of the axial fracture, present in each sample the carbonation front extends a distance varying from ~120 to 150 μm, after 1-month of reaction, to 130 to 230 μm after 2-months (Figures 6.6 a, b). This gives way to more pervasive carbonation, after 3-months of reaction, whereby it becomes difficult to delineate a carbonation front (Figure 6.6c). One of the most striking features present in the samples reacted for 1 and 2 months is the presence of a high porosity zone just beyond the front on each side of the fracture plane (Figures 6.6a, b). These porous zones are depleted in portlandite, ettringite and calcium silicate hydrate content. In the samples reacted for two and three months, the fracture plane became mineralized with fine-grained calcite, healing the fracture completely in places. The healed areas expanded with increasing reaction time from 30 % of the fracture surface at 2 months to 80 % at 3 months (Figures 6.6b and c). Focusing on these “healed areas” of the fractures in PCEM-2 and -3, secondary electron imaging revealed these zones to be rich in well-crystallized, micron and submicron-sized calcite grains, often precipitated in the pores of the sample on portlandite and C-S-H substrate (Figure 6.7).

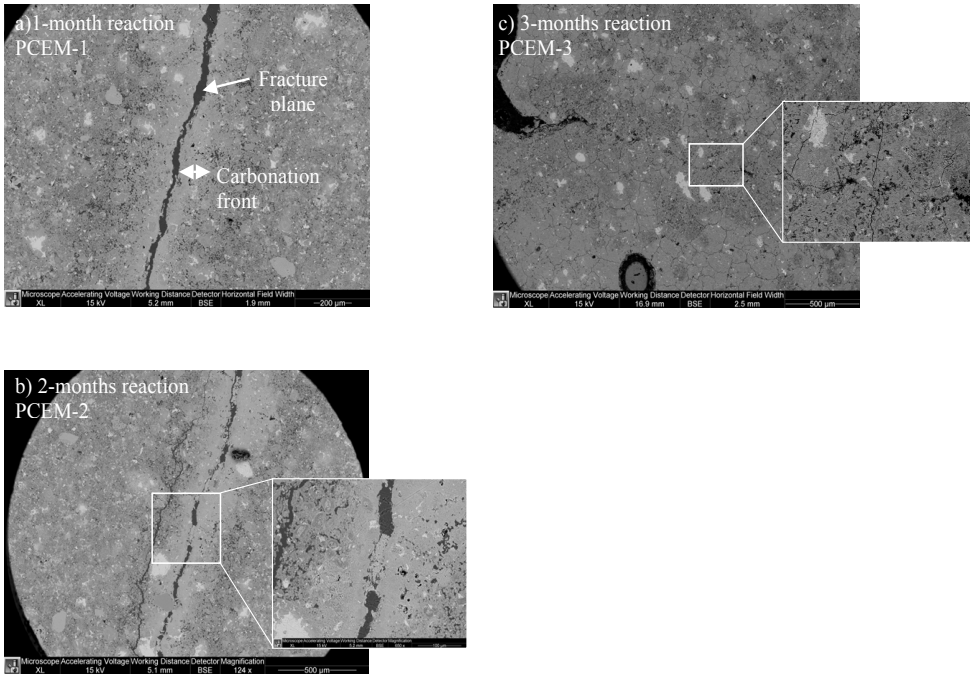


Figure 6.6. SEM (BSE) images of fractured samples, reacted at 30 MPa confining pressure, a temperature of 80°C in the presence of 10 MPa supercritical CO₂. Note the development of a carbonated front adjacent to the fracture planes and the healing of the fractures after 2-3 months. a) Sample PCEM-1, after 1-month of reaction showing a carbonation front with a thickness of ~120 to 150 μm. The fracture plane did not show any healing at this stage. One of the most striking features is the presence of a highly porous area adjacent to the carbonated area. b) Sample PCEM-2, after 2 months of reaction showing a carbonation front of 130 to 230 μm thickness plus healing of the fracture plane in several few areas. This sample also displays a porous zone just beyond the carbonation front. c) Sample PCEM-3, after 3 months of reaction showing pervasive carbonation, with the fracture plane healed over 80 % of its area. It is difficult to measure the carbonation front width in this case, as this does not occur as a distinct zone, as in the other cases.

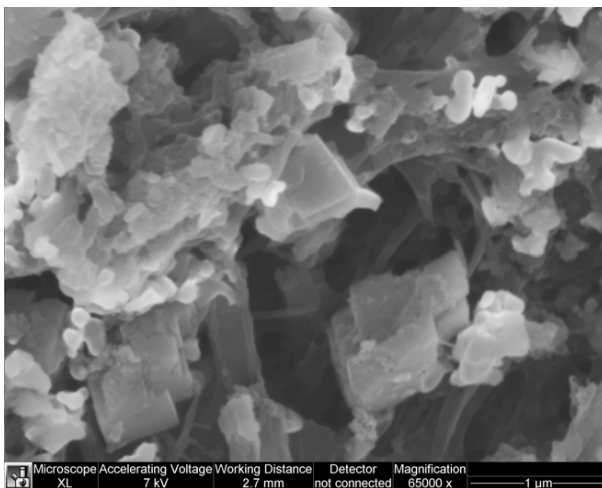


Figure 6.7. SEM secondary electron (SE) image of a healed portion of the fracture plane present in sample PCEM-3 after three months exposure to supercritical CO₂ at 80°C, 10 MPa CO₂ pressure and 30 MPa confining pressure. Note the well-crystallized calcite grains with grain size of less than 1 μm, which were precipitated in the fracture plane.

6.3.3 TGA analysis

For TGA analysis, the half cylinders cut axially from the fractured samples were further cut as shown in Figure 6.8, to obtain a 1 mm thick rectangular slice. This was subsequently cleaved into 8-17 prismatic or stick shaped samples measuring roughly 1 x 1 x 5 mm, such that a cross-sectional sequence of the samples was obtained, running from the axial fracture to the outer surface or the rim of the cylindrical sample (see Figure 6.8). For control purposes, unreacted cement sample PCEM-0 was similarly sliced and diced. Dicing into prisms was done manually with a razor blade carefully avoiding material loss. The resulting, often fragmented prisms were then collected and stored in airtight containers, to prevent carbonation of the material by exposure to air, until TGA analysis was performed.

TGA analysis of the prismatic samples described above (~0.20 to 0.24 grams) was carried out using a Cahn Electrobalance, 1000°C TGA system, with a detection limit ~0.002 wt. % for samples of the present mass. Analyses were performed by heating up the sample to 1000°C at a rate of 5°C/min. Weight loss during heating allowed accurate quantification of the percentage of portlandite and calcite present in both the reacted and untreated cement samples. Typically, the TGA curves revealed three weight loss episodes (Figure 6.8).

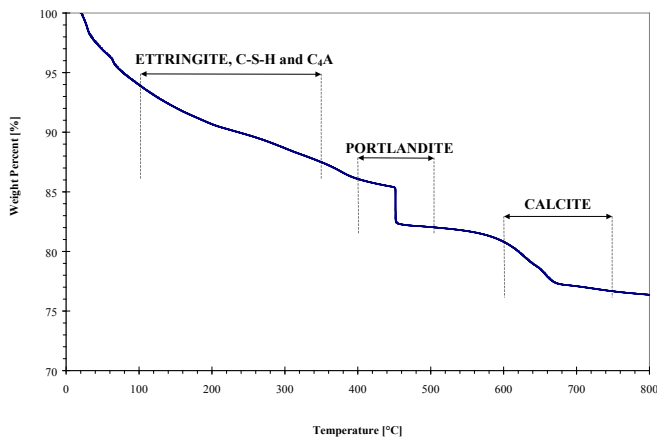


Figure 6.8. Typical thermogravimetric analysis data for a prismatic sample taken from sample PCEM 1. Note the three main regions of mass loss, interpreted as due to a) drying of free water plus dehydration of ettringite, C-S-H and C₄A. b) dehydration of portlandite and. c) CO₂ liberation from calcite respectively, (following Hidalgo et al., 2008; Lea, 1970; Thierry et al., 2007). The insert shows the manner in which our fractured samples were sliced and diced for TGA analysis, allowing subsequent construction of portlandite-calcite concentration profiles

The first episode appears in the temperature range 100 to 350°C and is attributed to the loss of free water from the samples, alongside dehydration of C-S-H, ettringite and calcium aluminate hydrate following [Lea, 1970; Taylor, 1992; Thierry et al., 2007; Hidalgo et al., 2008]). No quantitative data could be obtained from this dehydration episode, due to the lack of distinct mass loss steps and the associated uncertainty in interpretation. The second weight loss step occurs at about 450°C and corresponds to the dehydration of portlandite (Ca(OH)₂), while the final weight loss step occurs at about 700°C and corresponds to the decarbonation

of calcite [Lea, 1970; Thiery et al., 2007; Hidalgo et al., 2008]. Using these TGA signatures, the weight % concentrations of Ca(OH)_2 and CaCO_3 present in each prismatic sample were calculated from the H_2O and CO_2 weight losses, in terms of CaO equivalents.

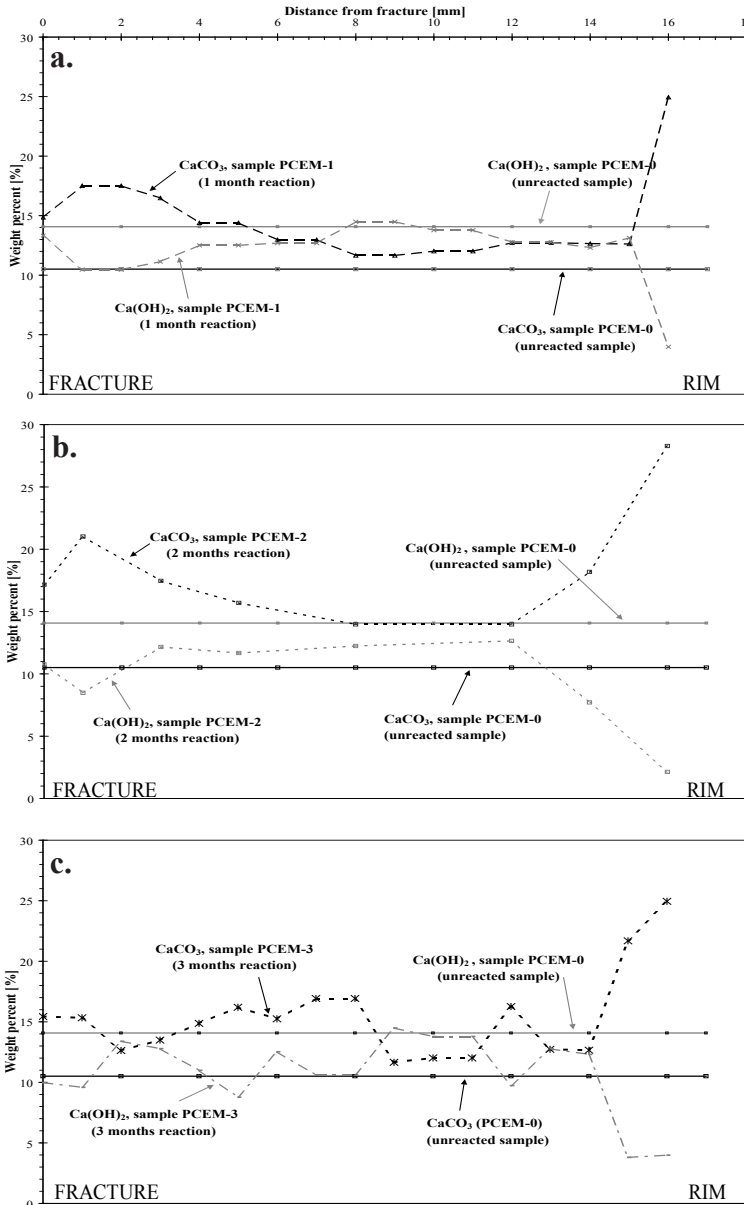


Figure 6. 9. Depth profiles showing the Ca(OH)_2 and CaCO_3 content of unreacted control sample PCEM-0 versus the data obtained for the reacted samples. a) PCEM-1, reacted for 1 month, b) PCEM-2, reacted for 2 months and, c) PCEM-3, reacted for 3 months. The data for control sample PCEM-0 form the horizontal baseline values. The profile for samples PCEM-1, -2, -3 run from the axial fracture to the rim of the samples.

From these values, Ca(OH)₂ and CaCO₃ concentration profiles were constructed for the unreacted control sample PCEM-0 and for all fractured samples (PCEM-1, -2, -3) – see Figure 6.9.

The profiles obtained for unreacted sample PCEM-0 show uniform concentrations of Ca(OH)₂ and CaCO₃ at levels of 14.1 and 10.5 wt % (Figure 6.9). These serve as baseline concentrations with which the profiles for the reacted (fractured) samples can be compared. The reacted samples all show a relative depletion in Ca(OH)₂ concentration, mirrored by enrichment in calcite. These effects were predominant near the fracture and at the rims of the samples in the first two months of exposure to SC CO₂ (Figures 6.9a and b), but were more pervasive after 3 months exposure time (Figure 6.9c). In more detail, the trends seen in the calcite and portlandite content of the individual fractured sample, after one, two and three months of exposure to SC CO₂, can be described as it follows.

Sample PCEM-1 exposed for 1-month shows a 40 % increase in calcite immediately adjacent to the fracture-plane (Figure 6.9a). This increase in calcite content is mirrored by a smaller decrease in portlandite content of 6 %. The increase in calcite content is more pronounced 1-3 mm away from the fracture, varying from 66 to 56 %, while the portlandite content is decreased by 25 to 21 %. The more remote parts of the sample (8 to 12 mm from the fracture plane) are characterized by similar amounts of portlandite as found in the untreated reference material, and by an increase of about 10 % in calcite content. The rim of the sample is characterized by a much greater degree of carbonation, evidenced by an increase in calcite content of about 130 % relative to unreacted material, i.e. an increase by a factor of 2.3, together with a marked decrease in portlandite content (to 72 %).

Sample PCEM-2 exposed to supercritical CO₂ for 2 months exhibits a similar carbonation pattern (Figure 6.9b), with pronounced carbonation at the fracture plane and at the rim of the sample. This is demonstrated by an increase in calcite content of 63 % and a decrease in portlandite content of 23 % near the fracture plane. More remote areas of the sample show an increase in calcite content varying from 33 % to 100 %, mirrored by a decrease in portlandite content of 10 to 40 %, compared with the unreacted sample. In comparison with the samples exposed to SC CO₂ for one month, two-months reaction with SC CO₂ brought about an increase in the calcite content of 10 to 27 % and a decrease in portlandite content of 7 to 25 % over the sample as a whole. Carbonation is again less pronounced at mid range depths in the sample (8-12 mm away from the fracture plane).

Sample PCEM-3 exposed for 3 months shows more pervasive carbonation throughout the sample, except at the rim (Figure 6.9c). Overall, three months reaction lead to an increase in calcite content of 10 to 50 % (150 % at the rim of the sample) corresponding to a decrease of 0 to 30% in portlandite content (130 % at the rim), in comparison with the unreacted material. By comparison with sample PCEM-1, PCEM-3 showed an increase in calcite content in the 4-9 mm range, mirrored by a decrease in portlandite content, while in the 9-16 mm range similar calcite and portlandite concentrations were measured. Sample PCEM-3 showed predominantly a decrease in calcite content at the fracture and at the rim of the sample in comparison with sample PCEM-2, while in the 5-9 mm range it showed a slight increase in

calcite content. This is mirrored by the trends shown by the portlandite contents in samples PCEM-2 and PCEM-3.

6.3.4 Permeability determinations

Bulk sample (i.e. whole sample) permeability measurements were performed on the unreacted control material cured for 6 months (PCEM-0), on the intact (unfractured) sample PCEM-U, which was incrementally reacted over 3 months, and on the three fractured samples exposed to SC CO₂ for 1, 2 and 3 months respectively (PCEM-1, -2, -3). The permeability tests were performed at room temperature, at a reference confining pressure of 1 MPa. Determinations were done at a constant, argon-buffered, water pressure at one end of the sample, while maintaining the other end of the sample at atmospheric pressure, such that a constant pressure difference of 0.2 – 0.3 MPa was maintained. In performing these measurements, the samples were sealed in an EMPD jacket between two grooved, stainless steel end-pistons. The EPDM jacket was sealed against the end pistons using a wire tourniquet method. The tests were carried out in a thin-walled, stainless steel vessel pressurized with argon.

Neglecting gravity effects, the permeability of the samples was calculated using Darcy’s law, written in the form:

$$Q = -\frac{\kappa A}{\eta} \frac{P_1 - P_2}{L} \tag{6.1}$$

where Q is the discharge rate (m³/s), κ is the absolute permeability of the material (m²), η is the dynamic viscosity of the fluid (Pa·s), A is the cross sectional area of the sample (m²), P₁ and P₂ represent the pressure at the fluid inlet and outlet to the sample (Pa) and L is the length of the sample (m).

The measured permeabilities are plotted against time in Figure 6.10. The scatter in the results comes from the fact that several successive measurements were performed on each sample, at different hydraulic heads.

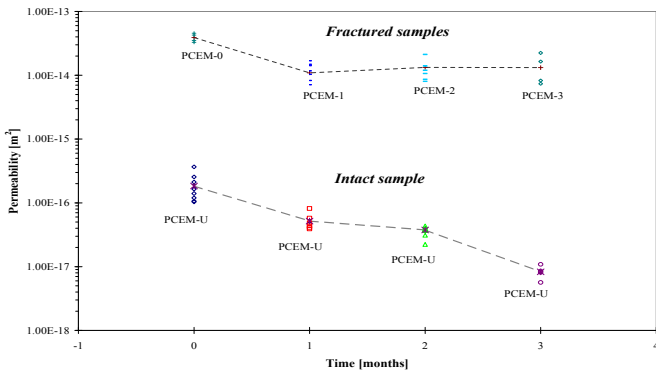


Figure 6.10. Whole sample permeability evolution with time for unfractured cement sample PCEM-U and for fractured samples PCEM-1, PCEM-2 and PCEM-3 retrieved from the reaction vessel after 1-3 months reaction with CO₂ and water at 10 MPa fluid pressure, 80°C and 30 MPa confining pressure. Note that sample PCEM-0 was unreacted but fractured, thus providing permeability of fractured samples after zero reaction time.



The mean permeability of intact (unfractured) sample PCEM-U, reacted for a total duration of 3 months, decreased rapidly with time from about $1.8 \times 10^{-16} \text{ m}^2$ before exposure to SC CO₂ to $5.2 \times 10^{-17} \text{ m}^2$, after one month, to $3.8 \times 10^{-17} \text{ m}^2$ after two months, and finally to $8.3 \times 10^{-18} \text{ m}^2$ after three months. The bulk sample permeability values obtained for the fractured samples were two to three orders of magnitude higher, showing mean values of $3.9 \times 10^{-14} \text{ m}^2$ before reaction to values that decreased after one month of reaction to $\sim 1 \times 10^{-14} \text{ m}^2$ and remained constant afterwards.

6.4 Discussion

Combining our SEM results on the unreacted and fractured samples, it is clear that exposure to CO₂ led to progressive carbonation seen as precipitation of calcite within the outside rims of the samples, notably at the top surface exposed directly to CO₂ (Figures 6.4a, b and c). Our data for this surface (Table 6.1) show that the front advanced at an average rate of $378 \pm 50 \text{ }\mu\text{m/month}$ over three months. In the fractured samples, similar carbonation fronts advanced from the fractures at an average rate of $157 \pm 32 \text{ }\mu\text{m/month}$, and were associated with the development of a porous zone at the leading edge of the front, at least in the first 2 months of reaction. Our TGA data show that these fronts represent at least in part a conversion of portlandite (Ca(OH)₂) into calcite. The carbonation process clearly led to progressive healing of the fractures present in the fractured samples and to an initial decrease in bulk permeability of the fractured samples followed by little change after 1 month (Figure 6.10). The single intact sample studied showed much lower initial permeability and major, on-going decrease in permeability as a result of reaction over 3 months.

In the following, we will analyze the carbonation process in more detail, attempting to explain the formation of the calcite-rich carbonation fronts, the formation of the associated porous bands in the fractured samples, the healing behaviour of the fractured samples, and the permeability changes seen in both the fractured and the unreacted samples. We go on to compare our results with previous experimental data and field observations on wellbore cement exposed to supercritical CO₂, and to assess the implications of our findings for CO₂ storage.

6.4.1 Analysis of the carbonation process

In the literature, chemical degradation of cement exposed to CO₂-rich fluids is described as a series of steps, starting with the dissolution of CO₂ and the dissociation of carbonic acid, followed by dissolution of the portlandite and C-S-H phases and precipitation of calcium carbonate, followed in some cases by re-dissolution of calcium carbonate. Overall, carbonation reactions are believed to dominate the interaction of supercritical CO₂ with wet cement. Following [Kutchko *et al.*, 2007], these reactions can be summarized as:



Such reactions have been reported on the one hand to increase strength and reduce porosity and permeability [Lange *et al.*, 1997; Knopf *et al.*, 1999; Thiery M, 2003; García-González *et al.*, 2008; Bachu and Bennion, 2009], but also to decrease strength and increase porosity and permeability [Duguid *et al.*, 2005; Barlet-Gouédard *et al.*, 2006; Barlet-Gouédard V., 2007; Kutchko *et al.*, 2007; Kutchko *et al.*, 2008; Barlet-Gouédard *et al.*, 2009].

Our SEM observations, TGA analyses and permeability measurements show good agreement with previous studies indicating that carbonation has a positive effect on the sealing properties of cement. Assuming that the carbonation reaction involves dissolution of portlandite and subsequent one-to-one precipitation of calcite (see Equations 6.2-6.5), a lowering of porosity and permeability is expected, due to the difference in molar volume (V_m) between the reactant and the product phases, i.e. Ca(OH)_2 ($V_m = 33 \text{ cm}^3\cdot\text{mol}^{-1}$) and CaCO_3 ($V_m = 37 \text{ cm}^3\cdot\text{mol}^{-1}$) respectively [Thiery *et al.*, 2005]. Making use of our TGA analyses on the fractured samples presented in Figure 6.9, we plotted the change in the number of moles of Ca^{2+} present in portlandite versus the change in the number of moles of Ca^{2+} present in calcite for individual prismatic samples analyzed using TGA, restricting attention to the prismatic samples of similar weight (within 5 %). The results are plotted in Figure 6.11, where they are compared with the initial ratio present in the untreated sample.

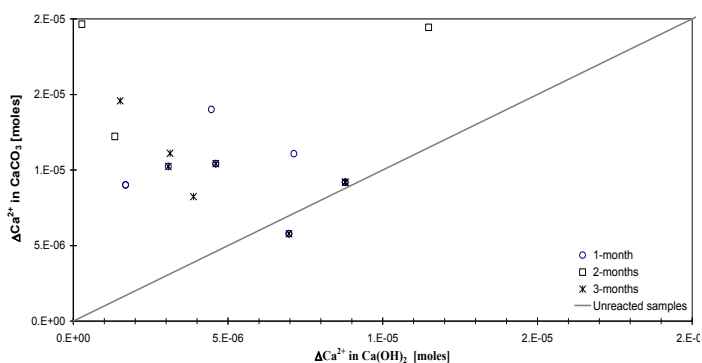


Figure 6.11. Ca^{2+} contained in calcite versus Ca^{2+} contained in portlandite for prismatic samples extracted at various distances from the fracture in fractured samples reacted for 1, 2 and 3 months (PCEM-1, -2, -3). Data are plotted only for prismatic samples of similar weight (within 5 % range). The initial ratio corresponding to the calcite vs. portlandite content present in the untreated material is added for comparison. Note that the samples taken from the reacted samples consistently show enrichment of calcite above that expected by conversion of portlandite only.

The plot shows that the content of calcite present in our samples is larger than the amount predicted by 1:1 conversion of local portlandite. This suggests another source for Ca^{2+} , besides local portlandite. Two possible sources for additional Ca^{2+} are the C-S-H phase, which through reaction (4) forms CaCO_3 , $\text{SiO}_2\cdot\text{H}_2\text{O}$ and Al_2O_3 [Thiery *et al.*, 2005; Castellote *et al.*, 2008], and ettringite. The large uncertainties in deriving the ettringite and C-S-H concentrations in our samples using TGA analysis, and in the molar volume of these phases [Bentz *et al.*, 1998; Bentz, 1999; Glasser *et al.*, 1999; Flatt and Scherer, 2008] prevent any useful estimates of the contribution of these phases to the formation of calcite. However reaction of these phases to

form calcite is generally expected to lead to an increase in porosity and permeability as their molar volumes are much higher [Bentz, 1999; Glasser *et al.*, 1999; Flatt and Scherer, 2008]. Since we observed a general tendency for porosity and permeability reduction, and in view of the clear correlation in Figure 6.9 between changes in portlandite and calcite concentrations, it thus seems likely that the dissolution of portlandite and precipitation of calcite dominated the interaction cement-water-CO₂ in our tests. A probable source of the excess calcite that formed in our fractured samples compared with portlandite (Figure 6.9) could be one of diffusion of Ca²⁺ from portlandite or other phases dissolving locally or at greater distances from the fracture.

Turning now to the SEM images of our fractured samples, a narrow zone of increased porosity, depleted in portlandite, ettringite and C-S-H phases, is visible next to the dense carbonated zone present adjacent to the fracture plane (Figure 6.6a, b, c). Both zones fall well within the first prismatic TGA sample taken next to the fracture. Such zonation can be explained as follows (see [Le Saout *et al.*, 2006; Neville *et al.*, 2009]). First, the pH at the cement - water interface (~ 12.5-13.5) will be lowered by the addition of supercritical CO₂ to the pore fluid (see equation 6.2) to values around 9 [García-González *et al.*, 2008; Xie *et al.*, 2008]. This will cause dissolution of portlandite, ettringite and C-S-H (equations 6.3 – 6.4) at the fracture plane where the sample is in contact with “free” CO₂-water solution, leading to an increase in Ca²⁺ concentration, supersaturating the pore fluid and precipitating calcite. In association with CO₂, H⁺ and HCO₃⁻ diffusion into the sample, an upward gradient in Ca²⁺ concentration in the pore fluid will develop between the carbonated zone (lower Ca²⁺ concentration buffered by precipitation of calcite) and the region just beyond it (high Ca²⁺ concentration due to ongoing dissolution of portlandite, ettringite or C-S-H). This gradient will lead to diffusion of Ca²⁺ ions from the high concentration zone just beyond the carbonated front (Zone 2 in Figure 6.12) towards the carbonated zone with lower Ca²⁺ concentration (Zone 1 in Figure 6.12).

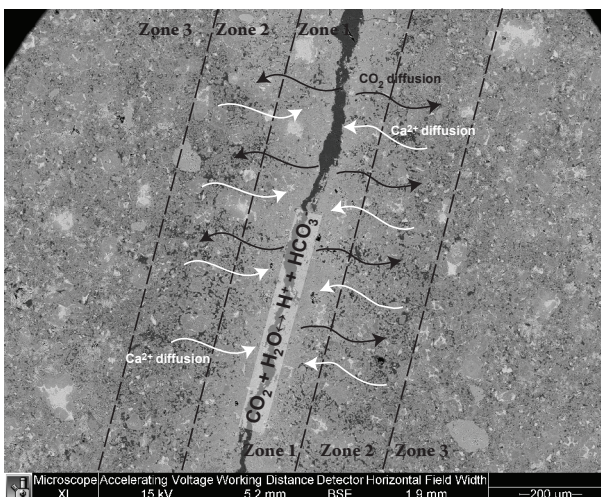


Figure 6.12. Backscatter SEM image showing three zones occurring at the fracture plane in sample PCEM-2 exposed to supercritical CO₂. The carbonation front seen in Zone 1 is characterized by a low porosity due to calcite precipitation. Zone 2 has a high porosity probably due to dissolution of the portlandite, ettringite and/or C-S-H phases. Zone 3 consists of relatively unreacted cement.

This diffusion of Ca²⁺ from Zone 2 into zone 1 will accordingly lead to depletion of Zone 2 in

portlandite (and possibly ettringite and C-S-H) thus producing the increased porosity, as seen in our SEM images of samples reacted for 1 and 2 months (Figures 6.6a, b, and 6.12).

This process, operating over a more extended length scale not reflected in the sample microstructure, probably explains the enrichment in calcite compared with portlandite seen in much of our TGA data on the fractured samples (Figures 6.9 and 6.11). After three months of reaction, the carbonation front is no longer clearly visible within our fractured samples. Rather, we observed distributed carbonation throughout the sample (Figures 6.6c and 6.9). However, as the fracture is cemented with calcite over extensive areas (Figure 6.6c), carbonation at the fracture plane must have occurred. This all suggest that beyond 2 months reaction time, the CO₂ and other components diffuse throughout the sample, such that the above gradients in concentration are reduced, leading to a more uniform structure and decreased porosity of the cement.

It is useful to recall at this point that the carbonation front developed at the fracture plane is much thinner than that formed at the top rim of the samples, i.e. at the point of CO₂ injection (cf. Table 6.1, Figures 6.6 vs. 6.4). This effect can be linked to the availability of CO₂ and its diffusion into the sample. At the top of the sample, more CO₂ is available for dissolution and diffusion, so that the carbonation front extends deeper into the cement than at the fracture plane, where diffusion is slowed down by the longer path length to the upper surface of the sample. This effect of diffusion path length may well be responsible for the fact that porous zone seen near the fractures in our samples were not observed near the sample top rim.

Overall, the zonation observed in our samples (at the rims and adjacent to the axial fractures) implies that the carbonation process was diffusion-controlled. Previous studies of carbonation rims in cement have also inferred the rate of carbonation to be diffusion limited (Hanecka et al., 1997; Duguid et al., 2005; Barlet-Gouédard et al., 2007), with the carbonation reactions being much faster than the diffusion of CO₂ through the cement. Assuming CO₂ diffusion control and a constant CO₂ concentration at the cement surface as boundary condition, Fick's laws yield a depth of carbonation (d) given by the relation:

$$d = \alpha t^{1/2} \quad (6.6)$$

where t is the time of exposure to supercritical CO₂ (days) and α is a rate constant related to the effective diffusivity of dissolved species through the cement (Duguid et al., 2005; Barlet-Gouédard et al., 2006). If CO₂ diffusion was the rate controlling mechanism responsible for the carbonation observed at the top surface of our samples, a plot of $\log(d)$ vs. $\log(t)$ should accordingly yield a slope of 0.5 (Duguid et al., 2005; Barlet-Gouédard et al., 2006; Barlet-Gouédard et al., 2009). Overall, our data for top surfaces show a best-fit line with a slope of 0.45 (Figure 6.13).

This is slightly lower than expected, but agrees well with most previous work on carbonation rims (Duguid et al., 2005; Barlet-Gouédard et al., 2006; Kutchko et al., 2007; Rimmelé et al., 2008), and implies that it is indeed CO₂ diffusion that largely controls top surface carbonation of our samples. We note, however, that our long term data (90 days) show a slope of only 0.2, suggesting that carbonation was more complex than the simple diffusion-controlled process embodied by equation (6.6).

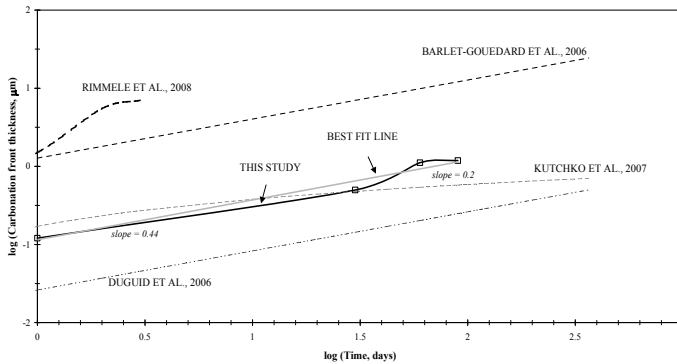


Figure 6.13. Log-log plot showing mean carbonation front thickness advancement vs. time, during exposure to supercritical CO₂. Data obtained for carbonation at the top surface of our samples, plus comparison with the relationships obtained in previous studies of surface (sample rim) carbonation (Barlet-Gouédard et al., 2006; Duguid et al., 2006; Kutchko et al., 2007; Rimmelé et al., 2008).

Similar behaviour was observed in the study of Kutchko et al. (2007) where $\log(d)$ vs. $\log(t)$ plots yielded α -values of 0.26 at long times. In line with these authors interpretation and our microstructural observations, we infer that rapid, initial carbonation near the sample surfaces was slowed down by the precipitation of a dense calcite layer, which in turn slowed down diffusion of CO₂ through the sample.

6.4.2 Effect of carbonation on cement permeability

We now consider the effect of carbonation on the transport properties of our cement samples, namely on their bulk or whole sample permeability (matrix plus induced fractures). The permeability measurements performed on the single intact (unfractured) sample PCEM-U showed a three-fold decrease after only one month of reaction and around 22 times lower permeability after three months of carbonation (Figure 6.10). Though performed on fractured samples (PCEM-1, -2, -3), our microstructural observations indicate that carbonation involves dissolution of cement phases and precipitation of calcite (see Figure 6.7) in the pore space, first at the sample rims and ultimately throughout the samples. On this basis, it is reasonable to suppose that bulk permeability evolution in our intact sample reflects the progress of inwardly sweeping carbonation. Linear extrapolating our steadily decreasing permeability data for intact cement in Figure 6.10 suggests that 1-D penetration of CO₂ into water-saturated, intact material will render the interfacial region of the cement effectively impermeable ($\kappa < 10^{-21}$ m²) after ~1 year. Similar effects will presumably occur under comparable *in-situ* conditions where intact Class A wellbore cement is exposed to CO₂, at least for exposure on similar length scales.

Turning to the permeability tests performed on our fractured samples, an initial reduction in bulk permeability by a factor of 3 was observed after one month of carbonation, whereas further carbonation did not result in any changes in the permeability of our samples, despite substantial healing (80% by area) of the axial fracture due to calcite precipitation. Since the bulk permeability of our intact sample was much lower and decreased continuously, the implication

is that the permeability of the fractured samples was controlled by the central fracture, notably in the first two months, and by the redistribution of porosity around the fracture, especially after 3 months (Figures 6.6a and b). In other words, the effect of progressive cementation of the fracture may have been offset by redistribution of porosity. Alternatively, it is possible that deposition of calcite in the fracture led to an increase in mean fracture width due to “force of crystallization” effects (Wiltschko and Morse, 2001), while the open fracture area decreased. This seems unlikely, however, as our microstructural observations showed no evidence of widening of crack aperture with time (Figure 6.6). Given the pervasive carbonation which led to the relatively homogeneous microstructure observed in sample PCEM-3 (Figure 6.6c), it seems reasonable to assume that in the longer term the sample permeability will follow a similar trend to the (homogeneous) intact material (PCEM-U, Figure 6.10). This predicts a reduction to an effectively impermeable state of initially fractured material within 2 years. If healing at the rate of intact material is delayed by 10 years and occurs at a 10 times slower rate, healing to the same “impermeable” state ($\kappa < 10^{-21} \text{ m}^2$) would take 30 years. On this basis, we infer that under *in-situ* conditions, self-healing of cement and of pre-existing fractures can be expected to occur at the cement-CO₂ interface within periods of several years to several decades. This is consistent with and thus confirmed by observation made on the cement samples recovered from the SACROC Unit, which showed self-healing of fractured cement within 30 years of exposure to CO₂ (Carey et al., 2007). However, final confirmation by means of long-term experiments is ideally needed.

6.4.3 Detailed comparison with previous work

The previous experimental studies regarding the effect of supercritical CO₂ on Portland cement (Classes A, G, H) fall into two categories:

1. Unconfined tests, where cement samples were exposed to free volumes of water-CO₂ mixtures, allowing varying degrees of external advective flow (Duguid et al., 2005; Barlet-Gouédard et al., 2006; Kutchko et al., 2006; Barlet-Gouédard et al., 2007; Kutchko et al., 2007; Rimmelé et al., 2008).

1. Confined, flow-through tests where CO₂-water mixtures were passed through cement samples under conditions of elevated T and confining P (Bachu and Bennion, 2009; Wigand et al., 2009).

In the unconfined tests, the cement showed an external zone of increased porosity, followed by a thin calcite-rich front with a very low porosity, and then the interior of the cement, which was unattacked by CO₂. The degradation/carbonation zone was found to vary from a thickness of $d \sim 21 \sim 24 \text{ mm}$, after one year of exposure to wet supercritical CO₂ or to CO₂ saturated water (Barlet-Gouédard et al., 2006; Barlet-Gouédard V., 2007; Rimmelé et al., 2008; Barlet-Gouédard et al., 2009) to thickness of around 1 mm in the same time frame (Duguid et al., 2005; Kutchko et al., 2006; Kutchko et al., 2007). By comparison, our confined samples showed dense outer carbonation fronts or rims. The generally thicker, more porous degradation layers observed by Duguid et al., (2005); Barlet-Gouédard et al., (2006; 2007; 2009); Kutchko et al., (2007); and Rimmelé et al., (2008) probably reflect the fact that their studies were performed

in relatively large, open volumes of fluid that were free to convect allowing advective transport around the sample. Moreover, the samples used were cured mostly for only 28 days, which did not allow for hydration of the initial phases and homogenization/densification of the cement microstructure (cf. Figures 6.2 and 6.3). Nonetheless, despite the differences in experimental configuration and carbonation front properties, most previous studies as well as our own show that the increase in thickness of the carbonation front over time can be roughly represented in terms of a process controlled by CO₂ diffusion (see equation 6.6).

More in line with our study, Bachu and Bennion, (2009) recently reported confined 90-day experiments addressing porosity/permeability evolution in intact Type G Portland cement exposed to through flowing, CO₂ saturated water. These experiments were performed at a fluid pressure of 15 MPa, a confining pressure of 29 MPa and a temperature of 65°C and showed a decrease in permeability from 10⁻¹⁹ m² to 10⁻²⁰ m². The reduction of permeability was achieved rapidly in the first five days of the test, remaining constant for the remaining 85 days. These results suggest that reaction under flow-through conditions improves the sealing properties of Class G cement. It was further concluded by Bachu and Bennion, (2009) that factors such as the presence of mechanical defects (i.e. cracks) might lead to higher permeability values, and ultimately perhaps to CO₂ leakage through wellbore cements. However, our data suggest that this is unlikely, certainly under static fluid conditions. Interestingly our findings are closely consistent with a very recent study performed at a pore pressure of 19.9 MPa, a confining pressure of 26.2 MPa and at 54°C on fractured Type G cement Wigand et al. (2009). In these experiments, similar partial healing of fractures occurred, again through precipitation of finely crystalline calcium carbonate within the fracture plane.

We now compare our finding with observations by Carey et al. (2007) on Type A cement retrieved from a wellbore penetrating the SACROC Unit, in West Texas, USA. The samples were taken after 30 years of exposure to CO₂ under *in-situ* conditions (i.e. $P_c = 18$ MPa and $T = 54^\circ\text{C}$), brought about both by CO₂ injection and production. The cement showed a heavily carbonated zone in the vicinity of the caprock (shale) and a less carbonated zone next to the wellbore casing (steel). One of the most interesting features is the presence of calcite-filled fractures in the cement. Our experimental results are in good agreement with such field observations, as heavily carbonated zones were observed in our samples both at the fracture plane and at the rim of the samples, i.e. where cement was in direct contact with CO₂ saturated water. The carbonation of our samples did not lead to complete fracture sealing, as shown by our permeability measurements (Figure 6.10). However, the progress of carbonation and precipitation of calcite in the pore space and along the fractures present in our samples with time, along with the SACROC observations, and the results of Bachu and Bennion, (2009) and of Wigand et al. (2009), suggest that cement has high capacity for self-healing and sealing under realistic, *in-situ* conditions (Carey et al., 2007).

6.5 Implications for CO₂ storage

Our Type A Portland cement is relevant for wells plugged prior to 1980 in The Netherlands and for many other locations elsewhere around the world. Our results show that reaction

with CO₂ saturated fluids has a positive impact on the sealing and transport properties of the material under static fluid conditions, and that, under these conditions, the progress of reaction in intact cement is controlled mainly by CO₂ diffusion. In our experiments, the permeability of unfractured cement decreased strongly and continuously during exposure to static CO₂ rich-fluids. Our data imply that carbonation reactions have the potential to reduce the permeability of intact cement, at the CO₂ cement interface, to values for which cement can be considered effectively impermeable ($\kappa < 10^{-21}$ m²) in around one year (Figure 6.10). For fractured samples, permeability reaction is not as rapid or as efficient as in the intact samples, despite the fact that our fractured samples showed heavy carbonation, precipitation of calcite in the fracture plane, and eventually homogenization of the cement. Assuming that subsequent carbonation proceeds as in intact material or up to ten times slower, our results indicate reduction of the permeability of exposed cement to an impermeable state (bulk permeability $< 10^{-21}$ m²) within 2 to 30 years. Under real *in-situ* conditions, carbonation reactions will likely be slower than observed in and predicted by our experiments as reaction progress depends on the availability of CO₂-saturated solution, which may be reduced due to a large length scale for transport from the source to the reaction site. On the other hand, the cement samples extracted from the SACROC Unit indeed confirmed healing within 30 years (Carey et al., 2007).

Overall, the above indicates that static exposure of Type A Portland cement will improve and not degrade sealing capacity under down-hole conditions. However, the assessment of long-term CO₂ storage efficiency and safety requires taking into consideration many additional factors such as the quality of the wellbore cementing job, the type of cement used for wellbore completion and for the wellbore plugs, the nature of any mechanical defects present in the cement, the chemistry of the formation fluid (i.e. salinity), the *in-situ* pressure and temperature, and interactions with the surrounding rocks. Moreover, considering the acidification of the pore fluid due to CO₂ injection and the consequent pH drop around the cement plugs or sheaths (i.e. from 12 to around 9), the corrosion of the casing is an important factor, which has not been fully investigated. Clearly, then, while Class A cement responds rather favorably to reaction with CO₂ and water, further investigation is necessary to evaluate the leakage risks in the wellbore system, taking into account all components in such systems.

6.6 Conclusions

We have investigated the reactions occurring in wet mature Class A wellbore cement exposed to supercritical CO₂ at simulated reservoir/caprock conditions, i.e. at confining pressure of 30 MPa, a CO₂ pressure of 10 MPa and at a temperature of 80°C. Our aim was to determine the effect of cement carbonation on the transport and sealing/healing properties of such materials under confined conditions representative of the downhole situation at a CO₂ storage site. In contrast to many previous studies, we used mature cement samples cured for 6 months instead for 28 days. Our main findings and conclusions are as follows:

1. SEM studies allowed us to qualitatively and quantitatively verify the progress of the carbonation reaction. Results showed that carbonation of intact material occurs from the outer surface of the sample where it is exposed to CO₂ towards the interior, with the

depth of carbonation increasing with the duration of exposure to CO₂. The carbonation fronts obtained extended to depths of around 1200 μm from surfaces in direct contact with CO₂ after 3 months of reaction. The carbonation fronts were characterized by dissolution of portlandite and precipitation of calcite in the pore space, leading to a densification of the material.

2. Axially fractured samples showed cementation of the fracture, and the development of adjacent carbonation fronts, similar to but thinner than the front observed at the rim of the samples, where directly exposed to CO₂. After 1-2 months of exposure, a porous zone depleted in portlandite, developed just beyond the carbonation front. After three months of carbonation, the fracture was hard to distinguish, as calcium carbonate filled about 80 % of the fracture surfaces and a more uniform distribution of porosity and reaction had developed throughout the sample.
3. The above (SEM) observations on carbonation patterns in the fractured samples were confirmed by results obtained using thermogravimetric analyses. The cement plugs showed an increase in weight % concentration of calcium carbonate especially in the fronts developed at the fracture plane and outer rim. This was mirrored by a decrease in portlandite content. However, the increase in calcium carbonate content could not be accounted for by a local decrease in portlandite on a 1:1 basis, which indicated that the calcium carbonate was provided by diffusion of Ca²⁺ from portlandite and other phases dissolving locally or elsewhere in the sample.
4. Permeability measurements of unfractured cement showed a continuous and strong decrease of during exposure to static CO₂ rich-fluids, thus implying that carbonation reactions have the potential to reduce the permeability of intact cement, at the CO₂ cement interface, to values for which cement can be considered effectively impermeable ($\kappa < 10^{-21}$ m²) in around one year. For fractured samples, permeability reaction is not as rapid or as efficient as in the intact samples, despite the fact that our fractured samples showed heavy carbonation, precipitation of calcite in the fracture plane, and eventually homogenization of the cement.
5. Assuming that subsequent carbonation proceeds in fractured cement, at similar rates as in intact material or up to ten times slower, our results indicate reduction of the permeability of exposed cement to an to an impermeable state (bulk permeability $< 10^{-21}$ m²) within 2 to 30 years, showing similarity to cement samples extracted from the SACROC Unit indeed confirmed healing within 30 years (Carey et al., 2007). Under real *in-situ* conditions, carbonation reactions will likely be slower than observed in and predicted by our experiments as reaction progress depends on the availability of CO₂-saturated solution, which may be reduced due to a large length scale for transport from the source to the reaction site. However, proper cementation of the wellbores and a good bonding with the casing and with the surrounding rocks is necessary to ensure the long-term confinement and safety of the storage.

Acknowledgments:

We thank Peter van Krieken, Gert Kastelein and Eimert de Graaff for technical support provided in the laboratory. We would also like to thank the Nederlandse Aardolie Maatschappij (NAM) for kindly providing us with advice on sample preparation. This project was jointly funded by TNO Bouw and Ondergrond and Utrecht Center of Geosciences (UCG), and was conducted in the framework of the CATO Dutch national programme on Carbon Capture and Storage.

REFERENCE LIST

- API, 1997 API Recommended Practice 10B, Washington, DC.
- Bachu, S., 2003. Screening and ranking of sedimentary basins for sequestration of CO₂ in geological media in response to climate change. *Environmental Geology*, 44(3): 277-289.
- Bachu, S., 2008. CO₂ storage in geological media: Role, means, status and barriers to deployment. *Progress in Energy and Combustion Science*, 34(2): 254-273.
- Bachu, S. and Bennion, D.B., 2009. Experimental assessment of brine and/or CO₂ leakage through well cements at reservoir conditions. *International Journal of Greenhouse Gas Control*, 3(4): 494-501.
- Barlet-Gouédard, V., Rimmelé, G., Goffé, B. and Porcherie, O., 2006. Mitigation strategies for the risk of CO₂ migration through wellbores, IADC/SPE Drilling Conference. SPE 98924-MS, Miami, Florida.
- Barlet-Gouédard, V., Rimmelé, G., Goffé, B. and Porcherie, O., 2007. Well technologies for CO₂ geological storage: CO₂-resistant cement. *Oil and Gas Science and Technology, Review IFP*, 62(3): 1-12.
- Barlet-Gouédard, V., Rimmelé, G., Porcherie, O., Quisel, N. and Desroches, J., 2009. A solution against well cement degradation under CO₂ geological storage environment. *International Journal of Greenhouse Gas Control*, 3(2): 206-216.
- Barlet-Gouédard V. , G.R., B. Goffé and O. Porcherie, 2007. Well technologies for CO₂ geological storage: CO₂-resistant cement. *Oil and Gas Science and Technology, Review IFP*, 62(3): 1-12.
- Bentz, D., 1999. Modelling cement microstructure: Pixels, particles, and property prediction. *Materials and Structures*, 32(3): 187-195.
- Bentz, D.P., Waller, V. and de Larrard, F., 1998. Prediction of adiabatic temperature rise in conventional and high performance concretes using a 3-D microstructural model. *Cement and Concrete Research*, 28(2): 285-297.
- Bonett, A. and Pafitis, D., 1996. Getting to the root of gas migration. *Oilfield review*, 8(1): 36-49.
- Carey, J.W., Wigand, M., Chipera, S.J., WoldeGabriel, G., Pawar, R., Lichtner, P.C., Wehner, S.C., Raines, M.A. and Guthrie, J.G.D., 2007. Analysis and performance of oil well cement with 30 years of CO₂ exposure from the SACROC Unit, West Texas, USA. *International Journal of Greenhouse Gas Control*, 1(1): 75-85.
- Castellote, M., Andrade, C., Turrillas, X., Campo, J. and Cuello, G.J., 2008. Accelerated carbonation of cement pastes in situ monitored by neutron diffraction. *Cement and Concrete Research*, 38(12): 1365-1373.
- Çolak, A., 2006. A new model for the estimation of compressive strength of Portland cement concrete. *Cement and Concrete Research*, 36(7): 1409-1413.
- Duguid, A., Radonjic, M. and Scherer, G., 2005. Degradation of Well Cement Exposed to Carbonated Brine, 4th Annual Conference on Carbon Capture and Sequestration. Exchange and Monitor Publications and Forum, Alexandria, VA.
- Dusseault, M.B., Gray, M.N. and Nawrocki, P.A., 2000. Why oilwells leak: Cement behavior and long-term consequences. , SPE International Oil and Gas Conference and Exhibition in China. SPE Beijing, China.
- Flatt, R.J. and Scherer, G.W., 2008. Thermodynamics of crystallization stresses in DEF. *Cement and Concrete Research*, 38(3): 325-336.
- Gale, J., 2004. Geological storage of CO₂: What do we know, where are the gaps and what more needs to be done? *Energy*, 29(9-10): 1329-1338.
- García-González, C.A., el Grouh, N., Hidalgo, A., Fraile, J., López-Periago, A.M., Andrade, C. and Domingo, C., 2008. New insights on the use of supercritical carbon dioxide for the accelerated carbonation of cement pastes. *The Journal of Supercritical Fluids*, 43(3): 500-509.
- Gasda, S.E., Bachu, S. and Celia, M.A., 2004. Spatial characterization of the location of potentially leaky wells penetrating a deep saline aquifer in a mature sedimentary basin. *Environmental Geology*, 46(6): 707-720.
- Gillfillan, S.M.V., Lollar, Barbara Sherwood, Holland, Greg, Blagburn, Dave, Stevens, Scott, Schoell, Martin, Cassidy, Martin, Ding, Zhenju, Zhou, Zheng, Lacrampe-Couloume, Georges, Ballentine, Chris J., 2009. Solubility trapping in formation water as dominant CO₂ sink in natural gas fields. *Nature*, 458(7238): 614-618.
- Glasser, F.P., Tyrer, M., Quillin, K., Ross, D., Pedersen, J., Goldthorpe, K., Bennett, D. and Atkins, M., 1999. The chemistry of blended cements and backfills intended for use in radioactive waste disposal, Environment Agency
- Hanecka, K., Koronhályová, O. and Matia Msovský, P., 1997. The carbonation of autoclaved aerated concrete. *Cement and Concrete Research*, 27(4): 589-599.
- Hidalgo, A., Domingo, C., García, C., Petit, S., Andrade, C. and Alonso, C., 2008. Microstructural changes induced in Portland cement-based materials due to natural and supercritical carbonation. *Journal of Materials Science*, 43: 3101-3111.
- Hofstee, C., Seeberger, F., Orlie, B., Mulders, F., van Bergen, F. and Bisschop, R., 2008. The feasibility of effective and safe carbon dioxide storage in the De Lier gas field. *First break*, 26(1): 53-57.
- Holloway, S., 2001. Storage of fossil fuel-derived carbon dioxide beneath the surface of the earth. *Annual Review of*

Energy and the Environment, 26(1): 145-166.

International Panel on Climate Control, I., 2007. Climate Change 2007: The Physical Science Basis. Contribution of Working Group I to the Fourth Assessment Report of the Intergovernmental Panel on Climate Change, Cambridge University Press, Cambridge, United Kingdom and New York, NY, USA.

International Panel on Climate Control, I. (Editor), 2005. Carbon Dioxide Capture and Storage. Special Report. Cambridge University Press, Cambridge, United Kingdom and New York, NY, USA, 442 pp.

Knopf, F.C., Roy, A., Samrow, H.A. and Dooley, K.M., 1999. High-Pressure Molding and Carbonation of Cementitious Materials. *Industrial & Engineering Chemistry Research*, 38(7): 2641-2649.

Kutchko, B., Strazisar, D., Dzombak, D.A. and Lowry, G., 2006. Degradation of well cements under geologic sequestration conditions, Wellbore Integrity network Meeting, Princeton, N.J.

Kutchko, B.G., Strazisar, B.R., Dzombak, D.A., Lowry, G.V. and Thaulow, N., 2007. Degradation of Well Cement by CO₂ under Geologic Sequestration Conditions. *Environmental Science & Technology*, 41(13): 4787-4792.

Kutchko, B.G., Strazisar, B.R., Lowry, G.V., Dzombak, D.A. and Thaulow, N., 2008. Rate of CO₂ Attack on Hydrated Class H Well Cement under Geologic Sequestration Conditions. *Environmental Science & Technology*, 42(16): 6237-6242.

Lange, L.C., Hills, C.D. and Poole, A.B., 1997. Effect of carbonation on properties of blended and non-blended cement solidified waste forms. *Journal of Hazardous Materials*, 52(2-3): 193-212.

Le Saout, G., Lécolier, E., Rivereau, A. and Zanni, H., 2006. Chemical structure of cement aged at normal and elevated temperatures and pressures: Part I. Class G oilwell cement. *Cement and Concrete Research*, 36(1): 71-78.

Lea, F.M., 1970. *The Chemistry of Cement and Concrete*. Edward Arnold Ltd, London.

Mainguy, M., Longuemare, P., Audibert, A. and Lecolier, E., 2007. Analyzing the risk of well plug failure after abandonment. *Oil & Gas Sci. and Tech. - Rev. IFP*, 62(3): 311-324.

Mehta, P. and Monteiro, P., 2006. *Concrete: Microstructure, Properties, and Materials* The McGraw-Hill Companies, Inc.

Mindess, S. and Young, J.F., 1981. *Concrete*. Prentice-Hall, Inc., Englewood Cliffs, New Jersey.

Neuville, N., Lécolier, E., Aouad, G., Rivereau, A. and Damidot, D., 2009. Effect of curing conditions on oilwell cement paste behaviour during leaching: Experimental and modelling approaches. *Comptes Rendus Chimie*, 12(3-4): 511-520.

Pruess, K., 2005. Numerical studies of fluid leakage from a geologic disposal reservoir for CO₂ show self-limiting feedback between fluid flow and heat transfer. *Geophys. Res. Lett.*, 32(L14404).

Regnault, O., Lagneau, V. and Schneider, H., 2009. Experimental measurement of portlandite carbonation kinetics with supercritical CO₂. *Chemical Geology*, 265(1-2): 113-121.

Rimmelé, G., Barlet-Gouédard, V., Porcherie, O., Goffé, B. and Brunet, F., 2008. Heterogeneous porosity distribution in Portland cement exposed to CO₂-rich fluids. *Cement and Concrete Research*, 38(8-9): 1038-1048.

Shtepencko, O., Hills, C.D., Brough, A. and Thomas, M., 2006. The effect of carbon dioxide on b-dicalcium silicate and Portland cement *Chemical Engineering Journal*, 118: 107-118.

Taylor, H.F.W., 1992. *Cement Chemistry*. Academic Press LTD., London.

Thiery, M., Dangla, P., Villain, G. and Platret, G., 2005. A prediction model for concrete carbonation based on coupled CO₂-H₂O-ions transfers and chemical reactions, 10DBMC International Conférence On Durability of Building Materials and Components, Lyon, France.

Thiery, M., Villain, G., Dangla, P. and Platret, G., 2007. Investigation of the carbonation front shape on cementitious materials: Effects of the chemical kinetics. *Cement and Concrete Research*, 37(7): 1047-1058.

Thiery M, G.V.a.G.P., 2003. Effect of carbonation on density, microstructure and liquid water saturation of concrete. In: K.L.S.a.J.M. D.A. Lange (Editor), *Advances in Cement and Concrete IX*, Engineering Conferences International, Copper Mountain, Colorado, USA, pp. 481-490.

Wigand, M., Kaszuba, J.P., Carey, J.W. and Hollis, W.K., 2009. Geochemical effects of CO₂ sequestration on fractured wellbore cement at the cement/caprock interface. *Chemical Geology*, In Press, Corrected Proof(265): 122-133.

Wiltschko, D.V. and Morse, J.W., 2001. Crystallization pressure versus "crack seal" as the mechanism for banded veins. *Geology*, 29(1): 79-82.

Xie, S.Y., Shao, J.F. and Burlion, N., 2008. Experimental study of mechanical behaviour of cement paste under compressive stress and chemical degradation. *Cement and Concrete Research*, 38(12): 1416-1423.

Xu, T., Apps, J.A., Pruess, K. and Yamamoto, H., 2007. Numerical modeling of injection and mineral trapping of CO₂ with H₂S and SO₂ in a sandstone formation. *Chemical Geology*, 242(3-4): 319-346.

Chapter 7

7.1 Conclusions

This thesis has investigated the effect of CO₂-water-rock interaction on creep phenomena in simulated carbonate rich reservoir rocks, failure behaviour of chalks and of wellbore cements, and on the healing and sealing behaviour of wellbore cements. Experimental techniques such as uniaxial compaction creep, triaxial compression and batch reaction tests were employed, under conditions equivalent to those in a geological system for CO₂ storage at a depth of 2-3 km. The main conclusions of this study are summarized below.

7.1.1 Coupled chemical and mechanical effects of CO₂ on creep in simulated carbonate rocks

Uniaxial compaction creep tests were performed on pre-compacted, porous aggregates of granular calcite, with grain sizes ranging from 1 to 250 μm, under dry and wet conditions, as well as under wet conditions with added supercritical CO₂. The experiments were conducted at temperatures of 28-100°C, effective axial stresses between 4 and 40 MPa, and CO₂ pressures up to 10 MPa.

Mechanical data and microstructural evidence indicated that minor, time-independent compaction occurred in dry samples due to microcracking, grain rearrangement and grain crushing. Addition of carbonate-saturated water led to enhanced creep, dominated by fluid-enhanced grain scale microcracking and probably some contribution by diffusion controlled pressure solution. Addition of supercritical CO₂ to wet samples after 1 hour of creep, at 10 MPa pressure, accelerated creep transiently by 1-3 orders of magnitude due to decrease in mean grain contact area, and an increase in porosity, caused by simple dissolution of grain surfaces upon addition of CO₂-producing grain rearrangement, followed by faster cracking and/or faster IPS at grain contacts on reloading. In experiments where CO₂ was added to wet samples before loading, diffusion-controlled, intergranular pressure solution dominated creep at fine grain size, giving way to subcritical cracking control at grain sizes above 106 μm. In the pressure solution regime, creep showed effects of temperature and CO₂ pressure that were crudely consistent with the effects of these variables on calcite solubility, confirming previous models for the effects of CO₂ on pressure solution creep in carbonates [Renard *et al.*, 2005]. Viewed overall, the results suggest that if a depleted carbonate reservoir exhibits measurable compaction creep, then injection of supercritical CO₂ has the potential to speed this up by amounts up to 50 times, notably if creep is due to diffusion-controlled pressure solution.

Tests performed using saline pore-fluid solutions containing 0, 0.6, 1, 2 and 3 M NaCl or 0, 1 and 2 M MgCl₂, with and without supercritical CO₂ at a pressure of 10 MPa, have shown that addition of either salt (NaCl or MgCl₂) to the pore fluid in samples compacted with CO₂ caused a reduction in compaction creep rate at low salt concentrations (0.6-1 M). As salt concentration was increased to values of 2-3 M, creep rates increased to approach or exceed those seen in salt-free experiments. By comparison with microphysical models for the effects of salinity on pressure solution and with data on the effects of salinity in the

absence of CO₂, it is suggested that the effect of increasing salt concentration in samples tested with supercritical CO₂ is the net result of progressive inhibition of pressure solution and enhancement of subcritical crack growth.

Taking into account the fact that the pore fluid present in most carbonate reservoir is saline, the full body of data obtained indicate that storage of CO₂ in highly porous carbonate formations has the potential to increase creep rates by up to 10 rather than 50 times, depending on the salt concentration. However, it remains difficult to quantify or predict the rate of compaction creep of specific carbonate reservoirs in the context of CO₂ storage, as the compaction behavior and the relative importance of pressure solution versus subcritical crack growth are strongly influenced by porosity and other microstructural and compositional factors, as well as by salinity.

7.1.2 Mechanical behaviour of chalk in the presence of supercritical CO₂

Triaxial compression tests performed on chalk taken from the Dutch Maastrichtian were aimed at assessing the effect of carbonate-saturated solution on the mechanical strength and failure behaviour of this material, and any additional effect of injecting supercritical CO₂. Tests were performed under dry conditions at 20 and 80°C, as well as wet and wet with supercritical CO₂ at 80°C, using effective confining pressures of 0.5 to 7 MPa and pore fluid pressures of 5 and 10 MPa. At low effective confining pressures ($P_{eff} < 3$ MPa) all the samples failed in shear failure mode characterized by localization as macroscopic shear fracture. At higher effective pressure a transition occurred towards homogeneous compaction and pore collapse (> 4 MPa). Dry samples showed a compressive strength characterized by a shear/compaction yield envelope typical for highly porous granular materials. Increasing test temperature did not produce any marked effects on the strength of the dry samples. Addition of chalk-saturated water to the samples resulted in a drastic reduction of the strength (about 10 to 65 % reduction of yield strength), both in the shear failure and pervasive compaction regimes. Addition of supercritical CO₂ to wet samples had no further effect on the mechanical strength. The weakening effect of aqueous solution was explained in terms of reduction in frictional resistance of the material, due to water-enhanced grain-contact cracking and pressure solution, or possibly to disjoining pressure effects caused by water adsorption. On long-term processes such as intergranular pressure solution have to be considered for assessing mechanical stability of chalk in the context of CO₂ storage or leakage in such formations.

7.1.3 Mechanical failure of wellbore cement and the influence of supercritical CO₂

Similar triaxial compression tests have also been performed on mature, Class A Portland cement, of the type typically used to seal wellbores upon abandonment or oil and gas fields before 1980. The experiments were carried out at simulated reservoir conditions of 2-3 km depth, namely at temperatures up to 80°C and (effective) confining pressures in the range 1.5-30 MPa. The tests were done under dry and wet conditions, as well as wet with added supercritical CO₂. Wet and wet/CO₂ experiments were performed using pore fluid pressures of 5 and 10 MPa respectively.

The tests demonstrated that regardless of detailed conditions (dry, wet, wet/CO₂) Class A cement samples fail in a brittle manner marked by localized shear fracture, at low (effective) confining pressures (1.5 to 10 MPa), and in a ductile manner characterized by pervasive compactional deformation and strain hardening, at higher confining pressures. The compressive strength of the dried samples, measured in terms of yield or peak strength was insensitive to temperature but about twice the value obtained for wet samples deformed at otherwise similar conditions. Addition of supercritical CO₂ to wet samples led to a strengthening of the material in the compaction field, though the strength remained well below that of dry samples.

From a simple quantitative consideration of a range of possible mechanisms, the weakness of the wet material compared with the dried samples was explained as due to a lowering of the surface energy of the cement by wetting, which promotes equilibrium (Griffith-type) crack extension. The presence of water may also promote subcritical or stress corrosion crack growth. The increase in strength of the wet samples deformed in the presence of supercritical CO₂ was inferred to be due to an increase in the net energy of the cement-fluid interface, caused by CO₂ dissolution in the pore fluid, and to a decrease in subcritical crack growth rates caused by a shift in the pH of the pore fluid towards the point of zero charge of the calcium silicate hydrate gel phase present in the cement.

Previous calculations on stress development in wellbore cement plugs located in a typical caprock show that injection of fluids into depleted reservoirs will result in increased compressive stresses developing in the plugs. However, when compared to strength envelopes constructed from the present data for Class A cement it is clear that such stress changes will not lead to compressive failure of the cement. Extensional failure cannot be eliminated but is unlikely to propagate, assuming that carbonation seals the cement plug thus preventing any significant penetration of the cement by CO₂. Moreover, both field evidence (SACROC Unit) and healing experiments (Chapter 6) show that any fractures, which do form, are expected to heal rapidly. For the case of CO₂ injection into a depleted gas or oil reservoir overlain by a typical caprock, we infer that the stress changes that are expected to occur in the plugs pose little risk for CO₂ storage integrity.

7.1.4 Healing and sealing of wellbore cement in the presence of supercritical CO₂

Aside from investigating the mechanical failure behaviour of wellbore cement, the question of whether carbonation reactions improve or degrade the sealing/healing capacity of matured wellbore cement was investigated. To this end, batch reaction experiments were performed for up to three months, on both intact and axially fractured Class A Portland cement cylinders, at a constant confining pressure of 30 MPa, a temperature of 80°C and a CO₂ pressure of 10 MPa, i.e. at typical *in-situ* conditions. The wet samples were exposed to CO₂ at one end. Scanning electron microscopy and thermogravimetric analyses have shown that a carbonation front developed at the exposed surface in fractured cement samples. The carbonation front developed at the surfaces exposed to supercritical CO₂-saturated solution (at the end exposed to CO₂ and at the planes of the axial fracture)

advanced in time, leading to a densification of the material. Furthermore, thermogravimetric analyses, Scanning Electron Microscopy observations and permeability measurements indicated that carbonation of wellbore cement leads to a decrease of the porosity of the material on the reaction front and moreover, has the potential for healing pre-existent fractures and for improving the sealing properties of good-quality cement samples in time, at reservoir conditions.

7.2 Future research

Many ideas and questions arisen during the investigations presented in this thesis and during writing up. These suggest directions for future research, which will provide a more complete understanding of the coupled chemical and mechanical processes that will occur in the reservoir-caprock-wellbore system during CO₂ injection and long-term storage. The main points emerging are as follows:

1. In the present experiments on porous calcite aggregates, two different mechanisms were found to control compaction creep, namely intergranular pressure solution and subcritical crack growth. Extrapolation of such mechanisms to under *in-situ* conditions and incorporation of their effect into numerical models, which could help predict creep rates in carbonate rocks in the presence of supercritical CO₂ over long periods of time, requires constitutive models that incorporate the kinetics of dissolution, diffusion and precipitation the kinetics of subcritical crack growth. While the present study has confirmed that aspects of pressure solution can be crudely modeled, a reliable constitutive model that takes into account the effects of impurities on kinetics is lacking. For progress in this direction, further investigations on the coarser grained aggregates will be necessary at lower effective pressures to elucidate whether pressure solution will dominate creep in carbonate aggregates, in detriment of microcracking.

In addition, the mechanism of creep due to grain failure by stress corrosion cracking has to be understood separately; as such mechanisms are very poorly understood. Several approaches can be taken to tackle this problem. First, a microphysical model is needed for this type of mechanism. Early attempts at this have been made by [Brzesowsky, 1995; Zhang *et al.*, 1990], but this needs to be extended to help understand the direct dependence of creep rate on grain size that seems to be associated with this process. Second, systematic uniaxial compaction experiments on fine grained wet and CO₂-bearing calcite aggregates (< 106 μm) need to be performed at sufficiently high effective stresses (above 40 MPa), to investigate the subcritical crack growth regime. Additional experiments investigating creep behaviour at various CO₂ pressures and temperatures will be necessary in order to determine whether CO₂ pressure has any effect on stress corrosion cracking or crack growth and to determine the activation energy of this mechanism. Finally, work is needed to explore the interaction between pressure solution and grain scale microfracture in carbonates [Renard *et al.*, 2000]. Indenter techniques such as those used by [Gratier, 1993; Zubtsov *et al.*, 2005] should be employed at simulated *in-situ* reservoir conditions, relevant for CO₂ storage, in order to investigate how the development of fractures can accelerate the pressure solution process in calcite and how

these mechanisms compete with each other. By combining microphysical models with these experimental results, it should be possible to construct a creep law for compaction by stress corrosion cracking.

2. The present experiments on simulated carbonate rocks and chalk have underlined the need for additional data on reaction rates in the calcite-water- CO_2 system notably under high pressure and temperature conditions characteristic of CO_2 storage. Along with *in-situ* reaction cells used in combination with Fourier Transform Infrared Spectroscopy and other spectroscopic methods offer opportunities for measuring the kinetics of dissolution and precipitation of fine-grained calcite reacting with CO_2 , water and brine at conditions relevant for CO_2 storage. This, together with additional data on creep mechanisms in calcite wet and CO_2 -bearing rocks, will provide better insight into kinetic parameters needed to construct microphysical models for compaction creep of carbonates under geological and CO_2 sequestration conditions.

3. The complex effect of salts on the creep of simulated carbonate rocks, as described in Chapter 3 point out the need for site specific investigations when considering carbonate reservoir rocks as potential hosts for CO_2 storage. Our experiments have shown that salts have opposite effects depending on their concentration in the pore fluid.

4. As indicated by our experiments described in Chapter 3, the failure strength of chalks is not significantly influenced by injection of supercritical CO_2 , at least on laboratory time scales. However, previous experimental work points to towards pressure solution creep occurring in chalks subjected to CO_2 -saturated solution for long times [Hellmann *et al.*, 2002a; Hellmann *et al.*, 2002b; Madland *et al.*, 2006]. These findings, together with our experimental investigations presented in Chapters 2 and 3, emphasize the need for further systematic investigations of the creep and failure behaviour of chalks and other carbonates, after long-term exposure to supercritical CO_2 . In addition, previous studies by [Austad *et al.*, 2005; Heggheim *et al.*, 2005; Homand, 2000; Puntervold and Austad, 2008] have indicated that the presence of ions such as Ca^{2+} , Mg^{2+} and SO_4^{2-} in the pore fluid, increases wettability of chalks, promoting thus water weakening of such material. Therefore, further triaxial compression tests on chalks samples, with added salts to the CO_2 -rich pore fluid are still needed. While the dramatic water weakening effect seen in chalk remains controversial, the present experiments have suggested it is due to reduction in frictional resistance of the material, caused by water-enhanced grain-contact cracking and pressure solution, or possibly to disjoining pressure effects caused by water adsorption. This raises the possibility of whether addition of dissolution/precipitation inhibitors can prevent water weakening. Such data would be highly beneficial mainly for enhanced oil recovery in chalk reservoirs.

5. While the present results on the mechanical strength of Class A Portland cement show that wellbore integrity is unlikely to be compromised by compressive stresses developed within the wellbore cement plug during CO_2 injection, it is unclear how such cements will respond to tensile stresses in the presence of CO_2 . Additional experiments investigating the tensile regime of failure of Class A Portland cement are needed under wet conditions

and in the presence of supercritical CO₂. Such data would provide more complete strength envelopes as input for geomechanical models aimed at assessing the long-term integrity of CO₂ storage. Given the relevance of wellbore integrity in the context of CO₂ storage, and the many new types of wellbore cement introduced in the recent years, similar triaxial experimental techniques to the ones presented here should be applied to a wider range of cements.

6. The batch reaction experiments reported here have shown high potential for self healing and sealing of pre-existent fractures present in Class A Portland cement when exposed to water and CO₂. The carbonation reaction has been shown to produce a densification of the cement at interfaces in contact with supercritical CO₂, due to the dissolution of portlandite and other cement phases, plus precipitation of calcite. Our results for fractured samples show slower rates of permeability decrease, which need better quantification. This could be addressed by long term experiments whereby fractures, wet cement samples are simply stored for several years in contact with supercritical CO₂. Considering the usage of various types of wellbore cements with different in composition in the recent years, work is also needed on these cements under realistic *in-situ*, wellbore conditions using site-specific cements and various types of pore fluid, including brines. Of particular importance are reaction experiments resembling those reported in this thesis but addressing all components of typical wellbore systems, i.e. cement, casing and caprock. Such work is needed to assess the effects of corrosion of the casing on reaction occurring in the cement, and to estimate the volume changes of the phases produced which could generate stress changes in cement sheath, steel casing or cement plug.

Reference list

- Austad, T., et al. (2005), Seawater as IOR fluid in fractured chalk. , in *Oilfield Chemistry Symposium*, edited, PE Paper 93000, Houston, TX.
- Brzesowsky, R. H. (1995), Micromechanics of sand grain failure and sand compaction, 180 pp, Universiteit Utrecht, The Netherlands, Utrecht.
- Gratier, J.-P. (1993), Experimental Pressure Solution of Halite by an Indenter Technique, *Geophysical Research Letters*, 20.
- Heggheim, T., et al. (2005), A chemical induced enhanced weakening of chalk by seawater, *Journal of Petroleum Science and Engineering*, 46(3), 171-184.
- Hellmann, R., et al. (2002a), Experimental pressure solution of chalk in aqueous solutions. Part 2. deformation examined by SEM, porosimetry, synthetic permeability, and X-ray computerized tomography, in *Water-rock interactions, ore deposits, and environmental geochemistry: a tribute to David A. Crerar*, edited by The Geochemical Society .
- Hellmann, R., et al. (2002b), Experimental pressure solution of chalk in aqueous solutions: Part 1. Deformation behaviour and chemistry., in *Water-Rock Interactions, Ore Deposits, and Environmental Geochemistry: A Tribute to David A. Crerar*, edited by The Geochemical Society.
- Homand, S., Shao, J. F. (2000), Mechanical behaviour of a porous chalk and effect of saturating fluid, *Mechanics of Cohesive-frictional Materials*, 5(7), 583-606.
- Madland, M. V., et al. (2006), The influence of CO₂ gas and carbonate water on the mechanical stability of chalk, *Journal of Petroleum Science and Engineering*, 51(3-4), 149-168.
- Mainguy, M., et al. (2007), Analyzing the risk of well plug failure after abandonment. , *Oil & Gas Sci. and Tech. - Rev. IFP*, 62(3), 311-324.
- Punternold, T., and T. Austad (2008), Injection of seawater and mixtures with produced water into North Sea chalk formation: Impact of fluid-rock interactions on wettability and scale formation, *Journal of Petroleum Science and Engineering*, 63(1-4), 23-33.
- Renard, F., et al. (2000), Kinetics of crack-sealing, intergranular pressure solution, and compaction around active faults, *Journal of Structural Geology*, 22(10), 1395-1407.
- Renard, F., et al. (2005), Numerical modeling of carbon dioxide sequestration on the rate of pressure solution creep in limestone: Preliminary results, *Oil & Gas Science and Technology*, 60, 381-399
- Rutqvist, J., et al. (2008), Coupled reservoir-geomechanical analysis of the potential for tensile and shear failure associated with CO₂ injection in multilayered reservoir-caprock systems, *International Journal of Rock Mechanics and Mining Sciences*, 45, 132-143.
- Soltanzadeh, H., et al. (2007), Poroelastic model for production and injection-induced stresses in reservoirs with elastic properties different from the surrounding rock., *International Journal of Geomechanics*, 7, 353-361.
- Zhang, J., et al. (1990), Micromechanics of pressure-induced grain crushing in porous rocks, *Journal of Geophysical Research*, 95(B1), 341-352.
- Zubtsov, S., et al. (2005), Single-contact pressure solution creep on calcite monocrystals, *Geological Society, London, Special Publications*, 243(1), 81-95.

Acknowledgements

This is the end of my PhD journey and I can finally thank to all the people that made my trip interesting, beautiful and different than I expected.

First of all I would very much like to thank to my HPT family for adopting me and for being my family away from home. And in this case my special thank goes to Chris Spiers, my supervisor and promotor for believing in me, for giving me the opportunity to work on such a fascinating topic and for showing me a different way of doing research. Chris, I know that many times I was stubborn but I enjoyed very much our long conversations debating pressure solution, microcracking, crappy microstructures, how to survive in the “Dutchland” or other life-related issues. Thanks for teaching me how to do and how not to do things and thanks most of all for inspiring me and for believing in me. I think our entire struggle was worth it, and now I can say out loud WE MADE IT! (without being afraid that an earthquake will hit Holland and I will never be able to defend).

My thanks goes also to my first co-promotor Colin Peach, who was first to welcome me in The Netherlands and later on helped me a lot when having troubles figuring out the machines in the lab. Colin, your passion for electronics was a great example for me. Hans, you joined the boat at a later stage, however it was great to have you around. First of all, I would like to thank you for showing me the dutch mountain, for helping me getting the chalk samples and most of all for being my co-author on several papers and for all the stimulating and fruitful conversations.

Our trio of technicians made a tremendous contribution to making this PhD happen. Eimert de Graaf, Gert Kastelein and Peter van Krieken have always done a great job of fixing or making from scratch pieces of equipment, or helping me deal with CO₂ – related leakage crisis. I am happy I could have such creative and great people to work with, who were always there when needed. Furthermore, Magda you were of great help whenever trying to figure out administrative issues or whatever other problems that I encountered during my Ph.D. – you can make miracles happen, can’t you? Thanks for having always a solution and for the most efficient secretary I have ever met. My later office mate – Saskia, it was a pleasure to spend my office time with you, thanks for being always objective and supportive, for helping me in my battle against microstructural evidence.

My PhD fellows – I will miss you all, our coffee breaks, the long lunchtjes and the funny and enthusiastic conversations about how to survive your PhD or how to deal with CO₂ leakages or o-rings friction. Thanks a bunch to Andre, Arthur, Esther (thanks for being there for nice conversations, for never ending complaining sessions, and for giving me a shoulder to cry on, it is great knowing you and I hope you will remain yourself, no matter what happens) Frank, Sabine, Sabrina, Sander (for promoting with such patience the Dutch culture), Suzanne, Reinier (those vampire or Romanians related jokes were actually very funny) for being my colleagues, for helping me learn Dutch (well, at least trying), for showing me how things are done in The Netherlands, how to make a plan and how to keep an agenda or how to enjoy krokettjes and kaasouffletje.

I would also like to thank the people from my sponsor – TNO for their interest in my project and for the helpful input, especially to Cor Hofstee, Arie Obdam and Tjirk Benedictus. Also it has been an honour to be a member of the CATO programme and to meet so many people that care or have so much knowledge on climate changes or CCS, such as Erik Lysen, Sander van Egmond, Henk Pagnier and Pascal Winthaegen, among many others

A big thank goes to my friends and colleagues from UU that were around for the past years: Andy, Ahmet, Come, David, Kristen and Brad, Siska, Thomas, my Romanian gang – Cornelia, Gabi, Iuliana, Marcela (multam fetele pentru pranzurile dementiale de la cantina, pe cand ne vedem la o ciorba?).

When I came to Holland I was so lucky to meet so many great people, that later became my friends and with whom I am happy to share a very warm friendship and amazing memories: Ale, Ana, Angeles (can't wait to see you in Madrid), Andy, Beth (I wish Cincinnati was next door so I can see you much more often), Caro, Eliana, Irene, John, Juliana, Julian, Kiki, Lih, Lo, Mar, Marco D'Alessandro, Marco Maneta, Martin, Matteo, Oded, Olga (I miss our dancing evenings), Ryan, Santi, Sara, Sonia, Vicky (a romantic weekend soon?), Takeshi, Tanja, Watse, Yoli, Zorica.

First I met Alejandro - Ale at first I did not really understand you, but soon I became fluent in Ale's spanglish and I came to realize how lucky I am to have you as one of my best friend, almost brother, my housemate, my "la penultima" buddy ...and so much more. Thank you so much for being a part of my life.

Wiebke – I know that we did not meet under the best circumstances, but at later stages of our friendship we made it up. Thanks so much for being such an amazing friend, and I hope you and Baris (geologists are cool, huh?) will be around for much longer, if you do so I promise I will cook even nicer food. To my crazy Lo, thanks for our "LCU at 12.30", for the collective diets, for the crazy laughs, for our endless compains, but most of all for being supportive and for always being my crazy French friend. Tanja, my sweet friend from the far north, I miss you so much around here, but I know that whenever we meet again we can start from where we were before, thanks for showing me how to be optimistic no matter what and...for teaching me the difference between tissue and napkin. Sabina, iti multumesc pentru toate dupa amiezile petrecute impreuna, pentru crizele de ras isteric, pentru pauzele de cico, pentru toata ciucalata furnizata si pentru ca imi esti prietena. Ma bucur enorm ca vom ramane impreuna in tara ploilor interminabile pentru ceva vreme si iti doresc mult success in calatorie spre un nou doctorat.

At last to my two my paranimphjtjes – you are the best paranimfs I can dream of – I am so lucky to have both of you as friends.

Su, you were for the past years my CO₂ twin, my SuperSu, my schatje, my dutchie friend – you are my almost everything, I wonder what else is on the list. But we will find out soon, aren't we? Sweetie I am so grateful that you were here, that we could discuss CO₂ related issues, that I got to share my machines and my couch with you, thanks for making the local culture understandable for me (well it must be difficult for you too- you come from the south anyway), for being my conscience and for all the motivational speeches and messages that at times helped me to go further.

Τίνα – αι τια μια, θυε βελλεζζα, θυε λοχχυρα, θυε αλεγρια το ηαπε μετ ψου. Ι μισσ ψου σο μυχη τηατ νοω Ι ωιση Ι χαν δεφενδ μυ τηεσις επερψδαμ σο ωε χαν γο τογετηερ φορ α θυιχκιε, το γο χηοπ χηοπ, το

Τιβόλι, το παψ α βισιτ το Σαν Μαρχο δ'εσπιννινγ (δον'τ φοργετ ψουρ παντσ της τιμε), το ενφοψ σομε καασ σουφφλετρε τογετηερ, το γετ α δυο πιερχινγ...ανδ σο μανψ οτηερ τηινγσ τηατ ωε διδ δυρινγ ψουρ σταψ ιν Ηοηολαλανδ. Βυτ Ι κνωω τηατ ωε ηαπε ουρ παχκπαχκ ανδ σο μανψ μορε πλαχεσ το βισιτ σο μανψ πενιχεσ, βαρχελονετασ, μαδριδιτασ αρε στιλλ λεφτ το δισχοπερ-ηαστα σιεμπρε.

Savvas, many thanks for your support, for listening to my endless complains, for being calm whenever I was a ball of fury, for encouraging me to go further and to reach my goal, for believing that I can make it and most of all putting up with all my endless cooking.

Prietenilor mei de acasa Gabi (abia astept sa ne vedem la urmatoarea runda de chicoteli si la o barfa mica) si Edi, Ioana si Aurel, Alina si Puf (sper sa re-editam in curand un munte ca in tinerete) va multumesc pentru ca ati fost intotdeauna alaturi de mine si pentru ca prietenia noastra a rezistat in ciuda distantei.

La final, multumesc familie mele pentru ca crezut mereu in mine si m-a incurajat intotdeauna sa imi urmez visele. Fara voi nu as fi reusit sa devin ceea ce sunt azi, sa fiu fericita si sa ajung unde sunt. Sunteti minunati si sper sa ramanti asa intotdeauna. Nico si Adi, va multumesc pentru incurajarile voastre, pentru suportul neconditionat, va multumesc pentru ca existati in viata mea, pentru ca mi-ati fost intotdeauna cel mai mare sprijin si pentru ca datorita voua am cele mai minunate nepotele Delia si Malina.



